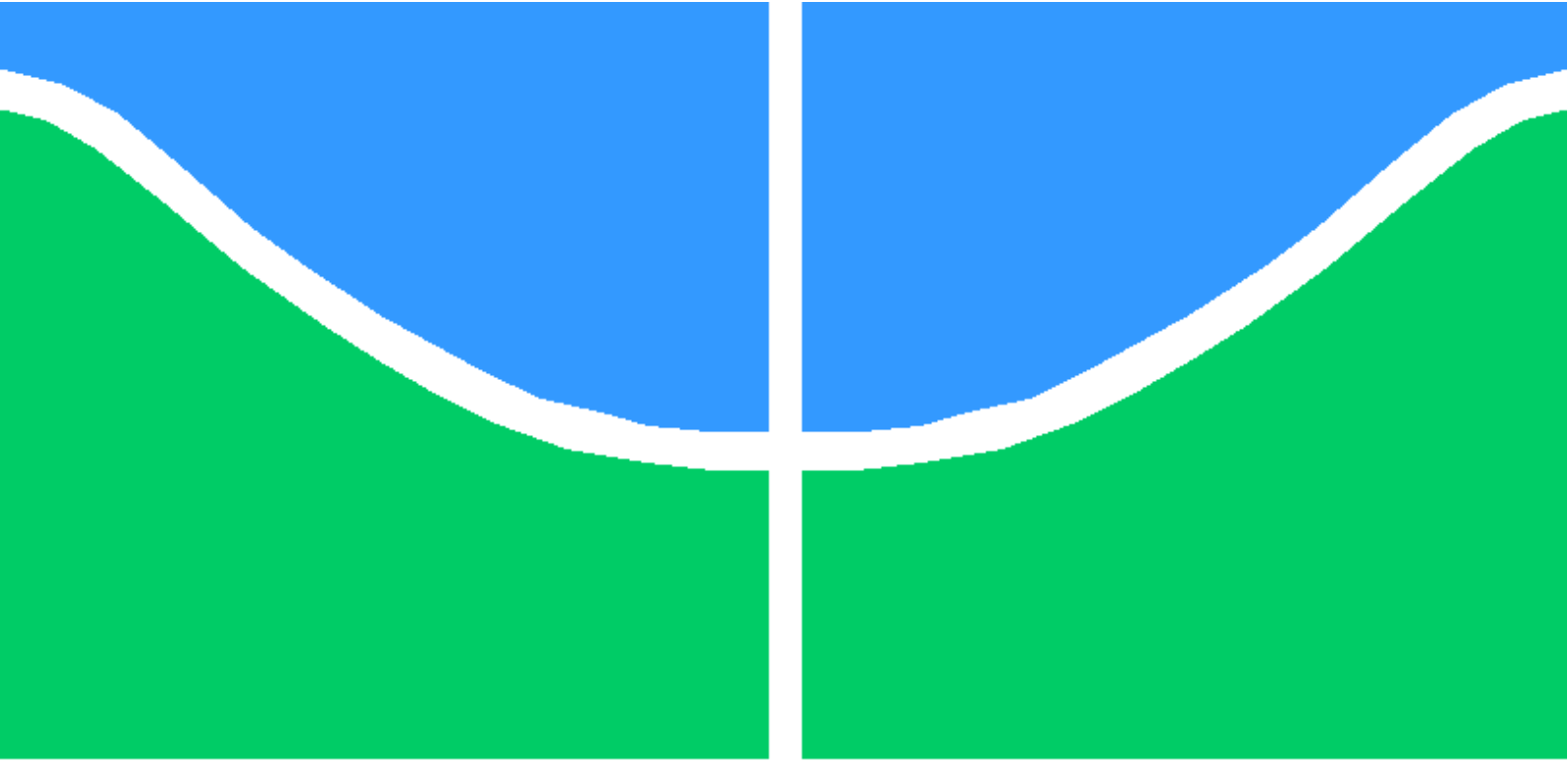

TESE DE DOUTORADO

ON THE MOTION OF ACTIVE PARTICLES IN NEWTONIAN AND NON-NEWTONIAN LIQUIDS

YVES-GARNARD IRILAN

Brasília, Abril de 2022

UNIVERSIDADE DE BRASÍLIA

FACULDADE DE TECNOLOGIA

UNIVERSIDADE DE BRASILIA
Faculdade de Tecnologia

TESE DE DOUTORADO

ON THE MOTION OF ACTIVE PARTICLES IN NEWTONIAN AND NON-NEWTONIAN LIQUIDS

YVES-GARNARD IRILAN

Thesis submitted to the Department of Mechanical Engineering of the Faculty of Technology of the University of Brasilia as part of the requirements required to obtain doctor grade in Mechanical Sciences.

Examining Committee Brasília, DF,

Dr. Francisco Ricardo da Cunha/(ENM-UnB) *Advisor*	_____
Dr. Paulo César de Morais/(UFC-DF) *External Member*	_____
Dr. Aristeu da Silveira Neto/(UFU-MG) *External Member*	_____
Dr. André von Borries Lopes/(ENM-UnB) *Internal Member*	_____
Dr. José Luiz A da Fontoura Rodrigues/(ENM-UnB) Alternate member	_____

Ficha catalográfica elaborada automaticamente,
com os dados fornecidos pelo(a) autor(a)

IIY88o

IRILAN, Yves-Garnard
ON THE MOTION OF ACTIVE PARTICLES IN NEWTONIAN AND NON NEWTONIAN LIQUIDS / Yves-Garnard IRILAN; orientador Francisco Ricardo Da Cunha. -- Brasília, 2022.
171 p.

Tese (Doutorado - Doutorado em Ciências Mecânicas) -- Universidade de Brasília, 2022.

1. Low Reynolds number flow. 2. Helical flagellum. 3. Slender Body Theory. 4. Viscoelastic effects. 5. Magnetic active matter. I. Da Cunha, Francisco Ricardo , orient. II. Título.

Dedication

I dedicate this work to God, who with his infinite wisdom, was an important guide in my trajectory, to my wife Deborah Angélica ZAMBRANO OLÉA, my children Rafael ZAMBRANO IRILAN and Daniel ZAMBRANO IRILAN and all my family, who spared no effort to help me in this so important stage of my life.

YVES-GARNARD IRILAN

Acknowledgements

First of all, I thank God for giving me the courage, the strength, and the patience to complete this modest work. I thank God, because during this journey has always given me signs that it is worthwhile to continue. I also thank you for the gift of intelligence and for a healthy life. I am grateful to Brazil, the University of Brasilia, and the graduate program in mechanical sciences for the opportunity and infrastructure, direction, and administration. Here has been really rewarding, personally, and I am grateful that the department trusts its postgraduate staff to do such important work. Special thanks to the CAPES program for the support and financial incentive over the four years of the doctorate. I thank my advisor, Professor Francisco Ricardo Cunha, who agreed to take me on as a Ph.D student. Thank you for introducing me to the world of the hydrodynamics of complex fluids and active suspensions and for allowing me to do this thesis work. I thank you too for the trust, friendship, dedication, and generosity in transmitting his deep knowledge in suspension theory during the four years of working together in the Fluid Mechanics Group. Complex flows. I would also like to thank Professor Francisco for allowing me, as well as the other students of the Group, access to a privileged work environment in the Vortex Group facilities. I thank my wife Deborah Angelica Zambrano Olea, my companion of all hours, thank you to you Debby for your patience in rereading my manuscript, you were able to flush out all the "flagella"well hidden in my manuscript. Special thanks to my children Rafael Zambrano Irilan, Daniel Zambrano Irilan, thank you for your patience and support at all times. I am grateful for the affection, love, and understanding that you had due to some periods of my absence. Without your love, life makes less sense. You complete me. I thank my family, my brothers, my father, especially my mother Alexis Filozia, although you are far away, they never stopped supporting me. I want to thank you for everything that you have already done. In particular, I must thank the colleagues of the Vortex group, especially my friends, Igor Pereira to help me in the experimental part mainly when teaching the operation of the Reometer and generating some experimental data that were used in this work. Big thanks to Filipe Evangelista for the kindness of having given the original code FORTRAN for the simulation of magnetic bacteria. I am grateful to the other friends and companions of Vortex: Andrey, Alvaro, Gesse, Yuri, Victor (Suarez), Victor(Shumyatski) with whom it was a great pleasure to share the work environment, talk about science and other matters of equal or less importance. I thank all the teachers with whom I had classes, particularly teachers Yuri Dumaresq, Taygoara, also, Edson the laboratory technician. I would like to thank Professor Dr. Paulo César de Morais, Professor André Von Borries Lopes, Dr. Aristeu da Silveira Neto for having been accepted to be part of my thesis jury and for the evaluation and suggestions presented to improve the work. I would like to thank in particular to Professor Dr. Rafael Gabler Gontijo and Professor Dr. José L. A Fontoura Rodrigues for agreeing to participate in the thesis qualifying examination and for the important evaluation and precise suggestions presented to make better this thesis.

Finally, I would like to thank all the people who participated, directly or indirectly, in the production of this thesis. A very big THANK YOU to everyone who gave me her love and provided the motivation. I send them all my gratitude from the bottom of my heart.

YVES-GARNARD IRILAN

RESUMO

Este trabalho apresenta uma investigação sobre a locomoção de partículas e organismos em baixos números de Reynolds usando modelos matemáticos, numéricos e estudos experimentais. Primeiramente, estudamos o efeito da elasticidade do fluido na força propulsora e torque no corpo e velocidade de velocidade do nadador em termos de dois parâmetros físicos: número de Deborah (De) e número de Strouhal (Sh). Para tanto, são realizados alguns experimentos com microrganismos protótipos em movimento de escoamento rasteiro. Nos experimentos, um nadador macroscópico que se impulsiona imitando flagelos helicoidais é desenvolvido e testado. Três modelos de natação impulsionados por uma cauda helicoidal com diferentes comprimentos de onda são investigados e seus movimentos examinados para ambos os casos: quando o solvente ambiente é um fluido viscoso newtoniano puro e quando o fluido base é uma solução polimérica elástica. Além disso, também aplicamos a Slender Body Theory (SBT) e o método de Stokeslet regularizado (RSM) para calcular teoricamente a força e o torque, em função do número de Strouhal (Sh), produzidos pelo nadador helicoidal em movimento em um fluido newtoniano. Os resultados teóricos são comparados com dados experimentais e uma concordância muito boa é observada especialmente para valores mais altos de Sh dentro das barras de erro dos dados experimentais. No caso de um fluido de base não newtoniano, o problema de escoamento de um fluido elástico Oldroyd-B é resolvido numericamente usando um código computacional baseado no método dos elementos finitos (CFD). A velocidade propulsiva do nadador helicoidal é calculada em função do parâmetro elástico número de Deborah e também comparada com a observação experimental quando o fluido base não é newtoniano. É mostrado experimentalmente que a velocidade de natação aumenta à medida que o efeito elástico no fluido de base aumenta até um número de Deborah crítico O(1), quando a velocidade satura para um valor constante dentro das barras de erro experimentais. A anisotropia de velocidade medida experimentalmente pela razão da velocidade do nadador em duas direções diferentes é insensível ao efeito elástico nos fluidos de base. Completamos nossa discussão sobre o movimento de nadadores helicoidais em escoamento rastejante, apresentando uma comparação entre as previsões da velocidade da velocidade dadas pela simulação CFD usando um modelo Oldroyd–B para o fluido elástico de base e dados experimentais. A concordância entre os dois conjuntos de resultados é muito boa dentro das barras de erro experimentais para o parâmetro elástico variando de 0 a 2. Pode-se notar, entretanto, que enquanto os dados experimentais tendem a saturar em De maiores, os resultados das simulações parecem ter um aumento contínuo de acordo com o modelo constitutivo de usado para descrever o líquido elástico base. Em segundo lugar, estudamos as bactérias magnetotáticas que se tornaram foco nas pesquisas sobre mecânica dos fluidos com baixo número de Reynolds. Esses microorganismos podem nadar no sangue e possuem ímãs dentro deles. Portanto, a investigação do movimento em líquidos viscosos deste tipo de partículas ativas para o transporte de drogas na circulação sanguínea sob aplicação de um campo magnético ainda não é suficientemente conhecida. Realizamos simulações numéricas Langevin do movimento de cadeias magnéticas compostas por partículas rígidas esféricas polidispersas. A estrutura das cadeias representa um modelo bruto de uma bactéria magnetotática movendo-se em um líquido viscoso com baixo número de Reynolds e também sob a ação do movimento browniano, um campo

magnético externo e sob influência de interações magnéticas dipolares. As equações governantes são feitas adimensionais e os parâmetros físicos para controlar o movimento do microrganismo são identificados. Enquanto as interações magnéticas dipolares entre as partículas são consideradas, as interações hidrodinâmicas viscosas são ignoradas nas presentes simulações. A configuração inicial da partícula magnética na simulação considera aquelas alinhadas como estrutura de cadeias com um número diferente de partículas magnéticas semelhante à estrutura de uma espinha de bactérias real que é formada por uma cadeia de cristais magnéticos. Examinamos a cinemática das bactérias magnéticas com diferentes números de partículas na cadeia.

Palavras-chave: Fluxo de baixo número de Reynolds, flagelo helicoidal, teoria do corpo delgado, efeitos viscoelásticos, movimento browniano, efeito coletivo, interações dipolares, partícula ativa, matéria ativa magnética.

ABSTRACT

This work presents an investigation on the locomotion of particles and organisms at low Reynolds numbers using mathematical, numerical models as well as experimental studies. Firstly, we study the effect of fluid elasticity on the propulsive force and torque on the body and speed velocity of the swimmer in terms of two physical parameter: Deborah number (De) and Strouhal number (Sh). For this end, some experiments with prototype microorganisms in creeping flow motion are conducted. In the experiments a macroscopic swimmer which propels itself by mimicking helical flagella are developed and tested. Three swimming models propelled by a helical tail with different wavelengths are investigated and their motions examined for both case: when ambient solvent is a pure Newtonian viscous fluid and when the base fluid is an elastic polymeric solution. In addition, we also apply the Slender Body Theory (SBT) and the method of regularized Stokeslet (RSM) in order to calculate theoretically the force and torque, as function of the Strouhal number (Sh), produced by the helical swimmer moving in a Newtonian fluid. The theoretical results are compared with experimental data and a very good agreement is observed specially for higher values of Sh within the error bars of the experimental data. In the case of a non-Newtonian base fluid, the flow problem of an Oldroyd-B elastic fluid is solved numerically using a computational code based on a finite element method (CFD). The helical swimmer propulsive velocity is calculated in terms of the elastic parameter Deborah number and also compared with the experimental observation when the base fluid is non-Newtonian. It is shown experimentally that the swimming speed increases as the elastic effect in the base fluid increases until a critical Deborah number number O(1), when the velocity saturates for a constant value within the experimental error bars. The velocity anisotropy measured experimentally by the ratio of the swimmer speed in two different directions is insensitive to the elastic effect in the base fluids. We complete our discussion on the helical swimmers motion in creeping flow by presenting a comparison between predictions of the speed velocity given by CFD simulation using an Oldroyd–B model for the base elastic fluid and experimental data. The agreement between the two sets of results is very good within the experimental error bars for the elastic parameter varying from 0 to 2. It may be remarked, however, that while the experimental data tends to saturate at larger De, the simulations results seems to have a continuous increase according to the constitutive model of used to describe the base elastic liquid. Secondly, we study magnetotactic bacteria that have become the spotlight in research on fluid mechanics at low Reynolds number. These microorganisms can swim in blood and they have magnets within them. Therefore the investigation of the motion in viscous liquids of this kind of active particles for carrying drugs in the blood circulation under application of a magnetic field is still not known sufficiently. We perform Langevin numerical simulations of the motion of magnetic chains composed of polydisperse spherical rigid particles. The chains structure represents a crude model of a magnetotactic bacteria moving in a viscous liquid at low Reynolds number and also under the action of Brownian motion, an external magnetic field, and under influence of dipolar magnetic interactions. The governing equations are made non-dimensional and the physical parameters in order to control the microorganism's motion identified. While the magnetic dipolar interactions between the particles are considered, the viscous hydrodynamic

interactions are ignored in the present simulations. The initial configuration of the magnetic particle in the simulation considers the ones aligned as chains structure with a different number of magnetic particles similar to the structure of a real bacteria spine which is formed by a chain of magnetic crystals. We examine the kinematics of the magnetic bacteria with different numbers of particles in the chain.

Keywords: Low Reynolds number flow, Helical flagellum, Slender Body Theory, Viscoelastic effects, Brownian motion, Collective effect, Dipolar interactions, Active particle, Magnetic active matter.

Contents

List of Figures

List of Tables

List of Symbols

Dimensionless Group

De	Deborah number
Re	Reynolds number
Pe	Péclet number
Sh	Strouhal Number
St	Stokes number
Wi	Weissenberg number
α	Magnetic field parameter
λ	Dipolar interaction parameter

Latin Symbols

$\mathbf{A}, \mathbf{B}, \mathbf{C}, \mathbf{D}$	Propulsion matrix coefficients $[m]$
a	Filament Radius $[m]$
C_t, C_n	Resistance Force Coefficient $[-]$
f	Force per unit length on the flagellum N/m
$\boldsymbol{F}$	Force $[N]$
$\mathbb{G}_h$	Matrix Propulsion []
$\mathbb{I}$	Tensor Identity $[-]$
$\mathbb{J}$	Oseen Tensor $[-]$
$\mathbb{K}$	Resistance tensor per unit length []
L	Apparent Length $[m]$
m	Mass $[Kg]$
$\mathbb{P}$	Mapping tensor []
$\boldsymbol{q}$	Auxiliary vector
$\boldsymbol{Q}$	Auxiliary vector
r_0	Position vector from s $[m]$
R	Helical Radius $[m]$
t	Time $[s]$
$\boldsymbol{T}$	Torque $[Nm]$
$\mathbf{D}$	Tensor strain rate $[s^{-1}]$
$\boldsymbol{u}$	Velocity field $[m/s]$
s	Point along the centerline of the flagellum
S	Stokeslets $[-]$
p	Pressure $[Pa]$
$\boldsymbol{v}$	Velocity $[m/s]$
$\mathbf{x}$	Position vector $[m]$
x, y, z	Cartesian coordinates
U	Linear velocity $[m/s]$
N	Number of turns $[-]$
Ω	Angular velocity $[rad/s]$

Greek Symbols

α	Euler angle
θ	Pitch Angle
β	Euler Angle
γ	Euler angle
$\dot{\gamma}$	Shear rate $[1/s]$
ϕ	radially symmetric cutoff function []
φ	construction Angle
ρ	Density $[m^3\, kg^{-1}]$
τ	Stress tensor []
ϵ	Regularization parameter $[-]$
δ	Natural cutoff $[m]$
λ	Wave length $[m]$
Λ	Wave length measured along the flagellum $[m]$
μ	Dynamic viscosity $[Pa\, s]$
ω	Angular velocity $[s^{-1}]$
π	mathematical constant $[-]$
∇	Nabla operator

Operators

∇	Gradient Operator
$\nabla\cdot$	Divergent Operator
$\nabla\times$	Rotational Operator
$\dfrac{\partial}{\partial t}$	Partial temporal derivative
$\Delta = \nabla^2 = \nabla \cdot \nabla$	Laplacian operator
$\dfrac{d}{dt}$	Ordinary Temporal Derivative
$\delta(t - t_0)$	Kronecker Delta Operator
$\det(\mathbf{A})$	Tensor Determinant $\mathbf{A}$
$\int$	Integral
$\in$	Belonging to the set
$\dfrac{D}{Dt}$	Material derived operator
$\|\|\mathbf{u}\|\|$	vector modulus $\mathbf{u}$.

Superscripts

$\triangledown$	Upper derivative
$*$	Non Dimensional form

Subscripts

h	Hydrodynamic
$Scale$	Scale

Acronyms and Abbreviations

ABNT	Associação Brasileira de Normas Técnicas
DC	Direct Current
BEM	Boundary Element Method
CFD	Computational Fluid Dynamics
MRS	Method of Regularized Stokeslets
RFT	Resistive Force Theory
SBT	Lighthill Slender Body Theory
SBT	Slender Body Theory
MEMS	Micro-Electro-Mechanical Systems
MIS	minimally invasive surgery (MIS)
FESEM	Field Emission Scanning Electron Microscope
UnB	Universidade de Brasília
MHD	Magneto-hydrodynamic
FHD	Ferro-Hydrodynamic
DL	Dynamic Langevin
MTB	Magnetotactic Bacteria
SMR	Magneto-rheological suspensions
GNF	Generalized Newtonian Fluid
PPM	Parts per million
PAMA	Anionic Polyacrylamide
FORTRAN	Formula Translation System
LED	Light-emitting diode

Chapter 1

Introduction

1.1 Contextualization

Suspensions of microorganisms such as bacterias or even man-made micro-swimmers are encompassed in the wider class of living fluids. The locomotion mechanics at the low Reynolds number of these microorganisms is fantastic, but this locomotion regime is not fully understood. An attractive theme of research that has long time provided different branches of natural sciences and engineering with an infinite list of problems is the physics of swimming micro-organisms. The physics of swimming micro-organisms has inspired many numerical and experimental simulations of self-propelled particles [5, 6, 7, 8]. The study of swimming organisms including bacteria, actives particles has long been of scientific interest. There are two types of swimmers, biological and synthetic. The first category includes biological micro-swimmers, which are mobile cells, such as swimming bacteria or sperm, and many other single-celled organisms, such a *archaea*, *protozoa*, *algae*, and *fungi*. The second category refers to different types of techniques or projects carried out, with direct applicability in nanotechnology, to transport medicines for cancer treatments or minimally invasive surgery, also called suspensions with artificial objects or micro-robots. Understanding how the system behaves is very important and both biological and synthetic micro-swimmers are used to understand how they move in a suspension and how they interact with their environments [9, 10, 11, 12].

The Scallop Theorem explains that the kinematic reversibility of the fluid flow at low Reynolds number regime due to the disappearance of the time relation in the Navier-Stokes equation results in zero net displacement when the motion performed by the swimmer is reciprocal [13]. Small swimmers in low Reynolds environments must adapt strategies to break the symmetry of the motion or the fluid flow with respect to time. Bacteria, microbes, spermatozoa swim in Stokes flow conditions and propel themselves with ease therefore, scientists look at nature for an answer to this problem. It is observed that the small organisms propel themselves by means of flagella, cilia, or complex body deformations. For a natural bacteria in water, the rotation frequency is approximately 100 Hz, and using as characteristic length the radius of the helix and knowing the microscopic dimension of a flagellum the Reynolds number is around $Re \sim 10^{-4}$, showing viscous

effects are dominant and inertial forces are insignificant. Some bacteria use a single flagellum for propulsion and shift orientation. These types of micro-organisms have inspired artificial micro-swimmer in simple designs with medical or other applications [14].

The study of the locomotion of self-propelled has captivated the interest of the scientist in the last seven decades. There have been many classic reviews from the locomotion of actives particles and organisms [15] and [16]. The beginning of the research on the subject started from biophysics and the biology of cell motility. Many previous studies of cell motility in viscous fluids have been found for the last 80 years. Ludwig [17] pointed out that a microorganism that waves rigid arms is incapable of net motion. Gray [15] experimental have studied the motility of swimming organisms were including marine worms, snakes, spermatozoa, as well as cilia. Taylor [18] used a mathematical model to analyzed the swimming of organisms using small amplitude and low Reynolds number assumptions and compared his results with experimental data.

Another issue of interest is to understand how this locomotion affects biological processes such as human reproduction or bacterial survival and infection. More recently using natural bacteria, reference [19] has presented a statistical analysis on the kinematics-wave motion of a suspension of *Caenorhabditis elegans* in a gel-like medium. They have studied two different populations from a biological perspective of the surrounding medium. They have found experimentally a linear correlation between the length and the wavelength of the individuals for both populations and proposed a theoretical correlation to justify this linear dependence. The results have indicated that *C. elegans* indeed uses sinusoidal propulsion to move in creeping flow. This nonlinear motion is used to break the time reversibility in which they are trapped due to their small sizes, known as kinematic reversibility in low Reynolds number flows. Another important finding by the authors is the discrepancy observed in the collective motion of both populations. They observed also that well-fed individuals tend to move in the direction of *Escherichia coli* colonies with less spreading in the surrounding medium. On the other hand, a starving population collectively behaves differently, seeking food in several possible directions and with much more strong head motion [20, 21, 22, 23].

An important aspect is the study of the hydrodynamic interactions of microorganisms using numerical and theoretical models. Kim *et al.* [24] studied the hydrodynamic interaction of a bacterium, they described the locomotion by the regularized Stokes formulation. The model of the single-flagellated micro-organism is able to mimic a swimming pattern that is well matched with the experimental observation. Furthermore, they find the critical thresholds of the rotational frequency of the motor and the bending modulus of the hook for the buckling instability, and investigate the dependence of the buckling angle and the reorientation of the swimming cell after buckling on the physical and geometrical parameters of the model. In the last years, magnetic nano-particles have played a great role in the creation of magnetic fluids with applications in biomedicine, magnetic resonances, deliberation of drugs in the human body, and the cancer treatment. Magnetic fluids are colloidal systems consisting of single-domain magnetic nanoparticles dispersed in a carrier liquid and are convenient model systems to explore fundamental properties of magnetic nano-particles systems, [25]. Also, we find a set of bacteria called Magnetotactic bacteria (MTB). An important characteristic is they can grow internally a microscopic magnet, hence providing an external handle to drive their swimming orientation. Then MTB are micro-

organisms of strong practical interest a great application of nano-magnetic particles used in a medical context. Also, the development of stable MTB has given rise to several applications for magnetic fluid. In medicine, biocompatible magnetic fluids can lead to future discoveries.

The magnetic alignment, combined with a micro-aerotactic swimming response, qualifiers such micro-swimmers as a promising vector for targeted drug therapy. Recently, it was proposed, on theoretical grounds, that a suspension of such magnetotactic bacteria could display original magneto-rheological properties novel pattern formation and hydrodynamic instabilities. In particular, the pearling hydrodynamic instability, the velocity condensation, and the emergence of new phases induced by a magnetic field are striking examples of these.

1.2 Literature Review

In the study of locomotion of microorganisms and particles, some synthetic devices have been designed to prove theoretical models [26, 27, 28] . A practical application is to study the motion of macro-swimmers in order to design micro and nanorobots. Rodenborn *et al.* [29] measured thrust, drag and torque for a macroscopic model flagellum and compared the measurements with theoretical predictions. The data compare very well with the slender body theories [17] and [30], respectively, and the regularized Stokeslet approach [31]. The effects of nonlinearities in a worm-like micellar solution can break time reversibility of the particle motion immersed in this solution and, consequently produce propulsion of an artificial swimmer [32]. Thawani *et al.* [33] built a macroscopic working model of a bacterium and visualized its detailed motion in high-viscosity liquid. The authors showed that a small asymmetry in the mass distribution in the head can lead to helical trajectories with large pitch and radius, which are reminiscent of the wiggling trajectories observed for swimming bacteria. The main results motion agrees well with the predictions from the slender-body theory that accounts for the asymmetric mass distribution in the head. Additionally, this research shows that the trajectory consists of two helical trajectories of different length scales a large one caused by the asymmetric mass distribution and set by the head rotation rate, and a smaller one caused by the rotating flagellum and set by its rotation rate. However, the investigation of this work does not include collective behavior. Collective behavior can be a way to separate hydrodynamic contributions from generic self-propulsion effects [32, 34]. Irilan and Cunha [35], used the Slender Body Theory (SBT) in order to describe the dynamics of swimming micro-organism with motion produced by helical flagellum propulsion. Numerical simulations are performed based on resistive force theories. The also carried out some experiments with a macroscopic prototype micro-organisms in creeping flow motion. Silicon oil is used in order to ensure a low Reynolds number around the particle. The propulsive velocity, angular velocity and propulsive thrust and torque are measured in the experiments and they are also compared with those predicted using numerical simulation. The predictions form Resistive Force Theory are found to be in very good agreement with the experimental observation of our artificial flagellum.

Shum [36] used numerical simulations and analyzed the motion of such a microswimmer in bulk fluid and close to a solid surface. The study shows that positioning the two flagella far apart on the

cell body reduces the rate of rotation of the body and increases the swimming speed. Near surfaces, the author found that swimmers with two flagella can swim in relatively straight trajectories or circular orbits in either direction. It is also possible for the swimmer to escape from surfaces, unlike a model swimmer of similar shape but with only a single flagellum. Thus, he concludes that there are important implications of swimming with two flagella or flagellar bundles rather than one. These considerations are relevant not only for understanding differences in bacterial morphology but also for designing micro-robotic swimmers. Soto *et al.* [37] used a 3D Lagrangian tracking technique to determine experimentally the trajectories of non-tumbling *E. coli* mutants swimming in a Poiseuille flow. They identify a typology of trajectories in agreement with a kinematic active Bretherton-Jeffery model, featuring an axisymmetric self-propelled ellipsoid. Using this model they derive analytically new features such as quasi-planar piece-wise trajectories, associated with the high aspect ratio of the bacteria, as well as the existence of a drift angle around which bacteria perform closed cyclic trajectories. These structures are recovered experimentally. However, they show that the presence of Brownian rotation noise affects the persistence of bacterial motion in given orbits.

Several related studies of active particle in suspensions are also available in the recent literature. The flow resistence, three dimensional structures and symmetry breaking in viscoelastic channel flow at low Reynolds number have been investigated experimentally using pressure measurements and particle tracking by Quin *et al.* [38, 39] . Dhar *et al.* [40] have analyzed the trajectory of a single and a pair of active particles in a two-dimensional periodically tapered channel with asymmetric bounding walls through a combined analytical-numerical approach. They assumed creeping flow condition for the flow inside the channel and both puller and pusher types of squirmers were explored in their work. A closed system of equations modeling an active suspension of non-spherical Janus particles using Eulerian spatial averaging approach under condition of creeping flow was derived for the fluid and solid phases separately such as done in theoretical models of typical multiphase flows [41, 42]. The authors also included a numerical study of channel flow, driven by the active forces of the particles and a pressure gradient. The influence of a linear concentration gradient on the swimming velocity and orientation of active particles has been also studied theoretically [43]. More recently shear induced hydrodynamics dispersion of active spherical and non-spherical magnetic particle at low Reynolds number has been investigated by Roure and Cunha [44] and by Sinzato and Cunha [45]. Effect of dipolar interactions between active magnetic particles on the viscoelastic response of dilute ferrofluids undergoing oscillatory shear has also been investigated [46]. Theoretical studies of nonlinear viscoelastic response of an active suspension of anisotropic particles undergoing oscillatory shear are also available [47]. Additionally, the dynamics of clustering under cohesive interactions of mobile microrobotic swarms have been examined by Yigit *et al.* [48]. They presented an useful approach for operating microrobots in collective motion. Microrobot swarms have been introduced to address the need for collective functions and navigation of large numbers of microrobots in complex environments. An extensive review on the fundamentals and application of mobile microrobotic is also available in the current literature [49].

The effects of fluid elasticity on the details of swimming while clearly important, are not well

understood, and have therefore received growing attention, then many authors developed models for swimming in viscoelastic fluids. Recent theoretical and computational work has also examined how elastic effects change swimming speed [50, 51, 52]. Spagnolie *et al.* [53] have studied the motion of a rotating helical body in a viscoelastic fluid. In the case of force-free swimming, they showed the introduction of viscoelasticity can either enhance or retard the swimming speed and locomotive efficiency, depending on the body geometry, fluid properties, and the body rotation rate. Numerical solutions of the Oldroyd-B equations show how previous theoretical predictions break down with increasing helical radius or with decreasing filament thickness. Helices of large pitch angles show the increase in swimming speed to a local maximum at the Deborah number of order unity ($De = 1$). The numerical results show how the small-amplitude theoretical calculations connect smoothly to the large-amplitude experimental measurements. Other authors claim the existence of a transition zone. Malvar *et al.* [54] have examined the transition from a Newtonian-like response $De \leq 1$ to a clear viscoelastic regime occurs at around $De \approx 2.5$, where the frequency is order of the fluid relaxation time scale, suggesting that elastic fluid stresses are modifying kinematics. The ratio of swimming velocity is consistently less than unity demonstrating that fluid elasticity hinders net locomotion. The decrease is quite substantial even for the relatively low values of De. For instance, fluid elasticity hinders the cell swimming speed, relative to Newtonian fluids, by as much as 50 for $De < 2$. They also have found an asymptotic limit e for the velocity ratio approximately 0.4 for $De > 2$. This asymptotic behavior has been also observed in theoretical studies [51]. More recently, Irilan and Cunha [55] have examined an individual bacteria swimming with helical flagellum in low Reynolds flow environmental conditions. For this reason, the authors have designed a workbench to carry out some experiments, they developed an experimental and theoretical analysis for a macroscopic model of the helical flagellum. In this study, three different helices were used for the experiments and they do measurement for propulsive velocity, as well as propulsive force and torque exerted by the rotating helix in a highly viscous fluid. They have also developed in this study an experimental and numerical investigation of flexible swimming in non-Newtonian (PAMA) fluids using Oldroy B model. The authors presented a comparison between predictions of the speed velocity given by a Finite Element CFD simulation, using an Oldroyd-B constitutive model for the base elastic fluid, and experimental data. They also used Slender body theory to compare experimental results with those predicted by literature. The results have shown clearly F, T decrease when Sh increases. The numerical results have shown that the Method of Regularized Stokeslet and the Lighthill Slender body Theory represents a very small deviation from the experimental results. Increasing the Deborah number, however, shows the force and torque increase for all three the helix used. The flow velocity is always faster in a non- Newtonian fluid and the velocity ratio between the two fluids gradually increases with the Deborah number. Analyzing the trajectory of swimmers with the same geometry and under the same initial conditions, the authors have found that trajectory is systematically enhanced by fluid elasticity. The results also showed when the Deborah number increases the velocity increase because the property of the visco-elasticity of the fluid show that swimming is systematically enhanced by fluid elasticity which is an advantage over the Newtonian fluid. The results from computational simulations shown also a saturation of v_{nn}/v_n for De above 1.

Xu [56] reported the motion mechanism of magnetic particles during curing and explored

through numerical simulation. The author analyzed the magnetic force and viscous force of magnetic particles in Magnetorheological elastomer and discussed the equations of motion of magnetic particles under the applied magnetic field. Also, he established a uniform magnetic field model through the finite element method and simulated the motion of two magnetic particles under the magnetic field and he discussed the effects of particle distribution angles, particle radii, applied magnetic field strength, and distance between particles on particle velocity and displacement. The results show that the distance between particles has the greatest influence on the motion of magnetic particles, and the size of the distance between particles will affect the contact time of the particles, thus affecting the chain formation of magnetic particles.

Kong [57] investigated the swimming motion of rod-shaped magnetotactic bacteria affiliated with the Nitrospirae phylum in a viscous liquid under the influence of an externally imposed, time-dependent magnetic field. By assuming that fluid motion driven by the translation and rotation of a swimming bacterium is of the Stokes type and that inertial effects of the motion are negligible, they derived a new system of the twelve coupled equations that govern both the motion and orientation of a swimming rod-shaped magnetotactic bacterium with a growing magnetic moment in the laboratory frame of reference. According to the authors, it is revealed that the initial pattern of swimming motion can be strongly affected by the rate of the growing magnetic moment. It is also revealed, through comparing mathematical solutions of the twelve coupled equations to the swimming motion observed in the laboratory experiments with rod-shaped magnetotactic bacteria, that the laboratory trajectories of the swimming motion can be approximately reproduced using an appropriate set of parameters in the theoretical model.

Barkley [58] studied and showed that analysis of the trajectories of cells exposed to an external magnetic field can be used to measure the average magnetic dipole moment of a cell population in at least five different ways. They applied this analysis to movies of Magnetospirillum magneticum AMB-1 cells and compare the values of the magnetic moment obtained in this way to that obtained by direct measurements of magnetosome dimension from electron micrographs. They found that methods relying on the viscous relaxation of the cell orientation give results comparable to that obtained by magnetosome measurements, whereas methods relying on statistical mechanics assumptions give systematically lower values of the magnetic moment. Since the observed distribution of magnetic moments in the population is not sufficient to explain this discrepancy, the results suggest that non-thermal random noise is present in the system, implying that a magnetotactic bacterial population should not be considered as similar to a paramagnetic material.

Cui [59] studied the swimming motion of spheroidal magnetotactic bacteria. They investigated via both theoretical and experimental methods, the swimming motion of magnetotactic bacteria having the shape of an elongated prolate spheroid in a viscous liquid under the influence of an imposed magnetic field. A fully three-dimensional Stokes flow, driven by the translation and rotation of a swimming bacterium, exerts a complicated viscous drag/torque on the motion of a non-spherical bacterium. By assuming that the body of the bacterium is non-deformable and that the interaction between different bacteria is weak and hence negligible, the author has derived a system of 12 coupled nonlinear ordinary differential equations that govern both the motion and the orientation of a swimming spheroidal magnetotactic bacterium.

1.3 Review of Magnetic Fluids Studies

Magnetic fluid or ferrofluid is a particular class of colloidal magnetic suspension, composed by the addition of small particles of magnetic material, having an average diameter of approximately 10nm in a fluid base such as synthetic oils, ester, or water. A typical magnetic fluid is usually composed of a set of particles of ferrite or magnetite at nanometric scales dispersed in a carrier fluid. For a magnetic fluid to be useful for practical applications, it must be stable concerning the formation of aggregates due to the attractive forces between particles. The interaction between particles occurs directly through three mechanisms: steric repulsion, van der Waals attractive forces, both short-range forces, and magnetic force due to the interaction between the dipole moments of the particles. To avoid short-range attractive forces generating aggregates in the suspension, a thin layer of surfactants is applied to the surface of the particles, which act as nano-springs repellents preventing the formation of aggregates. Another example of magnetic suspensions is magneto-rheological suspensions (SMR) synthesized with magnetizable particles of micrometer size, dispersed in a non-magnetic base fluid. This second class of magnetic suspensions differs from ferrofluids due to the micrometer size of the particles. Thus, magnetorheological suspensions are not subject to Brownian motion induced by molecular thermal agitation, resulting in greater instability concerning the formation of aggregates and greater magnetic memory. Applications of fluid dynamics in engineering, until recently, were restricted to systems in which electric and magnetic fields played no role. However, the combination of magnetic fields and polar fluids has attracted more attention due to several applications in various fields, such as controlled thermonuclear reactions, design of chemical reactors, drugs, and high-speed silent printing [60]. A statistical model was developed by [61] describing the magnetostatic properties of colloidal ferrofluids and the dielectric properties of polar fluids. This model is based on the relationship between magnetization and the correlation function of pairs of a homogeneous spatial system of dipole particles. This function was calculated with the aid of the theory of first-order disturbances on the intensity of the dipole-dipole interaction, in the presence of a field uniform external magnetic. In addition, a new type of two-dimensional model has been developed by Hirabayashi [62] using the *lattice*-Boltzmann method to study the rheological properties of magnetic fluids. This model is based on a continuous flow algorithm for particles that move in the same grid pattern hexagonal. In this way, each particle occupies a state marked by two vectors, making it possible to express the rotation of the effective magnetic moment. So the model proved to be suitable for simulating various behaviors of influenced magnetic fluids by the rotation of the magnetic moment. Another Comprehensive Numerical Model of Magnetic Nanoparticles was presented by [63] providing a foundation of fundamental understanding of the actual physics of nanoparticles and their interactions with dipoles. So, a soft sphere model approach was adopted to simulate the interactions of nanoparticles at the molecular level.

Using an aggregate formation model combined with the theory of middle field, [64] calculated the average magnetization properties of ferrofluids. Using a hypothesis for dipole interactions, they obtained expressions for magnetization and initial susceptibility. By comparing the results of the theory with dynamic simulations molecular model of the same model observed that, in large dipole couplings, the model of aggregate formation seems to have better predictions than

other analytical approaches, supporting the idea that the formation of aggregates is a fundamental element importance in the studies of strongly interacting dipole particles. Still, another numerical model of ferrofluid dynamics was developed by [65]. It is considered that the magnetocrystalline anisotropy of the material magnetic of ferrofluid particles is finite, so that the magnetic moment of the particle rotate about the particle itself. Therefore, the magnetization relaxation of a ferrofluid after switching off the external field. Thus, compared the results with those obtained for the dipole model "fixed" in the particles, showing that the inclusion of magnetic degrees of freedom is essential for a description correct ferrofluid dynamics.

Change in rheological behavior is often defined as a change in effective fluid viscosity. Zubieta [66] presented a magnetization model that seeks to capture the change in the rheological behavior due to the application of an external magnetic field in magnetic suspension. In the case of ferrofluid, a Newtonian model was used to model the variation in viscosity that is observed when a magnetic field is applied. In the past [67] studied the effect of a homogeneous magnetic field on the viscosity of a suspension, whose solid particles have intrinsic magnetic moments. The orientation field prevents the rotation of particles in a vortical liquid flow, increasing effective viscosity. However, Brownian motion and hydrodynamic forces exert a disorienting effect in magnetic moments. Also, Zubarev [68] studied experimentally and theoretically the properties rheological properties of dense ferrofluids. In experiments, the dependence on viscosity effective in the magnetic field proved to be much more significant than expected by known theories. So they developed a new theoretical model to explain and describe these results. This model is based on the assumption that the formation of aggregates and chains in ferrofluid induces a strong magneto-viscous effect. Taking into account the interactions between magnetic particles, [69] presented a quantitative description of the magneto-viscous effects, exposing that a small volumetric fraction of particles in the fluid, form chains and aggregates that dominate the properties rheological effects of fluids in the presence of magnetic fields also, showing that the viscosity of a magnetic fluid can be strongly influenced by the presence of an external field. Ilg [70] also studied, through computer simulations, the influence of these attractive forces between particles in the structure and dynamics of ferrofluids. Understanding in the presence of a magnetic field, sufficiently strong attractive forces conduct to the formations of a whole of chains and aggregates of magnetic particles and consequently a change on the rheological properties of the fluid. Also, [71] reviewed advances in the behavior of ferrofluids, focusing on issues of phase behavior and microstructure formation with and without an externally applied magnetic field and performed an analysis of the influence of polydispersity that is an almost unavoidable characteristic of any real ferrofluid. Furthermore, Rinaldi [60] presented advances in rheology and magnetic fluid flows, including studies on the relaxation of magnetization and governing equations of Ferro-hydrodynamics.

Another model proposed by [72] was developed for studies of microstructural evolution, rheological properties, and the potential energies of magnetic fluids under shear. The simulations of molecular dynamics were performed based on a dipole theory magnetic. Other simulations using the Monte Carlo method performed by [73] analyzed the influence of polydispersity on the equilibrium properties of systems with dipole interactions and short-range repulsive forces, and a high-field approximation perturbation theory, in which the concentrations of particles and the

mean magnetic moments are typical of real ferrofluids. The magnetization in weak and moderate magnetic fields was higher in the polydisperse system than monodisperse.

A model for the continuity and momentum equations described in terms of mean variables proposed by [74], the authors investigated the stability of a magnetic fluidized bed against small-amplitude plane wave disturbances. In addition, [75] presented the continuous equations that govern the movement of a magnetic fluid. The studies were applied to describe the movement of a magnetic droplet freely suspended in a viscous fluid subjected to a permanent magnetic field, determining asymptotic solutions for flows in tubes. Cunha [76] developed a new general formulation for the hydrodynamic-magnetic boundary integral three-dimensional for magnetic free surfaces in viscous flows of low Reynolds numbers.

A linear stability analysis to assess the behavior of waves of concentration in polarized fluidized beds was carried out by [77]. The interactions of magnetized particles with an external magnetic field produced a stronger stabilization of the linear instabilities in fluidized beds. Yet, using the Ewald Sums numerical method to compute the interactions long-range dipoles, [78] studied in detail the initial susceptibility, the magnetization curves and the microstructure of ferrofluids at different concentrations of particles and dipole moments varied, through molecular dynamics simulations. In the Ewald sum technique, a suspension with periodic boundary conditions is considered, it is replicated periodically in all directions, and their replicas are called image cells, also containing N particles. The instant suspension setting in each image cell it is identical to the configuration of the central cell at each instant of time. The boundary conditions of the particles in the central cell are periodic, so if a particle crosses the bottom of the cell, it reappears at the top through the periodicity condition, expressed mathematically by [79].

Lindner [80] performed simulations to understand the influence of magnetic properties in high magnetic separation processes gradient. Therefore, the external magnetic forces were simulated through of the finite element method and incorporated in a simulation computational fluid dynamics.

1.4 Motivation

From the second half of the 20th century to the present day, the self-propulsion of micro-organisms and particles has been the subject of many studies. Some applications are of great importance, for example in the medical field we can mention minimal invasive surgery, medication administration, cancer treatment, and others. Therefore, there is a growing need to better understand the movement mechanisms on the subject. Understanding how the system behaves is very important and both biological and synthetic micro-swimmers are used to understand how they move in a suspension and how how they interact with their environments.

A practical motivation has been the tendency to use magnetic active matter, also known as magnetic active suspension which is a mixture in which magnetic particles are dispersed throughout the bulk of a fluid that can move alone within a base fluid. Understanding the locomotion and spreading of living fluid in complex environments, undergoing significant flow variations are

relevant to many fundamental and technological issues and that generates several types of research and works on the subject. In addition, Magnetic nanoparticles have attracted a lot of interest in fields of application advanced biological and medical technologies such as drug release and imaging by magnetic resonance. Osaka [81] studied the synthesis of magnetic iron oxide nanoparticles for the development of a biomolecular system. Also, as a test system practical biological, the magnetic detection of biomolecular interactions is demonstrated using the combination of a modified patterned substrate with a monolayer self-assembled and magnetic nanoparticles.

An important result is controlling the viscosity of flowing magnetic fluid through the application of an external magnetic field. The effect of the change in suspension viscosity can due to the alignment of the orientation of the magnetic particles in the direction of an applied external field, generating an increase in the effective viscosity of the fluid.

Timko [82] explored the influence of the combined magnetic and electric field in the permissiveness of the transforming role used in power transformers. The experiments showed that the permissiveness of the system insulator consisting of pure transformer paper and impregnated transformer paper naturally depends on the number of layers of paper. It was found that the magnetodielectric effect depended on the concentration of nanoparticles of magnetite in magnetic fluids.

1.5 Aims and Objectives of the Thesis

1.5.1 Main

The main goal of this work is to study the motion of particles and organisms in viscous fluids, through an analytic, numerical, and experimental method to describe the kinematics and dynamics of particles motion. Other secondary goals need to be achieved. Here they are:

1.5.2 Secondary

- Carry out some experiments with helical macroscopic models that swims freely in a highly viscous Newtonian or non-Newtonian ambient fluids in order to ensure a low Reynolds number around the swimmer. The main goal is to investigate the mechanics of artificial helical swimmers moving under condition of low Reynolds number and address how the elastic effects of the base fluid can influence the motion of a swimmer such as its propulsion velocity. We calculate the force and torque acting on the swimmer moving at low Reynolds number as a function of the Strouhal number Sh (i.e. the inverse of a non-dimensional frequency) in the case of Newtonian fluid and also as a function of the Deborah number De (i.e. elasticity parameter) when the base fluid is an elastic liquid.

- Use theoretical models based on Slender Body Theory (SBT) and the method of regularized Stokeslet (RSM) in order to calculate the force and torque as function of the Strouhal number (Sh) acting on helical swimmer moving in a Newtonian fluid. Specifically, the

SBT calculation is applied in order to describe the dynamics of swimming microorganism with motion produced by the thin helical flagellum propulsion. We present some computer simulations based on a finite element method for describing the creeping flow motion of a helical swimmer in an elastic Oldroyd-B fluid.

- We compare the experimental measurements with the theoretical predictions to see the agreement within the error bars of the experimental data. In making these comparisons we have verified the consistency of our experiments with artificial active particles and the accuracy of our experimental data.

- Investigate the motion in viscous liquids of a kind of active particles. We realize Langevin numerical simulations of the motion of magnetic chains composed of polydisperse spherical rigid particles under the action of Brownian motion, an external magnetic field, and under influence of dipolar magnetic interactions. We develop a FORTRAN code to simulate the prototype of magnetic active matter. The initial configuration of the magnetic particle in the simulation considers the ones aligned as chains structure with a different number of magnetic particles similar to the structure of a real bacteria spine which is formed by a chain of magnetic crystals. We examine the kinematics of the magnetic bacteria with different numbers of particles in the chain.

1.6 Scope of this work

This thesis is divided into five chapters: Introduction, theoretical framework, helical flagellum movement, simulation of magnetic bacteria, and conclusions. In the first Chapter, the introduction is presented. Chapter two is a review of the fundamentals concepts at low Reynolds numbers flows, beginning with a more detailed description of the Balance Equations in fluid mechanics at low Reynolds numbers and the swimming propulsion for microorganisms. Chapter three introduces the Slender body method and of regularized Stokeslets and implementation for solving the Stokes equations which describes the low Reynolds number flows. The method is validated with theoretical values for a helical flagellum in a viscous fluid. In chapter four we study a magnetic bacteria, we perform Langevin numerical simulations of the motion of magnetic chains composed of spherical rigid particles. The chains structure represents a imitation of a magnetotactic bacteria moving in a viscous liquid at low Reynolds number and also under the action of Brownian motion, an external magnetic field and under influence of dipolar magnetic interactions. Finally, chapter five presents conclusions and suggestions for future works.

Chapter 2

Theoretical Backgrounds

2.1 FUNDAMENTAL CONCEPTS OF FLUID MECHANICS

In this chapter, we present the fundamentals of fluid mechanics, to understand the behaviour of particles and organisms, their dynamics, or kinematics. It is important to understand in what conditions they perform and to what forces they are subjected. For this end, Balance Equations are presented for Newtonian fluid and the hypotheses associated with the microhydrodynamics problems treated in this thesis. A significant part of these theories were consulted in the thesis by [83], in the master's thesis by [84] and [85] and in the lecture notes by professor Francisco [86].

2.1.1 Governing Equations of Fluid Mechanics

The cornerstone of fluid mechanics is the fundamental governing equations of flows: the continuity, momentum, and energy equations. These equations describe physics. They are the mathematical statements of three fundamental physical principles upon which all of fluid dynamics is based. Governing equations involve certain quantities, in particular the stress tensor, which require a specification of the characteristics of the fluid under consideration.

2.1.2 Stress Tensor And Governing Equations In Fluid Mechanics

In fluid flows, there are forces acting that cause the movement. These forces can occur due to advection (movement forces), interaction with fields, external forces (such as gravitational or electromagnetic forces), pressure gradients and interactions between fluid molecules (surface forces). The forces acting in a infinitesimal volume of the medium are defined as stress. Thus, the stress is defined as follows:

$$\sigma_{ij} = \lim_{\delta A_i \to 0} \frac{\delta F_j}{\delta A_i}, \tag{2.1}$$

where, σ_{ij} is the stress in the plane i and direction j, F_j a force in the direction j and A_i a area in the plane j. We use $i, j \in \{1, 2, 3\}$ or $\in \{x, y, z\}$ or even $\in \{r, \theta, z\}$. The stress tensor is then a mathematical entity that has nine degrees of freedom, so the best way to represent it is in matrix

form, as below according to the coordinate system used:

$$\boldsymbol{\sigma} = \begin{pmatrix} \sigma_{xx} & \sigma_{xy} & \sigma_{xz} \\ \sigma_{yx} & \sigma_{yy} & \sigma_{yz} \\ \sigma_{zx} & \sigma_{zy} & \sigma_{zz} \end{pmatrix} \text{ or } \begin{pmatrix} \sigma_{11} & \sigma_{12} & \sigma_{13} \\ \sigma_{21} & \sigma_{22} & \sigma_{33} \\ \sigma_{31} & \sigma_{32} & \sigma_{33} \end{pmatrix} \text{ or } \begin{pmatrix} \sigma_{rr} & \sigma_{r\theta} & \sigma_{rz} \\ \sigma_{\theta r} & \sigma_{\theta\theta} & \sigma_{\theta z} \\ \sigma_{zr} & \sigma_{z\theta} & \sigma_{zz} \end{pmatrix}. \tag{2.2}$$

The last matrix presented in equation (2.2) refers to the coordinate system cylindrical, where:

$$\begin{cases} x(r,\theta,z) = r\cos(\theta), \\ y(r,\theta,z) = r\sin(\theta), \\ z(r,\theta,z) = z. \end{cases} \tag{2.3}$$

Figure (2.1), shows this tensor in geometric form where we see its scalar components, in rectangular coordinates. In this figure, the observed components that have equal indices are called normal stresses, with those with different indices. called shear stresses. Sometimes it can happen that the stress tensor has a symmetric nature, that $\sigma_{ij} = \sigma_{ji}$, so, only six are enough components to determine the tensor. The stress normal to the sectioned face is by definition of the form $\tau_x x = \sigma_x$ and, the shear stresses acting on the sectioned face are by, $\tau_{xy} = \sigma_{xy}$, $\tau_{yx} = \sigma_{yx}$, $\tau_{xz} = \sigma_{xz}$, $\tau_{yz} = \sigma_{yz}$. It is verified that the tension tensor is symmetrical and then, $\tau_{xy} = \tau_{yx}$, $\tau_{zx} = \tau_{xz}$, $\tau_{yz} = \tau_{zy}$.

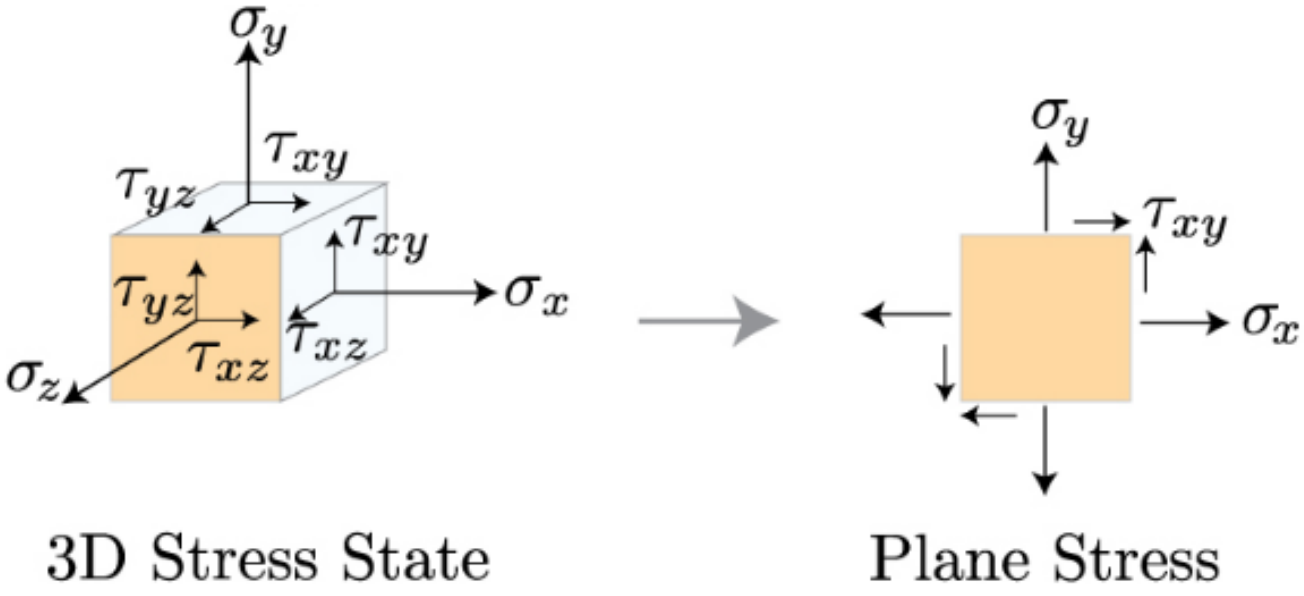

Figure 2.1: Stress tensor components in rectangular coordinates. Source: Mechanics of Slender structures [1]

The equations that govern the flow of fluids are formed by the mass conservation equation (or continuity equation), by the linear momentum of motion, by the energy equation and by the angular momentum equation. But, in general, only the mass and quantity conservation equations are considered, also called the Cauchy equation. We present these two equations below. Let us consider a material body Ω and in this body imagine an infinitesimal portion $\delta\Omega$ that has volume

δV and mass δm_c. The density, ρ, of this body Ω can be defined as:

$$\rho = \lim_{\delta V \to 0} \frac{\delta m_c}{\delta V}. \tag{2.4}$$

Assuming that there is a continuous and uniform mass distribution in the body, we can calculate the total mass of Ω to be:

$$m_\Omega = \int_V \rho \, dV. \tag{2.5}$$

Let ψ be any property (scalar, vector or tensor) of the fluid. By the principle of conservation which states that the net effects of any property ψ are null, we have, for example, the equation of conservation action of the dough

$$\frac{Dm_\Omega}{Dt} = 0, \tag{2.6}$$

where $\dfrac{D}{Dt}$ denotes the material derivative which ís defined as

$$\frac{D\psi}{Dt} = \frac{\partial \psi}{\partial t} + \mathbf{u} \cdot \nabla \psi, \tag{2.7}$$

and $\boldsymbol{u}$ represent the velocity field and ∇ the gradient operator.

Assuming that there is a continuous and uniform mass distribution in the body, we can calculate the total mass of Ω to be

$$m_\Omega = \int_V \rho \, dV. \tag{2.8}$$

Let's consider the equation (2.8) and apply the Reynolds Transport Theorem on it, from which we have:

$$\frac{D}{Dt} \int_V \rho \, dV = \int_V \frac{\partial \rho}{\partial t} \, dV + \int_S \rho \mathbf{u} \cdot \hat{\mathbf{n}} \, dS = 0. \tag{2.9}$$

Here, S denotes the surface of the volume δV and $\hat{\boldsymbol{n}}$ is the unitary normal vector that points away from this surface. Now, applying the divergence theorem to the equation (2.9), we can pass the entire integration to the volume V, leaving:

$$\frac{D}{Dt} \int_V \rho \, dV = \int_V \left(\frac{\partial \rho}{\partial t} + \nabla \cdot (\rho \boldsymbol{u}) \right) dV = 0. \tag{2.10}$$

Applying, now, the localization theorem, we finally have the equation of conservation mass equation:

$$\frac{D\rho}{Dt} = \frac{\partial \rho}{\partial t} + \nabla \cdot (\rho \boldsymbol{u}) = 0. \tag{2.11}$$

We can rewrite this last equation as being

$$\frac{\partial \rho}{\partial t} + \rho \nabla \cdot \boldsymbol{u} + \boldsymbol{u} \cdot \nabla \rho = 0 \iff \frac{D\rho}{Dt} + \rho \nabla \cdot \boldsymbol{u} = 0. \tag{2.12}$$

We will now describe the equation of momentum, also known as the Cauchy equation. For this, consider the definition of the linear momentum, $\mathbf{q}$, in the body Ω given by the equation:

$$\mathbf{q} = \int_V \rho \boldsymbol{u} \, dV. \tag{2.13}$$

By the same principle that gave rise to the equation (2.5), we can write:

$$\frac{D\mathbf{q}}{Dt} = \mathbf{f} \Leftrightarrow \frac{D}{Dt}\int_V \rho\mathbf{u}\, dV - \mathbf{f} = \mathbf{0}. \tag{2.14}$$

The rate of change of the linear momentum of a volume V is equal to the total forces (field and surface) acting on it. Note that the left side of the equation (2.14) represents Newton's second law, that is, the sum of the forces equal to zero. Here the vector force, $\mathbf{f}$, denotes an equilibrium. According to the theories of the continuous medium these forces are of field origins (forces that involve volume, of macroscopic origin, for example, the gravitational force) more surface forces (which have a microscopic origin associated with the random movement of molecules or particles in the material body). So we can write $\mathbf{f}$ as:

$$\mathbf{f} = \int_V \rho\mathbf{b}\, dV + \int_S \mathbf{T}^{(\mathbf{n})}\, dS, \tag{2.15}$$

where the vector $\mathbf{b}$ denotes a forceper unit of mass or field force and $\mathbf{T}^{(\mathbf{n})}$ stress vector.

Cauchy's Theorem states that the vector of stresses or traction, $\mathbf{T}^{(\mathbf{n})}$, refers to any surface (or plane) whose director and the vector $\mathbf{n}$ can be written as a linear combination of the mutually orthogonal vectors referring to the base $\{\mathbf{e}_i\}$ of space vector co $\mathbb{R}^3$. In this way we can write the vector $\mathbf{T}^{(\mathbf{n})}$ as being:

$$\mathbf{T}^{(\mathbf{n})} = \mathbf{n}.\boldsymbol{\sigma} = \boldsymbol{\sigma}^T.\mathbf{n},$$

where, $\boldsymbol{\sigma}$ is the tensor of tensions and T denotes its transpose. The figure (2.2) shows a schematic representation of this situation.

Again applying the divergence theorem to the equation (2.15) we obtain:

$$\mathbf{f} = \int_V (\rho\mathbf{b} + \nabla\cdot\boldsymbol{\sigma})\, dV. \tag{2.16}$$

Returning now to the equation (2.14) we can write

$$\frac{D}{Dt}\int_V \rho\mathbf{u}\, dV = \int_V (\rho\mathbf{b} + \nabla\cdot\boldsymbol{\sigma})\, dV, \tag{2.17}$$

and using the localization theorem we have the important equation

$$\rho\frac{D\mathbf{u}}{Dt} = \rho\mathbf{b} + \nabla\cdot\boldsymbol{\sigma}, \tag{2.18}$$

that is the Cauchy equation for the fluid movement. The divergence term from $\boldsymbol{\sigma}$, denoted by $\nabla\cdot\boldsymbol{\sigma}$, represents the surface forces per unit of volume.

2.1.3 Equation in Cylindrical Coordinates

We present in this section the equations (2.11) and (2.18) written in cylindrical coordinates, where for the Cauchy equation, we present the three. These equations refer to the three possible directions of the flow. We present the components of the tensor $\boldsymbol{\sigma}$ when in the hypothesis of a Newtonian fluid, as well as the equation of motion (equation (2.18)) for these fluids.

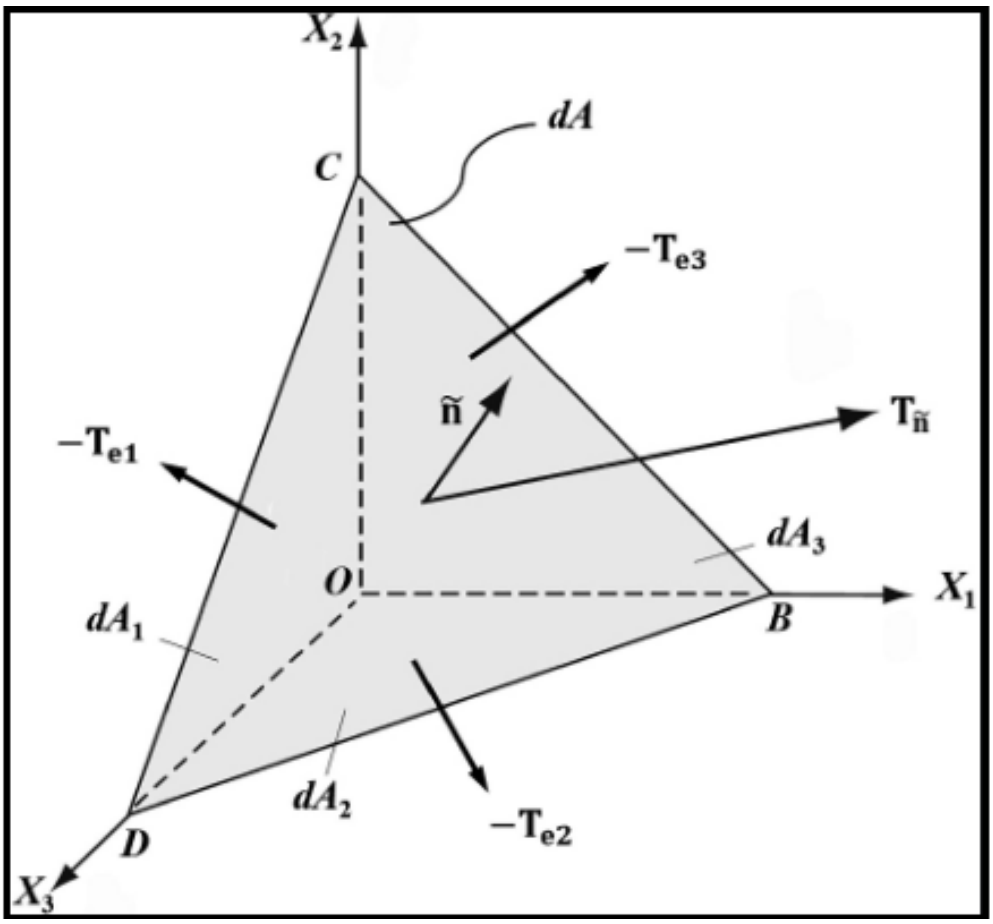

Figure 2.2: Forces acting instantly on a continuous medium inside a small element V in the form of a tetrahedron.

First consider any fluid with viscosity μ and specific mass ρ. And let the velocity field be given by:

$$\mathbf{u}(r,\theta,z) = (u_r(r,\theta,z), u_\theta(r,\theta,z), u_z(r,\theta,z)). \tag{2.19}$$

Also consider the pressure field inside the tube given by $p = p(r,\theta,z)$, and finally, the vector of force cas $\mathbf{b} = (b_r, b_\theta, b_z)$.

For the equation for the general case, we have the following equation for the general case:

$$\frac{\partial \rho}{\partial t} + \frac{1}{r}\frac{\partial}{\partial r}(r\rho u_r) + \frac{1}{r}\frac{\partial}{\partial \theta}(\rho u_\theta) + \frac{\partial}{\partial z}(\rho u_z) = 0. \tag{2.20}$$

For the Cauchy equation (2.18) we highlight the three directions, in the three equations (2.21), and (2.22), which follow:

$$\rho\left(\frac{\partial u_r}{\partial t} + u_r\frac{\partial u_r}{\partial r} + \frac{u_\theta}{r}\frac{\partial u_r}{\partial \theta} - \frac{u_\theta^2}{r} + u_z\frac{\partial u_r}{\partial z}\right) = -\frac{\partial p}{\partial r} + \rho b_r - \left[\frac{1}{r}\frac{\partial}{\partial r}(r\sigma_{rr}) + \frac{1}{r}\frac{\partial \sigma_{\theta r}}{\partial \theta} + \frac{\partial \sigma_{zr}}{\partial z} - \frac{\sigma_{\theta\theta}}{r}\right]. \tag{2.21}$$

$$\rho\left(\frac{\partial u_z}{\partial t}+u_r\frac{\partial u_z}{\partial r}+\frac{u_\theta}{r}\frac{\partial u_z}{\partial \theta}+u_z\frac{\partial u_z}{\partial z}\right)=-\frac{\partial p}{\partial z}+\rho b_z-\left[\frac{1}{r}\frac{\partial}{\partial r}(r\sigma_{rz})+\frac{1}{r}\frac{\partial \sigma_{\theta z}}{\partial \theta}+\frac{\partial \sigma_{zz}}{\partial z}\right]. \quad (2.22)$$

As a general form, we show in the six equations below, the components of the tension tensor $\boldsymbol{\sigma}$, in the case of a Newtonian fluid, where $\boldsymbol{\sigma}=-p\mathbf{I}+2\mu\mathbf{D}$, written in cylindrical coordinates:

$$\sigma_{rr}=-p+2\mu\frac{\partial u_r}{\partial r}. \quad (2.23)$$

$$\sigma_{\theta\theta}=-p+2\mu\left(\frac{1}{r}\frac{\partial u_\theta}{\partial \theta}+\frac{u_r}{r}\right). \quad (2.24)$$

$$\sigma_{zz}=-p+2\mu\frac{\partial u_z}{\partial z}. \quad (2.25)$$

$$\sigma_{z\theta}=\sigma_{\theta z}=\mu\left(\frac{\partial u_\theta}{\partial z}+\frac{1}{r}\frac{\partial u_z}{\partial \theta}\right). \quad (2.26)$$

$$\sigma_{rz}=\sigma_{zr}=\mu\left(\frac{\partial u_z}{\partial r}+\frac{\partial u_r}{\partial z}\right). \quad (2.27)$$

$$\sigma_{\theta r}=\sigma_{r\theta}=\mu\left(\frac{1}{r}\frac{\partial u_r}{\partial \theta}+\frac{\partial u_\theta}{\partial r}-\frac{u_\theta}{r}\right). \quad (2.28)$$

To finish this section we present the equations of motion in the case of a Newtonian fluid in terms of the velocity field, in the equations (2.29), (2.30) and (2.31) following:

$$\rho\left(\frac{\partial u_r}{\partial t}+u_r\frac{\partial u_r}{\partial r}+\frac{u_\theta}{r}\frac{\partial u_r}{\partial \theta}-\frac{u_\theta^2}{r}+u_z\frac{\partial u_r}{\partial z}\right)=-\frac{\partial p}{\partial r}+\rho b_r+ \mu\left[\frac{\partial}{\partial r}\left(\frac{1}{r}\frac{\partial}{\partial r}(ru_r)\right)+\frac{1}{r^2}\frac{\partial^2 u_r}{\partial \theta^2}+\frac{\partial^2 u_r}{\partial z^2}-\frac{2}{r^2}\frac{\partial u_\theta}{\partial \theta}\right]. \quad (2.29)$$

$$\rho\left(\frac{\partial u_\theta}{\partial t}+u_r\frac{\partial u_\theta}{\partial r}+\frac{u_\theta}{r}\frac{\partial u_\theta}{\partial \theta}+\frac{u_\theta u_r}{r}+u_z\frac{\partial u_\theta}{\partial z}\right)=-\frac{1}{r}\frac{\partial p}{\partial \theta}+\rho b_\theta+ \mu\left[\frac{\partial}{\partial r}\left(\frac{1}{r}\frac{\partial}{\partial r}(ru_\theta)\right)+\frac{1}{r^2}\frac{\partial^2 u_\theta}{\partial \theta^2}+\frac{\partial^2 u_\theta}{\partial z^2}+\frac{2}{r^2}\frac{\partial u_r}{\partial \theta}\right]. \quad (2.30)$$

$$\rho\left(\frac{\partial u_z}{\partial t}+u_r\frac{\partial u_z}{\partial r}+\frac{u_\theta}{r}\frac{\partial u_z}{\partial \theta}+u_z\frac{\partial u_z}{\partial z}\right)=-\frac{\partial p}{\partial z}+\rho b_z+\mu\left[\frac{1}{r}\frac{\partial}{\partial r}\left(r\frac{\partial u_z}{\partial r}\right)+\frac{1}{r^2}\frac{\partial^2 u_z}{\partial \theta^2}+\frac{\partial^2 u_z}{\partial z^2}\right]. \quad (2.31)$$

2.1.4 Momentum Equation

Momentum is advected about by the motion of the fluid itself and spatial variations of pressure and viscous stresses. Restricting ourselves to the motion of a continuous, viscous fluid (liquid or gas), the stress in a fluid is composed of two parts; a locally isotropic part proportional to the scalar pressure field and a non-isotropic part due to viscous friction. Cauchy's equation, which

expresses the momentum equations for a continuous medium can be deduced through Newton's second law applied to a body. We have the momentum equation is described by equation (2.32):

$$\rho \frac{D\boldsymbol{u}}{Dt} = \nabla \cdot \boldsymbol{\sigma} + \rho \boldsymbol{b} \tag{2.32}$$

where, ρ is the density field, $\boldsymbol{\sigma}$ the stress tensor field, and $matb$ is the force field strength per unit mass. Assuming no external torque acting on the fluid, the law of of angular momentum equation is expressed by the symmetry of the stress tensor $\boldsymbol{\sigma}$. In the flow, the rate at which the local deformation of the medium is changing over time (the strain rate) can be approximated by a strain rate tensor $\boldsymbol{E}$, which is defined by:

$$\boldsymbol{E} = \frac{1}{2}[\nabla \boldsymbol{u} + \nabla \boldsymbol{u}^T] \tag{2.33}$$

Now, the constitutive equation for a Newtonian fluid is:

$$\boldsymbol{\sigma} = -p\mathbb{I} + 2\mu \boldsymbol{E} \tag{2.34}$$

where p is the thermodynamic pressure and $\boldsymbol{E}$ is the dynamic stress, which is related to the velocities and μ is the dynamic viscosity. By setting the Cauchy stress tensor $\boldsymbol{\sigma}$ to be the sum of a viscosity term and a pressure term (volumetric stress) we arrive at:

$$\rho[\frac{\partial \boldsymbol{u}}{\partial t} + \boldsymbol{u} \cdot \nabla \boldsymbol{u}] = -\nabla p + \mu \nabla^2 \boldsymbol{u} + \rho \boldsymbol{b} \tag{2.35}$$

where the terms of the equation of motion represent, respectively, inertial forces, pressure forces, viscous forces and field forces for example gravity, inertial accelerations, electrostatic accelerations, (per unit volume).

2.2 Fundamentals of Hydrodynamics at Low Reynolds Number

The propulsion of microorganisms is typically slow, where a lot of effort has to be expended. This can be explained by the existence of the immense frictional resistance to motion. In this section we present the basic and fundamental concepts of microhydrodynamics.

2.2.1 Scaling arguments and the Stokes approximation

The importance of inertial effects compared to viscous effects in equation (2.35) is measured by the Reynolds number. Suppose the particle, have length L, translates with a velocity of magnitude U. Then the Reynolds number at the particle scale is:

$$Re = \frac{\rho U L}{\mu} \sim \frac{\mid (\boldsymbol{u} \cdot \nabla)\boldsymbol{u} \mid}{\mid \nu \nabla^2 \boldsymbol{u} \mid} \tag{2.36}$$

We are usually interested in small length-scales, typically between 10^{-2} and 10^2 μm. As a result of the smallness of particles, the velocity scale is often small, for example in sedimentation,

where the isolated particle settling velocity scales with the square of its size, as we will see later. For a particles with size $L = 1\mu m$, the settling velocity in water is of the order of $U = 1\ \mu m s^{-1}$ and the Reynolds number of the motion is thus of $O(10^{-6})$. Therefore, in many practical flows of suspensions, the Reynolds number is small and we may neglect the convective acceleration in the left-hand side of equation (2.35) according to [87].
At the asymptotic limit where $Re \ll 1$, the advection equations of fluid motion are Stokes equations, given by:

$$\begin{cases} \nabla \cdot \boldsymbol{u} = 0 \\ \nabla p + \mu \nabla^2 \boldsymbol{u} = 0 \end{cases} \tag{2.37}$$

Also called the creeping flow equations. The Reynolds number (Re) is still very small, we have to keep the unsteady term ($\frac{\partial \boldsymbol{u}}{\partial t}$), in which case we have the unsteady Stokes equations. We will not be concerned with this unsteady case here.

2.2.2 Linearity and Instantaneity

There is no $(\boldsymbol{u} \cdot \nabla \boldsymbol{u})$ in equation (2.2.1) therefore, $\boldsymbol{u}$, p, and $\boldsymbol{\sigma}$ are linearly forced by any boundary motion or body force. If for instance we have a falling sphere doubling the velocity will double $\boldsymbol{\sigma}$ and the drag force. Generally this property can be verified taking into account the problem of a rigid particle delimited by the surface S, translating with velocity $\boldsymbol{u(t)}$, in low number regime of Reynolds. Considering the symmetry of the stress tensor, since the fluid and the particles are not magnetic, that is, there are no induced internal torques in the material by magnetization, the hydrodynamic force on the particle given by:

$$\boldsymbol{F} = \int_S \sigma \cdot \mathbf{n} dS \tag{2.38}$$

where $\mathbf{n}$ is the unitary vector normal to the surface S, which points to the side of the fluid that exerts tension. Considering $\mid \mu \nabla^2 \boldsymbol{u} \mid \sim \mu \boldsymbol{u}/L^2$,and a scale of the viscous tensions and $\mid \nabla p \mid \sim \mathbf{F}/L^3$ and a pressure scale, where L represents a characteristic length of the flow, then $F/L^3 \sim \mu \boldsymbol{u}/L^2$, where it follows that:

$$\boldsymbol{F} = 6\pi \mu \boldsymbol{u} L \tag{2.39}$$

A Stokes flow has no dependence on time other than through time-dependent boundary conditions. This means that, given the boundary conditions of a Stokes flow, the flow can be found without knowledge of the flow at any other time. Instantaneity is an important property. There is no time in the Stokes equations, and so the predicted motion is said to be quasi-static. There is no history dependence of the fluid motion captured by these equations. All that is needed to determine the flow is the actual configuration given by the boundary conditions, coming both from the particle positions and outer boundaries. According to the steady Stokes equations, the

boundary motion is communicated to the entire fluid instantly. The latter is due to the harmonic properties of the Stokes equations which have instantaneous propagation of the information according to reference [87].

2.2.3 Reversibility Symmetry

If the velocity of the boundary of stokes flow is reversed then so is the velocity everywhere in the fluid. If a prescribed boundary motion is reversed over time, then each point retraces its history. This is beautifully illustrated in a short film by [88]. This film as well as other illustrative films can be found in reference [89]. In this film clip, a coloured drop is introduced into a viscous liquid contained in the annulus between two transparent concentric cylinders. When the inner cylinder is rotated through a full four revolutions, the coloured drop is sheared with the rest of the liquid and becomes scarcely visible. When the direction of the inner cylinder is reversed and passes back through four revolutions, the stretched ribbon of dyed fluid reforms the original spherical drop with only slight blurring due to molecular diffusion. It is a quite striking demonstration of the reversibility of the flow. Is an important property of Stokes flow and its reversibility in relation to time. Considering that in Stokes regimes the motion $\boldsymbol{u}(\boldsymbol{x}, t)$ is a linear function of the applied hydrodynamic force, then, if the direction of the force is reversed, the movement is reversed. That can be verified by the following argument: We consider $\boldsymbol{u}$ and p are solution of the Stokes equations given in equation (2.2.1), then we have $-\boldsymbol{u}$ and $-p$ are also solution. It is noted that the case of Reynolds arbitrary, the non-linear term $\mid \boldsymbol{u} \cdot \nabla \boldsymbol{u} \mid u^2/L$ hold their signal when the direction of velocity is reversed, so that the reverse flow is not solution of the problem. For example, the relative movement between two smooth shear spheres produces reversed closed relative trajectories. Inverting the direction of shear, the particles return to the along the same relative trajectories, without lateral migration. This phenomenon is direct consequence of the linearity and reversibility in the time of the equations of Stokes. It is worth mentioning that this condition of symmetry can be broken by intrinsic characteristics of the system, such as surface roughness, deformation in relation to spherical shape, colloidal forces, or effect of inertia according reference [90], producing migration of particles along the current lines of the Stokes equation.

The reversibility property in Stokes flow leads to the impossibility of certain movements. Organizations biology, free from the action of gravity and performing reversibility in time, are not able to move in Stokes. This is because there is symmetry in time, liquid motion and zero, since the force on the body depends linearly speed, as shown in figure (2.3). In other words, if a micro-organism performs a movement with a certain velocity, the fluid exerts on it a force with opposite direction. Therefore, if the movements are alternating, after each cycle the resultant force on the body is zero. Generally, to produce movement, micro-organisms need to break the symmetry at the time of flow, for example, by performing helical or high frequencies [91].

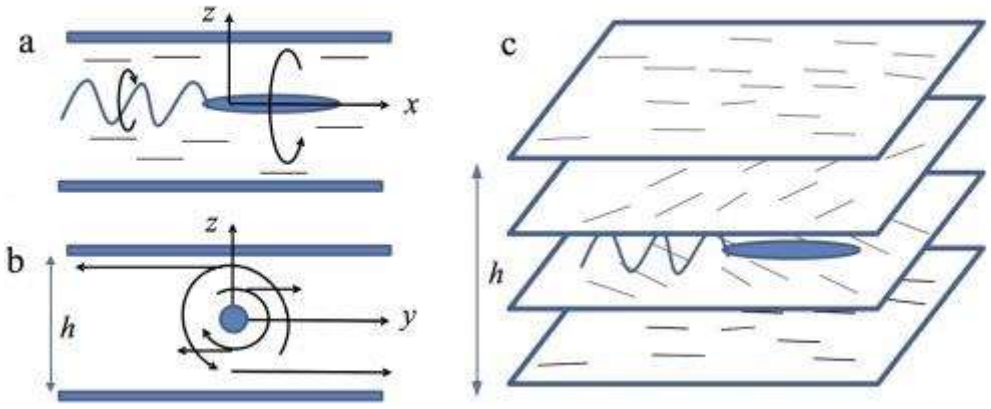

Figure 2.3: Symmetry breaking of the living particle, Oliveira (2007)

2.2.4 Stokes Flow Theorem

2.2.4.1 Uniqueness

In order to demonstrate the uniqueness of the solution of the Stokes equations, we take the rate of dissipation of momentum in internal energy for an incompressible Newtonian fluid, $\Phi = 2\mu \boldsymbol{E} : \boldsymbol{E}$. In this case, we consider a region of space V, delimited by the surface S in which the velocity boundary conditions are known. We assume that $\boldsymbol{u}$ and $\boldsymbol{u'}$ are two solutions of the Stokes equations in this domain, such that both satisfy the boundary conditions in S, see reference [86]. The rate of dissipation internal energy throughout the V domain, due to the difference between the velocity fields, $\boldsymbol{u^d} = \boldsymbol{u} - \boldsymbol{u'}$ can then be calculated by:

$$\Phi_V^d = \int_S 2\mu \boldsymbol{E^d} : \boldsymbol{E^d} dV, \tag{2.40}$$

where $\boldsymbol{E^d} = \frac{1}{2}[\nabla \boldsymbol{u}^d + (\nabla \boldsymbol{u}^d)^T]$ e $\nabla \boldsymbol{u}^d = \nabla \boldsymbol{u} - \nabla \boldsymbol{u'}$ but $\boldsymbol{E^d}$ is symmetric.
$\nabla \boldsymbol{u}^d = \boldsymbol{E^d} + \boldsymbol{W^d}$, where $\boldsymbol{W^d} = \frac{1}{2}[\nabla \boldsymbol{u}^d - (\nabla \boldsymbol{u}^d)^T]$ is antisymmetric. with $\nabla \boldsymbol{u}^d$ we have $\boldsymbol{E^d} : \boldsymbol{E^d} = \boldsymbol{E^d} : \nabla \boldsymbol{u}^d$ because $\boldsymbol{E^d} : \boldsymbol{W^d} = 0$. Using the expression $\mathbf{E^d} : \nabla \mathbf{u}^d = \nabla \cdot (\boldsymbol{E^d} \cdot \boldsymbol{u}^d) - (\nabla \cdot \boldsymbol{E^d}) \cdot \boldsymbol{u}^d$ e $\nabla \cdot \boldsymbol{E^d} = \frac{1}{2}\nabla^2 \boldsymbol{u}^d$ the equation (2.40) became:

$$\Phi_V^d = \int_V 2\mu \nabla \cdot (\boldsymbol{E^d} \cdot \boldsymbol{u^d}) dV - \int_V \mu \nabla^2 \boldsymbol{u^d} \cdot \boldsymbol{u^d} dV \tag{2.41}$$

Applying the divergence theorem in the first integral on the right side of the equation (2.41), we obtain $\int_V 2\mu \nabla \cdot (\boldsymbol{E^d} \cdot \mathbf{u^d}) dV = \int_S 2\mu \nabla \cdot (\boldsymbol{E^d} \cdot \mathbf{u^d}) \cdot \boldsymbol{n} dS$. As the two solutions $\boldsymbol{u}$ and $\boldsymbol{u'}$ satisfying the boundary conditions follows that $\boldsymbol{u}^d(x) = 0$ at $\boldsymbol{x} \in S$, then said integral is zero. On the other hand, the equations of Stokes $\mu \nabla \boldsymbol{u^d} = \nabla p^d$ where $p^d = p - p'$

$$\Phi_V^d = -\int_V \nabla p^d \cdot \boldsymbol{u^d} dV \tag{2.42}$$

With $\nabla p^d \cdot \boldsymbol{u^d} = \nabla \cdot (p^d u^d) - p^d \nabla \cdot \boldsymbol{u^d}$ e $\nabla \boldsymbol{u^d} = 0$ we can write also:

$$\Phi_V^d = -\int_V \nabla \cdot (p^d \mathbf{u^d}) dV = -\int_S (p^d \boldsymbol{u^d}) \cdot \boldsymbol{n} dS = 0 \tag{2.43}$$

The surface integral in equation (2.43) also cancels out because $\boldsymbol{u^d(x)} = 0$, if $x \in S$. Therefore, $\Phi_V^d = 0$ if the flow is governed by the equations of Stokes. Returning to the equation (2.40) and observing that the integral of this equation Is a non negative quantity, provided that the volume of integration is arbitrary and $\boldsymbol{E^d}$ And a continuous field, we conclude, by the localization theorem, what is $\boldsymbol{E^d} = 0$, this is $\boldsymbol{E} = \boldsymbol{E'}$ throughout $\boldsymbol{V}$. So, $\boldsymbol{u}$ and $\boldsymbol{u'}$ may differ only by a rigid body movement. However, since in velocity fields are identical, since they must satisfy the conditions of contour, then $\boldsymbol{u(x)} = \boldsymbol{u'(x)}$ $\forall \boldsymbol{x} \in V$ according to reference [92], requiring thus the uniqueness of the solution of the Stokes equations, as a direct consequence of its linearity.

2.2.4.2 Minimum Energy Dissipation

We consider two flows $(\boldsymbol{u}, p)$ and $(\boldsymbol{u'}, p')$ incompressible and satisfying the boundary conditions in a given area V delimited by the surface S. Consider that the flow $(\boldsymbol{u}, p)$ satisfies the Stokes equations, while $(\boldsymbol{u'}, p')$ not necessarily. The least energy dissipation theorem says that $(\boldsymbol{u}, p)$ has the lowest rate of dissipation of internal energy among all incompressible flows,$(\boldsymbol{u'}, p')$ satisfying the conditions according to reference [86]. This fact can be demonstrated from the expression for the the energy dissipation rate of $(\boldsymbol{u'}, p')$ in volume V.

$$\Phi' = \int_V \boldsymbol{E'} : \boldsymbol{E'} dV \tag{2.44}$$

It is possible to write also:

$$\int_V (\boldsymbol{E'} - \boldsymbol{E}) : \boldsymbol{E} dV = 0 \tag{2.45}$$

Using a developments similar to those in the demonstration of the uniqueness the solution of the Stokes equations. Subtracting equation (2.44) from equation (2.45), we have that $\Phi' = \int_V [(\boldsymbol{E'} : \boldsymbol{E'} - (\boldsymbol{E'} - \boldsymbol{E}) : \boldsymbol{E}] dV$, that mean:

$$\Phi' = \int_V [(\boldsymbol{E} : \boldsymbol{E} + (\boldsymbol{E'} - \boldsymbol{E}) : \boldsymbol{E'}] dV \tag{2.46}$$

Again subtracting from the integral at equation (2.44) the expression (2.45), we determined:

$$\Phi' = \int_V [(\boldsymbol{E} : \boldsymbol{E} + (\boldsymbol{E'} - \boldsymbol{E}) : \boldsymbol{E'} - (\boldsymbol{E'} - \boldsymbol{E} : \boldsymbol{E}] dV = \int_V [(\boldsymbol{E} : \boldsymbol{E} + (\boldsymbol{E'} - \boldsymbol{E}) : \boldsymbol{E'} - \boldsymbol{E}] dV \tag{2.47}$$

Then combining equation (2.45) and equation (2.47)

$$\int_V \boldsymbol{E'} : \boldsymbol{E'} dV = \int_V \boldsymbol{E} : \boldsymbol{E} dV + \int_V (\boldsymbol{E'} - \boldsymbol{E}) : (\boldsymbol{E'} - \boldsymbol{E}) dV \tag{2.48}$$

Since the second integral on the right side of 2.48 is always a quantity not negative, we can conclude that

$$\int_V \boldsymbol{E} : \boldsymbol{E} dV \leq \int_V \boldsymbol{E'} : \boldsymbol{E'} dV \tag{2.49}$$

which demonstrates the Stokes' minimum dissipation theorem. From an analytical point of view, this result can be interpreted as a variational principle according to which the solution of the Stokes equations in a determined domain, subject to specific boundary condition which promotes the minimum rate of energy dissipation of the flow through the viscous.

2.2.4.3 Reciprocal Theorem

The reciprocal theorem allows one to determine results for one Stokes flow field based upon the solution of another Stokes flow in the same geometry, i.e. having the same boundaries but different boundary conditions. The reciprocal theorem states a relationship between two Stokes flows in the same region. Consider fluid filled region V bounded by surface S. Let the velocity fields $\boldsymbol{u}$ and $\boldsymbol{u'}$ solve the Stokes equations in the domain V, each with corresponding stress fields $\boldsymbol{\sigma}$ and $\boldsymbol{\sigma'}$. Then the following equality holds:

$$\int_S \boldsymbol{u} \cdot (\boldsymbol{\sigma'} \boldsymbol{n}) dS = \int_S \boldsymbol{u'} \cdot (\boldsymbol{\sigma} \boldsymbol{n}) dS \tag{2.50}$$

where $\boldsymbol{n}$ is the unit normal on the surface S. The reciprocal theorem can be used to show that Stokes flow transmits unchanged the total force and torque from an inner closed surface to an outer enclosing surface. The reciprocal theorem can also be used to relate the swimming speed of a microorganism, such as bacterium, to the surface velocity which is prescribed by deformations of the body shape via cilia or flagella according to [92].

2.2.5 Fundamental Solution of the Stokes Flow

The fundamental solution of the Stokes equations corresponds to the flow generated by the presence of a force point in a three-dimensional domain infinity of fluid (free space), represented by the following system of equations.

$$\mu \nabla^2 \boldsymbol{u} = \boldsymbol{F} \delta(\boldsymbol{x} - \boldsymbol{x_0}) \tag{2.51}$$

$$\nabla \cdot \boldsymbol{u} = 0 \tag{2.52}$$

Here $\boldsymbol{x}$ is in $\mathbb{R}^3$, $\boldsymbol{F}$ is a concentrated force (or monopole) applied on the fluid, $\boldsymbol{x_0}$ is the position of the force point and $\delta(\boldsymbol{x} - \boldsymbol{x_0})$, the Dirac delta distribution in the three-dimensional space. More generally, the presence of a particle in a Stokes flow is represented by: $\boldsymbol{F}\delta(\boldsymbol{x} - \boldsymbol{x_0}) + \boldsymbol{D} \cdot \nabla \delta(\boldsymbol{x} - \boldsymbol{x_0}) + \boldsymbol{Q} : \nabla\nabla\delta(\boldsymbol{x} - \boldsymbol{x_0}) + \cdots$ where $\boldsymbol{D}$ and $\boldsymbol{Q}$ represent moments (dipole and quadrupole) generated by the particle on the fluid. In the present context, one strength point or particle produces a long-range velocity and pressure disturb in the fluid. In a region sufficiently distant from the location x_0 of the same, such that high order moments that decay with $\frac{1}{r^2}$, or faster than that is, they become second order contributions that $\boldsymbol{r} = \| \boldsymbol{x} - \boldsymbol{x_0} \| \gg 1$. It is worth noting that the Dirac delta distribution satisfies the following properties, Lighthill (1976).

$$(i) \int_{-\infty}^{\infty} \delta(\boldsymbol{x} - \boldsymbol{x_0}) dV = 1, \ (ii) \int_{-\infty}^{\infty} \delta(\boldsymbol{x} - \boldsymbol{x_0}) f(x) dV = f(\boldsymbol{x_0}) \tag{2.53}$$

where, $f(\boldsymbol{x_0})$ is a regular function. The solution of the differential problem represented by equations (2.53) can be found via three-dimensional Fourier transform, defined by the pair of transformed.

$$\mathcal{F}\{f(\boldsymbol{x})\} = \hat{f}(\boldsymbol{k}) = \frac{1}{2\pi^{3/2}} \int_D f(\boldsymbol{x}) e^{-i\boldsymbol{kx}} d\boldsymbol{x} \tag{2.54}$$

$$\mathcal{F}^{-1}\{\hat{f}(\boldsymbol{k})\} = f(\boldsymbol{x}) = \frac{1}{2\pi^{3/2}} \int_D \hat{f}(\boldsymbol{k}) e^{i\boldsymbol{kx}} d\boldsymbol{k} \tag{2.55}$$

here we have $D = \mathbb{R}^3$
The equation (2.55) can be interpreted as the projection of the function $f(\boldsymbol{x})$in a (Gaussian auto functions) where, $f(\boldsymbol{k})$ is the amplitude of each wave is $e^{i\boldsymbol{kx}}$. The vector $\boldsymbol{k}$ is defined as $\boldsymbol{k} = 2\pi(1/\lambda_j)\boldsymbol{e_j}$ and in which the unitary vector in each direction $j = 1, 2, 3$ and λ_j is the length wave in the direction $\mathbf{e_j}$. It is important to point out the following properties of Fourier transform:

$$\mathcal{F}\{\nabla \cdot \boldsymbol{a}(\boldsymbol{x})\} = i\boldsymbol{k} \cdot \hat{\boldsymbol{a}}(\boldsymbol{k}) \tag{2.56}$$

$$\nabla \mathcal{F}^{-1}\{\hat{\boldsymbol{a}}(\boldsymbol{k})\} = \Im\{i\boldsymbol{k}\hat{\boldsymbol{a}}(\boldsymbol{k})\} \tag{2.57}$$

According to equation (2.57) we have that $\mathcal{F}\{\nabla^2\} = -k^2$
here $k^2 = \boldsymbol{k}.\boldsymbol{k}$. Then, the equation of continuity in the Fourier (or of wave number) is:

$$\boldsymbol{k} \cdot \hat{\boldsymbol{u}}(\boldsymbol{k}) = 0 \tag{2.58}$$

Applying the Fourier transform to the momentum equation, and considering for the moment that the monopole is concentrated in the origin, we obtain:

$$\mu k^2 \hat{\boldsymbol{u}}(\boldsymbol{k}) + i\boldsymbol{k}\hat{p}(\boldsymbol{k}) = -\boldsymbol{F}\frac{1}{2\pi^{3/2}} \int_D \delta(\boldsymbol{x}) e^{i\boldsymbol{kx}} d\boldsymbol{x} \tag{2.59}$$

Using property of the Dirac delta distribution, we have: $\int_D \delta(x) e^{i\boldsymbol{kx}} dx = e^{ik.0} = 1$
and the equation (2.59) of the momentum in the reciprocal space reduces to

$$\mu k^2 \hat{\boldsymbol{u}}(\boldsymbol{k}) + i\boldsymbol{k}\hat{p}(\boldsymbol{k}) = -\boldsymbol{F}\frac{1}{2\pi^{3/2}} \tag{2.60}$$

Multiplying scalarly the equation 2.60 by k and using the equation of continuity we have:

$$\hat{p}(\boldsymbol{k}) = -\boldsymbol{F}\frac{1}{2\pi^{3/2}}\frac{i\boldsymbol{k}}{k^2} \tag{2.61}$$

Substituting (2.61) in (2.60) and isolating $\hat{\boldsymbol{u}}(\boldsymbol{k})$, we have

$$\hat{\boldsymbol{u}}(\boldsymbol{k}) = -\frac{1}{(2\pi)^{3/2}\mu k^2}\boldsymbol{F} \cdot (\boldsymbol{I} - \frac{\boldsymbol{kk}}{k^2}) \tag{2.62}$$

The equations (2.61) and (2.62) are expressions for the pressure fields and velocity, respectively, in the reciprocal space. To determine the fields corresponding in the physical space the inverse Fourier transform and property, so that:

$$p(x) = \mathcal{F}^{-1}\{-\boldsymbol{F}\frac{1}{2\pi^{3/2}}\frac{i\boldsymbol{k}}{k^2}\} = \frac{1}{8\pi}\boldsymbol{F}\int_D \frac{ike^{ikx}}{k^2} dk = \frac{1}{8\pi}\mathbf{F} \cdot \nabla \int_D \frac{e^{i\boldsymbol{kx}}}{k^2} d\boldsymbol{k} \tag{2.63}$$

and therefore since $\int_D \frac{e^{i\boldsymbol{k}\boldsymbol{x}}}{k^3} d\boldsymbol{k} = \frac{2\pi^2}{x}$ where $x = \sqrt{\boldsymbol{x}\cdot\boldsymbol{x}}$ it is possible to show ;

$$p(\boldsymbol{x}) = -\frac{1}{8\pi}\boldsymbol{F}\cdot(2\frac{\boldsymbol{x}}{x^3}) \tag{2.64}$$

Similarly, the velocity field in the physical space is determined as:

$$\hat{\boldsymbol{u}}(\boldsymbol{k}) = -\frac{1}{(2\pi)^{3/2}\eta k^2}\boldsymbol{F}\cdot\left(\boldsymbol{I} - \frac{\boldsymbol{k}\mathbf{k}}{k^2}\right). \tag{2.65}$$

Application transform of Fourier inverse:

$$\boldsymbol{u}(\boldsymbol{x}) = \mathcal{F}^{-1}\{\hat{\boldsymbol{u}}(\boldsymbol{k})\} = -\frac{1}{8\pi^3\eta}\boldsymbol{F}\cdot\left[\boldsymbol{I}\int_{\mathbb{R}^3}\frac{e^{i\boldsymbol{k}\cdot\boldsymbol{x}}}{k^2}d\boldsymbol{k} - \nabla\nabla\int_{\mathbb{R}^3}\frac{e^{i\boldsymbol{k}\cdot\mathbf{x}}}{k^4}d\boldsymbol{k}\right]. \tag{2.66}$$

Again using spherical coordinates, one has:

$$\int_{\boldsymbol{R}^3}\frac{e^{i\boldsymbol{k}\cdot\boldsymbol{x}}}{k^4}d\mathbf{k} = -\pi^2|\boldsymbol{x}|, \tag{2.67}$$

replacing the last two equations, we obtain the following velocity field in three-dimensional physical space, given by:

$$\boldsymbol{u}(\boldsymbol{x}) = -\frac{\boldsymbol{F}}{8\pi\eta}\cdot\left(\frac{\mathbf{I}}{r} + \frac{\boldsymbol{x}\boldsymbol{x}}{r^3}\right). \tag{2.68}$$

We have now the more general case in which $x = x_0$, the velocity field in space modified by only one translation, assuming the following form:

$$\boldsymbol{u}(\boldsymbol{x},\boldsymbol{x}_0) = -\frac{\boldsymbol{F}}{8\pi\eta}\cdot\left[\frac{\boldsymbol{I}}{|\boldsymbol{x}-\boldsymbol{x}_0|} + \frac{(\boldsymbol{x}-\boldsymbol{x}_0)(\boldsymbol{x}-\boldsymbol{x}_0)}{|\mathbf{x}-\boldsymbol{x}_0|^3}\right]. \tag{2.69}$$

The velocity field $\boldsymbol{u}$ can be expressed by:

$$\boldsymbol{u}(\boldsymbol{x},\boldsymbol{x}_0) = \frac{-\boldsymbol{F}}{8\pi\eta}\cdot\boldsymbol{\mathcal{G}}(\boldsymbol{x},\boldsymbol{x}_0), \tag{2.70}$$

Where

$$\boldsymbol{\mathcal{G}}(\boldsymbol{x},\boldsymbol{x}_0) = \left[\frac{\boldsymbol{I}}{|\boldsymbol{x}-\boldsymbol{x}_0|} + \frac{(\boldsymbol{x}-\boldsymbol{x}_0)(\boldsymbol{x}-\boldsymbol{x}_0)}{|\boldsymbol{x}-\boldsymbol{x}_0|^3}\right], \tag{2.71}$$

Is a second-order symmetric and positive nest tensor, called the Green function to the field of velocity or propagator of the hydrodynamic disturbance, or else, tensor of Oseen-Burgers, of a purely geometric nature and therefore independent of the properties of the fluid. In addition, the disturbs propagate with slow decay of the order of $\mathcal{O}(1/r)$ where r is the distance with respect to the pole $\boldsymbol{x}_0$.

This way, this slow decay characterizes the long-range hydrodynamic interactions and even particles relatively distant from each other interact meaningfully leading to problems of divergence of sums or superposition of fields of disturbance induced by a large number of singularities.

The stress tensor associated with a Green function can be obtained from the constitutive equation for the stress tensor of an incompressible Newtonian fluid. For this, it is enough to apply the equations described early in the strain rate tensor $\boldsymbol{\sigma}\ \boldsymbol{\sigma} = -p\boldsymbol{I} + \eta[\nabla \boldsymbol{u} + (\nabla \boldsymbol{u})^T]$. After some calculation we obtain:

$$\boldsymbol{\sigma}(\boldsymbol{x}, \boldsymbol{x}_0) = \frac{\boldsymbol{F}}{8\pi} \cdot \boldsymbol{\mathcal{T}}(\boldsymbol{x}, \boldsymbol{x}_0), \tag{2.72}$$

in which the third-order tensor, given by:

$$\boldsymbol{\mathcal{T}}(\boldsymbol{x}, \boldsymbol{x}_0) = \frac{6(\boldsymbol{x} - \boldsymbol{x}_0)(\boldsymbol{x} - \boldsymbol{x}_0)(\boldsymbol{x} - \boldsymbol{x}_0)}{|\boldsymbol{x} - \boldsymbol{x}_0|^5}\,, \tag{2.73}$$

is a Green tensorial function associated with the propagation of the voltage disturbance generated by a hydrodynamic dipole in a Stokes flow.

2.2.6 Integral Representation of the Stokes Flow

According to the differential version of the reciprocal theorem, in the case of strength of the field, we have :

$$\nabla \cdot (\boldsymbol{\sigma}' \cdot \boldsymbol{u}) - \nabla \cdot (\boldsymbol{u}' \cdot \boldsymbol{\sigma}) = 0\,, \tag{2.74}$$

where, $(\boldsymbol{u}, \boldsymbol{\sigma})$ is the solution of the field of velocities and tensions of a Stokes flow arbitrary and $(\boldsymbol{u}', \boldsymbol{\sigma}')$, represent the solution of the field of velocities and stress of a flow, being in this case the fundamental solution of the Stokes equations. Applying the version differential of the reciprocal theorem, together with the fundamental solution, we obtain that

$$\nabla \cdot \left(\frac{1}{8\pi} \boldsymbol{F} \cdot \boldsymbol{\mathcal{T}} \cdot \boldsymbol{u} + \boldsymbol{\sigma} \cdot \frac{1}{8\pi\eta} \boldsymbol{F} \cdot \boldsymbol{\mathcal{G}} \right) = 0\,. \tag{2.75}$$

Consider now two possibilities for the integration of equation (2.75) into every volume V of the fluid. First, assume that the uniqueness that generates a disturbance in the velocity field of the liquid, is not within V. In this way, the function of equation equation (2.75) is regular in V. Consequently, the entire volume V, as it is a region can be reduced to a point, preserving the physical contours. Therefore, we have:

$$\int_V \nabla \cdot (\eta \boldsymbol{\mathcal{T}} \cdot \boldsymbol{u} + \boldsymbol{\sigma} \cdot \boldsymbol{\mathcal{G}}) dV = 0\,. \tag{2.76}$$

Applying the divergence theorem we have:

$$\int_S \eta \boldsymbol{\mathcal{T}} \cdot \mathbf{u} \cdot \boldsymbol{n} dS + \int_S \boldsymbol{\sigma} \cdot \boldsymbol{\mathcal{G}} \cdot \boldsymbol{n} dS = 0\,. \tag{2.77}$$

Now consider the second possibility. In this case, the point of singularity lies in the interior of V. As shown in figure (2.4).

Note that equation (2.77) is regular in the volume $V - V_e$, in which V_e is the volume of the sphere of radius R. Thus, it follows that

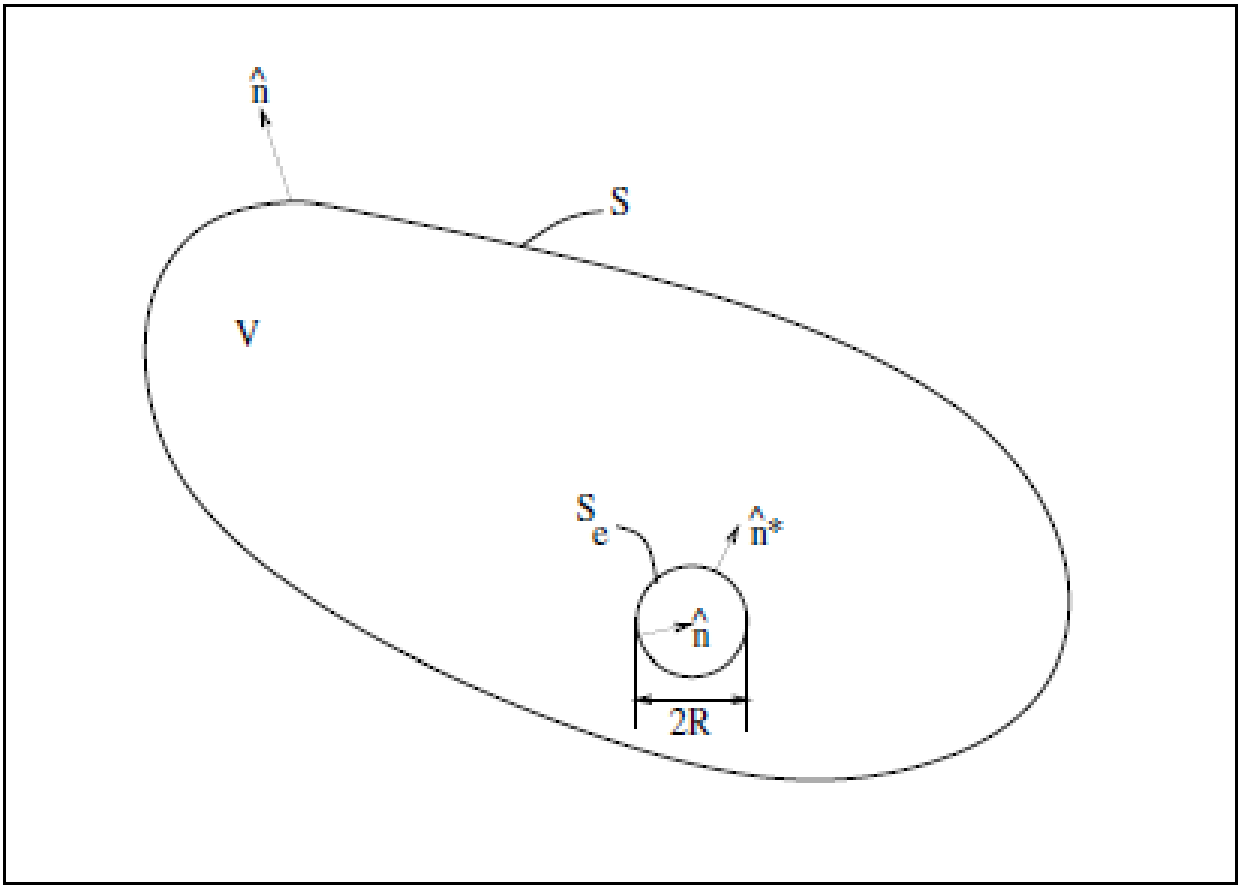

Figure 2.4: Schematic for the second possibility.

$$\int_{V-V_e} \nabla \cdot (\eta \boldsymbol{\mathcal{T}} \cdot \boldsymbol{u} + \boldsymbol{\sigma} \cdot \boldsymbol{\mathcal{G}}) dV = 0\,, \tag{2.78}$$

applying the divergence theorem in the equation 2.78, we have:

$$\int_{S-S_e} \eta \boldsymbol{\mathcal{T}} \cdot \boldsymbol{u} \cdot \boldsymbol{n} dS + \int_{S-S_e} \boldsymbol{\sigma} \cdot \boldsymbol{\mathcal{G}} \cdot \boldsymbol{n} dS = 0\,, \tag{2.79}$$

Again, applying the divergence theorem in equation (2.79), one has:

$$\boldsymbol{u}(\boldsymbol{x}_0) = -\frac{1}{8\pi\eta} \int_S \boldsymbol{\mathcal{G}}(\mathbf{r}) \cdot \boldsymbol{\sigma}(\boldsymbol{x}) \cdot \boldsymbol{n} dS - \frac{1}{8\pi\eta} \int_S \boldsymbol{u}(\boldsymbol{x}) \cdot \boldsymbol{\mathcal{T}}(\boldsymbol{r}) \cdot \boldsymbol{n} dS\,. \tag{2.80}$$

2.2.7 Faxén's Law

For the development of the global mobility matrix, which describes the hydrodynamic interactions between all the particles in a suspension, it is used the Faxing Law, which determines the hydrodynamic force on a spherical particle in the domain of a liquid. Suppose initially, that before the introduction of a rigid spherical particle, the distribution of velocity in a fluid domain is $\boldsymbol{u}_\infty(\boldsymbol{x})$. Applying to the fluid a distribution density strength $\boldsymbol{t} = \boldsymbol{\sigma} \cdot \boldsymbol{n}$ on a spherical surface

S_α and radius a_α,centered in $\boldsymbol{x}_0$, its initial velocity distribution will change. Thus, by the integral representation of the Stokes flow for a fast particle, the additional speed $\boldsymbol{u}'(\boldsymbol{x})$ in $\boldsymbol{x}$ due to the distribution of the forcing of surface density $\boldsymbol{t}$, given by:

$$\boldsymbol{u}'(\boldsymbol{x}) = -\frac{1}{8\pi\eta}\int_{S_\alpha} \boldsymbol{\mathcal{G}}(\boldsymbol{x}-\boldsymbol{x}')\cdot\boldsymbol{t}(\boldsymbol{x}')dS(\boldsymbol{x}'). \tag{2.81}$$

By the superposition principle, the total field velocity $\boldsymbol{u}(\boldsymbol{x})$, is given by:

$$\boldsymbol{u}(\boldsymbol{x}) = \boldsymbol{u}_\infty(\boldsymbol{x}) - \frac{1}{8\pi\eta}\int_{S_\alpha} \boldsymbol{\mathcal{G}}(\boldsymbol{x}-\boldsymbol{x}')\cdot\boldsymbol{t}(\boldsymbol{x}')dS(\boldsymbol{x}'). \tag{2.82}$$

Consider the more general case of a rigid sphere that translates with velocity $\boldsymbol{U}$ and rotates around its center with angular velocity $\boldsymbol{\omega}$. Thus, on the surface of the sphere S_α the flow satisfies the following boundary condition:

$$\mathbf{U} + \boldsymbol{\omega}\times(\boldsymbol{x}-\boldsymbol{x}_0) = \boldsymbol{u}_\infty(\boldsymbol{x}) - \frac{1}{8\pi\eta}\int_{S_\alpha} \boldsymbol{\mathcal{G}}(\boldsymbol{x}-\boldsymbol{x}')\cdot\boldsymbol{t}(\boldsymbol{x}')dS(\boldsymbol{x}'). \tag{2.83}$$

Integrating the equation (2.83) on the surface of the sphere, we have

$$\begin{aligned}\int_{S_\alpha} \boldsymbol{U}dS(\boldsymbol{x}') \quad &+ \quad \int_{S_\alpha} \boldsymbol{\omega}\times(\boldsymbol{x}-\boldsymbol{x}_0)dS(\boldsymbol{x}') = \int_{S_\alpha}\boldsymbol{u}_\infty(\boldsymbol{x}')dS(\boldsymbol{x}') \\ &- \quad \frac{1}{8\pi\eta}\int_{S_\alpha}\left[\int_{S_\alpha}\left(\frac{\boldsymbol{I}}{r}+\frac{\boldsymbol{r}\boldsymbol{r}}{r^3}\right)\cdot\boldsymbol{t}(\boldsymbol{x}')dS(\mathbf{x}')\right]dS(\boldsymbol{x})\end{aligned} \tag{2.84}$$

Where $\boldsymbol{r} = \boldsymbol{x}-\boldsymbol{x}'$ e $r = |\boldsymbol{x}|$. Solving the last equation for $\boldsymbol{F}$,

$$\boldsymbol{F} = \int_{S_\alpha}\boldsymbol{t}(\boldsymbol{x}')dS(\boldsymbol{x}'), \tag{2.85}$$

it follows that the total force at the surface of the sphere is given by:

$$\boldsymbol{F} = \frac{3\eta}{2a}\int_{S_\alpha}\left[\boldsymbol{u}_\infty(\boldsymbol{x}')-\boldsymbol{U}\right]dS(\boldsymbol{x}'). \tag{2.86}$$

To solve the integral (2.86), we will consider the effect of particle size, $\boldsymbol{u}_\infty(\boldsymbol{x}')$ around the center $\boldsymbol{x}_0$ of the sphere, we arrive at the following expression:

$$\begin{aligned}\boldsymbol{u}_\infty(\boldsymbol{x}') \quad &= \quad \boldsymbol{u}(\mathbf{x}_0) + (\boldsymbol{x}'-\boldsymbol{x}_0)\cdot\nabla\boldsymbol{x}_\infty(\boldsymbol{x}_0) + \\ &+ \quad \frac{1}{2}(\boldsymbol{x}'-\boldsymbol{x}_0)(\boldsymbol{x}'-\boldsymbol{x}_0):\nabla\nabla\boldsymbol{u}_\infty(\boldsymbol{x}_0)+\cdots\end{aligned} \tag{2.87}$$

Integrating the equation (2.87) on the surface of the sphere S, we obtain S_α, we have:

$$\begin{aligned}\int_{S_\alpha}\boldsymbol{u}_\infty(\boldsymbol{x}')dS \quad &= \quad \boldsymbol{u}(\boldsymbol{x}_0)4\pi a^2 + \left[\int_{S_\alpha}(\boldsymbol{x}'-\boldsymbol{x}_0)dS\right]\cdot\nabla\boldsymbol{x}_\infty(\boldsymbol{x}_0) + \\ &+ \quad \frac{1}{2}\left[\int_{S_\alpha}(\boldsymbol{x}'-\boldsymbol{x}_0)(\mathbf{x}'-\boldsymbol{x}_0)dS\right]:\nabla\nabla\boldsymbol{u}_\infty(\boldsymbol{x}_0)+\cdots.\end{aligned} \tag{2.88}$$

Noting that for Stokes flows the term $\nabla^{2n+2}\boldsymbol{u}_\infty = 0$ for $n = 1, 2, \ldots$, is then the integrals below present and we get the following results:

$$\int_{S_\alpha} (\boldsymbol{x}' - \mathbf{x}_0) dS = \mathbf{0} \tag{2.89}$$

and:

$$\int_{S_\alpha} (\boldsymbol{x}' - \boldsymbol{x}_0)(\boldsymbol{x}' - \boldsymbol{x}_0) dS = \frac{4}{3}\pi a^4 \boldsymbol{I} \tag{2.90}$$

, it follows, by substituting these results into equation (2.89), we obtain the following expression of the first law of Faxén for the translation of a rigid sphere, given by:

$$\boldsymbol{F} = 6\pi\eta a \left[\left(1 + \frac{a^2}{6}\nabla^2 \right) \boldsymbol{u}_\infty(\boldsymbol{x}_0) - \mathbf{U} \right] \tag{2.91}$$

In this sections, we have considered the motion induced by a particle immersed in a flow for which $\nabla_\infty \boldsymbol{u}$ is a constant and have determined the resulting force and the first force moments of torque and stresslet. Ideally, one would like to determine the force and these moments from the motion of a body and a general ambient flow field, and this is our purpose here. The linear relations between the motion (of the particle and fluid) and the force and its moments are known as Faxén laws and contain additional pieces owing to the curvature of the flow $\nabla^2 \boldsymbol{u}_\infty$. The development of these results are involved and uses again the reciprocal theorem (see reference [92], Chapter 3). Here we simply give the results for the hydrodynamic force and force moments applied to a sphere:

$$\boldsymbol{F} = 6\pi\mu a[(1 + \frac{a^2}{6}\nabla^2)\boldsymbol{u_\infty(x = x_0)} - \boldsymbol{u^p}] \tag{2.92}$$

$$\boldsymbol{T} = 8\pi\mu a^3[\boldsymbol{\omega^\infty(x = 0)} - \boldsymbol{\omega^p}] \tag{2.93}$$

$$\boldsymbol{S} = \frac{20}{3}\pi a^3 (1 + \frac{a^2}{10}\nabla^2)\boldsymbol{E}^\infty(\boldsymbol{x} = 0) \tag{2.94}$$

2.2.8 Mobility Formulation and Mobility Tensor

In this paragraph we use the Faxen's Law for the development of the mobility matrix global. This result determines the force exerted by a sphere of radius a on the fluid. In this way, we can write the equation (2.92) as

$$\boldsymbol{F}_\alpha = 6\pi\eta a_\alpha \left[\boldsymbol{U}_\alpha - \left(1 + \frac{a_\alpha^2}{6}\nabla^2 \right) \boldsymbol{u}'(\boldsymbol{x}_\alpha) \right] , \tag{2.95}$$

where $\boldsymbol{u}'$ Is the velocity field resulting from the flow induced by the other particles of the suspension, in which the particle is immersed with a α is immersed with a speed $\boldsymbol{U}_\alpha$. For diluted system the field $\boldsymbol{u}'$ is determined by applying the superposition principle, due to the linearity of the Stokes equations, in the first order disturbances induced by every particle $\beta \neq \alpha$ we obtain:

$$\boldsymbol{u}'(\boldsymbol{x}) = \sum_{\beta=1}^{N} \frac{1}{8\pi\eta} \left(1 + \frac{a_\beta^2}{6}\nabla^2\right) \boldsymbol{\mathcal{G}}(\boldsymbol{x} - \boldsymbol{x}_\beta) \cdot \boldsymbol{F}_\beta, \tag{2.96}$$

where $\boldsymbol{\mathcal{G}}(\boldsymbol{r})$ is the Oseen-Burgers Tensor with $\boldsymbol{r} = \boldsymbol{x} - \boldsymbol{x}_\beta$. Substituting equation (2.96) in equation (2.97), we obtain the expression for the force induced in the sphere α due to the field speed caused by other spheres β moving in the same suspension. Of that way we have to

$$\boldsymbol{F}_\alpha = 6\pi\eta a_\alpha \boldsymbol{I} \cdot \left[\boldsymbol{U}_\alpha - \frac{1}{8\pi\eta} \sum_{\beta=1}^{N} \left(1 + \frac{a_\alpha^2}{6}\nabla^2\right)\left(1 + \frac{a_\beta^2}{6}\nabla^2\right) \boldsymbol{\mathcal{G}}(\boldsymbol{r}) \cdot \boldsymbol{F}_\beta\right], \tag{2.97}$$

with $\alpha = 1, \ldots, N$ e $\mathbf{r} = \boldsymbol{x}_\beta - \boldsymbol{x}_\alpha$. By means of the equation (2.97), the following can be defined: tensor mobility, given by

$$\mathbf{G}^{\alpha\beta} = \frac{1}{8\pi\eta}\left(1 + \frac{a_\alpha^2}{6}\nabla^2\right)\left(1 + \frac{a_\beta^2}{6}\nabla^2\right) \boldsymbol{\mathcal{G}}(\mathbf{r})\,. \tag{2.98}$$

Using $\nabla^2\nabla^2\boldsymbol{\mathcal{G}} = 0$ and the relation

$$\nabla^2\boldsymbol{\mathcal{G}}(\boldsymbol{r}) = \frac{2}{r^3}\boldsymbol{I} - \frac{6}{r^5}\boldsymbol{r}\boldsymbol{r}\,, \tag{2.99}$$

the tensor $\mathbf{G}^{\alpha\beta}$ is :

$$\mathbf{G}^{\alpha\beta} = \frac{1}{8\pi\eta}\left\{\frac{1}{r}[\mathbb{I} + \hat{\boldsymbol{r}}\hat{\boldsymbol{r}}] + \frac{1}{3r^3}(a_\alpha^2 + a_\beta^2)[\boldsymbol{I} - 3\hat{\mathbf{r}}\hat{\boldsymbol{r}}]\right\}. \tag{2.100}$$

This tensor is called the mobility tensor of Rotne-Prager and describes the interactions hydrodynamics between particlesα e β. This tensor only depends on of the particulate system in a given instant of time and has decay slow, or long-range, of the order of $1/r$. For a monodisperse suspension, that is $a_\alpha = a_\beta = a$ the tensor mobility can be written as

$$\mathbf{G}^{\alpha\beta} = \frac{1}{8\pi\eta}\left\{\frac{1}{r}[\boldsymbol{I} + \hat{\boldsymbol{r}}\hat{\boldsymbol{r}}] + \frac{2}{3r^3}a^2[\boldsymbol{I} - 3\hat{\boldsymbol{r}}\hat{\boldsymbol{r}}]\right\}. \tag{2.101}$$

For the development of tensor global mobility, we work with the tensor $\boldsymbol{M}^s$ and $\boldsymbol{M}^p$, respectively referred to as automotive and mobility tensioners between pairs, whose components are given by:

$$M^s_{\alpha\alpha,ij} = \frac{\delta_{ij}}{6\pi\eta a}, \quad \alpha = 1, \ldots, N \tag{2.102}$$

and

$$M^p_{\alpha\beta,ij} = G^{\alpha\beta}_{ij}, \quad \alpha, \beta = 1, \ldots, N \;\; \alpha \neq \beta. \tag{2.103}$$

Thus, equation (2.103) after the isolation of the term$\mathbf{U}_s$, can be written as:

$$\boldsymbol{U}_\alpha = \boldsymbol{M}^s \cdot \boldsymbol{F}_\alpha + \sum_{\alpha\neq\beta} \boldsymbol{M}^p \cdot \boldsymbol{F}_\beta\,. \tag{2.104}$$

We define $\boldsymbol{M}$, the global mobility matrix, as the sum of the matrices or mobility tensors and mobility between peers, so that

$$\boldsymbol{M} = \boldsymbol{M}^s + \boldsymbol{M}^p\,, \tag{2.105}$$

and equation (2.105) can be expressed in this form:

$$\boldsymbol{U} = \boldsymbol{M} \cdot \boldsymbol{F}\,. \tag{2.106}$$

and therefore, equation (2.106) can be expressed in summary form, as:

$$\begin{pmatrix} \boldsymbol{U}_1 \\ \boldsymbol{U}_2 \\ \vdots \\ \boldsymbol{U}_N \end{pmatrix} = \begin{pmatrix} \boldsymbol{M}_{11} & \boldsymbol{M}_{12} & \cdots & \boldsymbol{M}_{1N} \\ \boldsymbol{M}_{21} & \boldsymbol{M}_{22} & \cdots & \boldsymbol{M}_{2N} \\ \vdots & \vdots & \ddots & \vdots \\ \boldsymbol{M}_{N1} & \boldsymbol{M}_{N2} & \cdots & \boldsymbol{M}_{NN} \end{pmatrix} \cdot \begin{pmatrix} \boldsymbol{F}_1 \\ \boldsymbol{F}_2 \\ \vdots \\ \boldsymbol{F}_N \end{pmatrix}, \tag{2.107}$$

where $\boldsymbol{U}_1, \boldsymbol{U}_2, \ldots, \boldsymbol{U}_N$ denotes the velocities of the particles $1, 2, \ldots, N$. The tensor $\boldsymbol{M}_{ij}$ for $i = 1, \ldots, N$ and $j = 1, \ldots, N$, depend on the configuration of the suspension. Also, $\boldsymbol{M}_{ii}$ matrix diagonal, are responsible for to couple the effect of the forces acting on each part α of the suspension in his company velocity. The elements$\boldsymbol{M}_{ij}$ para $i \neq j$, represent the percussions in the velocities of the particles $\alpha \neq \beta$ due to a force $\boldsymbol{F}_\beta$ active in each part β.

2.3 Theoretical Components In Non Newtonian Fluids

Flow of non-Newtonian fluids occurs not only in nature, for example, mud slides and avalanches, but also in many industrial processes involving chemicals (polymers), biological materials (blood), food (honey, ketchup, yogurt), pharmaceutical and personal care items (shampoo, creams), etc. In general, these fluids exhibit certain distinct features such as shear-rate dependency of the viscosity (related to shear-thinning or shear-thickening aspects of the fluid), normal stress effects (related to die-swell and rod-climbing), creep or relaxation (viscoelasticity), yield stress effects (viscoplasticity), history effects (time dependent response), etc. There are many different models which can be used for different fluids under different conditions. This section presents non-Newtonian fluids in order to support the modeling and some theoretical components in non Newtonian fluids.

2.3.1 Mathematical Modeling of a Polymeric Suspension

The starting point for the analysis of incompressible flow of polymeric fluids is the continuity equation (or mass conservation equation) and the momentum equation which are given respectively by:

$$\nabla \cdot \boldsymbol{u} = 0, \tag{2.108}$$

and

$$\nabla \cdot \boldsymbol{\Sigma} = 0. \tag{2.109}$$

When the interest and solve the problem of a flow of non-Newtonian fluid some additional difficulties arise, because we have to lead to more complex constitutive equations. The equation

of the amount of movement is usually written, for polymeric fluids, highlighting the part referring to the contribution of the solvent and the part referring to macromolecules, as well:

$$\rho\frac{D\boldsymbol{u}}{Dt} = \rho\boldsymbol{u} + \nabla\cdot\boldsymbol{\sigma}_s + \nabla\cdot\boldsymbol{\sigma}_m, \tag{2.110}$$

Where $\boldsymbol{\sigma}_s$ is the contribution of the solvent (which has Newtonian behavior) and $\boldsymbol{\sigma}_m$ is the contribution of the macromolecules present in the polymer. The additional stress tensor $\boldsymbol{\sigma}_m$ must be obtained through constitutive equations derived from theories on fluid rheology, such as the kinetic theory, the theory of concentrated suspension networks and fused polymers and the theory of the reaction.In this case, the tensor cannot be written explicitly in function of the velocity gradient (as in the case of the Newtonian contribution) so it has to be written in terms of other tensors as will be seen later.

2.3.2 Generalized Newtonian Fluid

As we find in the literature, there are a large number of constitutive equations, which seek to describe the rheological behavior of polymeric fluids. These equations can be framed in different groups, according to their shape, their mathematical nature and their ability to predict material functions. Initially, the Generalized Newtonian Fluid (FNG) is mentioned, this consists of the generalization of the Newtonian fluid model for fluids in which viscosity is a function of the magnitude of the strain rate $\mathbf{D}$. The FNG models are a first generalization of classical fluid mechanics to non-Newtonian fluid mechanics. In this situation, the elastic effects are not predicted, since this category of models does not yet consider the calculation of the tensor $\boldsymbol{\sigma}_p$, these models can be applied satisfactorily only in cases where shear flows and flow rates occur. For FNG we have to replace the equation (2.111) below in the equation (2.110).

$$\boldsymbol{\sigma}_s = 2\mu(\dot{\gamma})\mathbf{D} \text{ e } \boldsymbol{\sigma}_p = \mathbf{0}, \tag{2.111}$$

where the viscosity $\mu(\dot{\gamma})$ is now a function of the shear rate $\dot{\gamma}$ which is equal to the second invariant of the strain rate tensor $\mathbf{D}$. There are many empirical models that provide mathematical relationships for viscosity as a function of the deformation rate but are generally only valid for certain fluids or in certain application regions.

Noteworthy, again, we have the simplest and best known model for $\dot{\gamma}$ dependent viscosity which is called the Power law (*Power-Law*) [83].

$$\mu(\dot{\gamma}) = C\dot{\gamma}^{n-1}, \tag{2.112}$$

where C is a consistency parameter and n is the index of this model. These parameters are fluid dependent and are obtained by adjusting curves to experimental data. This model allows analytical solutions to be obtained for a wide variety of flows, and it is even possible to represent the pseudo-plastic effect (*shear-thinning*). The FNG model has the deficiency of not predicting the elastic effects characteristic of polymeric fluids. From a numerical point of view, the use of FNG does not present great difficulties in comparison to the study of Newtonian fluids. For this reason, these models are widely used in the study of industrial applications, such as extrusion

and injection processes, to predict some stages or characteristics of the referred processes that are associated only with purely viscous phenomena and for which the effects of non-Newtonian viscosity are of great importance.

2.3.3 Non-Linear Viscoelastic Fluid

The mathematical models for non-linear viscoelastic fluids are more robust because they allow to describe at least qualitatively elastic effects and non-linear characteristics, such as differences in normal stresses and non-Newtonian viscosity and therefore will not be treated in this thesis. The nonlinear differential models can be obtained from the model for linear viscoelastic fluid, in differential form, as seen in others theoretical approach. The modifications consist of the substitution of the derivatives time by the Oldroyd derivative and / or the inclusion of non-linear terms and other parameters in the equations. Thus, the constitutive equations obtained will be objective.

Below, the relationship that defines the high Oldroyd derivative of the stress tensor $\boldsymbol{\sigma}$,

$$\frac{\delta_{-}(\boldsymbol{\sigma})}{\delta t} = \frac{D\boldsymbol{\sigma}}{Dt} - \boldsymbol{\sigma}(\nabla \mathbf{u})^{T} - (\nabla \mathbf{u})\boldsymbol{\sigma}. \tag{2.113}$$

These models are not limited to small deformations, as is the case with linear viscoelasticity, they are models closer to reality that allow to obtain qualitative information regarding linear and non-linear viscoelastic effects in various types of flows. Sometimes the models are found using the conformation tensor, which is related to the spatial configuration (extension) of the polymer macromolecules and can be related to the stress tensor. However, although there are some advantages over stability, there are some disadvantages in relation to the greater amount of computational memory required.

2.3.4 Oldroyd-B model

The Oldroyd-B model [93] derives from the kinetic theory for concentrated polymeric suspensions and fused polymers. The polymeric chain is represented by a set of two spheres joined by a spring as shown in the figure (2.5). In this configuration, the spheres represent the center of mass of the system and are related to the hydrodynamic interaction between the solvent and the macromolecules of the polymeric suspension (the viscous drag force of the solvent on the macromolecules). The springs represent the elasticity effect of macromolecules or the restorative effect of the polymer. This ball-spring configuration called *dumbbell* is simplified by assuming a linear spring or Hooke spring behavior.

At this point the balance between the forces due to the Brownian motion F_b and the elastic forces F_e, ie $F_b \approx F_e$,, where Hooke's linear spring is used to model the Brownian force of macromolecule restoration.

$$F_b \approx C_m r, \tag{2.114}$$

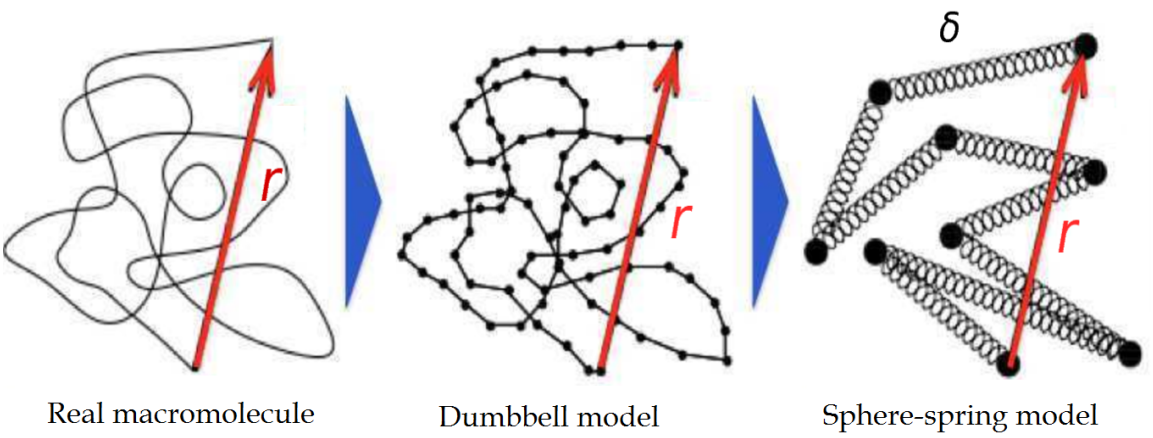

Figure 2.5: Schematic representation of a macromolecule in the *dumbbell* model. The **r** vector links the ends of the end-to-end macromolecule and δ is the length of an individual monomer.

Here C_m is the spring constant and $r = ||\mathbf{r}||$ is the end-to-end distance of the macromolecule as in the figure (2.5). At this point note that evidently r varies over time, ie, $r = r(t)$ and it is assumed that, at $t = 0$, the macromolecule is in its totally relaxed regime (equilibrium).

Brownian motion has energy $E = K_B T$, where K_B is the Boltzmann constant and T is the absolute temperature. We have also $E = \mathbf{F} \cdot \mathbf{r}$, can be written

$$F_b = \frac{3K_B T}{a}. \tag{2.115}$$

Here $||\mathbf{r}|| = r \approx a$ as a typical choice of the distance between the ends of the macromolecule in random configuration corresponding to the configuration of balance, as previously stated. From (2.114) and (2.115) it is determined, by way of illustration, that the elastic coefficient of the spring (or constant of the spring) in terms of the energy E will be given by:

$$G = \frac{3K_B T}{a^2} = \frac{3E}{a^2}. \tag{2.116}$$

The hydrodynamic interaction between the molecule and the solvent is represented by the viscous drag over 'the spheres that constitute it. In this model *dumbbell*, the viscous force, F_v, is defined as the force exerted on an isolated sphere of radius.

a for the viscosity solvent μ. For low Reynolds numbers we have, as

$$F_v = 6\pi\mu a \frac{dr}{dt}. \tag{2.117}$$

In thermodynamic equilibrium, the balance between F_e and F_v results in

$$\frac{dr}{dt} = \frac{G}{C_v} r, \tag{2.118}$$

where $C_v = 6\pi\mu a$ is the viscous drag coefficient. If we integrate the equation (2.118) with the initial condition $r(0) = r_0$, we obtain:

$$r(t) = r_0 \exp(t/\tau). \tag{2.119}$$

And this last equation provides the variation of the average equilibrium length r as a function of time $t \geq 0$. Note that this variation is increasing in t and varies exponentially. Here it is important to note that

$$\tau = \frac{C_v}{G} = \frac{2\pi\mu a^3}{K_B T}, \tag{2.120}$$

is defined as the relaxation time of the macromolecule.

By way of illustration, replacing the equation which says that $a \approx \sqrt{N}\delta$, in the equation (2.120), we obtain

$$\tau \approx \frac{2\pi\mu N^{3/2}\delta^3}{K_B T}. \tag{2.121}$$

As stated in the section the number N corresponds to the total number of monomers and thus we can define $N = Pt/P_i$, where Pt is the total weight of the polymer and P_i is the weight of a single monomer. Hence it is concluded that

$$\tau \propto (P/P_i)^{3/2}. \tag{2.122}$$

The equation shows an important result where it is seen that polymers of high molecular weights have longer relaxation times. In other words, the elastic or memory effect of a fluid suspension consisting of these polymers can cause major changes in flow. This explains (among other factors) why only a few *ppm* of a high molecular weight polymer added to turbulent flows can considerably reduce the pressure drop.

2.3.5 Nonlinear Stress Tensor and the Adaptation Tensor

As in the equation we have that the tension tensor of the Oldroyd fluid will be given by

$$\boldsymbol{\Sigma} = -p\mathbf{I} + \boldsymbol{\sigma}. \tag{2.123}$$

We use the deviatory part $\boldsymbol{\sigma}$ as being

$$\boldsymbol{\sigma} = 2\mu_s(\phi, \dot{\gamma})\mathbf{D} + \bar{\boldsymbol{\sigma}}_B, \tag{2.124}$$

where $\mu_s(\phi, \dot{\gamma})$ is the dynamic viscosity, p is the mechanical pressure, $\dot{\gamma}$ is the shear rate. The tensor $\bar{\boldsymbol{\sigma}}_B$ is the contribution of elastic tension, due to the presence of macromolecules. This tensor can be interpreted as a correlation between the microscopic behavior of the macromolecules and the macroscopic response obtained in the flow.

For a diluted polymer suspension, $\phi \ll 1$, it can be assumed that the effective viscosity of the fluid can be calculated by $\mu_s(\phi, \dot{\gamma}) \approx \mu(1 + c\phi) = \mu_s(\phi)$, as seen in the early. Here μ is the viscosity of the Newtonian base fluid. In the case of rigid spheres Einstein calculated that $c = 5/2$. As seen in the section, experiments in rheology showed that for a diluted suspension of PAMA the best fit for the parameter c was determined as $c = 1.53 \times 10^5$. Note that this parameter found experimentally for PAMA is much larger than in the case for rigid spheres, one of the explanations of this fact is that PAMA has a high molecular weight.

Cross's dimensionless model is also used in this work to have the dimensionless viscosity $\tilde{\mu}_s$ as a function of De, as seen at previously. Such a dimensionless model is transcribed, due to its importance.

$$\tilde{\mu}_s(De) = \frac{\mu_s(De)}{\mu_w} = \frac{\tilde{\mu}_0 + \tilde{\mu}_\infty (KDe)^m}{1 + (KDe)^m}, \tag{2.125}$$

where: $\tilde{\mu}_0 = \mu_0/\mu_w$, $\tilde{\mu}_\infty = \mu_\infty/\mu_w$, $K = k/\tau_p$ and $De = \tau_p \dot{\gamma}$.

A proposal for the $\boldsymbol{\sigma}_B$ tensor that is non-Newtonian and arises due to the presence of macromolecules is given by:

$$\bar{\boldsymbol{\sigma}}_B = \lim_{V \to \, infty} \frac{1}{V} \int_0^V \boldsymbol{\sigma}_B d\boldsymbol{x} = n\langle \boldsymbol{\sigma}_B \rangle, \tag{2.126}$$

where $\langle\ \rangle$ represents an ensemble average, (i.e.,) $\bar{\boldsymbol{\sigma}}_B$ is a volumetric average over a control volume V large enough to contain a significant number of macromolecules for if you take this average.

The elastic restoring force vector is given by $\mathbf{F}_v = G\mathbf{r}$, where G is an elasticity coefficient and $\mathbf{r}$ is the vector figure (2.5). The associated stress tensor to a macromolecule is given by the dyadic product , $\boldsymbol{\sigma}_B = G\boldsymbol{r}\boldsymbol{r}^T$ E taking an average under the element volume N_m, has:

$$\langle \boldsymbol{\sigma}_B \rangle = G \left(\frac{1}{N_m} \sum_{s=1}^{N_m} \boldsymbol{r}\boldsymbol{r}^T \right), \tag{2.127}$$

since $n = N_m/V$, then it can be concluded that

$$\bar{\boldsymbol{\sigma}}_B = n\langle \boldsymbol{\sigma_B} \rangle = nG\Big\langle \boldsymbol{r}\boldsymbol{r}^T \Big\rangle. \tag{2.128}$$

The adaptation tensor or the tensor of the moment of inertia of deformation or the conformation tensor of the macromolecules is defined by

$$\boldsymbol{B}(t) = \Big\langle \boldsymbol{r}\boldsymbol{r}^T \Big\rangle = \frac{1}{N_m} \sum_{s=1}^{N_m} \boldsymbol{r}\boldsymbol{r}^T. \tag{2.129}$$

Note that $\boldsymbol{B}(t)$ is by definition a defined positive tensor and can be interpreted as the tensor that describes the movement of macromolecules, showing both the position in which they are being oriented, and how much they deform over time, when applying a flow. And finally the $\boldsymbol{\Sigma}$ stress tensor given by the equation will become

$$\boldsymbol{\Sigma} = -p\boldsymbol{I} + 2\mu_s(De)\boldsymbol{D} + nG\boldsymbol{B}(t), \tag{2.130}$$

where the tensor $\boldsymbol{\sigma}$ is explained in terms of $\boldsymbol{B}$, in the equation below

$$\boldsymbol{\sigma} = 2\mu_s(De)\boldsymbol{D} + nG\boldsymbol{B}(t). \tag{2.131}$$

To close the equation (2.130) a time evolution equation is needed for the tensor $\boldsymbol{B}$ and the relationship between drag and viscous forces, it is possible to write

$$6\pi\mu a \frac{d\mathbf{r}}{dt} + G\boldsymbol{r} = 0. \tag{2.132}$$

From equation ((2.132)), we conclude, after multiplying by $\mathbf{r}^T$ on both sides and subtracting the term of the rigid body translation and assume a frame of reference that rotates and deforms with the macromolecule, the equation (2.133):

$$3\pi\mu a\frac{\delta_{-}(\mathbf{B})}{\delta t} + G\boldsymbol{B} - K_BT\boldsymbol{I} = 0, \tag{2.133}$$

where

$$\frac{\delta_{-}(\mathbf{B})}{\delta t} = \frac{D\mathbf{B}}{Dt} - \nabla\mathbf{u}\cdot\mathbf{B} - \mathbf{B}\cdot(\nabla\mathbf{u})^T, \tag{2.134}$$

is the high Oldroyd derivative which can be understood as the rate of change of $\boldsymbol{B}$ seen by an observer that is deformed and translated with the macromolecule.

Thus the equation (2.133) will be:

$$\frac{D\mathbf{B}}{Dt} = \nabla\mathbf{u}\cdot\mathbf{B} + \mathbf{B}\cdot(\nabla\mathbf{u})^T - \frac{K_BT}{\pi\mu aN\delta^2}\mathbf{B} + \frac{K_BT}{3\pi\mu a}\mathbf{I}. \tag{2.135}$$

Also note that, as the relaxation time τ can be written as $\tau = 2\pi\mu N^{3/2}\delta^3/K_BT$, then the equation ((2.135)) will finally be in the form:

$$\frac{D\mathbf{B}}{Dt} = \underbrace{\nabla\mathbf{u}\cdot\mathbf{B} + \mathbf{B}\cdot(\nabla\mathbf{u})^T}_{First\ term} - \underbrace{\frac{2}{\tau}\left(\mathbf{B} - \frac{a^2}{3}\mathbf{I}\right)}_{Second\ term}, \tag{2.136}$$

where $\dfrac{D}{Dt}$ represents the derivative material. In the equation (2.136), the first term represents the stretch of the macromolecule by flow and the second term represents the relaxation of the polymer due to the Brownian motion.

The conformation tensor $\mathbf{B}$ describes the instantaneous configuration of the macromolecules, being a measure of the deformation and the orientation in which the macromolecules are submitted once a stronger flow is applied. Note that the differential equation for the conformation tensor was obtained by a microstructural analysis, considering the thermodynamic balance of the system, in which the viscous forces are in balance with the Brownian restorative forces. This analysis was also considered based on a volumetric average over all the macromolecules of the polymer, and a reference turning and deforming with the macromolecule (high Oldroyd derivative) was considered in order to preserve the material indifference of the equation (2.136) to any system reference.

Before proceeding, the fundamental physical parameters are shown below:

1. For a flow of a fluid of density ρ and viscosity μ through an object of characteristic length x and characteristic speed u_c, define the Reynolds number, Re, as $Re = \rho u_c\, x/\mu$. Here it is important to mention that the viscosity μ is by convention taken to be the shear viscosity at the limit of small strain rates γ_0.

2. The most important dimensionless parameter is the Deborah number, which is given by the ratio between the main relaxation time of the polymer τ_p for a characteristic time of the flow t_f. Thus

$$De = \frac{\tau_p}{t_f}. \tag{2.137}$$

It is important to highlight that the main relaxation time τ_p is defined as the longest relaxation time, representing the main mechanism of interaction between macromolecules. This time τ_p is followed by several other secondary relaxation times, which are associated with the end of the stress relaxation process, that is, the return of the material to its undeformed condition, as seen previously.

The Deborah number De, provides us with a list of how altered the elastic effect will be, that is, high value of De, indicate that the elastic effect is greater, since when De tends to zero there are purely viscous flows. In this way, it can be said that Deborah number can be seen as the dimensionless shear rate of the flows.

3. The extensibility of the L polymer is given by the ratio between the size of the fully stretched macromolecule ℓ, where $\ell \approx N\delta$ is in accordance with the average distance corresponding to the random equilibrium state a. Thus $L = \ell/a$.

   Note that $L \approx \ell$, if, and only if, $De \approx 1$ or $De \geq 1$, as can be seen later in the case of the extensional flow, for example.

2.4 Maxwell's equations

We end this chapter with theoretical concepts necessary for the study of a magnetic particles, we present Maxwell's equations for electromagnetism.

Maxwell's equations of electromagnetism are represented by a system of four partial differential equations, which form the governing laws of electromagnetism: Gauss' laws for electricity, Gauss' law for magnetism, Faraday's law and Ampère-Maxwell law. All four of these four governing equations will be described here.

2.4.1 Gauss' law of electricity

Gauss' law of electricity postulates that a charge density contained within a regular region induces a liquid flow of electric field, through any surface that encompasses the distribution of non-zero sum loads. Therefore, given an electrical field $\boldsymbol{E}$ and let S be a closed surface of volume V with full charge q within this region. In a surface element $\boldsymbol{n}dS$, the field rate electric $\boldsymbol{E} \cdot \boldsymbol{n}dS$ and when integrated across the entire surface S of V, results as a consequence of the divergence theorem, in

$$\int_S \boldsymbol{E} \cdot \boldsymbol{n}dS = \int_V \nabla \cdot \boldsymbol{E}dV = \frac{q}{\epsilon_0}, \tag{2.138}$$

where $\epsilon_0 = 8.854 \times 10^{-12} C^2/N.m^2$ and the electrical permittivity in the vacuum. For a continuous charge distribution in V with bulk density of charge ρ_c, we have that $dq = \rho_c dV$, then we write the equationção (2.138), as

$$\int_V \left(\nabla \cdot \boldsymbol{E} - \frac{\rho_c}{\epsilon_0} \right) dV = 0, \tag{2.139}$$

and through the localization theorem of Continuum Mechanics see [94], we have that the equation (2.139), results in

$$\nabla \cdot \boldsymbol{E} = \frac{\rho_c}{\epsilon_0}\,, \tag{2.140}$$

which corresponds to the differential form of the Gaussian law of electricity. In the case of $\rho_c = 0$ the electric and sinusoidal field, defined by

$$\nabla \cdot \boldsymbol{E} = 0\,. \tag{2.141}$$

2.4.2 Gauss Law of Magnetism

Gauss' law of magnetism states that the magnetic induction flux that through a closed surface is zero. Physically, the result show that there are no sources or magnetic induction sinks that lead to a non-zero $\boldsymbol{B}$ divergence of this so the magnetic induction lines of $\boldsymbol{B}$, cannot end on the surface of V, forming closed *loops* or extending indefinitely, consequently none field line created or finalized inside this surface. Therefore, there are not free magnetic charges corresponding to the electric charges in the electrostatic field given by:

$$\nabla \cdot \boldsymbol{B} = 0\,. \tag{2.142}$$

The magnetic field effect can be characterized by the magnetic induction $\boldsymbol{B}$, being a vector field defined in terms of the external magnetic field $\boldsymbol{H}$ and the magnetization $\boldsymbol{M}$, as the product of the sum $\boldsymbol{H} + \boldsymbol{M}$ by the permeability magnetics of free space $\mu_0 = 4\pi \times 10^{-7} H.m^{-1}$ expressed by

$$\boldsymbol{B} = \mu_0(\boldsymbol{H} + \boldsymbol{M})\,. \tag{2.143}$$

The condition of the magnetization vector, aligned with the applied field, corresponds to the state of superparamagnetism, being defined by:

$$\boldsymbol{M} = \chi \boldsymbol{H}\,, \tag{2.144}$$

where χ is the magnetic susceptibility. From equation 92.143), we have:

$$\boldsymbol{B} = \mu_0(1 + \chi)\boldsymbol{H}\,. \tag{2.145}$$

The scalar coefficient $\mu = \mu_0(1+\chi)$ is defined as the magnetic permeability of the domain and $\kappa_m = \mu/\mu_0$, the relative permeability. So there are the following linear relations

$$\boldsymbol{M} = (\kappa_m - 1)\boldsymbol{H} = \chi \boldsymbol{H}\,, \tag{2.146}$$

$$\boldsymbol{B} = \mu_0(1 + \chi)\boldsymbol{H} = \mu \boldsymbol{H}\,. \tag{2.147}$$

The magnetization in free space is zero as long as $\chi = 0$ or $\kappa_m = 1$. In this case, there are no magnetic dipoles to be aligned with the field, so the equation (2.143) results in

$$\boldsymbol{B} = \mu_0 \boldsymbol{H} \,. \tag{2.148}$$

2.5 Faraday's law of induction

Faraday's law of induction relates the circulation of the magnetic field vector in a closed circuit C, with the negative of the temporal variation of the magnetic flux density that crosses the surface A bounded by C, establishing a relation between the field electric and the magnetic field. Faraday's law of induction is expressed as:

$$\int_C \boldsymbol{E} \cdot d\boldsymbol{l} = -\frac{D}{Dt} \int_A \boldsymbol{B} \cdot \boldsymbol{n} dA \;\; , \tag{2.149}$$

and can be interpreted physically as an electromotive force around a closed circuit. The differential form of Faraday's law relates spatial derivatives of $\boldsymbol{E}$ at any point $\boldsymbol{x}$ of space, with the time rate of $\boldsymbol{B}$ in the same point, being represented by

$$\nabla \times \boldsymbol{E} = -\frac{\partial \boldsymbol{B}}{\partial t} \,. \tag{2.150}$$

2.5.1 Ampere-Maxwell's Law

The Ampère-Maxwell law describes the relationship between a magnetic field and the current electricity that originates, establishing that a magnetic field can either be generated by a electric current as by the local temporal variation of an electric field. The shape integral of the Ampère-Maxwell law and given by:

$$\int_C \boldsymbol{H} \cdot d\boldsymbol{l} = \int_S \left(\mu_0 \boldsymbol{J} + \mu_0 \epsilon_0 \frac{\partial \boldsymbol{E}}{\partial t} \right) \cdot \boldsymbol{n} dS \,, \tag{2.151}$$

where the left side of this equation represents the integral of the magnetic field $\boldsymbol{H}$ along a closed path and the right side represents normal current flow the surface delimited by the closed path C. The differential form is given by:

$$\nabla \times \boldsymbol{H} = \mu_0 \left(\boldsymbol{J} + \epsilon_0 \frac{\partial \boldsymbol{E}}{\partial t} \right) \,. \tag{2.152}$$

2.5.2 Maxwell's Magnetostactic limit

Maxwell's magnetostatic limit corresponds to neglecting the effects of current flow electric and electric field, due to a small order of magnitude, we have then:

$$\boldsymbol{E} = 0 \,, \tag{2.153}$$

$$\boldsymbol{J} = 0\,. \tag{2.154}$$

Under these conditions, Maxwell's equations are simplified in a way significantly and reduces to

$$\nabla \cdot \boldsymbol{B} = 0\,, \tag{2.155}$$

$$\frac{\partial \boldsymbol{B}}{\partial t} = 0\,, \tag{2.156}$$

$$\nabla \times \boldsymbol{H} = 0\,. \tag{2.157}$$

From a practical application , the approximation of the magnetostatic limit is validate for the condition in which the magnetic particles dispersed in the fluid domain are coated with a layer of insulating material that inhibits the conduction of electric current.

Chapter 3

Investigation On The Kinematics And Dynamics of Helical Flagellum

In this chapter, we present first theories for flagella swimmer, beginning with a detailed description of different analytical approaches for the prediction of swimming at low Reynolds numbers. Also, we present mathematical approaches of the motion of helical flagellum at low Reynolds numbers in an unbounded fluid based on the Resistive Force Theory (RFT), Slender Body Theory (SBT) and the Method of Regularized Stokeslets (MRS). Finally, numerical simulations based on Resistive Force Theories RST and Slender Body Theories RST and the Method Regularized Stokesless (MRS) of the unsteady flow around a rigid, finite length rotating helix. Additionally, we present some experiments with a macroscopic prototype micro-organisms in creeping flow motion.

3.1 Theory For Flagella Swimmer At Low Reynolds Number

The physics governing locomotion in fluids at small scales is qualitatively different from other locomotion. For swimming bacteria or flagella, inertia plays a negligible role while viscous forces dominate. In Chapter (2) we see, the motion of a Newtonian fluid is governed by the Navier-Stokes equation:

$$\rho(\frac{\partial \boldsymbol{u}}{\partial t} + \boldsymbol{u} \cdot \nabla \boldsymbol{u}) = -\nabla p + \mu \nabla^2 \boldsymbol{u} \tag{3.1}$$

In equation (3.1), $\boldsymbol{u}(\boldsymbol{x}, t)$ is the velocity of the fluid at $\boldsymbol{x}$ in space and time t, μ is the viscosity of the fluid, ρ is the density of the fluid and p is the pressure. If we put in dimensionless form the Navier-Stokes equations with respect to a characteristic length scale of the microorganism L and a characteristic velocity scale U_0, additionally, we have the dimensionless equation given by the equation (3.2):

$$\left(\frac{Re}{Sh}\right) \frac{\partial \boldsymbol{u}}{\partial t} + Re(\boldsymbol{u} \cdot \nabla \boldsymbol{u}) = \nabla p + \nabla^2 \boldsymbol{u} \tag{3.2}$$

In the mathematical limit of zero Reynolds number, we have the Stokes equations governing the motion. The linearity and time independence of the Stokes equations leads to kinematic

reversibility, which is well-described by Purcell's famous *scallop theorem* states that a reciprocal motion (a deformation that exhibits time-reversal symmetry) cannot generate any net propulsive thrust [13]. In order to break the constraint of time-reversibility, many micro-organisms including flagellated bacteria and spermatozoa achieve self-propulsion by passing deformation waves along their slender flexible body. In the next section we will discuss the slender body theory related to helical flagella.

3.1.1 Slender Body Definitions

To describe the motion of thin filaments immersed in a viscous fluid, a way to approximate is the Slender Body Theory. Is it an important modeling problem in mathematical biology, engineering, and physics. Numerical simulations of slender fibers have been used to help explain the role of *cilia* in embryonic development. For a helical flagellum, the theory was first elaborated by [15], and later it was perfected by [16]. If the length of a swimming helical body L is much larger than its radius r that means ($\frac{r}{L} \ll 1$), in this case, instead of solving the Stokes equations in the fluid domain, we can obtain a local drag law, which is the so-called Resistive Force Theory (RFT) or by slender Body Theory.

We can define also, slender body as a body in which its radius is small with respect to its height or length. The effect of a slender body moving in a fluid at low Reynolds numbers can be approximated by a suitable line distribution of Stokeslets, [95]. The Stokeslet strength density $F(x)$ in a slender body with length L and radius r can be roughly approximate, independently of the body shape, but for a better approximation the body cross-section and the way how it changes along the length needs to be considered [95]. The linearity of the Stokes equations allows us to superpose the fundamental singularities to obtain the solution to a given problem and other singularities besides Stokeslets are needed to satisfy the no-slip boundary condition on the body surface. However, in a different investigation it was probe that for a slender body the total drag and torque can be well approximated by only a distribution of Stokeslets over a line enclosed by the body.

3.1.2 Slender Body Geometry

Before we introduce the Slender Body Theory, we must precisely describe the slender geometry under consideration. The equation of a left-handed helix is given by equation (3.3).

Figure (3.1), we have a schematic of a flagellum with filament radius a, helix radius R, pitch λ, axial length L, and pitch angle θ. We considerer θ very small and ($\theta = \frac{2\pi R}{\lambda}$). A filament segment ds is shown in the inset with tangential, normal, and bio-normal directions denoted as $\mathbf{t}(x)$, $\mathbf{n}(x)$, $\mathbf{b}(x)$ respectively.

$$\mathbf{r}(\varphi) = \frac{\lambda}{2\pi}\varphi\mathbf{i} + b\cos\varphi\mathbf{j} - b\sin\varphi\mathbf{k} \tag{3.3}$$

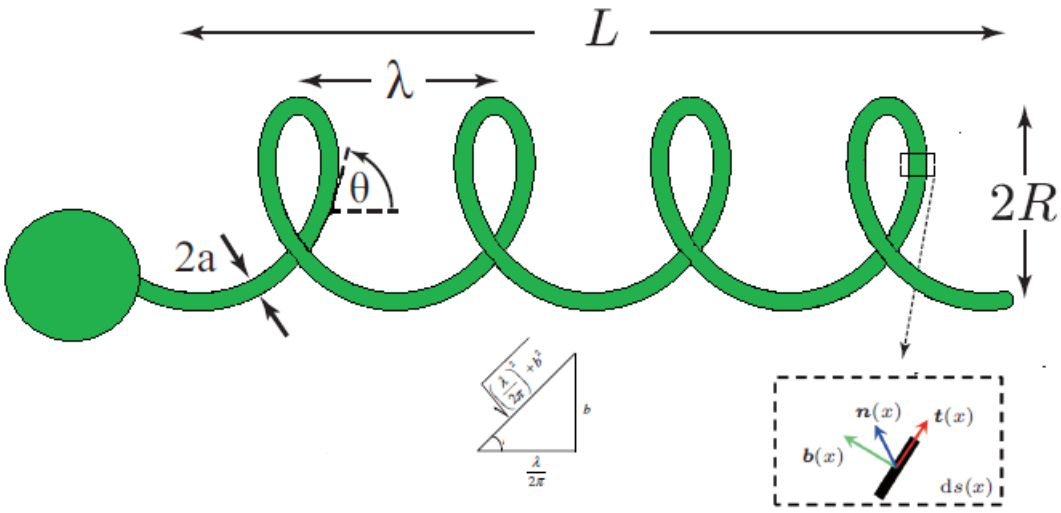

Figure 3.1: The geometry of the flagella

which is useful to calculate the tangent unit vector which is given by equation (3.4)

$$\mathbf{t}(\varphi) = \lambda/\mathbf{2}\pi\sqrt{(\lambda/2\pi)^2 + b^2}\mathbf{i} - \frac{b\sin\varphi}{\sqrt{(\lambda/2\pi)^2 + b^2}}\mathbf{j} - \frac{b\cos\varphi}{\sqrt{(\lambda/2\pi)^2 + b^2}}\mathbf{k} \tag{3.4}$$

that can be rewritten as equation (3.5) by using the triangle of figure (3.1) which is obtained by using the equation to calculate the pitch angle which is given by:

$$\mathbf{t}(\varphi) = \cos\theta\mathbf{i} - \sin\theta\sin\varphi\mathbf{j} - \sin\theta\cos\varphi\mathbf{k} \tag{3.5}$$

Once the tangent unit vector is known, the normal unit vector can be also calculated and is given by equation (3.6)

$$\mathbf{n}(\varphi) = -\cos\varphi\mathbf{j} + \sin\varphi\mathbf{k}, \tag{3.6}$$

the binormal unit vector can be also calculated and is given by equation:

$$\mathbf{b}(\varphi) = \mathbf{t}(\varphi) \times \mathbf{n}(\varphi) = -\sin\theta\mathbf{i} - \cos\theta\sin\varphi\mathbf{j} - \cos\theta\cos\varphi\mathbf{k}, \tag{3.7}$$

we find the arc length of the helix as: by using equation (3.7), the equations of the helix, its tangent, normal and binormal vectors can be rewritten as equations (3.8 to 3.11).

$$s = \int_0^{\varphi} (D\varphi\mathbf{r}\varphi)d\varphi = \sqrt{(\lambda/2\pi)^2 + b^2}\varphi = \frac{\varphi}{k}, \tag{3.8}$$

with:

$$k = \frac{1}{\sqrt{(\lambda/2\pi)^2 + b^2}}. \tag{3.9}$$

Using equation (3.6), the equations of the helix we have

$$\mathbf{r}(s) = s\cos\theta\mathbf{i} + b\cos ks\mathbf{j} - b\sin ks\mathbf{k} \tag{3.10}$$

and then:

$$\mathbf{t}(s) = \cos\theta\mathbf{i} - \sin\theta\sin ks\mathbf{j} - \sin\theta\cos ks\mathbf{k}. \tag{3.11}$$

The normal vector can be rewritten as;

$$\mathbf{n} = -\cos ks\mathbf{j} + \sin ks\mathbf{k} \tag{3.12}$$

Generally, the movement of helical flagellum is represented as a translation along the x-axis with a constant velocity (U) and a rotation around the x-axis with a frequency f is given with rotation velocity $\omega = 2\pi f$. an we can write:

$$\mathbf{r}(s,t) = (s\cos\theta + Ut)\mathbf{i} + b\cos(ks+\omega t)\mathbf{j} - b\sin(ks+\omega t)\mathbf{k} \tag{3.13}$$

As in the low Reynolds numbers flows, what happens in the motion of a body is not affected by the history of motion of it, time can be consider negligible therefore, equation (3.3) represents the motion of a helical flagellum at low Reynolds number and it can be use to find the normal, binormal and tangential unit vectors.

3.1.3 The classic Lighthill Slender Body Theory

Normally bacteria flagella are slender, and their filament radius a is usually much smaller than other geometric parameters. Taking advantage of this slenderness, [16] developed Slender Body Theory, which represents a flagellum with an arrangement of Stokeslets and doublets along the flagellum's centerline. Since dipolar fields fall off as r^{-2} while Stokeslets fall off as r^{-1}, Lighthill [16] reasoned there should be some intermediate distance q from any given point on the flagellum where only the dipoles within q are important in determining the flow at that point, although all of the Stokeslets on the centerline must be considered because they are longer ranged. He showed that the sum of the near and far field solutions for the induced fluid flow on a given segment could be made independent of q by the choice of dipoles of the form:

$$-\frac{a^2\mathbf{f}_\perp(s)}{4\mu}. \tag{3.14}$$

Here, $\mathbf{f}_\perp(s)$ is the component of the Stokeslet strength $\mathbf{f}$ in the plane perpendicular to the flagellum's centerline at a location s along the centerline of the flagellum [16]. This combination of a Stokeslet plus a dipole determines the flow induced by each element of the flagellum. Lighthill showed the local velocity of a segment of the helix located at s is related to the force per unit length (i.e., Stokeslet strength) along the filament $\mathbf{f}_\perp(s)$ by:

$$\boldsymbol{u(s)} = \frac{\mathbf{f}_\perp(\mathbf{s})}{4\mu} + \int_{|\mathbf{r_0}(\mathbf{s}',\mathbf{s})|>\delta} \mathbf{f}(\mathbf{s}')\cdot\boldsymbol{J}(\mathbf{r_0})d\mathbf{s}'. \tag{3.15}$$

Where $\delta = a\frac{\sqrt{e}}{2}$, is the natural cutoff, $\mathbf{r_0}$ is the position vector from the point s on the centerline relative to the point s', and $\boldsymbol{J}$ is the Oseen tensor given by

$$\boldsymbol{J}(\mathbf{r}) = \frac{1}{8\pi\mu}\left(\frac{\boldsymbol{I}}{|\mathbf{r}|} + \frac{\mathbf{r}\mathbf{r}^{\mathbf{T}}}{|\mathbf{r}|^3}\right) \tag{3.16}$$

To evaluate equation (3.15), we can use the rectangular rule of numerical integration to calculate the thrust, torque, and drag for flagella. To parametrize the spatial locations we use the helical

phase: $(\varphi = ks\cos\theta)$, where $(k = \dfrac{2\pi}{\lambda})$ and then:

$$\mathbf{r}(\varphi) = R(\varphi\cot\theta, \cos\theta, \sin\varphi) \tag{3.17}$$

Now, the equation (3.15) can be written as:

$$\mathbf{u_n} = \frac{(\boldsymbol{I} - \hat{t}_n\hat{t}_n + D_n)\cdot\mathbf{f_n}}{4\pi\mu} + \frac{R\Delta\varphi\csc\theta}{8\pi\mu}\sum_{m\neq n}\frac{\boldsymbol{I} + \hat{r}_{nm}\hat{r}_{nm}}{r_{nm}}\cdot\mathbf{f_m} + \mathbb{O}(\Delta\varphi) \tag{3.18}$$

In equation (3.18), n, m are indices ranging from 1 to N, and $\mathbf{r}_{nm} = \mathbf{r}(\varphi_n) - \mathbf{r}(\varphi_m)$ is the position vector between spatial locations. The term $\mathbf{t}_n = (\cos\theta, -\sin\theta\sin\varphi_n, \sin\theta\cos\varphi_n)$ is the tangential unit vector at $\mathbf{r}_n$, and $\Delta\varphi_n$ is the mesh size of the helical phase.

We can see the integral in equation (3.18) is divided into two terms. The first part of the integral is represented by the tensor D_n, which is the integral from the lower bound (natural cutoff) to the size of the grid spacing. D_n is solved explicitly because this portion of the integral is below the grid resolution and would otherwise be unresolved. The remainder of the integral appears as the second term in equation equation (3.18), [29].

The next step is to use a rotated frame with the helical phase to determine expressions for the velocity components that are invariant along the helix. Taking these invariant velocity components to create a linear mapping between the velocity and force per unit length, which can be evaluated for a specified helical geometry, helical axial velocity U, and rotation rate Ω to give the thrust, torque, and drag.

The tensor D_n is symmetric and is the contribution of the helical segment centered at $\mathbf{r}$, located at a distance between the cutoff length δ and the grid size away from $\mathbf{r}_n$ that mean $|\mathbf{r}-\mathbf{r}_n| \in (\delta, \delta')$ where

$$\delta' = \frac{1}{2}R\Delta\varphi\csc\theta \tag{3.19}$$

and D_n is the expansion of the following integral to the lowest order of the grid size $\Delta\varphi$

$$D_n = \frac{1}{2}\int_{|\mathbf{r}-\mathbf{r}_n|\in(\delta,\delta'} ds(\varphi)\left(\frac{\boldsymbol{I}}{|\mathbf{r}-\mathbf{r}_n|} + \frac{(\mathbf{r}-\mathbf{r}_n)(\mathbf{r}-\mathbf{r}_n)}{|\mathbf{r}-\mathbf{r}_n|^3}\right)\boldsymbol{R}_z(\varphi-\varphi_n) \tag{3.20}$$

where $\boldsymbol{R}_z]$, the rotation operator along the axial direction, can be expressed as

$$\boldsymbol{R}_z(\varphi) = \begin{pmatrix} \cos\varphi & -\sin\varphi & 0 \\ \sin\varphi & \cos\varphi & 0 \\ 0 & 0 & 1 \end{pmatrix} \tag{3.21}$$

A new velocity density vector is introduced

$$\mathbf{u}_\mathbf{n}^{'} = \boldsymbol{R}_z(-\varphi_n)\cdot\mathbf{u} \tag{3.22}$$

and a new force density vector is introduced

$$\mathbf{f}_\mathbf{n}^{'} = \boldsymbol{R}_z(-\varphi_n)\cdot\mathbf{f_n} \tag{3.23}$$

we have, $\mathbf{u_n^{'}}$ is invariant along the helical filament. For a rigid helix that rotates at rate Ω and translates at speed U along its axial direction, then

$$\mathbf{u_n^{'}} = (0, \Omega R, U)^T \tag{3.24}$$

for the force along its axial direction is

$$\sum_n \mathbf{f_n'} R\Delta\varphi \csc\theta = (0, \frac{T}{R}, F_x)^T \tag{3.25}$$

with these modifications made above we can rewrite the Lighthill's slender body theory as:

$$\mathbf{u_n'} = \frac{(\boldsymbol{I} - \hat{t}'\hat{t}' + D_n') \cdot \mathbf{f_n'}}{4\pi\mu} + \frac{R\Delta\varphi \csc\theta}{8\pi\mu} \sum_{m\neq n} \frac{\boldsymbol{R}_z(\varphi_m - \varphi_n) + \boldsymbol{R}_z(-\varphi_n) \cdot \hat{r}_{nm}\hat{r}_{nm} \cdot \boldsymbol{R}_z(-\varphi_n)}{r_{nm}} \cdot \mathbf{f_m'} + \mathbb{O}(\Delta\varphi) \tag{3.26}$$

with $\hat{t}'$ invariant along the helical filament,

$$\hat{t}' = (0, \sin\theta, \cos\theta) \tag{3.27}$$

and D_n' invariant along the helical filament,

$$D_n' = \int_{k\delta\cos\theta}^{k\delta'\cos\theta} d\varphi \frac{1}{\varphi}[\boldsymbol{I} + \boldsymbol{T}] = \ln(\frac{\delta'}{\delta})(\boldsymbol{I} + \hat{t}'\hat{t}') \tag{3.28}$$

where

$$\boldsymbol{T} = \begin{pmatrix} 0 & 0 & 0 \\ 0 & \sin^2\theta & \sin\theta\cos\theta \\ 0 & \sin\theta\cos\theta & \cos^2\theta \end{pmatrix}$$

From this we can establish the linear relationship between the velocity $\mathbf{u}'$ map and the force $\mathbf{f}'$ we have then:

$$(\mathbf{u_1'}, \mathbf{u_2'}, \mathbf{u_3'}, ...\mathbf{u'^n}) = \boldsymbol{G}(\mathbf{f_1'}, \mathbf{f_2'}, \mathbf{f_3'}, ...\mathbf{f'^n}) \tag{3.29}$$

Inverting the last relation and for a prescribed motion of a rigid helix $\mathbf{u'}_n = \mathbf{u'}_0 = (0, \Omega R, U)^T$, we obtain the net axial hydrodynamic force F_x and the net torque T.

$$(0, \frac{T}{R}, F_x)^T = \sum_{i=1}^{N} \mathbf{f_n'} R\Delta\varphi \csc\theta \tag{3.30}$$

3.1.4 Resistive Force Theory

The application of the Slender Body Theory is important to the prediction and understanding of swimming propulsion, but it is very common to use an approximation of the slender body known as resistive force theory.

In Slender Body Theory to determine the force on each segment of the flagellum we have to evaluate integrals of the form. This methodology is usually tedious, reference[15] and reference

[16] present a solution for the distribution of Stokeslets and doublets for a flagellum. They sought to further simplify the problem by considering each segment of the flagellum represented by the Stokeslets and dipole as an independent slender rod. The resistance of the fluid to the slender rod's motion is calculable if the local coefficient of drag for the segment and its velocity are known. Typically, the coefficient of drag is expressed in terms of normal and tangential drag coefficients per unit length, C_n, and C_t, respectively.

The next step is to find the force and torque resulting for the movement of the flagellum. This can be done by performing an integration of all the forces and torques of each small segment, as can be seen in figure shows such a small segment (see inset) and defines geometric parameters that describe a flagellum: filament radius a, helical radius R, helical pitch λ , and axial length L, which is use for such calculations, [29].

The orientation of the flagellum is along $\mathbf{x}$ direction considering a pitch angle θ. Then we can parametrize the flagellum using the x-coordinate so that the center line is given by:

$$\mathbf{r}(x) = [x, R\cos(kx), R\sin(kx)], \tag{3.31}$$

where $k = \dfrac{2\pi}{\lambda}$.

To calculate the local forces at this point $\mathbf{r}(x)$ on the flagellum in terms of parallel and perpendicular drag coefficients we need to define both a tangential direction:

$$\mathbf{t}(x) = \frac{1}{\sqrt{1+R^2k^2}}[1, Rk\sin(kx), Rk\cos(kx)] \tag{3.32}$$

and the normal direction:

$$\mathbf{n}(x) = [0, -\cos(kx), -\sin(kx)] \tag{3.33}$$

We consider now the force acting by an element ds on the fluid is given by $d\mathbf{f} = \mathbf{K}\cdot\mathbf{u}dx$, where $\mathbf{u}$ is the local velocity and $\mathbf{K}$ is the resistance tensor per unit length of a filament element, depends only on the geometry of the filament element and can be written as:

$$\mathbf{K} = C_n\boldsymbol{I} + (C_t - C_n)\mathbf{tt} \tag{3.34}$$

The total force exerted on the fluid by the flagellum is then:

$$\mathbf{F} = \int \mathbf{K}\cdot\mathbf{u}ds \tag{3.35}$$

The total torque exerted on the fluid by the flagellum is then:

$$\mathbf{T} = \int \mathbf{r}\times\mathbf{K}\cdot\mathbf{u}ds \tag{3.36}$$

here, $\mathbf{u}(\mathbf{x})$ is the filament velocity, and ds is the segment length how we describe early

The motion of the helix, is completely described by equations (3.35) and (3.36) but, in a different way than the resistance matrix description provided. A very interesting exercise is to be

able to use resistive force theory to calculate elements of the flagellum's resistance matrix under the following simplifying assumptions.

We need to solve the reduced problem of the flagellum rotating and translating in the axial direction (i.e. bacterial swimming). Because of the reduced dimensionality. We have to find the force and torque in the x direction, $\mathbf{F_t}$ and $\mathbf{T_x}$, resulting from a velocity and rotation in the x direction, U_x and x.
The symmetric 2×2 propulsive matrix in equation (3.37) depends only on the geometry of the flagellum. This matrix simplifies array made of the $\mathbf{A_{111}}$, $\mathbf{B_{111}}$, and $\mathbf{C_{111}}$, components of the sub-block matrices We can simplify the problem as :

$$\begin{pmatrix} \mathbf{F} \\ \mathbf{T} \end{pmatrix} = \begin{pmatrix} \mathbf{A} & \mathbf{B} \\ \mathbf{C} & \mathbf{D} \end{pmatrix} \begin{pmatrix} \mathbf{U} \\ \omega \end{pmatrix} \tag{3.37}$$

We can imagine two categories of movement, the first refers to the flagellum being rotated in the axial direction with an angular velocity but with the flagellum doesn't have linear velocity $U = 0$. We can find two resistance matrix elements and we have:

$$F_x = B\Omega \tag{3.38}$$

$$T_x = C\Omega \tag{3.39}$$

The second, we consider a flagellum without rotation velocity $\Omega = 0$ and being towed at some constant velocity U. The drag on this flagellum is given by:

$$D_x = AU \tag{3.40}$$

The subscript indicates the direction of the force in the flagellum.

Next step is calculate the propulsive force and the torque in the $\mathbf{x}$ direction for these two types of motion using resistive force theory. The results will be in terms of the drag coefficients C_n and Ct. Then we will make the determination based on the work refrence [15, 16] reported by [29].

When a flagellum rotates at an angular frequency the local velocity of an element is $\mathbf{u}(\mathbf{x}) = R\Omega[0, \sin(kx+t), \cos(kx+t)]$. The inner product of the local velocity with the segment's tangential and normal unit vectors gives the parallel and perpendicular velocities. Using local parallel and perpendicular drag coefficients for the segment, the force $\boldsymbol{df}$ generated by an element has cartesian components:

$$df_x = \mathbf{x} \cdot \boldsymbol{K} \cdot \mathbf{u} ds = -\Omega R(C_n - C_t) \sin\theta \cos\theta ds. \tag{3.41}$$

In y direction:

$$df_y = \mathbf{y} \cdot \boldsymbol{K} \cdot \mathbf{u} ds = -\Omega R(C_n \cos^2\theta + C_t \sin^2\theta) \sin(kx + \Omega t) ds. \tag{3.42}$$

And z direction:

$$df_z = \mathbf{z} \cdot \boldsymbol{K} \cdot \mathbf{u} ds = -\Omega R(C_n \cos^2\theta + C_t \sin^2\theta) \cos(kx + \Omega t) ds. \tag{3.43}$$

Now we can write the torque in the **x** direction exerted by each segment on the

$dT_x = \mathbf{r} \times d\mathbf{fx}$

$$dT_x = -R\sin(kx + \Omega t)df_y + R\cos(kx + \Omega t)df_z = -R(R\Omega)(C_n \cos^2\theta + C_t \sin^2\theta)ds \tag{3.44}$$

Integrating in the contour we obtain:

$$F_x = -\Omega R(C_n - C_t)\sin\theta\cos\theta\frac{L}{\cos\theta} \tag{3.45}$$

and the torque:

$$T_x = -R^2\Omega)(C_n \cos^2\theta + C_t \sin^2\theta)\frac{L}{\cos\theta} \tag{3.46}$$

with the elements of the propulsive matrix: $B = \frac{F_x}{\Omega}$ and $C = \frac{T_x}{\Omega}$.

We can use a similar strategy for a translating, non rotating flagellum. We can find the axial drag on this flagellum using:

$$df_x = \mathbf{x} \cdot \mathbb{K} \cdot \mathbf{u}ds = -u(C_n \sin^2\theta + C_t \cos^2\theta)ds \tag{3.47}$$

Then, the total drag is:

$$D_x = -u(C_n \sin^2\theta + C_t \cos^2\theta)\frac{L}{\cos\theta} \tag{3.48}$$

finallty giving $A = D_x/U$.

Resistive force theory gives predictions about the propulsive force, torque and drag on a rotating flagellum at low Reynolds number, and thereby predicts the form of the flagellum's reduced resistance matrix in terms of the flagellum geometry and the local drag coefficients C_n and C_t.

In order to determine the propulsive forces associated with swimming propulsion, [15] have related the propulsive forces with velocities using resistive force coefficients in the tangential (C_t) and normal direction (C_n), by:

$$C_n = \frac{2\pi}{\ln(\frac{2\lambda}{a}) - \frac{1}{2}} \tag{3.49}$$

Gray [15], reasoned that there was only a logarithmic dependence on the length scale in their expression so the choice was not terribly important, and chose the axial wavelength of the flagellum. Gray [15], also assumed that $C_n = 2C_t$ based in part on results obtained by [96] for an infinitely long filament undergoing sinusoidal motion in a plane [96], and probably based on experimental measurements of the wave speed of a sperm's flagellum relative to it's propagation velocity, which implies a ratio close to 2:1. Thus, the normal drag coefficient per unit length is:

$$C_t = \frac{4\pi}{\ln(\frac{2\lambda}{a}) + \frac{1}{2}} \tag{3.50}$$

The change of sign in the denominator of equation (3.50) was not part of [15] original work, but was later adopted based on work by [16]. As part of a proof of his fundamental theorem of

flagellar hydrodynamics, he derived the same expression for the tangential force which implies C_t is given by equation (3.50). Rather than assuming a ratio for the two drag coefficients, [16] derived the normal force per unit length, which implies the form for C_n in equation (3.49) that has subsequently been associated with [15].

Basing on the work of Gray, [16] showed that the results could be improved and that the accuracy of the drag coefficients expressions could be improved by using his slender body theory formulation for the flow field near the flagellum, which was more accurate along with making a choice more proper of the length scale over which higher order terms are important. He used a small fraction of the contour length of one wavelength for the length scale $q = 0,09(\frac{\lambda}{\cos\theta})$ we have:

$$C_t = \frac{2\pi}{\ln(\frac{0,18\lambda}{a\cos\theta})} \tag{3.51}$$

In this last relation [16] did not assume the ratio of the drag coefficients had some specific value, and derived C_n by taking the ratio of the normal force exerted by the segment acting over length q divided by the normal velocity on the segment, which gives:

$$C_n = \frac{4\pi}{\ln(\frac{0,18\lambda}{a\cos\theta}) + \frac{1}{2}} \tag{3.52}$$

Note that the zero-thrust condition implies that the torque generated by the flagellum it is cancelled out by the drag that is produced only by it, without considering the effect of the drag produced by the head as seen in [97]. For helical propulsion at zero-thrust condition, the axial velocity decays exponentially with the distance from the helical axis [97]. Others authors also analysed, the zero-thrust condition by helices of finite length. Johnson [98] applied direct numerical calculations to solve the RST and considering that the helices can translate along its centre of symmetry and rotate with and specify angular velocity.

A compilation of expressions for C_n and C_t,the most commonly used expressions for resistive force theory drag coefficients in the literature is presented in table (3.1).

Table 3.1: Typical coefficients for calculations of the drag force.

Cn	Ct	Author
$\frac{4\pi}{\ln(2\lambda/a)+1/2}$	$\frac{2\pi}{\ln(2\lambda/a)-1/2}$	[15]
$\frac{4\pi}{\ln(0.18\lambda/a\cos\theta)+1/2}$	$\frac{4\pi}{\ln(0.18\lambda/a\cos\theta)}$	[16]
$\frac{4.05\pi}{\ln(0.271\lambda/(a\cos\theta)^{-6.23a/b+3.1})}$	$\frac{2.21\pi}{\ln(0.105\lambda/(a\cos\theta)^{1.77})}$	[26]
$\frac{4\pi}{\ln(2\lambda/a)+0.193}$	$\frac{2\pi}{\ln(2\lambda/a)-0.807}$	[99]

3.1.5 Method of Regularized Stokeslets

The method of regularized Stokeslets (MRS) is a method that represents the fluid velocity in Stokes flow by a collection of regularized forces. Cutoff functions are introduced to regularize the singular fundamental solutions known as Stokeslets. This regularization removes the singular nature from the velocity field, hence the velocity can be evaluated anywhere in the fluid, including at the location of a regularized Stokeslet. There exists a linear relationship between regularized Stokeslet forces and the velocity anywhere in the fluid. Hence, regularized Stokeslets strengths can be computed to impose velocity constraints at a collection of points in the flow. In the particular application of interest here, the velocity constraints correspond to the motion of an immersed boundary in the flow, [100].

The method of regularized Stokeslets (MRS) was developed [31] and [101] by applying boundary integral methods. In this method, the Stokes flow equations are solved with concentrated forces of magnitud $\phi_\epsilon(\mathbf{r})$ and is given by equation (3.53), where $\mathbf{r} = |\mathbf{x} - \mathbf{x_0}|$ and ϵ is known as the regularization parameter which controls the efect of the force around its source point. This function eliminates the singularities presented by using non-regularized Stokeslets according to [101].

$$\phi_\epsilon(\mathbf{r}) = \frac{15\epsilon^4}{8\pi(r^2+\epsilon^2)^{7/2}} \tag{3.53}$$

The flow generated by a regularized force $\mathbf{f}\phi_\epsilon(\mathbf{r})$ can be calculated by the Stokes flow equations as:

$$\begin{cases} \nabla \cdot \mathbf{u} = 0 \\ \mu\nabla^2\mathbf{u} - \nabla p = \mathbf{f}\phi_\epsilon(\mathbf{r}) \end{cases} \tag{3.54}$$

The solution to the previous equations can be formulated by introducing the regularized Green's function $S_{ij}^\epsilon = (\mathbf{x}, \mathbf{x_o})$ for the velocity [31], which can be written as:

$$u_i(\mathbf{x}) = \frac{1}{8\pi\mu} S_{ij}^\epsilon(\mathbf{x}, \mathbf{x_0}) f_j \tag{3.55}$$

Similarly, and expression for the pressure associated with the flow can be calculated as:

$$p(\mathbf{x}) = \frac{1}{8\pi} P_j^\epsilon(\mathbf{x}, \mathbf{x_0}) f_j \tag{3.56}$$

And the stress tensor associated with the flow can be obtain using:

$$\sigma_{ik}(\mathbf{x}) = \frac{1}{8\pi} T_{ijk}^\epsilon(\mathbf{x}, \mathbf{x_0}) f_j \tag{3.57}$$

In equations (3.1.5) to (3.57) the expressions $T_{ijk}^\epsilon(\mathbf{x}, \mathbf{x_0})$,$S_{ij}^\epsilon(\mathbf{x}, \mathbf{x_0})$ and $P_j^\epsilon(\mathbf{x}, \mathbf{x_0})$ are regularized versions of the fundamental solutions of the Stokes flow equations given by:

$$S_{ij}^\epsilon(\mathbf{x}, \mathbf{x_0}) = \delta_{ij}\frac{r^2+2\epsilon^3}{(r^2+\epsilon^2)^{3/2}} + \frac{(x_i - x_{0,i})(x_k - x_{0,k})}{(r^2+\epsilon^2)^{3/2}} \tag{3.58}$$

And also we have:

$$T^{\epsilon}_{ijk}(\mathbf{x},\mathbf{x_0}) = -6\frac{(x_i - x_{0,i})(x_j - x_{0,j})(x_j - x_{0,j})}{(r^2+\epsilon^2)^{5/2}} - 3\epsilon^2[\frac{(x_i - x_{0,i})\delta_{jk}(x_j - x_{0,j})\delta_{ik}(x_j - x_{0,j})\delta_{ij}}{(r^2+\epsilon^2)^{5/2}}] \tag{3.59}$$

And finally:

$$P^{\epsilon}_{j}(\mathbf{x},\mathbf{x_0}) = (x_j - x_{0,j})\frac{2r^2+5\epsilon^2}{(r^2+\epsilon^2)^{5/2}} \tag{3.60}$$

where δ_{ij} is the Kronecker delta. When a flagellum moving in a viscous fluid is analysed by the method regularized Stokeslets, the surface is discretized into a number of regularized Stokeslets (N) that are located on the surface's body.

Then, equation (3.1.5) transforms into equation (3.61)

$$u_j(\mathbf{x_0}) = \frac{1}{8\pi\mu}\sum_{n=1}^{N}\sum_{i=1}^{3} S^{\epsilon}_{ij}(\mathbf{x},\mathbf{x_0}) f_{n,i} A_n \tag{3.61}$$

In this last equation we have, $f_{n,i}$ is the $-ith$ component of the force on the fluid applied at location x_n. Also we have, A_n is the quadrature weights which depend on the numerical integration method applied. The quadrature errors are small in comparison with regularization errors and the error presented in the method itself see reference [100]. Because of that, some author use the midpoint rule as quadrature rule. The errors in the method are mainly due the discretization of the surface and the cut-off parameter ϵ as in the case when $\epsilon \to 0$ the velocity cannot be calculated be this method because the singular version of the Stokes equations is obtained [101].

When we use the MRS an important aspect is the number of stokeslets or collocation points that are used to discretize a surface. If the number of elements aplied to represent a body is small then the approximation of its area is inadequated which produces an error due to discretization. Some authors choose a body that is moving in a fluid with 6 degrees of freedom, and that its velocity is known and it is given by the vector:

$$\mathbf{u} = [u_{x1}, u_{y1}, u_{z1} ... u_{xN}, u_{yN}, u_{zN}]^T \tag{3.62}$$

In equation (3.62), $[T]$ denotes the transport of the velocity vector and N the number or collocation points in the surface of the body. In the previous equation the velocity vector is given by:

$$\mathbf{u} = \mathbf{V} + (\mathbf{W} \times \mathbf{x}) \tag{3.63}$$

here $\mathbf{V}$ is the linear velocity and $\mathbf{W}$ the angular velocity, which allows the six degrees of freedom. If the number of collocation points is the same as the number or regularized Stokeslets, then the velocity and force vectors of length $3N$ are related by a matrix A with dimension $3N \times 3N$, and equation (3.64) can be written in matrix form:

$$\mathbf{u} = \frac{1}{8\pi\mu} A\mathbf{f} \tag{3.64}$$

If we know the velocity, we can obtain the distribution of forces by inverting the matrix A.

Once the distribution of forces is known, it is possible to calculate the total hydrodynamic force by integrating the distribution of forces over the surface:

$$\mathbf{F} = \int_{\delta s} \mathbf{f}(\mathbf{x}) ds(\mathbf{x}, \tag{3.65}$$

or by adding up the force at every location in the correspond direction:

$$f_i = \sum_{1}^{N} (f_{uij} + f_{wij}), \tag{3.66}$$

where $i, j = 1, 2, 3$ represents the direction of the force in Cartesian coordinates.

The total hydrodynamic torque that is produced by the moving body can be calculated in terms of the distribution of forces and its location by:

$$\mathbf{T} = \sum_{1}^{N} \mathbf{x_i} \times \mathbf{f}(x_i), \tag{3.67}$$

knowing the forces distribution , we can determine the velocity field that is produced by the moving body in the viscous fluid by applying equation (3.1.5) in any location of the fluid domain.

3.1.6 Johnson Slender Body Theory

The Johnson Slender Body Theory derivation is more rigorous than Lighthill Slender Body Theory [16]. Is build on idea of [6]. Its formulation takes details that were ignored by Lighthill [16]. The first difference between the two formulations is that Johnson's slender body is a long slender prolate spheroid that terminates smoothly. The velocity of a point on the filament is broken into local and non-local terms on a helical flagellum.

$$\mathbf{u}(\mathbf{r}) = \mathbf{u_{local}}(\mathbf{r}) + \mathbf{u_{nonlocal}}(\mathbf{r}) \tag{3.68}$$

where the local velocity is defined by:

$$\mathbf{u_{local}}(\mathbf{r}) = \frac{1}{8\pi\mu}[-\ln(k^2 e)(\boldsymbol{I} + \mathbf{t}(\mathbf{r})\mathbf{t}(\mathbf{r}) + 2(\boldsymbol{I} - \mathbf{t}(\mathbf{r})\mathbf{t}(\mathbf{r}))] \cdot \mathbf{f}(0), \tag{3.69}$$

in this case $k = \dfrac{a}{\Lambda}$, with Λ is the contour length defined by $\Lambda = \dfrac{L}{\cos\theta}$.

The radius of the cross section vanishes at either end of the slender body and is given by: $a(s) = a\sqrt{1 - 4\dfrac{s^2}{\Lambda}^2}$, where $s \in [-\dfrac{\Lambda}{2}, \dfrac{\Lambda}{2}]$. The filament radius has an average value, $\dfrac{a\pi}{4}$, therefore in Johnson slender body theory calculations he set the filament radius to be $\dfrac{4}{\pi}$ times the radius used in the experiments and other simulations [29].

The non-local velocity is defined by:

$$\mathbf{u_{nonlocal}}(\mathbf{r}) = \int \boldsymbol{J}(\mathbf{r}' - \mathbf{r}) \cdot \mathbf{f}(\mathbf{r}') d\mathbf{r}' - \frac{1}{8\pi\mu} \int \frac{\boldsymbol{I} + \mathbf{t}(\mathbf{r}')\mathbf{t}(\mathbf{r}')}{|s - s'|} \cdot \mathbf{f}(\mathbf{r}') d\mathbf{r}' \tag{3.70}$$

.

As it was used in [16] slender body theory the same rotational mapping and the rectangular rule of integration are used to obtain:

$$\begin{aligned}\mathbf{u}'_{\mathbf{n}} = \frac{1}{8\pi\mu}[-\ln(k^2 e)(\boldsymbol{I} + \hat{\mathbf{t}}\hat{\mathbf{t}}' + 2(\boldsymbol{I} - \hat{\mathbf{t}}\hat{\mathbf{t}}') \cdot \mathbf{f}'_{\mathbf{n}} \\ + \frac{R\Delta\varphi \csc\theta}{8\pi\mu} \sum_{m\neq n} \frac{\boldsymbol{R}_x(\varphi_m - \varphi_n) + \boldsymbol{R}_x(-\varphi_n) \cdot \hat{r}_{nm}\hat{r}_{nm}\boldsymbol{R}_x(\varphi_n)\cdot}{r_{nm}} \cdot \mathbf{f}'_{\mathbf{m}} \\ -\frac{1}{8\pi\mu} \sum_{m\neq n} \frac{1}{r_{nm}} (\boldsymbol{I} + \hat{\mathbf{t}}'\hat{\mathbf{t}}') \cdot \mathbf{f}'_{\mathbf{n}} + \mathbb{O}(\boldsymbol{\Delta}\varphi)\end{aligned} \tag{3.71}$$

Setting $K = \frac{1}{2}[\sum_{m\neq n} \frac{1}{r_{nm}} + \ln(k^2 e)]$ after adding the terms we finally obtain:

$$\begin{aligned}\mathbf{u}'_{\mathbf{n}} = \frac{1}{4\pi\mu}[-K(\boldsymbol{I} + \hat{\mathbf{t}}'\hat{\mathbf{t}}' + (\boldsymbol{I} - \hat{\mathbf{t}}'\hat{\mathbf{t}}'] \cdot \mathbf{f}'_{\mathbf{n}} \\ + \frac{R\Delta\varphi \csc\theta}{8\pi\mu} \sum_{m\neq n} \frac{\boldsymbol{R}_x(\varphi_m - \varphi_n) + \boldsymbol{R}_x(-\varphi_n) \cdot \hat{r}_{nm}\hat{r}_{nm}\boldsymbol{R}_x(\varphi_n)\cdot}{r_{nm}} \cdot \mathbf{f}'_{\mathbf{m}} \\ + \mathbb{O}(\boldsymbol{\Delta}\varphi)\end{aligned} \tag{3.72}$$

3.1.7 Asymptotic Theory for a Helical Flagellum

Let's use the equation of a flagellum parametrized by contour position s with a length L much greater than R and λ. According to the section on slender body theory, the local velocity of a segment of the helix located at $s = 0$ is correlated with the force distribution along the entire filament $f(s)$:

$$\mathbf{u}(0) = \frac{\mathbf{f}(0) \cdot \hat{n}\hat{n}}{4\pi\mu} + \int_{|r(s',0)|} \boldsymbol{J}(s', 0) \cdot \mathbf{f}(s')ds'. \tag{3.73}$$

If we consider a long propeller we can affirm end effects are minimal so each segment is essentially the same. Therefore, the force per unit length can be written by:

$$\mathbf{f}(s) = (f_x, -f_\Omega \sin\varphi, f_\Omega \cos\varphi), \tag{3.74}$$

in this equation we have f_x is the force per unit length in the x direction and f_Ω is the tangential force per unit length perpendicular to the x direction, which has components in the y and z directions, depending on the helical phase ($\varphi = ks\cos\theta$ of the segment and $k = \frac{2\pi}{\lambda}$). The associated velocity of the helical filament is:

$$\mathbf{u}(s) = (U - \Omega R\sin\varphi, \Omega R\cos\varphi) \tag{3.75}$$

Returning in the [16] equation we can rewrite the velocity for the x direction as:

$$U = \frac{(f_x \sin\theta - f_\Omega \cos\theta)\sin\theta}{4\pi\mu} + \int_{k\delta\cos\theta}^{kL/2} \csc\theta d\varphi \left(\frac{f_x}{4\pi\mu\xi} + \frac{f_\Omega\varphi\sin\varphi\cot\theta + f_x\varphi^2\cot\theta^2}{4\pi\mu\xi^3}\right). \tag{3.76}$$

The velocity for the tangential direction is given by:

$$\Omega R = \frac{(-f_x \sin\theta + f_\Omega \cos\theta)\sin\theta}{4\pi\mu} + \int_{k\delta\cos\theta}^{kL/2} \csc\theta d\varphi \left(\frac{f_\Omega\cos\varphi}{4\pi\mu\xi} + \frac{f_\Omega\sin^2\theta + f_x\varphi\sin\varphi\cot\theta}{4\pi\mu\xi^3}\right). \tag{3.77}$$

3.2 EXPERIMENTAL ANALYSIS AND COMPUTATIONAL VALIDATION OF FLAGELLUM MOTION IN CREEPING FLOW

In order to investigate the validity of the developed model, an experimental setup was built to measure the force and torque as well as the propulsive velocity and the trajectory produced by a single flagellum at Reynolds numbers close to those of microorganisms locomotion. The experimental apparatus used in this study is shown in figure (3.2).

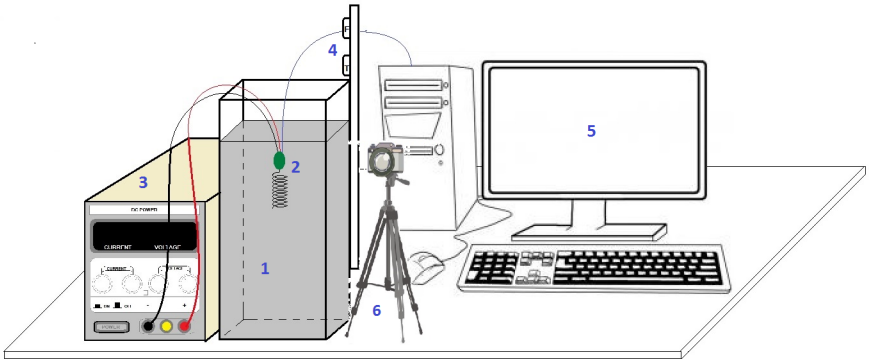

Figure 3.2: Sketch of the experimental apparatus to investigate the model of the flagellum motion in creeping flow. The experimental setup is basically formed by a tank filled with a viscous fluid, component (1), the artificial flagellum component (2), a DC power supply component (3), electronic system for force and torque measurements (4), a computer system (5), the tracking image system - video-camera (6).

The tank set-up consists of a rectangular glass 500 mm × 500 mm with a thickness of 3 mm and 650 mm height filled with the viscous fluid. In order to reduce the wall effect on the swimmer, we use dimensions of the tank at least 10 times larger than the flagellum length. The swimmer was carefully placed inside the tank. The swimmer generates propulsion in which force and torque are measured and also its trajectory analyzed. The artificial swimmer developed in the present work consisted of two components, a spherical head and a helical tail which is joined to each other via a coupling. The body of the helical swimmer is made from a plastic tube having 16 mm in diameter, 28 mm in length, and a hemispherical cap. The body contains a micro DC motor inside that was ideal for compact Arduino robot projects. The main specifications of the DC motor are: an operating voltage between 3-6V, a shaft diameter: 2mm, a shaft length: 9mm total dimensions: $(25x20x15)$ mm, and weight: of 14g. Under this condition, it was possible to assemble projects that require high rotation like our artificial flagellum. Swimmers' tails are made by wrapping a 1.8mm diameter aluminum wire around a mandrel bar. The wire is stiff enough to ensure it stay in shape. The three helices used in the present experiments have wavelengths 2, 4.32 and 7.25 mm, respectively. In the present study, the stretched lengths of the helical tails are chosen to be the same apparent length and this value was 50 mm. The diameter of the propellers used was 9, 4.5 and 8 mm, respectively. For this models, the body size is dictated primarily by the weight of the metal tail and the requirement to reach a state of neutral buoyancy for the swimmer. However,

the proportions between the diameter and the length of the helical tail must be carefully chosen. The helical head and tail were joined to each other by means of a coupling. The assembly was done as follows. The small motor shaft projects through a hole drilled in the plastic shell (head) and the end of the shaft is connected to the helical tail using a coupling. The connection between the motor and tail is made with a plastic sleeve coupling material, which is constructed by drilling from opposite sides with respect to the diameters of the motor shaft and the helical tail. The plastic sleeve coupling is secured to the tail by applying glue for plastic to ensure a stable rotation of the tail. A plastic film fixed around the motor shaft is used to prevent oil from seeping into the motor housing compartment. The flagellum is powered by a DC source of 15V, 2A (Adjustable Digital Power Supply - PS1502DD). The power supply determines the rotational frequency of the flagellum. The motion of the helical tail in the viscous fluid, the drag force and torque break the time-reversibility for the artificial flagellum and leads to a propulsion. The use of the PS-1502DD Power Supply was ideal to obtain several variations of the frequency of the movement of the flagellum helices. The technical specifications are the output voltage: DC between 0 to 15V; preset voltage output: 1.5V, 3.6V, 4.8V, 6.0V, and 7.2V; the adjustment of protection current: 0 to 2A, basic accuracy: 0.07%, the dimension 17.5 x 12.5 x 14.5 cm; and weight: 1.5 Kg. The force measurement system is an Arduino weighing scale formed by a standard Arduino Uno, an HX711 on breakout board used microchip made for amplifying the signals from load cells and reporting them to the microcontroller and finally, a 1 kg load cell. The torque measurement system used is a rotary torque sensor fitted with slip ring electronics to transmit the torque signal while rotating. The main function of the torque sensor is to perform the reading of encoder disks, as it counts an emitter and an infrared receiver at its ends, which serves to define the torque of the motor of the flagellum.

The tracking system used in the experiments was a mechanical parameter meter of the particle kinematics based on a computer vision algorithms applied to process the images of a moving objects digitally to obtain the position and speed in time. The image acquisition of the helical swimmer was a fundamental step of our experimental investigations and it was performed using a high-speed camera of the PCO@R brand, capable of capturing 640 images/s in its highest resolution (1024X1024). When obtaining the images, some care was taken with respect to the lighting of the experimental bench, as the quality and speed of capturing the images depend on the level of light intensity used. Lamps with low heat dissipation were used in order to avoid changing the test conditions due to the heating of the working fluid. The best option was to use LED lamps. Another important feature was positioning the system camera/lamp, which must be able to minimize the effects of shadows and reflections on the experimental bench. The image sequences of the particle swimming were recorded with the camera and subsequently captured on the PC as successive images with time intervals of 1/30 second. The image processing software (CVmob) developed by researchers on computer science of the Federal University of Bahia (Brazil) was used to obtain the two-dimensional coordinates of the helical swimmer for each frame, from which the swimming speed and trajectory were analyzed [102]. This software was validated by Peña et al.[102] and now is an open-source software. Essentially, this software uses techniques of computer vision, recognition of patterns, and optical flow to enable the tracking of objects in videos generating data of trajectory and velocity. Data were averaged over 30 successive tables

for each type of swimmer investigated in this work. Actually, with the CVMob software we were able to analyze the trajectories and determinate the main kinematic quantities from videos of the particle motion.

Close attention was paid to the preparation of the base fluids. A Newtonian silicone oil and a viscoelastic anionic Polyacrylamide solution (Separam, AP30, Dow Chemicals) were used as the base fluid in order to ensure a low Reynolds number around the helical swimmers and to confer elastic effect in the case of the second fluid. For both fluids, the maximum Reynolds number in the experiments was less than 0.01. Viscosity measurements were carried out using an Anton Paar Physica MCR 301 model Rheometer of rotating parallel disk geometry available in the laboratory of Microhydrodynamics and Rheology of the University of Brasilia see figure 3.3. This measuring system is powered by a permanent magnet synchronous drive motor placed on the measuring head, which is able to aply torques form 0.1μ Nm to 200μ Nm with resolution of 0.001 μ Nm and accuracy of 0.2μ Nm. The measuring cell in the MCR 301 Rheometer is a Peltier-temperature-controled bottom plate. The rheological properties of the fluids can be assessed as functions of time, shear-rate and, especially, due to the fact that this parameter is precisely controlled in this assembly. The gap between the discs is a function of the fluid viscosity and should be optimized for each type of fluid under analysis. It is important to note that the device is equipped with the TruGap technology, which permits the precise adjustment of the gap between the parallel plates to the value prescribed by the operator, independently of the temperature and thermal expansion of the assembly components. For the case of silicone oil the optimal gap used was 0.8mm whereas for the anionic PAMA solution at a polymer volume fraction of 0.05 the gap was 0.4mm. Small gaps (i.e. $<$ 0.5mm) can be achieved with micrometric precision.

- Rheometer - Anton Paar Physica MCR 301;
  - Geometry: parallel disks (Couette);
  - Rotating disk
    - PP50 series;
  - Pneumatic control system
    - 0.1 a 200 mN.m;
    - Maximum shear rate: 5000 s^{-1}.
- Positioning control system:
  - *TruGap* tecnology
  - $\pm$ 0.001 *mm*
- Temperature control:
  - Climatized room;
  - *Peltier* system on the fixed plate:
    - (-40 to 200) $\pm$ 0,01 C;
  - Thermal bath (Lauda);

Figure 3.3: Rheometer used for the viscosity measurement courtesy (Vortex) by Pereira, I. D. O. (2017).

The viscoelastic effects in our work are attributed only to the elasticity of the basis fluid. The

swimmer was placed in a vertical direction on the test bench at the center of the rectangular tank. First, we carried out a buoyancy test, in this test the flagellum is placed in the fluid with the motor turned off. Adjustments of the density contrast between the particle and ambient fluid is made by adding small spheres, so that the weight of the flagellum is balanced with the fluid. Under this condition the particle stays neutrally buoyant inside the tank for a long time scale compared with a typical experiment time scale. Three prototypes of the artificial swimmers with different helix geometry were used in order to carry out the experimental tests. In the table (3.2) are listed the properties of the flagellum. Figure (3.4) shows the schematic of the prototypes and the geometrical quantities of the active particle.

Table 3.2: Properties of the model of the three types of flagellum studied experimentally (i.e. helix 1, helix 2 and helix 3): wavelength (mm), apparent length (mm), helical radius(mm).

Type of Flagellum	Helix 1	Helix 2	Helix 3
Wavelength $(\lambda)(mm)$	2.00 ± 0.05	4.32 ± 0.05	7.25 ± 0.05
Apparent length $(L)(mm)$	50 ± 0.05	50 ± 0.05	50 ± 0.05
Helical radius $(R)(mm)$	9.00 ± 0.05	4.50 ± 0.05	8.00 ± 0.05

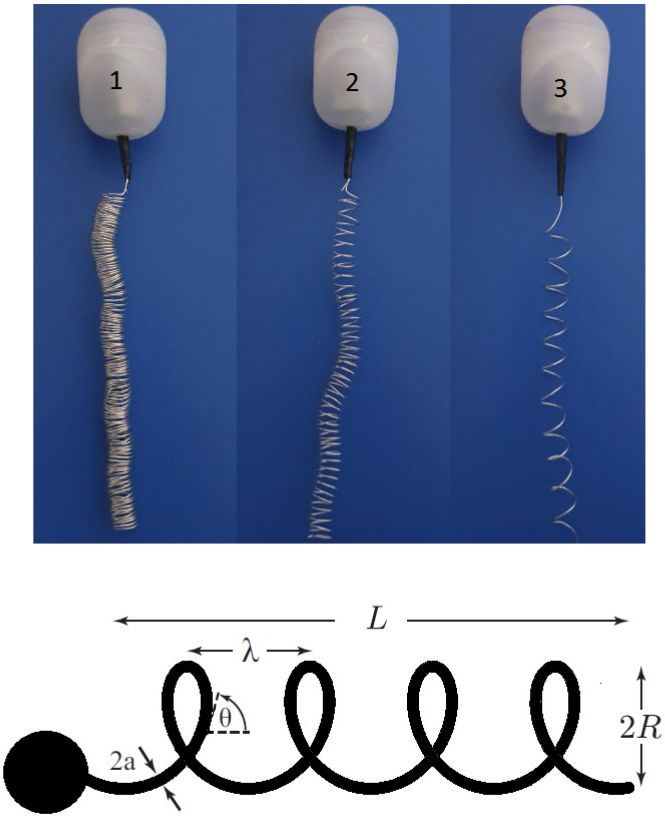

Figure 3.4: The three prototypes of flagellum investigated here and a schematic of the geometrical parameters of a typical flagellum.

The first step of the experiments was to measure the viscosity of the surrounding fluids. As already described at the beginning of this section, in this work two fluids were tested: A silicone oil (a nearly Newtonain fluid) and an anionic polyacrylamide solution (PAMA) that is an shear-thinning elastic fluid. The viscosities were measured at room temperature using an Anton Paar Physica MCR 301 model Rheometer with parallel disk geometry and an intelligent controlled gap. The viscosities of the silicone oil were made normalized by the mean viscosity of the silicone oil evaluated in the interval of shear rate considered; $\overline{\mu}_{so} \approx 220$ Pa.s at $25°C$. Additionally for the case of the silicone oil the shear rate was made non-dimensional using the maximum shear rate of the experiments as the main scaling, $\dot{\gamma}_{max} = 993.5\ s^{-1}$. Therefore, the value of $\dot{\gamma}^* = 0.01$ in the plot of Figure (3.5) corresponds approximately to 10 s^{-1}. In this work, the analysis of the experimental uncertainties associated to a measured variable followed the protocol prescribe in the paper by Kline and McClintock [103]. The associated error bars were all presented in the experimental plots. The maximum experimental uncertainties observed were always greater than 1%, but less than 10%. We chose the maximum error between the one found by the uncertainty analysis and the one based on statistics over at least 10 experimental realizations.

Figure (3.5) presents the normalized viscosity of the silicone oil measured in steady shear as a function of the normalized applied shear rate. The associated error bars of the experimental data are also shown in the plot. We can see that the viscosity of the silicone oil used is nearly independent of the shear rate ranging from $10^{-4}\ s^{-1}$ to 10 s^{-1}. Under this condition, the silicone oil in our experiments showed Newtonian behavior within the error bars of the experimental data. The existence of a weak shear thinning behavior of the silicone oil at higher shear rate can be related to the high cross-linking property of this fluid [104].

Experiments under condition of steady simple shear, oscillatory shear and step strain in the Rheometer MCR 301 were also carried in our laboratory for samples of the anionic polyacrylamide solution PAMA at 0.05 in volume concentration of macromolecules. The condition of small values of strain amplitude and a given frequency is a way of guaranteeing that the maximum amplitude of the applied shear rate is small enough to validate the desirable regime of linear viscoelasticity during all experimental runs. The viscoelastic modules were obtained by means of the rheometer software Rheoplus (Anton Paar) as being the Fourier coefficients of the shear stress. The anionic PAMA main relaxation time τ was calculated from the stress relaxation function $\Phi(s)$, where s is the shift time $t - t'$, t is the current time and t' denotes past times for a fluid having memory (i.e. elastic liquid). The following relation defining the PAMA relaxation time can be also evaluated by using our small amplitude oscillatory shear (SAOS) experimental data, as following:

$$\tau = \lim_{\omega \to 0} \frac{\eta''(\omega)/\omega}{\eta'(\omega)}, \tag{3.78}$$

where ω is the forcing frequency of the small amplitude oscillatory shear (SAOS); $\dot{\gamma}(t') = \dot{\gamma}_0 cos(\omega t')$. Here $\eta'(\omega)$ and $\eta''(\omega)$ are the viscous and elastic moduli of the PAMA calculated by the Fourier transform of the stress relaxation function as [105]:

$$\eta^*(\omega) = \eta'(\omega) - i\eta''(\omega) = \int_{-\infty}^{t} \Phi(s) e^{-i\omega s} ds, \tag{3.79}$$

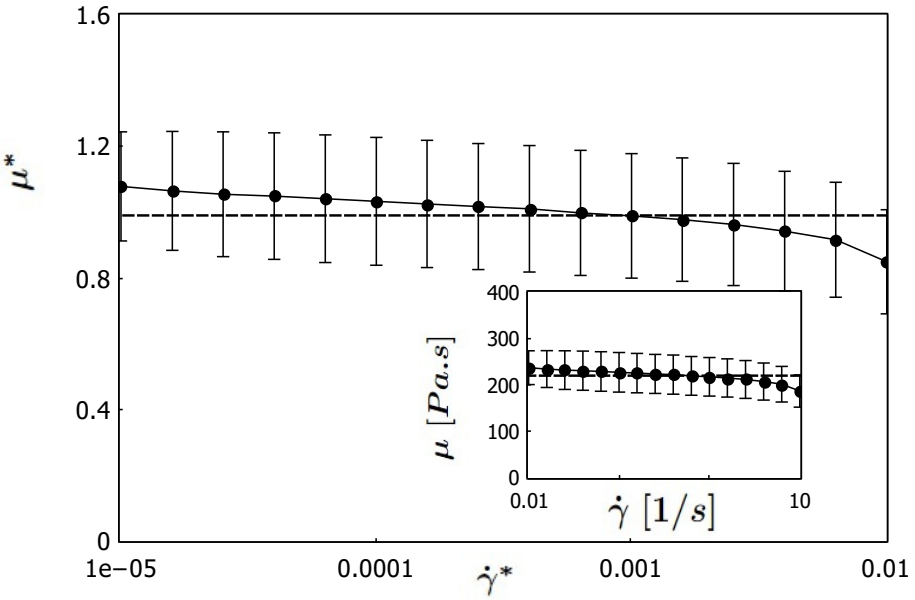

Figure 3.5: Non-dimensional viscosity of the silicone oil as function of the normalized shear rate at $25°C$. The viscosity in this plot was normalized by the the mean value of the silicone oil viscosity in the interval of shear rate used, 220 Pa.s. The shear rate in the plot was made non-dimensional using the maximum value of the shear rate $\dot{\gamma}_{max} = 993.5\ s^{-1}$. The experimental error bars are also shown in this plot. The inset in the plot shows the dimensional viscosity (Pa. s) of the silicone oil as a function of the shear rate (s^{-1}).

where η^* is the complex viscosity. Therefore, the main relation of the viscoelastic fluid can be determined in terms of the stress relaxation function $\Phi(s)$ as follows:

$$\tau = \lim_{\omega\to 0} \frac{\eta''(\omega)/\omega}{\eta'(\omega)} = \lim_{\omega\to 0} \left[\frac{\int_{-\infty}^{t} \frac{\Phi(s)\sin(\omega s)}{\omega} ds}{\int_{-\infty}^{t} \Phi(s)\cos(\omega s) ds} \right] = \frac{\int_{-\infty}^{t} s\Phi(s)\cos(\omega s) ds}{\int_{-\infty}^{t} \Phi(s) ds}. \tag{3.80}$$

Figure (3.6) shows a strong shear dependence viscosity of the shear rate. In this plot, the viscosities of the PAMA were normalized by the viscosity of the water $\mu_w = 0.89 \pm 0.0.1$ mPa.s at $25°C$. As we can see, the viscosity o the PAMA decays with the Deborah number (De) (i.e. a shear thinning behavior). For the case of the non-Newtonian fluid we use De as being our non-dimensional shear rate. Here, the elastic parameter De is calculated by the product between $\dot{\gamma}$ and the PAMA's main relaxation time and it represents the dimensionless relaxation time. In both analysis, from SAOS data (i.e. based on the viscoelastic moduli) and step strain (based on the stress relaxation function), the relaxation time of the PAMA at 5% of macromolecule volume fraction was approximately $\tau = 43$ s. It is seen in Figure (3.6) that for small De numbers the flow is not sufficiently strong to produce a stretching of the macromolecules and the structure of the elastic liquid remains in a state of equilibrium. This condition gives rise to constant viscosity plateau, observed for the others volume fractions tested. This Newtonian plateau represents a region where the fluid viscosity is almost constant. The associated error bars are also presented

in the plot.

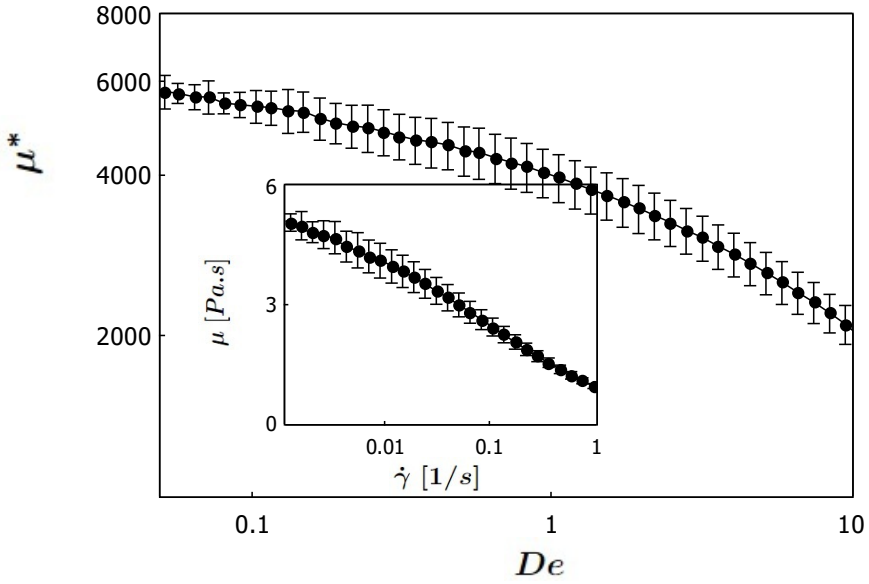

Figure 3.6: Non-dimensional viscosity of the anionic PAMA as function of the Deborah number for a volume fraction of the polymer $\phi = 0.05$. The associated error bars are also shown in the plot. The experimental data are very well fitted with an Cross ad-hoc model of shear dependence viscosity in a non-dimensional form: $\mu^*(De) = \mu_w^{-1}[(\mu_0 - \mu_\infty)/(1 + C(De/\tau)^m) + \mu_\infty]$ [2, 3]. Th parameter of the model were determined form the experimental data: $\mu_0 = 4.71 \times 10^2$, $\mu_\infty = 5.50 \times 10^{-3}$, $m = 0.77$, $C = 11.98$ and the main relaxation time τ of the anionic PAMA at $\phi = 0.05$ determined by equation (3.80) is approximately 43 s. The inset in the plot shows in a mono-log scale the dimensional viscosity (Pa. s) of the anionic PAMA as a function of the shear rate (s^{-1}) ranging from 0 to $10s^{-1}$.

Figure (3.7) depicts the result of our step strain experiment for a volume fraction of polymer $\phi = 0.05$. The stress relaxation function $\Phi(s)$ was made non-dimensional using the main relaxation of the PAMA at this concentration and the water viscosity μ_w a $20°C$. Hence,

$$\widetilde{\Phi}(\tilde{s}) = \frac{\Phi(s/\tau)\tau}{\mu_w} = \frac{\Phi(\tilde{s})\tau}{\mu_w}, \tag{3.81}$$

where $\widetilde{\Phi}(\tilde{s})$ is the non-dimensional stress relaxation function and $\tilde{s}$ is the non-dimensional shift time. In this work the experimental curve of $\widetilde{\Phi}(\tilde{s})$ is fitted very well using the classic non-dimensional stress relaxation function of a Maxwell fluid. For $\phi = 0.05$ we found a time spectrum of five relaxation time as shown in the inset of Figure (3.7). We can write:

$$\widetilde{\Phi}(\tilde{s}) = \sum_{j=1}^{5} A_k \exp\left(\tilde{s}/\tilde{\alpha}_k\right), \tag{3.82}$$

where A_k and $\tilde{\alpha}_k$ are, respectively, the stress amplitude and the relaxation of a k Maxwell element. Both parameters for each Maxwell element were determined by the experimental curve of the stress

relaxation function. Again, applying equation (3.80) we also determined the main relaxation time of the PAMA at 5% as being approximately 43 s.

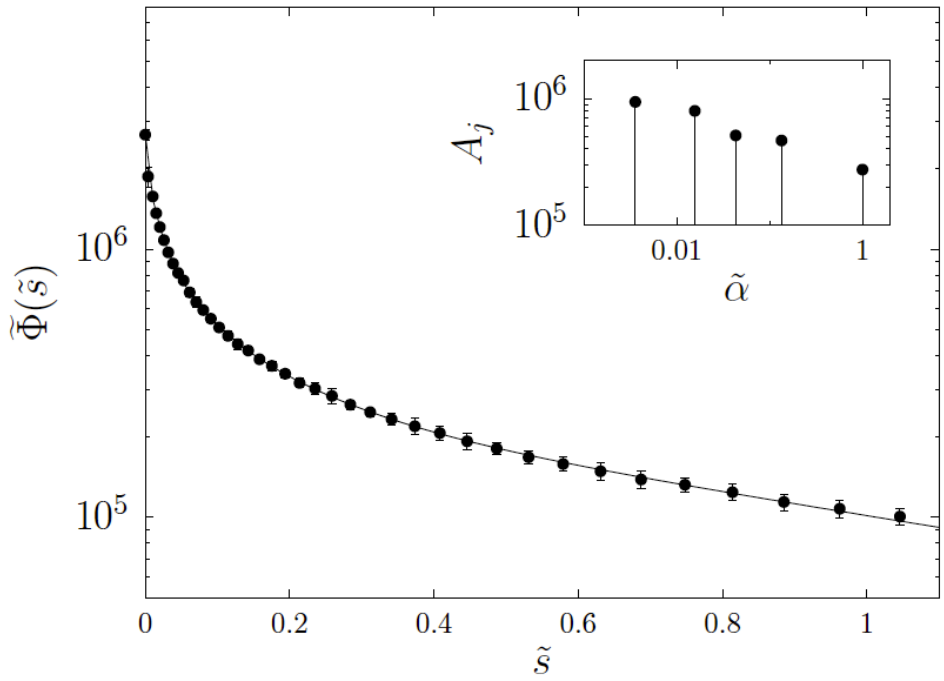

Figure 3.7: Non-dimensional stress relaxation function $\widetilde{\Phi}(\tilde{s})$ from a step strain experiment as a function of the non-dimensional time shift $\tilde{s} = s/\tau = (t - t\prime)/\tau$. The main relaxation time of the anionic PAMA for a volume fraction of polymer $\phi = 0.05$ was calculated by equation (3.80) as being $\tau \approx 43s$. The inset in the plot show the spectrum of relaxation times at this concentration. The associated error bars are also shown in the plot.

3.3 Creeping Flow Approaches - an overview

Creeping flow theoretical approaches are also used in order to investigate the motion of swimmers, induced by helical flagellum propulsion in creeping flow. In this section, we present the governing equations and the imposed boundary conditions related to the models explored in this work. The theoretical and numerical solutions presented here consist of three approaches: (i) the Resistive Force Theory (RFT) [15], (ii) the Slender Body Theory (LSBT) [16], and (iii) the Method of Regularized Stokeslets (MRS) [31]. Full details about implementations of the numerical procedures regarding these low Reynolds methods can be found in reference [29].

Now, the incompressible continuity equation and the unsteady force balance equation in creeping flow for a Newtonian viscous fluid of constant density and constant viscosity are given, respectively, in reference [106]:

$$\nabla \cdot \boldsymbol{u} = 0, \tag{3.83}$$

$$\left(\frac{Re}{Sh}\right)\frac{\partial \boldsymbol{u}}{\partial t} = -\nabla p + \nabla^2 \boldsymbol{u}. \tag{3.84}$$

Dimensionless equations (3.83) and (3.84), $\boldsymbol{u}(\boldsymbol{x}, t)$ is the eulerian fluid velocity at $\boldsymbol{x}$ and time t, p denotes the pressure. Here, Sh is the Strouhal number which is defined in the present context as being $Sh = U/(\omega R) = \lambda f/(2\pi f R)$, where U is a characteristic velocity and $\omega = 2\pi f$ is the angular frequency, λ is the wavelength and R is the transverse dimension of the flagellum tail as illustrated in figure (3.4). Therefore, this parameter denotes the inverse of the non-dimensional frequency of the investigated system. We have defined Sh this way in order to keep this parameter compatible with the non-dimensional parameter λ/R which appears in the theoretical papers (e.g. [15] and [16]). The Sh number in terms of λ/R is simply written as being $Sh = (1/2\pi)(\lambda/R)$. The Reynolds number, Re is defined as $Re = (\rho R U)/\mu$. If in this unsteady creeping flow problem the parameter Re/Sh is small (e.g. for $Re \ll 1$ and $Sh \sim 1$), we have a *quasi-steady* Stokes regime of the flow around the swimmer. Under this condition the force and torque on the swimmer is not time dependence. Otherwise, if $Re/Sh \sim 1$, the hydrodynamic force and torque are time dependent. In the present study, we consider $Re/Sh \ll 1$, and therefore the absence of force and torque time-dependent. Consequently, the induced propulsion force and torque only depend on the propeller's position.

Having the flow around the particle, the flagellum motion is determined from the integral representation of a creeping flow around the swimmer. The fundamental solution of a creeping flow around a point particle determines the velocity fields, pressure, and stress induced by a point force in a Newtonian fluid. In particular, the solution of (3.83) and (3.84) for creeping flows in steady state with the appropriated non-slip boundary condition on the particle surface can be expressed in terms of a resistance formulation described by [107]. We solve the reduced flagellum rotating and translating in the axial direction. By the resistance formulation the force and torque on the active particle in the x-direction, F_x, and T_x, are determined in terms of the translational and rotational velocity of the particle in $\boldsymbol{u}$ and $\boldsymbol{\omega}$. The resistance formulation is expressed here as follows:

$$\begin{pmatrix} \mathbf{F} \\ \mathbf{T} \end{pmatrix} = \begin{pmatrix} \mathbf{A} & \mathbf{B} \\ \mathbf{C} & \mathbf{D} \end{pmatrix} \begin{pmatrix} \boldsymbol{u} \\ \boldsymbol{\omega} \end{pmatrix} \tag{3.85}$$

The matrix in equation (3.85) is referred to as the grand (resistance) matrix and all elements of this mobility function depend only on the geometry of the flagellum. The sub-matrices $\mathbf{A}$, $\mathbf{B}$, $\mathbf{C}$ and $\mathbf{D}$ are three-dimensional and symmetric as the entire resistance matrix. If this matrix is known, the trajectory of the helical flagellum can be fully determined. In the present work, we focus on some kinematic properties and the calculations of force and torque on the active flagellum-micro-organism. Reference [16] has shown that the local velocity of a segment of the helix located at $\mathbf{s}$ is related to the force per unit of length (i.e., Stokeslet strength) along the filament $\mathbf{f}_\perp(\mathbf{s})$:

$$\mathbf{u}(\mathbf{s}) = \frac{\mathbf{f}_\perp(\mathbf{s})}{4\mu} + \int_{|\mathbf{r_0}(\mathbf{s}',\mathbf{s})|>\delta} \mathbf{f}(\mathbf{s}') \cdot \mathbf{J}(\mathbf{r_0}) d\mathbf{s}', \tag{3.86}$$

where $\delta = a\frac{\sqrt{e}}{2}$ is a natural cutoff, $\mathbf{r_0}$ is the position vector from the point $\mathbf{s}$ on the centerline relative to the point $\mathbf{s}'$, and $\mathbf{J}$ is the Oseen tensor given by

$$\boldsymbol{J}(\boldsymbol{r}) = \frac{1}{8\pi\mu}(\frac{\boldsymbol{I}}{|\boldsymbol{r}|} + \frac{\boldsymbol{rr}}{|\boldsymbol{r}|^3}). \tag{3.87}$$

3.3.1 Resistive Force Approach

A good approximation for solving the motion of a swimmer is the Resistive Force Theory (RFT). This theory can be used to predict the force and torque by the helical motion of the flagellum. Hydrodynamic force and torque at low Reynolds numbers are proportional to the local velocity of the particle. This can be done by performing the integration of all the forces and torques of each small segment along the particle. The force acting on an element ds of the fluid is given by $d\mathbf{f} = \mu\mathbf{K}\cdot\boldsymbol{u}dx$, where $\boldsymbol{u}$ is the local velocity and $\boldsymbol{K}$ is the resistance tensor per unit length of a filament element which depends only on the geometry of the filament element. We can expressed $\mathbf{K}$ in terms of an normal and an tangential contribution as follows:

$$\mathbf{K} = C_n\mathbf{I} + (C_t - C_n)\hat{t}\hat{t}. \tag{3.88}$$

Now, the total force exerted on the fluid by the swimmer is

$$\mathbf{F} = \frac{1}{\mu}\int \mathbf{K}\cdot\boldsymbol{u}ds, \tag{3.89}$$

and consequently the total torque is given by:

$$\mathbf{T} = \frac{1}{\mu}\int \mathbf{r}\times\mathbf{K}\cdot\boldsymbol{u}ds. \tag{3.90}$$

and the total $\boldsymbol{u(x)}$ is the filament velocity, and ds is the segment length how. Integrating in the contour we obtain the intensity of the force and the torque in a non-dimensional form as being:

$$F = -2\pi(C_n - C_t)\left(\frac{L}{\lambda}\right)\sin(\theta), \tag{3.91}$$

and the torque :

$$T = 2\pi\left(\frac{L}{\lambda}\right)\left(C_n\cos^2(\theta) + C_t\sin^2(\theta)\right)\left(\frac{1}{\cos(\theta)}\right). \tag{3.92}$$

Now, in order to calculate the propulsive forces and torques exerted on the swimming by the viscous flluid for different types of flagella we use the coefficients C_n and C_t proposed in the references [15] and [16]. Table (3.3) presents the expressions for both drag coefficients.

Table 3.3: Drag coefficients.

C_n	C_t	Reference
$4\pi[\ln(2\lambda/R)+1/2]^{-1}$	$2\pi[\ln(2\lambda/R)-1/2]^{-1}$	[15]
$4\pi[\ln(0.18(\lambda/R)\cos(\theta))+1/2]^{-1}$	$2\pi[\ln(0.18(\lambda/R)\cos(\theta))]^{-1}$	[16]

3.3.2 Slender Body Theory

The Slender Body Theory (SBT) is an asymptotic technique that can be use to determine creeping flows around a rod or slender fiber whose lenght is large compared to its thickness. This approach has been done successfully implemented by several authors (e.g. [16], [108],[109]). Here we just show the general idea behind the method based on the numerical calculation developed in the reference [29]. Now, equation (3.86) can be used in order to determine the force distribution on the flagellum for a fixed velocity of the flagellum. First, the grid size was chosen to be larger than the cutoff length. The discretized equation (3.86) for the ith node ($i = 1...M$), was divided into two parts. The first one is an integral from δ to the grid size while the second one is the velocity contribution of the stokeslets singularities located on the neighboring nodes. In this way, the discretized equation is solved in the local coordinates of each discretized point for the local forces $\mathbf{f_i}'$. The force at each discretized node is then converted back into the body frame via a coordinate transformation ($\mathbf{f_i}' \Rightarrow \mathbf{f_i}$). Additionally, the discretized form of equation in the body frame becomes:

$$\mathbf{P}\begin{bmatrix}\mathbf{f_1}\\ \mathbf{f_2}\\ \vdots\\ \mathbf{f_m}\end{bmatrix}+\begin{bmatrix}\mathbf{q_1}\\ \mathbf{q_2}\\ \vdots\\ \mathbf{q_m}\end{bmatrix}=\begin{bmatrix}\boldsymbol{u_1}\\ \boldsymbol{u_2}\\ \vdots\\ \boldsymbol{u_m}\end{bmatrix}. \tag{3.93}$$

In equation (3.93), $\mathbf{q_i}$ depends only on the geometry of the flagellum and on the input value of angular velocity. The torque contribution of each stokeslet acting on the flagellum is given by, $\mathbf{t_i} = \mathbf{r} \times \mathbf{f_i}$. From this discretization and using the total force and the torque contributions of each stokeslet, we can find the propulsion matrix $\mathbf{G}_h$ for the flagellum, so that:

$$\begin{bmatrix}\mathbf{F_h}\\ \mathbf{L^{-1}T_h}\end{bmatrix}=\mathbf{G}_h\begin{bmatrix}\boldsymbol{u}\\ \mathbf{L}\boldsymbol{\omega}\end{bmatrix}+\mathbf{Q}. \tag{3.94}$$

Here $\boldsymbol{F_h}$ and $\boldsymbol{T_h}$ are, respectively, the net hydrodynamic propulsion force and net hydrodynamic torque exerted by the flagellum. In addition, $\mathbf{Q}$ is obtained by propagating the constants $\mathbf{q_i}$ as

described above.

3.3.3 Implementation Using Regularized Stokeslet

The Method of Regularized Stokeslets is also used in order to evaluate the force and torque on the artificial flagellum. The rigid helix dynamics can be modeled by forces applied on the flagella points and by a torque at the base of each points using regularized stokeslet and rotlet theory. Here we will give a brief explanation of the implementation. The fluid velocity field due to the forces is described by regularized stokeslets and the velocity due to the torques by the associated regularized rotlets. In the typical stokeslet and rotlet theory. Singularities in the velocity expression are due to the assumption of having point-forces and point-torques. However, by a regularized approach, the singularities can be eliminated through the systematic regularization of the flows described above by considering forces and torques that are applied not at single points but within small points forces centered at those points. In this way, the forces and torques are highly concentrated but are spread over a small neighborhood of the application points. The regularized Stokeslets simulation eases the evaluation of integrals with singular kernels by replacing the delta distribution of forces, $\delta(r)$, with a smooth, localized distribution:

$$\phi_\epsilon(\mathbf{r}) = \frac{15\epsilon^4}{8\pi(r^2+\epsilon^2)^{7/2}}, \tag{3.95}$$

where $\mathbf{r} = |r|$ and regularization parameter ϵ is assumed to be small. This parameter ϵ prevents non-integrable kernels, but also has a physical meaning of representing surface area over which the force is distributed. For N regularized point forces $\mathbf{f}\phi_\epsilon\mathbf{r_n}$ at locations $\mathbf{r_n}$ on the surface of a body in motion, the fluid velocity at any point $\mathbf{r}$ is given by:

$$u_i(\mathbf{x}) = \frac{1}{8\pi\mu} S_{ij}^\epsilon(\mathbf{x}, \mathbf{x_0}) f_j. \tag{3.96}$$

From f_j the force and torque on the body can be directly computed.

Now, in the arrangement of the computational domain for a helical flagellum, we discretize the surface with cross-sections along its length and use twelve regularized Stokeslets on the perimeter of each circular cross-section. We separate adjacent cross-sections by a distance equal to one-half of the filament single layer potential on the parallel surface and a related double-layer potential on the flagellum. The two potentials have a unique solution that depends on the no-slip boundary condition of the flagellum. This method was first presented by [31] and the advantage of this formulation is that the results are independent of the choice of the parallel offset parameter.

The force and torque on the artificial swimmers here are calculated using the procedure described in reference [31]. A program in Matlab following the algorithm presented in reference [29] was used in order to perform numerically the flagellum dynamics calculations. The numerical procedure takes as input the parameters for helical flagellum R, L, a and λ and gives as output F and T. The helical radius $2\pi R$ is used as the characteristic length in the numerical program so that in terms of non-dimensional quantities we have: $R = 1/2\pi$, $L/(2\pi R)$, $a/(2\pi R)$ and $\lambda/(2\pi R)$ and F^*, T^* as the main output non-dimensional quantities. As discussed before the main dynamics parameter here for the case of an ambient Newtonian fluid is the Strouhal number , $Sh = (1/2\pi)(\lambda/R)$

and we keep the Reynolds number under creeping flow condition (i.e. $Re \ll 1$). Note that in this paper Sh denotes the inverse of a non-dimensional frequency of flagellum oscillating motion and therefore a typical non-dimensional time scale of the motion. The trajectory of the swimmers are described when considering the motion of the head and the tail of the flagellum. Additionally, the total force acting on the flagellum is composed of the stokeslet force, $\mathbf{F}_s$, on the head due to translation and the hydrodynamics force on the tail, $\mathbf{F}_h$. At low Reynolds number the relaxation time of flagellum (i.e. the Stokes number) is much smaller)= than the Sh, so that the inertial effect of the particle cab be neglected. Under this condition, the net force on the flagellum is zero at all times whenever the one is displaced from its equilibrium position. Hence:

$$\mathbf{F_h} + \mathbf{F_s} = \mathbf{0}. \tag{3.97}$$

Here, $\mathbf{F_h}$ is calculated by the Slender Body theory according to equation (3.94), whereas the force $\mathbf{F_s}$ corresponds simply to the drag force on the head and it is given by expression by the Stokes's drag past a spherical particle, i.e. $\mathbf{F_s} = -6\pi\mu a\boldsymbol{u}$. We solve the equilibrium equation and the non-dimensional time step used in this case is given by $\delta t = (1/10)min(0.01, Sh)$. Solving the particle velocity, the position of the particle is calculated using the standard Euler method to integrate the first order ordinary differential equation:

$$\frac{d\boldsymbol{x}}{dt} = \boldsymbol{u} \tag{3.98}$$

3.4 Computer Simulations: helical body in an elastic liquid

The effects of viscoelastic fluid on the flagella swimming are also considered. We study the flow of a non-Newtonian Oldroyd-B liquid past a helical filament between two parallel plates. The fluid is composed of a dilute solution of polymer in a Newtonian liquid solvent of viscosity μ_s. The flow is two-dimensional (2D) and schematically shown in figure (3.8). The aspect ratio of the helical radius to the channel half-width is 1/10.

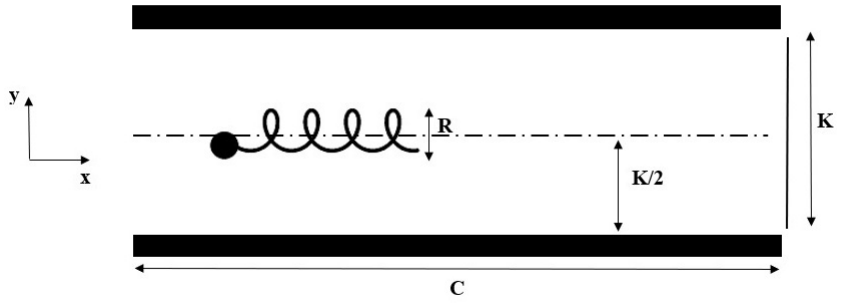

Figure 3.8: Schematic of 2D flow around the flagellum.

Now, a viscoelastic constitutive model provides the additional relation needed to solve the

governing equations of the flow. The complete set of non-dimensional governing equations for describing the flow of a Oldroyd-B liquid under creeping flow condition is given by:

$$\left(\frac{Re}{Sh}\right)\frac{\partial \boldsymbol{u}}{\partial t} = -\nabla p + \nabla\cdot\boldsymbol{\sigma} + (1-\xi)\nabla^2\boldsymbol{u} \tag{3.99}$$

$$\nabla\cdot\boldsymbol{u} = 0 \tag{3.100}$$

$$\left(\frac{Wi}{Sh}\right)\left(\frac{\partial \boldsymbol{\sigma}}{\partial t} + \nabla\cdot(\boldsymbol{u}\boldsymbol{\sigma}) - (\nabla\boldsymbol{u})\cdot\boldsymbol{\sigma} - \boldsymbol{\sigma}\cdot(\nabla\boldsymbol{u})^T\right) = -\boldsymbol{\sigma} + \xi(\nabla\boldsymbol{u} + \nabla\boldsymbol{u}^T), \tag{3.101}$$

where $\boldsymbol{\sigma}$ is the stress tensor of the elastic liquid, ξ is the ratio between the polymer viscosity and the ambient fluid viscosity. Here, Wi denotes the elastic parameter called Weissenberg number which measure the relative importance between the elastic liquid relaxation time scale τ_r and the flow time scale ℓ/U, i.e. $Wi = U\tau_r/\ell$. Additionally, we define the Deborah number $De = \omega\tau_r$ so that the ratio Wi/Sh can be represented by De in equation (3.101). So, in this paper we shall use De as the non-Newtonian elastic parameter of the flow. Note that when $De = Wi/Sh$ goes to zero the set of equations (3.99), (3.100) and (3.101) reduces to the model of a Newtonian fluid given by equations (3.83) and (3.84). The above governing equations were solved numerically. The non-dimensional parameters used in the numerical simulation with typical values compatible with the ones of the experiments were $Re = 0.01$ (i.e. creeping flow condition); $De = 1/2$ and $\xi = 3/7$. It is straightforward to show that a Dumbbell model of two constitutive equation discussed by Rallison and Hinch [110, 111] with Hookean spring may produces unlimited elongation of the Dumbbell (i.e. the model allows the polymers to stretch indefinitely) and the pair of constitutive equation reduces to the most common Oldroyd-B elastic fluid with the material constant of the model equal to $\tau/2$, where τ denotes the relaxation time of an extended macromolecule to the randomly-coiled state. From the Dumbbelll model with a linear spring τ is estimated as being $\tau = 2\pi\mu a^3/(k_BT)$ [112]. Here k_B is the Boltzmann constant, T the absolute temperature and a is the mean end-to-end distance of the polymer. In this model the macromolecule is composed of N rigid segments (individual monomers) of lenght δ, with each individual monomer randomly oriented with respect to the adjoining segments. Therefore, the equilibrium configuration distribution of the macromolecule is then given by a random walk of N steps and from the central limit theorem $a \sim N^{1/2}\delta$. Since N can be calculated by the ratio between the molecular weight of the polymer (M) and the molecular weight of a single monomer (M_o) [105], it results that the polymer relaxation time of the Oldroyd Fluid - B used in this work can be estimated as: $\tau = (2\pi\mu/k_BT)\delta^3(M/M_o)^{3/2})$.

Before proceeding with the presentation of the main experimental and theoretical results of this section, we give a brief overview of the numerical technique used in this work for solving the set of governing equations (3.99), (3.100) and (3.101). The values of the non-dimensional parameters examined in the numerical simulations were always compatible with the ones considered in the experiments. In this way we can compare the simulations results with our experimental data. We use $Re = 0.01$ (i.e. creeping flow condition), $\xi = 3/7$ and $De \sim 1$. The mesh of the flow

domain kinematics is illustrated in figure (3.9) for a Cartesian coordinate system with origin on the center of the head of the helical swimmer. The channel aspect ratio was defined as being the height of the channel (k) over the helical swimmer radius (R), i.e. $k/R = 10$ as suggested in reference [113]. The particle is placed in a rectangular domain $[0\ ;25] \times [0\ ;2]$. No-slip boundary conditions are enforced at the sidewalls as described below in the boundary conditions, subsection (3.4.1). The problem is solved using a boundary-increased mesh with the extended finite element according to the numerical procedure first described in reference [114]. Three sub-domains $D1$, $D2$, $D3$ were explored with the base mesh shown in figure (3.9). We use a total mesh with the following characteristics: (i) free triangular mesh on the uniform for the glass as shown in figure (3.9a) and (ii) extra fine mesh figure (3.9b). The number of mesh vertices used was 19680, the numbers of triangles equal to 32898, numbers of quads equal to 2790, numbers of edges elements of 1115 and the number of vertex elements 24. In the entire grid domain we have used 35688 elements. Additionally, the minimum elements quality was 0.01653, the average element quality was 0.9286, the element area ratio was approximately 1.4×10^{-4}, and the mesh area 49.55. The averaged computational time observed in the simulations was about $12h$ and the resulting system equations has a total degree of freedom total (DOFs): 234395. In our computer simulations the configuration of the flow was taken as being symmetric so that only half of the whole domain needs to be solved. Flow enters at the left boundary where a velocity inlet condition was applied. In particular, the top boundary and the helical swimmer surface were considered solid walls, while the right boundary is a pressure outlet. The solver used here is based on an iterative procedure so that an estimation of the error in the solution was necessary on order to control the convergence of the numerical method. The estimated error is based on the convergence criterion defined as $\mid \zeta_{(n+1)} - \zeta_{(n)} \mid \leq tol$, where ζ is a dependent variable and tol denotes an adopted tolerance typically equal 10^{-3} (i.e the default value in the numerical code). However, in the current simulations performed in this work the residual convergence criteria was set to 10^{-4}. Higher accuracy in the simulations results can be obtained with an increased number of grid points distributed close to the body surface, but the computational cost increases accordingly. We have balanced the accuracy and computational cost when comparing the simulation results with our experimental data. We shall show a good agreement between the numerical and experimental results (within the error bars of the experimental data) for De varying between zero to approximately 2.

3.4.1 Boundary conditions

In order to solve the set of equations (3.99), (3.100) and (3.101) it is necessary to impose boundary conditions for the velocity field $\boldsymbol{u} = (u, v)$ for the components of the non-Newtonian stresses. In the present case the flow is two-dimensional which means that the flow quantities depends on x and y directions only. The inlet conditions imposed for x and y components of the velocity are, respectively: $u = 1.5(1-y^2)$ and $v = 0$. The imposed boundary conditions at the solid walls of the flow domain are: $u = v = 0$; $\partial u/\partial x = \partial v/\partial x = 0$; $\partial \sigma_{xx}/\partial x = \partial \sigma_{yy}/\partial x = \partial \sigma_{xy}/\partial x = 0$ and $\partial p/\partial x = 0$. Additionally, we impose the following outlet and inlet boundary conditions for the stresses: $\sigma_{xx} = 2De(\partial u/\partial y)^2$; $\sigma_{yy} = 0$ and $\sigma_{xy} = \xi \mu_s (\partial u/\partial y)$.

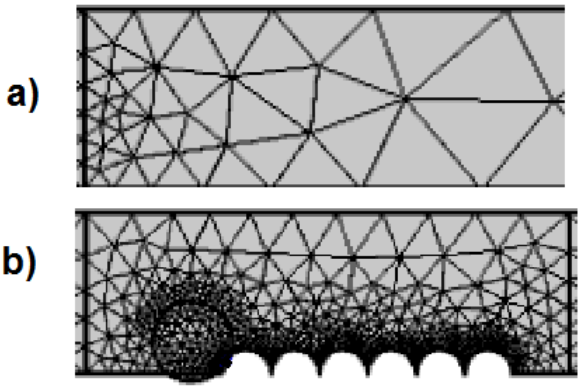

Figure 3.9: CFD model of the flagellum and grid discretization. a) Shows a mesh of the global domain. b) A local mesh on the particle.

3.5 Results and Discussions

In this section we first report experimental results for velocities and trajectories of the helical swimmer as well as the hydrodynamic force and torque on it when the base fluid is Newtonian and also viscoelastic. In order to verify accuracy of the experiments carried out in this work, at the end of this section we also shall present a comparison between experimental measurements and theoretical predictions based on SBT and Stokeslet methods discussed in the subsections (3.3.1) and (3.3.3), when $De = 0$ (i.e. Newtonian fluid), and a similar comparison with CFD simulations presented in section (3.4), when the base fluid is viscoelastic, i.e. $De \neq 0$.

The swimmer placed inside the container with the base fluid was approximately neutrally buoyancy. Therefore it persists suspended in the container as illustrated in figure (3.2), without submersion nor climbing, for a period of time sufficiently large in order to make the measurements in the absence of gravity effect. The interval of time that the swimmer must stay suspended in the base fluid can be estimated as being a period of time much larger than the typical time scale of the swimmer motion, i.e. L/V_p, but much smaller than the characteristic Stokes time scale $\mu/(Lg\Delta\rho)$. Namely, $L/V_p \ll (\Delta t)_{exp} \ll \mu/(Lg\Delta\rho)$, where L is a typical size of the swimmer movement and V_p denotes a typical value of the propulsion velocity of the swimmer, g is the gravity, μ the viscosity of the base fluid and $\Delta\rho$ is the density contrast swimmer and base fluid. In our experiments the value of this time interval was about 120 s, that is a consistent value with the scaling described above and a sufficient time for recording a realization of the helical swimmer movement. In addition, a constant rotational frequency by the DC power supply was provided in order to actuate the small synthetic swimmer system. The swimmer was connected to the force and torque measurement system and the motion of the swimmers was filmed with the digital camera as described in section (3.2). Then, the images were then processed digitally and the position and speed determined in time. Several realizations of the experiments were done with the three prototype of swimmers in order to have a meaningful statistics (i.e. small error bars) over the experimental data. Taking

into account that base fluids used had different viscosity, we monitored the angular frequency in order to carry out the experiments for both fluids tested with approximately the same Reynolds and Strouhal numbers. In this way, we were able to focus on the elastic effects of the base fluid, represented by the Deborah number, on the propulsion motion of our prototypes of swimmers.

Now, in order to determine the force exerted on the helical swimmer by the fluid, the swimmer helix was rotated at a given frequency, f. For this end, we monitored the electrical power supplied by the DC voltage during the experimental tests to the system to achieve different frequencies. The average propulsive force (F^*), the propulsive torque (T^*), velocity U, Strouhal number (Sh), Reynolds number (Re) and consequently Re/Sh, $U/\lambda f$ associated with each helical tail are calculated using the procedure already described in section (3.3). The average force and torque are made non-dimensional by using the scalings $F_0 = \mu\omega R^2$ and $T_0 = \mu\omega R^3$, respectively. The average values of these quantities for the three model of swimmer helices investigated here are summarized in Table (3.4) and Table (3.5) when the base fluid is Newtonian and an elastic liquid, respectively. It should be important to note that the e helical tail type (1) is seen to produce the highest non-dimensional average force (17.21) and torque (144) when the base fluid is the elastic liquid (PAMA) and 14.21 e 127 in the case of the Newtonian fluid (i.e. silicone oil) which seems to be consistent with the trend of the generated propulsive velocity. This results seems to indicate that the base fluid elasticity increases the average propulsive force and torque required for the swimmer motion. Consequently it may be indicating that the extra elastic forces which appear in the base fluid due to the anisotropy (i.e. additional normal stresses) produced by macromolecules stretching along the flow streamlines may increase significantly the speed velocity of the swimmer in the swimming direction.

Table 3.4: Typical non-dimensional parameters used in the experiments carried out to determine the propulsive force and torque on a swimmer suspended in Newtonian fluid (silicone oil). Three types of swimmer helices were examined.

Types	L/R	a/R	Re	Sh	Re/Sh	$U/\lambda f$	F^*	T^*
Type 1	5.5	0.06	0.0507	0.0704	0.720	14.2	14.21	127
Type 2	8.33	0.09	0.072	0.116	0.640	8.62	9.29	81.8
Type 3	6.25	0.07	0.124	0.154	0.805	6.5	7.32	66.9

Table 3.5: Typical non-dimensional parameters used in the experiments carried out to examine the propulsive force and torque on a swimmer suspended in non-Newtonian fluid (elastic liquid - PAMA). Three different types of swimmers helices were examined. So we consider in this case Deborah number varying from 0 to approximately 2.

Types	L/R	a/R	Re	Sh	Re/Sh	$U/\lambda f$	F^*	T^*
Type 1	5.5	0.06	0.041	0.0699	0.586	14.3	17.21	144
Type 2	8.33	0.09	0.073	0.114	0.640	8.77	10.91	91.2
Type 3	6.25	0.07	0.108	0.1431	0.754	6.98	7.62	71.8

According to tables (3.4) and (3.5), the Reynolds numbers (Re) for the three configurations of flagellum is much less than one, that means a creeping flow condition of the swimmer motion. In table (3.4) and (3.5), the Strouhal numbers (Sh) for the three helical tails were calculated and compared. The maximum difference between each helical tail being about 10% with the highest value of Strouhal number occurring for the flagellum helix type (3). In addition, it can be seen that for both base fluids (i.e. Newtonian and Non-Newtonian fluids used) the Reynolds number presents a similar trend with the highest value occurring at helix type (3). Moreover, smaller Reynolds numbers are achieved by the flagellum with helix type 1. Actually, we noted that this flagellum although having the same length as other other two, it has a greater number of turns N. Consequently the wavelength (λ) of the flagellum type (1) is smaller and adjacent turns of the flagellum become closer in space. This configuration makes the flagellum more robust and presenting a higher hydrodynamic viscous force for its motion on the base fluid. It should be important to note that the ratio Re/Sh is also small in the investigated creeping flows. In the case of unsteady creeping flows, the relative magnitude of the Eulerian acceleration is determined by the ratio Re/Sh. Our experimental results from table (3.4) and (3.5) indeed show small values for both Re and the ratio Re/Sh. Therefore, we have explored a quasi-steady Stokes regime of flow in the experiments and simulations. Under these conditions, the hydrodynamic force and torque on the micro swimmers are considered approximately time independent. Additionally, we have also calculated the non-dimensional velocity $U/\lambda f$ that represents a slip parameter expressing the relative importance between a typical linear velocity of the swimmer motion and the wave velocity λf generated by the flagellum motion. Here λ and f are the wavelength and the frequency of the swimmer flagellum, respectively. The small motor controlling the motion of the flagellum has

operated in our experiments at a constant frequency $f \leq 10Hz$. The motor provides a linear stage that translates with velocity, 0.3 mm/s along the axial direction of the helix. In the table (3.6) we present some typical experimental data. The uncertainty of the DC power is the uncertainty in the voltage source given by the manufacturer as being equal to 0.01. For the other parameters, the uncertainty was calculated from a set of measurements. For instance, we found 0.04 as being the uncertainty in the frequency and finally for linear velocity, force and torque the uncertainty was approximately 0.02.

The experimental results of the ratio $U/\lambda f$ shown in tables (3.4) and (3.5), were just slightly different for the viscous and elastic fluid for the same type of flagellum. Therefore, the elasticity of the base fluid does not appear to have a considerable influence on the slip between the propulsion velocity of a swimmer and the wave velocity propagation produced by its helical flagellum motion. It is seen that $U/\lambda f \approx 14$, 9 and 7, for the flagellum type 1, 2 and 3, respectively. This result seems to be different of the slip parameter observed in absence of helical motion as the one examined in the studies presented in the references [19] and [115] for nematic active suspensions in Newtonian and non-Newtonian fluids, where $U/\lambda f \approx 1$.

Results for non-dimensional force and torque, as a function of the Strouhal number (Sh), generated by the flagella for the three different configurations investigated in silicone oil (Newtonian base fluid), are presented in Figure (3.10). The force and torque on the swimmers here were obtained by using the systems load cell measurements already described in section (3.2). Firstly, we can see that the flagellum with smaller wavelength λ experiences larger hydrodynamic force and torque as keeping the helices with the same length. Secondly, we observe that all examined flagellum configurations result in a nonlinear Strouhal force and torque dependence. These results indicates that the propulsive force and torque required to generate the motion of the swimmer remain varying with its speed during the time scale of an experimental realization. Actually, the propulsive force and torque are generated in the swimmer tail by storing elastic energy in the buckling and this mechanism competes with the viscous hydrodynamic drag. This behavior should also be associated with the velocity variations between each pitch of the flagellum helix. Additionally, as already expected figure (3.10) shows that both F^*, T^* decrease as Sh increases since in this paper Sh has been defined as being the inverse of the non-dimensional frequency.

The influence of the base fluid viscoelasticity on the dynamics of the swimmer motion is also investigated here. Figure (3.11) shows the non-dimensional force and torque on the swimmer as a function of the elastic parameter De for the three different configurations of the flagellum explored in this work. The base fluid is an elastic liquid (i.e. the polymeric solution - PAMA). Comparing the results of force and torque shown in the plots of Figures (3.10) and (3.11) respectively, we observe values of forces torques with the same order of magnitude for both cases: that is, as the base fluid is Newtonian or viscoelastic one. It is seen that the flagellum configuration with shorter wavelength helix (i.e. helix 1) leads to larger values of force and torque on the swimmer flagellum. Additionally, figure (3.11) shows a nonlinear dependence of propulsive force and torque on the elastic parameter De. More important, the dynamic quantities F^* and T^* increases as the elastic parameter De varies from 0 to 2.5. As we will see next, the increase in F^* and T^* with De can be directly related to the increase of the swimmer speed in the presence of the elastic force when

Table 3.6: Dimensional experimental measurements and associated errors for: frequency (Hz), propulsion velocity (mm/s), force (mN) and torque N m).

helix (1)			
f [Hz]	U [mm/s]	F[mN]	T[Nm]
error (4%)	error (2 %)	error (2%)	error (2%)
1.25—8.44	0.025—0.107	42.92— 47.04	0.084—0.997
helix (2)			
f [Hz]	U [mm/s]	F[mN]	T[Nm]
error (4%)	error (2 %)	error (2%)	error (2%)
2.05—9.15	0.037—0.137	30.05— 37.11	0.107–0.118
helix (3)			
f [Hz]	U [mm/s]	F[mN]	T[Nm]
error (4%)	error (2 %)	error (2%)	error (2%)
2.76—10.12	0.056—0.205	22.32— 29.65	0.113–0.131

De is nonzero. As discussed in section (3.3), under condition of creeping flow the hydrodynamic force and torque on a body must scale like $L_s U_s$ and $L_s^3 \omega_s$, respectively. Here L_s, U_s and ω_s are typical scales of the length, velocity and angular velocity of the swimmers.

Now, we investigate the influence of the base fluid elasticity on trajectory and the swimming speed. For this end, we set the initial position of the swimmer closer to the top of the box and the swimmer is released freely in the fluid as described in section (3.2). The experiments were conducted for swimmer with similar kinematics in both base fluids. So, we expect to be exploring much more the elastic contribution to the motion of our swimmers than changes produced by

variation in the kinematics. Figure (3.12) (a,b) shows, respectively, a typical trajectory and the speed of the swimming for the three flagellum configurations studied here. The trajectory of the helix is shown in in terms of non-dimensional variables in the x^*-y^* two-dimensional space. Therefore, x^* y^* and u^*, v^* denote non-dimensional position and velocity respectively. In order t present the results in terms of non-dimensional quantities, we have used the following appropriate scales: $t^* = t_{exp}/t_{scale}$; $x^* = x/L_{scale}$; $y^* = y/L_{scale}$; $u^* = u\ t_{scale}/L_{scale}$; $v^* = v\ t_{scale}/L_{scale}$. In the present context, t_{exp}, is the time scale of experiment, $t_{scale} = 1/f$ is the time scale based on a typical frequency of the body motion, $L_{scale} = L_{box}$.

The results are presented for both base fluids: the swimmer immersed in the Newtonian fluid (silicon oil) and the elastic liquid (PAMA) for $De = 1.3$. In figure (3.12 a), we can see that while the shape of the trajectories are qualitatively similar for the three types of flagellum tested, the transversal displacement of the swimmer inside the elastic liquid is considerable faster as compared with its motion inside the Newtonian viscous liquid. In figure (3.12 b) we can observe a remarkable increase in the transversal speed (at the same value of u^*) of the swimmer as the base fluid is the viscoelastic liquid. Same observations are seen for the three different types of flagella. The results point out that the elastic forces arising from the macromolecules stretching in the non-Newtonian liquid acting on the swimmer surface is a favorable effect to its motion, promoting a remarkable increasing in the velocity of the body along the main swimming direction. As the swimmer moves its head sideways, a net forward motion is produced.

Additionally to the results shown in figure (3.12), we present in figure (3.13) a supplementary plot of the non-dimensional transversal velocity v_{NN}/v_N as function of the elastic parameter De, for the case of helix type (1), in order to compare the motion response as the helical swimmer is suspended in the Newtonian and the elastic liquid (PAMA). It is interesting to note the remarkable increase of the transversal swimming speed v_{NN}/v_N in the elastic liquid as the Deborah number increases until approximately one (i.e. $De \sim 1$). The maximum ratio v_{NN}/v_N observed in the experiments was about 1.3, for $De \approx 1$, which corresponds to an significant increase of about 23% when just few ppms of the macromolecules is used in the polymeric solution of PAMA. We verify similar behavior for the other types of flagellum models. It is also see from figure (3.13) that for De number below 0.5 the elastic effect on the swimmer speed is not perceptible. In this condition the macromolecules are not sufficiently stretched to produce stress anisotropy and an elastic force on the body surface. Above $De = 0.5$, however, there is a systematic increase of the speed velocity until a critical Deborah number close to 1. The streamlines surrounding the helical swimmer may produce a net force on the particle that pushes it enchaining its propulsion speed until a saturated value, depending on the De at a given macromolecules concentration. For larger De (i.e.$De > 1$) we can see clearly this saturation of the v_{NN}/v_N. At these larger values of De, we conjecture that the macromolecules have reached the maximum possible stretch for the volume fraction of the polymer used and further increases of De may produce degradation in the elastic base fluid. The slightly variations in v_{NN}/v_N when $De > 1$ can be associated to the fluctuations in the measurements associated with the experimental error bars also shown in the plots.

Another interesting finding was to see that the ratio between the velocity component in the transversal direction and longitudinal direction v/u (i.e. velocity anisotropy) was approximately

independent of the De number. This anisotropy varies just slightly with De (i.e. within the experimental error bars) with an average value approximately to 1.2. In contrast, this result indicates that an increase of the elastic effects in the base fluid has not produced appreciable changes in the velocity anisotropy of the swimmer motion.

In summary, our experimental results have found that the non-dimensional velocity of the swimmers appears to be incremented by the action of elastic force on the active body as it is suspended in a non-Newtonian fluid. For all cases investigated in this work, the swimming speed was seen to be larger when the surrounding liquid was viscoelastic. Therefore, our results seems to be at least in qualitative agreement with the previous experimental results presented in a different context of active macroscopic magnetic swimmers (e.g. [53] and [51]).

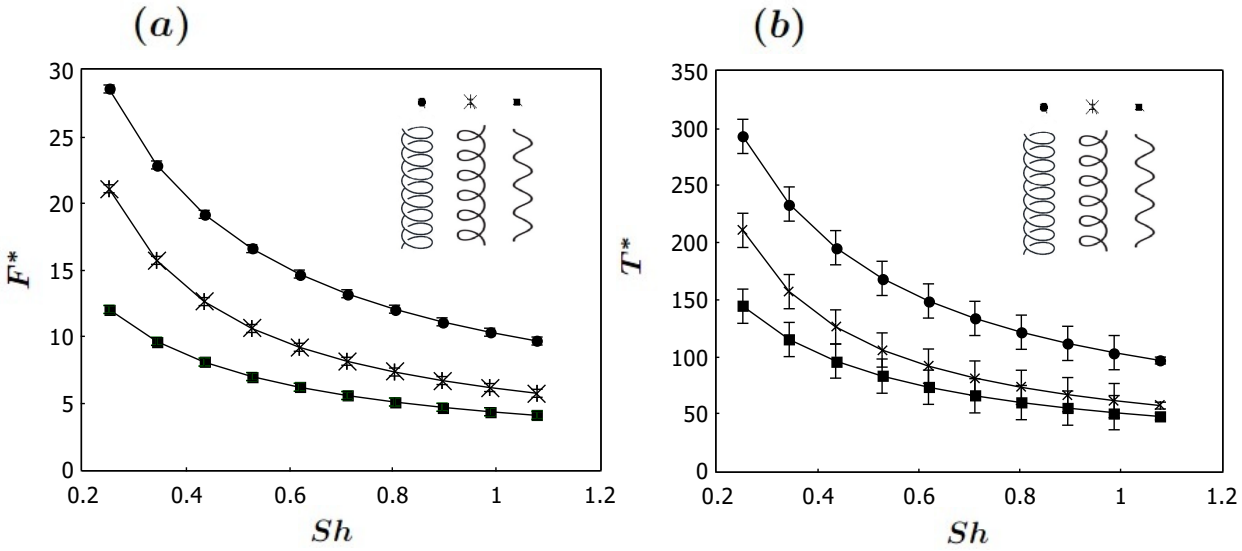

Figure 3.10: Experimental results of the hydrodynamics force and torque on the flagella as a function of Sh for the three different configurations examined in this work. The base fluid associated with these plots was the silicone oil (i.e.Newtonian fluid). (a) Non-dimensional force versus Sh and (b) Non-dimensional torque versus Sh.

Now, we test the accuracy of our experimental method by performing numerical simulations for a Newtonian ($De = 0$) and a non-Newtonian base fluid ($De \neq 0$). For the case of Newtonian fluid we performed numerical calculations using both slender body theory (SBT) and the method of regularized Stokeslet (RSM) presented in section (3.3). For this end, we show in Figure (3.15) (a) and (b) the non-dimensional hydrodynamic force and torque, respectively, on the artificial helical swimmer for a fixed axial length of the flagellum as a function of Sh varying from 0 to about 1.2. As mentioned before the Reynolds number was considered very small and $De = 0$. We can see a very good agreement between the theoretical predictions of F^* and T^*, given by SBT and RSM, and the experimental data in the interval of Sh considered. Clearly, the good agreement is observed specifically for the higher Sh, within the error bars of the experimental data, i.e. when the ratio $Re/Sh \lll 1$ and the hydrodynamic drag on the particle is indeed very close to the stationary condition. One other significant observation evident from Figure (3.15)a,

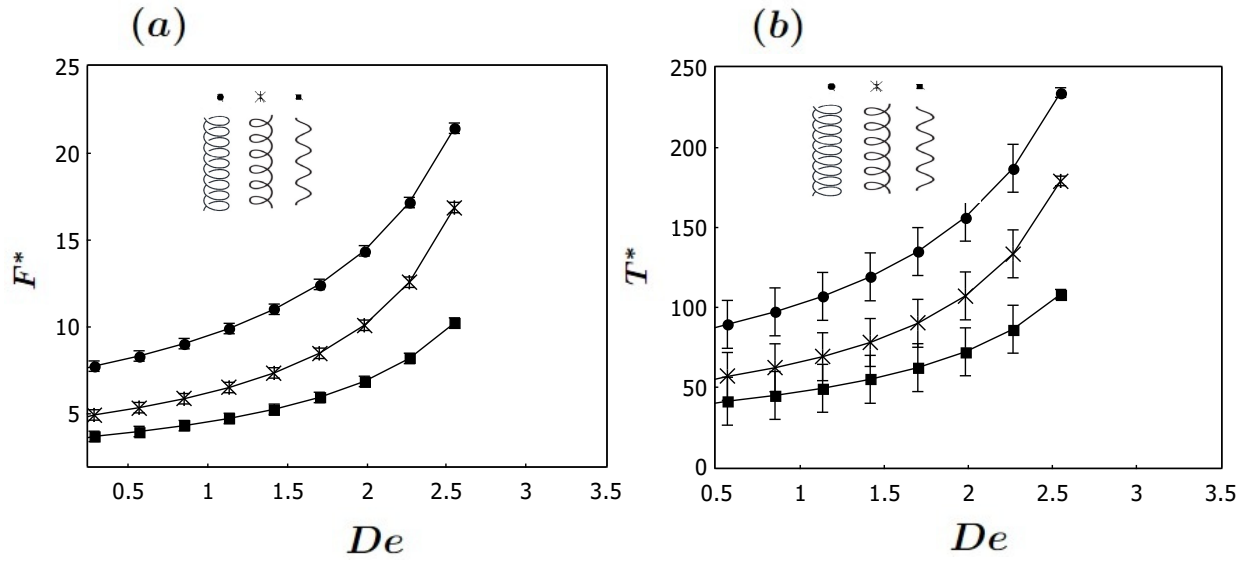

Figure 3.11: Experimental results of hydrodynamics force and torque on the flagella as a function of De for the three different configurations investigated here. The base fluid associated with these plots was a polymeric solution - PAMA (i.e. an elastic liquid). (a) Non-dimensional force versus De and (b) Non-dimensional torque versus De.

b is that the theoretical results given by SBT and RSM can be seen as a type of lower and upper bounds, respectively, for the experimental data as $Sh > 5$. These comparison also demonstrates the consistency of our experimental procedures and the accuracy of the measured data at creeping flow condition.

Finally, we present a comparison for the non-Newtonian and Newtonian velocity ratio v_{nn}/v_n as a function of De measured experimentally and calculate numerically by the CFD procedure for a viscoelastic fluid described in section (3.4). Here the ratio Re/Sh is also kept small and De is varying from 0 to approximately 2. In figure (3.16) we can see a good agreement between experiments and simulation results within the error bars of the experimental data. However, while the experiments have shown a saturation of v_{nn}/v_n for $De \sim 1$, the numerical simulations predicts a systematic increase of the speed velocity with De. A possible explanation of this discrepancy in the behavior of v_{nn}/v_n is the fact that the viscoelastic-Oldroyd model described in section (3.4) is not capturing correctly the viscoelastic response of the base fluid as De increases, since Oldroyd B model assumes infinite extensibility of the polymer chain. We argue that the macromolecules in the numerical simulations continue being stretched by the flow at larger De in contrast with the experiments. However the simulations performed here were nonetheless a first step in the more general and complete problem of active helical swimmers in elastic liquids, which may be relevant to understand the physics of dilute active suspension.

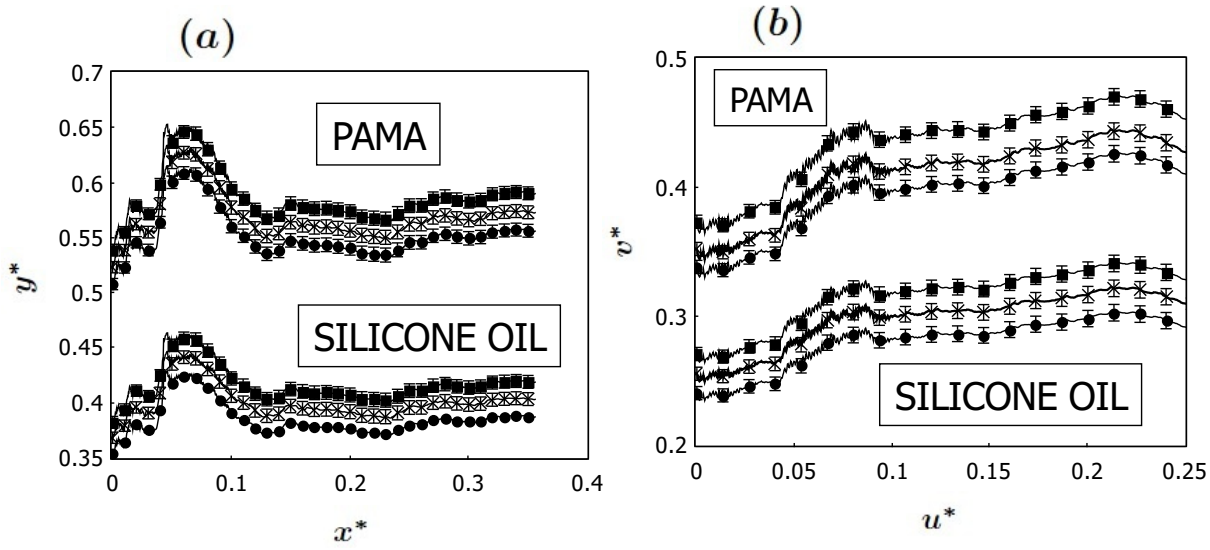

Figure 3.12: A comparison between the trajectories and speed of the swimmer immersed in a Newtonian fluid (silicon oil) and non-Newtonian fluid (PAMA) for $De = 1.3$. The different curves in the plot represent the three types of flagella examined. (a) Normalized swimming trajectory and (b) non-dimensional swimmer speed (transversal component versus longitudinal one). The experimental error bars are also shown in the plot. The symbols in the plot are: black circles represent helix (1); black crosses represents helix (2); and squares denote helix (3) measurements.

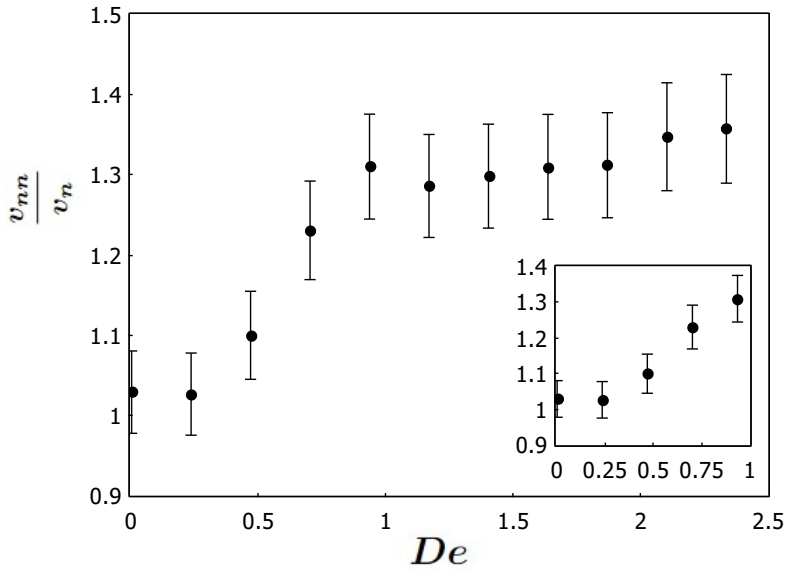

Figure 3.13: The ratio between the swimmer transversal velocity for the case of non-Newtonian fluid (PAMA) v_{NN} and the swimmer transversal velocity for the case of Newtonian fluid (silicon oil) v_N as a function of the elastic parameter Deborah number. The helix configuration used was the type (1).

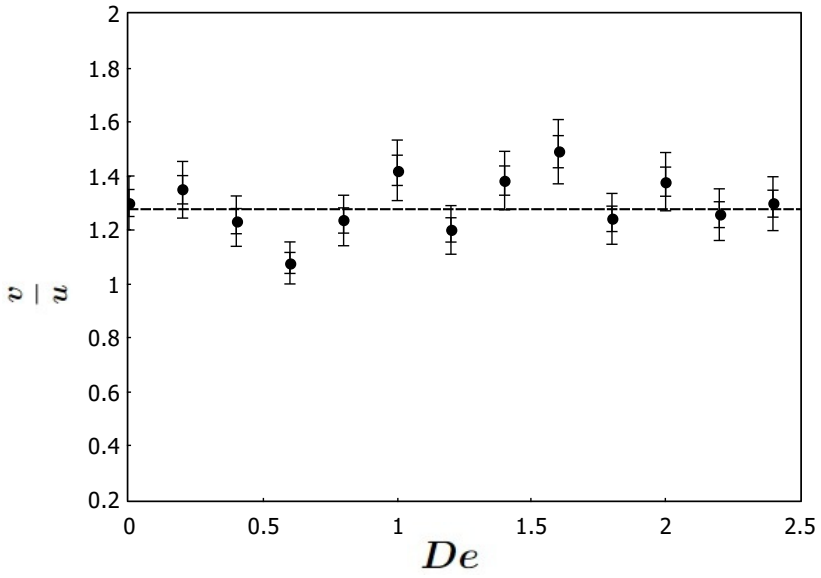

Figure 3.14: The ratio between the velocity component in the transversal direction and longitudinal direction v/u as a function of the elastic parameter Deborah number. The helix configuration used was the type (1).

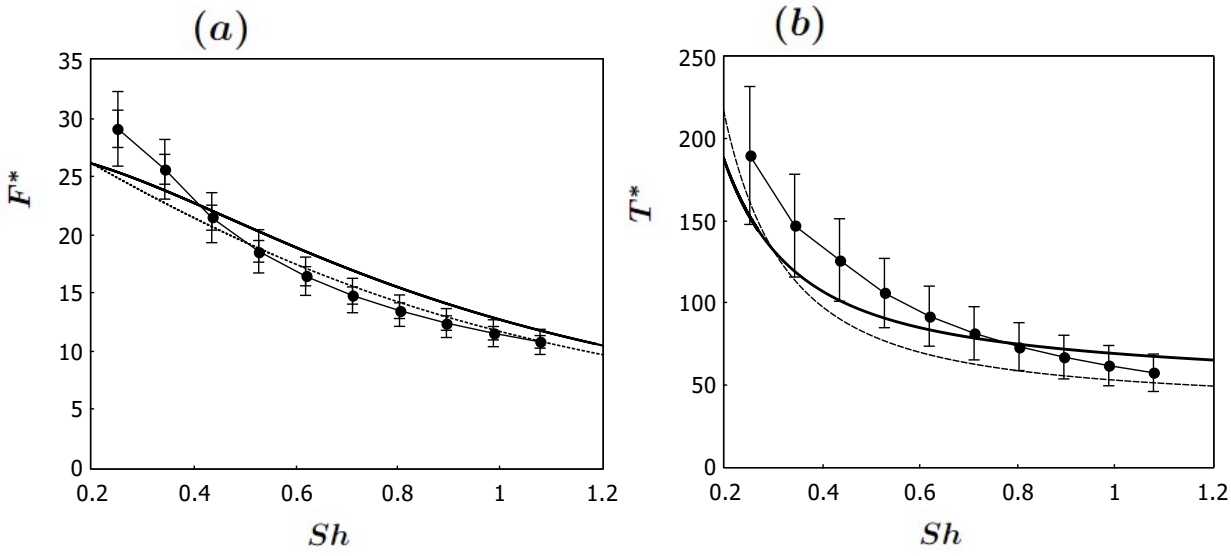

Figure 3.15: Non dimensional propulsive force (a) and non-dimensional torque (b) for a helical swimmer for the case of a Newtonian base fluid ($Re \ll 1$ and $D = 0$). Numerical results from SBT theory are represented by the dotted line whereas the predictions based on the Reguralized Stokeslest method are represented by the solid lines. The experimental data are represented by the black circles and the associated error bars are also shown.

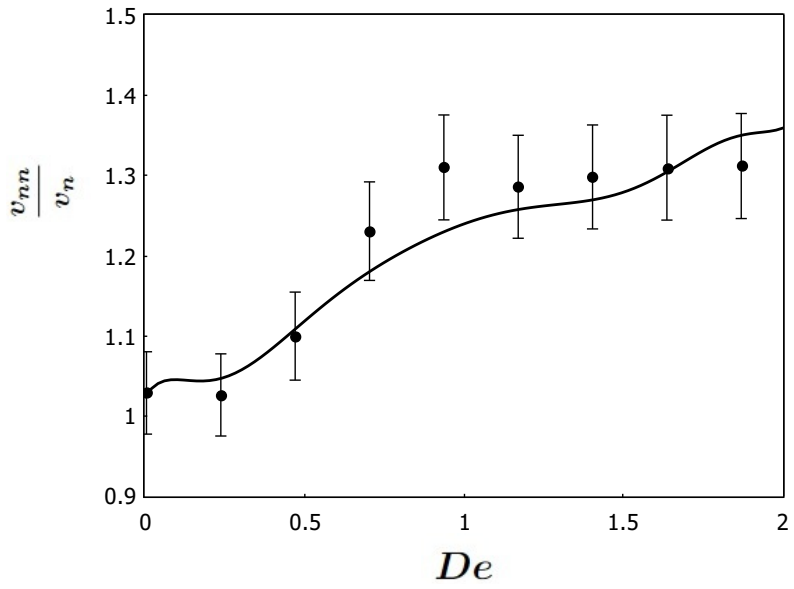

Figure 3.16: The ratio between the swimmer transversal velocity for the case of non-Newtonian fluid (PAMA) v_{NN} and the swimmer transversal velocity for the case of Newtonian fluid (silicon oil) v_N) as a function of the elastic parameter Deborah number. The helix configuration used was the type (1). Numerical results are represented by the solid line and experimental results are indicated with black circles. The experimental error bars are also shown in this plot.

Chapter 4

Study of kinematic simulations of magnetic bacteria in creeping flow

In this chapter, we explore the kinematics of magnetic bacteria with different numbers of particles in the chain. We study chain of particles consisting of set of spheres linked with each other. For this end, we propose a numerical procedure to study the motion of chains of magnetic particles representing a magnetic bacterium. For this end, we use Langevin Dynamics simulations with defined boundary condition in the numerical box of the suspension. The governing equation for low Reynolds number are integrated and the time developing of the suspension can be explored.

4.1 Formulation of the Problem

The configuration under study consists of an individual or a chain of spherical particles as shown in figure (4.1). These chains of particles, which we call magnetic snakes represent a column of a magnetic bacterium. Let's explore the kinematics of representation with different numbers of particles in the chain. This configuration is important because, in addition to the particle-particle interactions in the chain, we have also the interaction of the chain with the particles in the suspension in its neighbor of isolated particles. We note that the suspension generated in the vicinity of the magnetic chain could be mono-dispersed, but the chain itself is composed of poly-dispersed particles because the representation shows that we have the larger head and the tail has a line with particles smaller than the head.

Here we consider a dilute suspension composed of two species of rigid smooth magnetic spheres of radius a_1 and a_2, and respective densities ρ_1 and ρ_2. We associate to each particle and magnetizations $\mathbf{M_1}$ and $\mathbf{M_2}$ suspended in a Newtonian fluid of density ρ and viscosity μ. We assume the inertial effects are neglected, as we have small particle Reynolds numbers so that the creeping flow equations can be applied in the scale of the particle motion. The suspension is submitted to a settling motion so that the uniform gravitational force per unit mass.

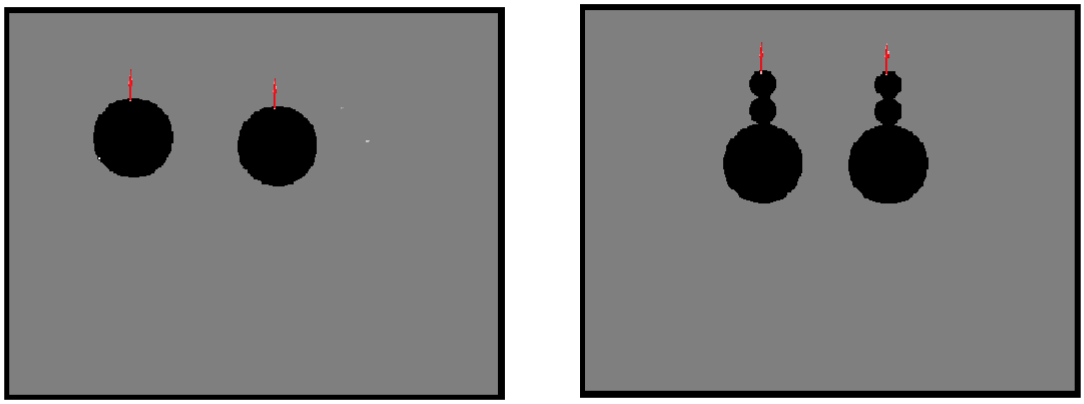

Figure 4.1: Assemblies of magnetic bacterium, here the chain contains 1 particle (Np=1) or 3 particles (Np=3).

4.1.1 Formulation for modelling the movement of one spherical swimmer

We start our study by describing the motion of one swimmer. We determine the movement for one snake under gravitational, viscous forces, and the Brownian movement imposed by molecules of the base liquid. We consider small particles, with diameters 10^{-6} m. We note that the viscous effect due to the viscous forces over the particle dominates inertial effect ones and since the particle itself is small.

The dimensional equation that governs the movement of the particle is given by Newton's second law, expressed by the well-know stochastic Langevin equation, namely:

$$m_s \frac{d\boldsymbol{u}}{dt} = -6\pi\mu a_s \boldsymbol{u} + \boldsymbol{f_b} + m\boldsymbol{g}, \tag{4.1}$$

where m_s denotes the mass of the particle, $\boldsymbol{u}$ is the velocity of the particle, t is the variable time, μ is the fluid's dynamic viscosity, a_s represents a typical radius of the spherical particle, $\boldsymbol{g}$ is the acceleration vector of gravity, $\boldsymbol{f_b}$ is the stochastic Brownian force.

Then lets us write the non-dimensional form of the equation (4.1).

$$St\frac{d\boldsymbol{u}^*}{dt} + \boldsymbol{u}^* = \sqrt{\frac{2}{Pe}}\boldsymbol{f}^* - \hat{\boldsymbol{e}}_3. \tag{4.2}$$

In this case the characteristic scales used are:

$$|\boldsymbol{u}| \sim \boldsymbol{u_s},\ t \sim \frac{a_s}{\boldsymbol{u_s}},\ |\boldsymbol{f_b}| \sim \left(\frac{2D_0\boldsymbol{u_s}}{a_s}\right)^{\frac{1}{2}} 6\pi\mu a_s. \tag{4.3}$$

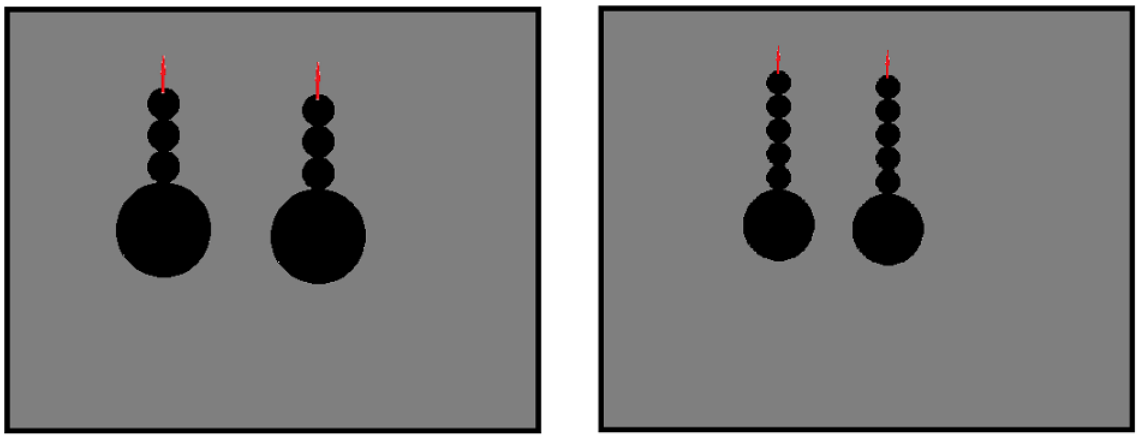

Figure 4.2: Assemblies of magnetic bacterium, here the chain contains 4 particle (Np=4) or 6 particles (Np=6).

where $\boldsymbol{u}_s$ is the Stokes velocity of a isolated particle. Here, St is Stokes number, which represents a ratio between relaxation time of the particle and the convective flow time, and Pe Peclet number, associated with a ratio between a Brownian diffusion time scale and a convective flow time. In addition, D_0 is the Stokes-Einstein Brownian diffusion coefficient given by the expression

$$D_0 = \frac{k_B T}{6\pi\mu a_s}, \tag{4.4}$$

where k_B is the Boltzmann constant, T the temperature. The non-dimensional parameters St and Pe are given respectively by:

$$St = \frac{m_s u_s}{6\pi\mu a_s^2}, \; Pe = \frac{u_s a_s}{D_0} \tag{4.5}$$

We use fourth-order Runge-Kutta method to solving the particle velocity, and the position of the particle is calculated using the Euler method applied to the equation:

$$\frac{d\boldsymbol{x}^*}{dt^*} = \boldsymbol{u}^*. \tag{4.6}$$

Now, it is possible to calculate the following properties of interest, such as autocorrelation of velocity fluctuations, their variance, and the diffusivity.

The expression of the autocorrelation is given by:

$$\tilde{C}(\tilde{\tau}) = \frac{e^{-\tilde{\tau}/St}}{PeSt}\boldsymbol{I}. \tag{4.7}$$

Here, $\boldsymbol{I}$ is the identity second-rank tensor, $\tilde{\tau} = 1/St$ dimensionless correlation time.

The variance of velocity is given by :

$$\langle \boldsymbol{u}^*(t)\boldsymbol{u}^*(t)\rangle = \frac{\boldsymbol{I}}{PeSt} \tag{4.8}$$

For the calculation of the diffusivity tensor, the kinematic definition of velocity is used, and by Einstein's argument for the self-diffusion coefficient according to reference [116], and we have:

$$\langle \boldsymbol{x}^*(t)\boldsymbol{x}^*(t)\rangle = 2\boldsymbol{D}t. \tag{4.9}$$

4.2 Langevin Dynamics applied to magnetic swimmers

In the Langevin Dynamics method applied to magnetic swimmers, the hydrodynamic and the magnetic equations are integrated, and thus, the temporal evolution of the suspension is carried out. In this case, a system of equations coupled stochastic differentials for translation and rotation of each particle are integrated numerically. So the suspension starting from an initial particle configuration, evolves dynamically over time, to a structure determined through this integration numeric. The dimensional equations that govern the movement of each particle of the suspension monodisperse magnetic field with hydrodynamic interactions and other forces are given by:

$$m_i \frac{d\boldsymbol{u}_i}{dt} = \boldsymbol{f}_h^i + \boldsymbol{f}_d^i + \boldsymbol{f}_{e_m}^i + \boldsymbol{f}_b^i + \boldsymbol{f}_r^i + \boldsymbol{f}_c^i + \boldsymbol{f}_g^i. \tag{4.10}$$

In equation (4.10), m_i is the mass of the particle i, $\boldsymbol{u_i}$ is the velocity of the particle i, $\boldsymbol{f}_h^i$ is the hydrodynamic force, $\boldsymbol{f}_d^i$ is the magnetic dipolar force, $\boldsymbol{f}_{e_m}^i$ is the external magnetic force, $\boldsymbol{f}_b^i$ Brownian force, $\boldsymbol{f}_r^i$ is the repulsive force, $\boldsymbol{f}_c^i$ is the contact force, finally $\boldsymbol{f}_g^i$ is the gravitational force.

For the rotational motion of the particles, we consider all the torques acting on the particles. The dimensional equations that govern the movement of each particle of the suspension a monodisperse magnetic field with hydrodynamic interactions and other torques are given by:

$$J_i \frac{d\boldsymbol{\omega}_i}{dt} = \boldsymbol{T}_h^i + \boldsymbol{T}_d^i + \boldsymbol{T}_{e_m}^i + \boldsymbol{T}_b^i. \tag{4.11}$$

In equation (4.11), J_i is the polar moment of inertia of the particles i, $\boldsymbol{\omega_i}$ is the angular velocity of the particle i, $\boldsymbol{T}_h^i$ is the hydrodynamic torque, $\boldsymbol{T}_d^i$ is the magnetic dipolar torque, $\boldsymbol{T}_{e_m}^i$ is the external magnetic torque, $\boldsymbol{T}_b^i$ Brownian torque.

4.2.1 Calculation of the hydrodynamic forces and torques

The hydrodynamic forces and torques can be found by inverting the equation (4.12). Here a_{ij}, b_{ij}, c_{ij} are second-rank tensors which together form the mobility matrix. See [92] for details about these coefficients. In this form, the linear relation is called mobility formulation. Knowledge of the mobility matrix enables the determination of the hydrodynamic forces and torques over the particles via inversion of (4.12), once the linear and angular velocities are known. In this inverted

form, where the forces and torques are the dependent variables, the linear relation is named the resistance formulation. In this form, the equations for force and torque are often written as:

$$\begin{bmatrix} \boldsymbol{u}_1 \\ \vdots \\ \boldsymbol{u}_n \\ \boldsymbol{\omega}_1 \\ \vdots \\ \boldsymbol{\omega}_n \end{bmatrix} = -\frac{1}{\mu} \begin{bmatrix} a_{11} & \cdots & a_{1n} & b_{11} & \cdots & b_{1n} \\ \vdots & \ddots & \vdots & \vdots & \ddots & \vdots \\ a_{n1} & \dots & a_{nn} & b_{n1} & \dots & b_{nn} \\ b_{11} & \dots & b_{1n} & c_{11} & \dots & c_{1n} \\ \vdots & \ddots & \vdots & \vdots & \ddots & \vdots \\ b_{n1} & \dots & b_{nn} & c_{n1} & \dots & c_{nn} \end{bmatrix} \begin{bmatrix} \boldsymbol{f}_1^h \\ \vdots \\ \boldsymbol{f}_n^h \\ \boldsymbol{T}_1^h \\ \vdots \\ \boldsymbol{T}_n^h \end{bmatrix} \tag{4.12}$$

4.2.2 Calculation of Magnetic Forces and Torques

Based on [25] and [117] we can write the expression for the potential of magnetic interaction in the dipolar matter. Magnetic forces and torques acting on a particle, or magnetic dipole, due to particle-field or particle-particle interaction. To calculate the magnetic force, consider a small magnetized body due to the application of an external magnetic field as shown in the figure (4.3).

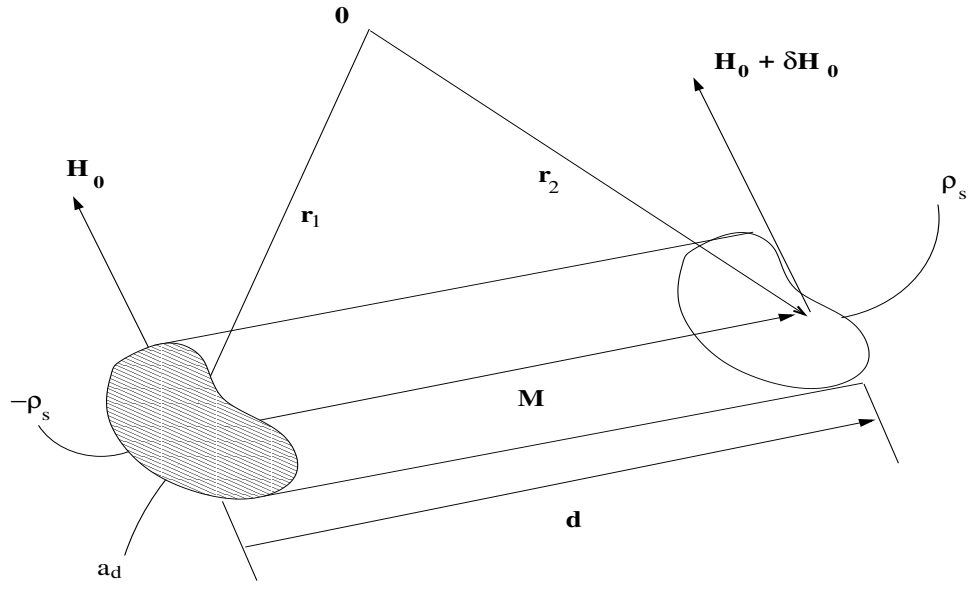

Figure 4.3: Magnetic forces due to the application of a magnetic field to a small element of polarized magnetic substance, [4]

This figure represents a small cylindrical element of a magnetically polarized substance, in which the magnetization vector $\boldsymbol{M}$ is aligned with the geometric axis in the direction $\boldsymbol{d}$. An external magnetic field $\boldsymbol{H}_0$ acts on this material, and poles of densities $\rho_s = \mu_0 M$ appear in the

same quantities and with inverted polarities in the side areas a_d. It is also observed that the particle volume is given by $\delta V = a_d d$. The applied external magnetic field can be interpreted as a magnetic force by magnetic pole, thus, the force acting on the element due to the H field is given acording to reference [4] by:

$$\boldsymbol{f}_m^h = -\boldsymbol{H}_0 \rho_s a_d + (\boldsymbol{H} + \delta \boldsymbol{H}_0)\rho_s a_d = \delta \boldsymbol{H}_0 \rho_s a_d \,, \tag{4.13}$$

where $\delta \boldsymbol{H}_0$ is the variation of $\boldsymbol{H}_0$ along the direction $\boldsymbol{d}$. Using the Taylor series, for a first order approximation in $\delta \boldsymbol{H}_0$, it turns out that

$$\delta \boldsymbol{H}_0 = \boldsymbol{H}_0(\boldsymbol{x} + \boldsymbol{d}) - \boldsymbol{H}_0(\boldsymbol{x}) = (\boldsymbol{d} \cdot \nabla)\boldsymbol{H}_0 \,. \tag{4.14}$$

Since $\boldsymbol{d}$ and $\boldsymbol{M}$ are parallel, you can write $\boldsymbol{d} = d\dfrac{\boldsymbol{M}}{M}$, where d is the magnitude of $\boldsymbol{d}$. Thus the term $\delta \boldsymbol{H}_0$ can be expressed as

$$\delta \boldsymbol{H}_0 = (\boldsymbol{d} \cdot \nabla)\boldsymbol{H}_0 = \frac{d}{M}(\boldsymbol{M} \cdot \nabla)\boldsymbol{H}_0 \,, \tag{4.15}$$

replacing the equation (4.15) in (4.13), we have to

$$\boldsymbol{f}_m^h = \delta \boldsymbol{H}_0 \rho_s a_d = \frac{d}{M}(\boldsymbol{M} \cdot \nabla)\boldsymbol{H}_0(\rho_s a_d) \,. \tag{4.16}$$

Dividing the equation (4.16) by $\delta V = a_d d$ and noting that $\dfrac{\rho_s}{M} = \mu_0$, we have that the force per unit of volume that acts on the element is given by

$$\frac{\boldsymbol{f}_m^h}{\delta V} = \mu_0(\boldsymbol{M} \cdot \nabla)\boldsymbol{H}_0 \,. \tag{4.17}$$

From the figure (4.3), we can also deduce the magnetic torque that acts over the magnetized element. Consider d small, such that the applied magnetic field be spatially uniform, so that $\delta \boldsymbol{H}_0 = 0$. It follows that the torque is given by:

$$\boldsymbol{T}_m^h = \rho_s a_d(-\boldsymbol{r}_1 \times \boldsymbol{H}_0 + \boldsymbol{r}_2 \times \boldsymbol{H}_0) = \rho_s a_d(\boldsymbol{r}_2 - \boldsymbol{r}_1) \times \boldsymbol{H}_0 \,, \tag{4.18}$$

note that from the figure (4.3), we have that $\boldsymbol{r}_2 = \boldsymbol{r}_1 + \boldsymbol{d}$, like this $\boldsymbol{d} = \boldsymbol{r}_1 - \boldsymbol{r}_2$. Substituting this result in (4.18), we have to:

$$\boldsymbol{T}_m^h = \rho_s a_d \boldsymbol{d} \times \boldsymbol{H}_0 \,, \tag{4.19}$$

like $\rho_s a_d \boldsymbol{d} = \mu_0 \boldsymbol{M} \delta V$, we obtain

$$\frac{\boldsymbol{T}_m^h}{\delta V} = \mu_0 \boldsymbol{M} \times \boldsymbol{H}_0 \,, \tag{4.20}$$

or:

$$\boldsymbol{T}_m^h = \mu_0 \boldsymbol{m} \times \boldsymbol{H}_0 \,. \tag{4.21}$$

And therefore, due to the misalignment between the magnetization vector and the magnetic field, the element is in the presence of magnetic torques.

4.2.3 Modelling Brownian Forces and Torques

Two hypotheses characterize the random force $\boldsymbol{f_b}(t)$. First, Brownian forces are considered random in direction and magnitude, so $\boldsymbol{f_b}(t)$ is a random vector with isotropic characteristic, and the second, the non-correlation in the temporal scale of the particle. Thus, according to these hypotheses, the Brownian movement is characterized by a random signal in time known as white noise. These conditions can be expressed mathematically by:

$$\langle \boldsymbol{f_b}(t) \rangle = \mathbf{0}, \qquad \langle \boldsymbol{f_b}(t)\boldsymbol{f_b}(t') \rangle = \boldsymbol{F}\delta(t-t'), \tag{4.22}$$

where $\delta(t-t')$ is Dirac's delta function, $\boldsymbol{F}$ is an associated second-order tensor the intensity of Brownian forces. To determine the autocorrelation of the speed of a particle subject to Brownian motion, an average of achievements in the Langevin equation . In this way, it is obtained that:

$$\langle \boldsymbol{u}(t) \rangle = \frac{e^{-\zeta t}}{m} \int_0^t e^{\zeta \alpha} \langle \boldsymbol{f_b}(\alpha) \rangle \, d\alpha \,, \tag{4.23}$$

in sequence, taking the average of realizations in the $\boldsymbol{u}(t)\boldsymbol{u}(t')$ tensor and applying the white noise condition, equation (4.22), we have to

$$\begin{aligned} \langle \boldsymbol{u}(t)\boldsymbol{u}(t') \rangle &= \frac{e^{-2\zeta t}}{m^2} \int_0^t \int_0^t e^{\zeta(\alpha+\alpha')} \langle \boldsymbol{f_b}(\alpha)\boldsymbol{f_b}(\alpha') \rangle \, d\alpha d\alpha' \\ &= \frac{e^{-2\zeta t}}{m^2} \int_0^t \int_0^t e^{\zeta(\alpha+\alpha')} \boldsymbol{F}\delta(\alpha-\alpha') d\alpha d\alpha' \,. \end{aligned} \tag{4.24}$$

Now consider the following result we have then:

$$\int_0^t e^{\zeta(\alpha-\alpha')} \boldsymbol{F}\delta(\alpha-\alpha') d\alpha = \boldsymbol{F}e^{2\alpha'\zeta}, \tag{4.25}$$

using the equation (4.25) in (4.24) and after calculating the integral, the following expression is obtained for the autocorrelation function of velocities:

$$\boldsymbol{R}(t-t') = \langle \boldsymbol{u}(t)\boldsymbol{u}(t') \rangle = e^{-\zeta(t-t')} \frac{\boldsymbol{F}}{12m\pi\eta a} \,, \tag{4.26}$$

where $t-t'$ is an interval in which $\boldsymbol{f_b}(t)$ suffers many fluctuations, but the enough that $\boldsymbol{u}(t)$ does not vary significantly, which represents the condition of quasi-permanent Stokes regime. Note that autocorrelation has a characteristic of the stationary process because it depends only on $t-t'$.

According to [95], the kinetic energy of particles is divided equally between the three translation modes, so from the principle of energy equipartition, the expression is given by:

$$\frac{m}{2} \langle \boldsymbol{u}(t)\boldsymbol{u}(t') \rangle = \frac{k_B T}{2} \boldsymbol{I} \,, \tag{4.27}$$

where k_B is the Boltzmann constant and T is the absolute temperature of the fluid. Comparing the equations (4.26) and (4.27) for $t-t'=0$, we obtain

$$\boldsymbol{F} = 12\pi\eta a k_B T \boldsymbol{I}. \tag{4.28}$$

The equation (4.28) relates the intensity of the Brownian force to the frictional forces that dissipates the energy of fluctuations. Both stem from the interaction between the particle and the fluid environment but differ substantially in time scales, [116]. You can write that the Brownian force scales with the radius of the particle, while the weight with the radius raised to the cube, explaining why aggregates with more particles are dominated by the differential sedimentation process, while smaller aggregates are subject to Brownian movement, [4]. As observing processes on the time scale a nanosecond is difficult, the main consequence observable in the Brownian movement is the displacement instead of speed. Replacing the equation (4.28) in (4.22) and later taking the trace, the Fluctuation-Dissipation theorem is obtained, given in terms math by:

$$\langle \boldsymbol{f_b}(t) \cdot \boldsymbol{f_b}(t') \rangle = 12\pi\eta a k_B T 3\delta(t-t') = (6\pi\eta a)(6k_B T)\delta(t-t')\,, \tag{4.29}$$

where the term $6\pi\eta a$ is responsible for the energy dissipation of the system, whereas the term $6k_BT$ is associated with the thermal agitation of the fluid, inducing speed fluctuations in the evaluated particle. Through the equation (4.29), one can infer a typical magnitude (module) for the random force vector $\boldsymbol{f_b}(t)$ in its dimensional form. note that

$$|\boldsymbol{f_b}| = \sqrt{\langle \boldsymbol{f_b}(t) \cdot \boldsymbol{f_b}(t') \rangle} = \sqrt{\frac{(6k_BT)(6\pi\eta a)}{\delta\tau}} = 6\pi\eta a \left(\frac{6\mathcal{D}}{\delta\tau}\right)^{1/2}, \tag{4.30}$$

here we have $\delta\tau = 1/\delta(t-t')$ is a time associated with the impulse of the Brownian movement and

$$\mathcal{D} = \frac{k_B T}{6\pi\eta a}\,, \tag{4.31}$$

is the Stokes-Einstein Brownian diffusion coefficient. In this way, the Brownian force is given by:

$$\boldsymbol{f_b}(t) = 6\pi\eta a \left(\frac{6\mathcal{D}}{\delta\tau}\right)^{1/2} \boldsymbol{\xi}\,, \tag{4.32}$$

where $\boldsymbol{\xi}$ is the random vector that has a uniform distribution $[-1, 1]$. Brownian torque is given by:

$$\boldsymbol{T_b} = 8\pi\eta a^3 \left(\frac{6\mathcal{D}_r}{\delta\tau}\right)^{1/2} \boldsymbol{\xi}\,, \tag{4.33}$$

where $\mathcal{D}_r$ is the Stokes-Einstein Brownian Diffusion Rotational Coefficient expressed as:

$$\mathcal{D}_r = \frac{k_B T}{8\pi\eta a^3}\,. \tag{4.34}$$

4.2.4 Repulsive and Contact Forces

We account for mechanisms which prevent the overlap of particles throughout the simulation. Instead of considering the detailed lubrication forces arising from hydrodynamic interactions at a

short-range, which are computationally costly, we only consider short-range repulsion due to surfactants or contact. Nevertheless, the effect produced is qualitatively the same, the superposition of particles is avoided. The surfactant layer repulsion force between two particles is given by [25].

$$\boldsymbol{F}_{\boldsymbol{ij}}^{\boldsymbol{r}} = \begin{cases} -\dfrac{\pi N_{sup} K_B T (a_i + a_j - 2\delta_s)^2}{2\delta_s} \ln\left(\dfrac{a_i + a_j}{r_{ij}}\right) \hat{\boldsymbol{r}}_{\boldsymbol{ij}}, & -2\delta_s < \varepsilon_{ij} < 0, \\ 0, \qquad \text{otherwise.} \end{cases} \tag{4.35}$$

Here we have N_{sup} is the surface density of surfactants, δ_s is the thickness of the surfactants layer, finally the gap between particles is defined $\epsilon_{ij} = r_{ij} - a_i - a_j$ Now describing the Hertz force due to contact of two overlapping spheres we have:

$$\boldsymbol{F}_{\boldsymbol{ij}}^{\boldsymbol{c}} = \begin{cases} -\kappa \left[\left(\dfrac{1}{a_i - \delta_s} + \dfrac{1}{a_j - \delta_s} \right)^{-1} \delta_{ij}^3 \right]^{\frac{1}{2}} \hat{\boldsymbol{r}}_{\boldsymbol{ij}}, & \delta_{ij} > 0, \\ 0, \quad \text{otherwise.} \end{cases} \tag{4.36}$$

Here κ is a constant related to material properties of the particles and $\delta_{ij} = \varepsilon_{ij} - 2\delta_s$ is the virtual overlap of the magnetic cores. The total repulsion and contact forces are given by sums of equation (4.35) and (4.36) over all the particles.

4.2.5 Dimensionless Form of The Equations

After presenting the equations of the forces and torques, we need to write in dimensionless form each equation to reduce the number of parameters to improve the performance of the numerical code and to identify the dimensionless groups effectively relevant to the simulation of the system, to research the influence of such on the variables under study. The dimensionless equations for the swimmers become:

$$St \frac{d\boldsymbol{u}_{\boldsymbol{i}}^*}{dt} a_i^{*3} = \boldsymbol{f}^{*i}_h + \boldsymbol{f}^{*i}_d + \boldsymbol{f}^{*i}_{e_m} + \boldsymbol{f}^{*i}_b + \boldsymbol{f}^{*i}_r + \boldsymbol{f}^{*i}_c + \boldsymbol{f}^{*i}_g, \tag{4.37}$$

and

$$St \frac{3}{10} \frac{d\boldsymbol{\omega}_{\boldsymbol{i}}^*}{dt} a_i^{*5} = \boldsymbol{T}_{\boldsymbol{h}}^{*i} + \boldsymbol{T}_{\boldsymbol{d}}^{*i} + \boldsymbol{T}_{\boldsymbol{e_m}}^{*\boldsymbol{i}} + \boldsymbol{T}_{\boldsymbol{b}}^{*i}. \tag{4.38}$$

The characteristic scales adopted are:
$r_{ij} \sim \langle a \rangle$, $u_i \sim \langle u_s \rangle$, $t \sim \dfrac{\langle a \rangle}{u_s}$, $\omega_i = \dfrac{u_s}{\langle a \rangle}$, $F^i = 6\pi\mu\langle a \rangle u_s$, $T^i = 8\pi\mu\langle a \rangle^2 u_s$ and $H \sim H_0$.

Here we have:

$$u_s = \frac{2\Delta\rho g \langle a \rangle^2 g}{9\mu}, \tag{4.39}$$

is the Stokes velocity of a particle with radius $\langle a \rangle$ and H_0 is the suitable scale of the external magnetic field: the intensity of a constant field or $\dfrac{M}{4\pi}$.

4.2.5.1 Dimensionless hydrodynamic force and torque model

We define a procedure to obtain the coefficients of the dimensionless form for hydrodynamic force and torque. We propose the following non-dimensional mobility matrices:

$$\begin{bmatrix} \boldsymbol{u}_1^* \\ \vdots \\ \boldsymbol{u}_n^* \\ \boldsymbol{\omega}_1^* \\ \vdots \\ \boldsymbol{\omega}_n^* \end{bmatrix} = - \begin{bmatrix} a_{11}^* & \cdots & a_{1n}^* & b_{11}^* & \cdots & b_{1n}^* \\ \vdots & \ddots & \vdots & \vdots & \ddots & \vdots \\ a_{n1}^* & \cdots & a_{nn}^* & b_{n1}^* & \cdots & b_{nn}^* \\ b_{11}^* & \cdots & b_{1n}^* & c_{11}^* & \cdots & c_{1n}^* \\ \vdots & \ddots & \vdots & \vdots & \ddots & \vdots \\ b_{n1}^* & \cdots & b_{nn}^* & c_{n1}^* & \cdots & c_{nn}^* \end{bmatrix} \begin{bmatrix} \boldsymbol{f_1^{*h}} \\ \vdots \\ \boldsymbol{f_n^{*h}} \\ \boldsymbol{T_1^{*h}} \\ \vdots \\ \boldsymbol{T_n^{*h}}. \end{bmatrix} \tag{4.40}$$

In the new model the coefficients are defined by:

$$a_{ii}^* = \frac{\boldsymbol{I}}{a_i^*},\ a_{ij}^* = \frac{3}{4r_{ji}^*}\left[\boldsymbol{I} + \hat{\boldsymbol{r}}_{ji}\hat{\boldsymbol{r}}_{ji} + \frac{a_i^{*2} + a_j^{*2}}{3r_{ji}^{*2}}\left(\boldsymbol{I} - 3\hat{\boldsymbol{r}}_{ji}\hat{\boldsymbol{r}}_{ji}\right)\right],\ j \neq i \tag{4.41}$$

$$b_{ii}^* = 0,\ b_{ij}^* = -\frac{3\varepsilon \cdot \hat{\boldsymbol{r}}_{ji}}{4r_{ji}^{*2}},\ j \neq i, \tag{4.42}$$

and

$$c_{ii}^* = \frac{\boldsymbol{I}}{a_i^{*3}},\ c_{ij}^* = \frac{1}{2r_{ji}^{*3}}\left(\boldsymbol{I} - 3\hat{\boldsymbol{r}}_{ji}\hat{\boldsymbol{r}}_{ji}\right),\ j \neq i. \tag{4.43}$$

4.2.5.2 Dimensionless magnetic dipolar force and torque model

Now, let's introduce the dimensionless form for the magnetic dipolar force and torque model. Then, the new expression is:

$$\boldsymbol{f_i^{*d}} = \lambda \sum_{j=1,\ j\neq i}^{N} \frac{\left(a_i^* - \delta_s^*\right)^3 \left(a_j^* - \delta_s^*\right)^3}{r_{ij}^{*4}} [(\hat{\boldsymbol{m_i}} \cdot \hat{\boldsymbol{m_j}})\hat{\boldsymbol{r}}_{\boldsymbol{ji}} + (\hat{\boldsymbol{m_i}} \cdot \hat{\boldsymbol{r}}_{\boldsymbol{ji}})\hat{\boldsymbol{m_j}} + (\hat{\boldsymbol{m_j}} \cdot \hat{\boldsymbol{r}}_{\boldsymbol{ji}})\hat{\boldsymbol{m_i}} - 5(\hat{\boldsymbol{m_i}} \cdot \hat{\boldsymbol{r}}_{\boldsymbol{ji}})(\hat{\boldsymbol{m_j}} \cdot \hat{\boldsymbol{r}}_{\boldsymbol{ji}})\hat{\boldsymbol{r}}_{\boldsymbol{ji}}] \tag{4.44}$$

and

$$\boldsymbol{T_i^{*d}} = \frac{3\lambda}{4} \sum_{j=1,\ j\neq i}^{N} \frac{\left(a_i^* - \delta_s^*\right)^3 \left(a_j^* - \delta_s^*\right)^3}{r_{ij}^{*3}} [(\hat{\boldsymbol{m_j}} \cdot \hat{\boldsymbol{r}}_{\boldsymbol{ji}})\hat{\boldsymbol{m_i}} \times \hat{\boldsymbol{r}}_{\boldsymbol{ji}} - \frac{1}{3}(\hat{\boldsymbol{m_i}} \times \hat{\boldsymbol{m_j}}] \tag{4.45}$$

In the this equations we define $\delta_s^* = \dfrac{\delta}{\langle a \rangle}$. For the external magnetic in the non-dimensional form field, the following form relations are obtained for force and torque are:

$$\boldsymbol{f_i^{*m}} = \alpha a_i^{*3} \hat{\boldsymbol{m}}_{\boldsymbol{i}} \cdot \nabla^* \boldsymbol{H}^*, \ \boldsymbol{T_i^{*m}} = \frac{3}{4} \alpha a_i^{*3} \hat{\boldsymbol{m}}_{\boldsymbol{i}} \cdot \times \boldsymbol{H}^*. \tag{4.46}$$

4.2.5.3 Dimensionless Brownian force and torque model

Expressions in the Brownian force and torque equations can be combined to dimensionless form. We have:

$$\boldsymbol{F_i^{*b}} = \left(\frac{2a_i^*}{Pe \Delta t^*} \right)^{\frac{1}{2}} \boldsymbol{n}^F, \ \boldsymbol{T_i^{*b}} = \left(\frac{3a_i^*}{2Pe \Delta t^*} \right)^{\frac{1}{2}} \boldsymbol{n}^T, \tag{4.47}$$

where: $\langle \boldsymbol{n^F} \rangle = \langle \boldsymbol{n^T} \rangle = 0$ also $\langle \boldsymbol{n^F(t^*) n^F(t^*)} \rangle = \langle \boldsymbol{n^T(t^*) n^T(t^*)} \rangle = \boldsymbol{I}$.

4.2.5.4 Dimensionless Repulsive, Contact and Gravitational force model

We propose a new expression changing the formula in the expressions for repulsive, contact, and gravitational force to the dimensionless form. The expressions became respectively:

$$\boldsymbol{F_{ij}^{*r}} = \begin{cases} -\dfrac{\pi N_{sup}^* K_B T (a_i^* + a_j^* - 2\delta_s^*)^2}{2\delta_s^* Pe} \ln\left(\dfrac{a_i^* + a_j^*}{r_{ij}^*}\right) \hat{\boldsymbol{r}}_{\boldsymbol{ij}}, & -2\delta_s < \varepsilon_{ij} < 0, \\ 0, \qquad \text{otherwise.} \end{cases} \tag{4.48}$$

$$\boldsymbol{F_{ij}^{*c}} = \begin{cases} -\kappa^* \left[\left(\dfrac{1}{a_i^* - \delta_s^*} + \dfrac{1}{a_j^* - \delta_s^*} \right)^{-1} \delta_{ij}^{*3} \right]^{\frac{1}{2}} \hat{\boldsymbol{r}}_{\boldsymbol{ij}}, & \delta_{ij} > 0, \\ 0, \quad \text{otherwise.} \end{cases} \tag{4.49}$$

and

$$\boldsymbol{F_i^{*g}} = -a_i^{*3} \hat{\boldsymbol{e}}_3 \tag{4.50}$$

Finally we get:

$$\boldsymbol{F_i^{*r}} = \sum_{\substack{i=j \\ i \neq j}}^{N} \boldsymbol{F_{ij}^{*r}}, \tag{4.51}$$

and

$$\boldsymbol{F_i^{*c}} = \sum_{\substack{i=j \\ i \neq j}}^{N} \boldsymbol{F_{ij}^{*c}}. \tag{4.52}$$

Choosing: $N_{sup}^* = N_{sup} \langle a \rangle^2$, $\kappa^* = \langle a \rangle \dfrac{\kappa}{6\pi\mu u_s}$ and $\delta_{ij}^* = \dfrac{\delta_{ij}}{\langle a \rangle}$

4.3 Computational Procedure

4.3.1 Non-dimensional physical parameters parameters used in modelling

After writing the equations in in a non-dimensional form, note that there are some parameters that appear in dimensionless form. Non-dimensional physical parameters numbers are fundamental importance in the parametric analysis of our problem. This section refers to the definition of these parameters.

The Stokes number and the Péclet number are the physical parameters of the problem. In our model we denote by: St, the Stokes number, which represents a relationship between time scales of the paticle relaxation time and the convective time of the flow, and Pe. Peclet number, associated with a relationship between a Brownian diffusion time scale and a convective flow time. The non-dimensional physical parameters St and Pe are given by:

$$St = \frac{mu_s}{6\pi\mu\langle a\rangle^2} \qquad and \qquad Pe = \frac{D_0}{\langle a\rangle u_s}, \tag{4.53}$$

the mass of the particles is given by $m = \frac{4}{3}\pi\langle a\rangle^3\rho_s$ and the Stokes-Einstein ordinary Brownian diffusivity is given by:

$$D_0 = \frac{\kappa_B T}{6\pi\mu\langle a\rangle} \tag{4.54}$$

Additionally, we define two magnetic non-dimensional parameters representing, respectively, the non-dimensional strength of the applied magnetic field and the intensity of the dipolar interactions.

$$\alpha = \frac{\mu_0 m_0 H_0}{6\pi\mu\langle a\rangle^2 u_s},\ \lambda = \frac{\mu_0 m_0^2}{8\pi^2\mu\langle a\rangle^5 u_s}, \tag{4.55}$$

where, m_o is the intensity of the magnetic dipole and μ_0 is the magnetic permeability of the free space ($\mu_0 = 4\pi \times 10^{-7} H/m$).

4.3.2 Generation of Initial and Contour condition

This section is dedicated to the description of methodology used to generate the suspensions under study, we also describe a part of the numeric code. The code, originally developed by [84]. The FORTRAN code simulates the prototype of magnetic active matter. Then an initial condition where the particles are lined up in chains and submit them to the action of the magnetic field. Here the chain of particles which moves with velocity of constant modulus and periodically changing sign. Using the Langevin dynamics, we simulate the motion of suspensions of chain of magnetic particles and non-magnetic particles in sedimentation.

We also consider a parallelepiped domain with dimensions $L_x = 25a \times L_y = 25a \times L_z = 75a$. The spheres impenetrability imposes that the center of a ray test particle cannot occupy the

exclusion volume. We generate the initial positions at random inside the parallelepiped (box). We emphasize that the generation has a uniform probability distribution eliminating the volume that had already been filled by the particles. For simulation of isolated particles, the initial orientations are uniformly distributed over a sphere of unit radius and their initial angular velocities are zero. For the simulation of particle aggregates we consider chains of particles, which we call magnetic-snakes that represent a column of a magnetic bacterium. We report that the time used to integrate the equation of particles: fourth-order Runge Kutta with the time step is carefully chosen. The non-dimensional time step is given by:

$$\Delta t^* = \frac{1}{100} min\left(Pe, St, \varepsilon^*\right) \tag{4.56}$$

chosen small enough, technique used in order to enable the implementation of this condition in the code. In this case we choose $\varepsilon^* = max(min(\varepsilon_{ij}), 10^{-4})$. Finally we define the volumetric fraction ϕ as:

$$\phi = \frac{4\pi\langle a\rangle^3 N}{3L_x L_y L_z}, \tag{4.57}$$

here, L_x, L_y , L_z are the lengths of the box. It should be important to note that in terms of time scales of the particile motion, the Péclet number is the ratio between the characteristic Brownian diffusion time $\tau_b = a^2/D$ and the characteristic sedimentation time, $\tau_s = a_s/U$. Also we have, the ratio between the inertial relaxation time or particle response $\tau_r = m/6\pi\mu a_s$ and the characteristic time sedimentation τ_s as being the Stokes number $St = mU/6\pi\mu a_s^2$, which will be the parameter for controlling the inertia of the particle, and finally we use $t/\tau_s = \tau^*$ in all results presented in this work. Finally, we have considered a boundary condition of periodicity in all directions, such that the particles whose centers exit the box through one side are brought back inside through the opposite one. If this translation would result in an overlap of particles, Brownian displacements are applied to the center of the translated particle until no overlap occurs. Ensemble averages of all properties are calculated as averages first in the particles comprised in the box, then in the realizations. In our simulation the inertia of the particles is considered, such that the resistance formulation is adopted. in this case, conditions must be generated position and initials velocities (initial velocities zero) and for the positions, we want to study the effect of linear stratification in the vertical direction on the volumetric fraction.

4.4 Preliminary Results and Discussions

4.4.1 Motion of Isolated Chain

The results of the trajectory of an isolated chain of particle are summarized in figure (4.4), as a function of time. Here we consider the longitudinal motion of the particles (parallel to gravity). Then we have $X_{\parallel} = X^*$, $V_{\parallel} = V^*$ and $\tau^* = t/\tau_s$. In this work, chains of different number of particles are simulated. We consider chains of 3 particles, 6 particles and long chains for more than 6 particles, respectively. Results were obtained for both $Pe = 0.5$ and $Pe = 10$ and $St = 0.2$.

We observe that as the number of particles decreases, the approximation of displacement and curves becomes more flattened. In the theories we know that the purely Brownian motion, where

$Pe = 0$, where the linearity of this variable with time can be accurately observed. Here, with $Pe = 0.5$ we can see still a nearly linear dependence as $X*$ scaling with $t^1/2$. It can be observed that as $Pe = 10$ increases, the net gravity effect (i.e. particle sedimentation) starts to play a more important role in the chain displacement, introducing dependence like t^2 of the chain displacement on time t.

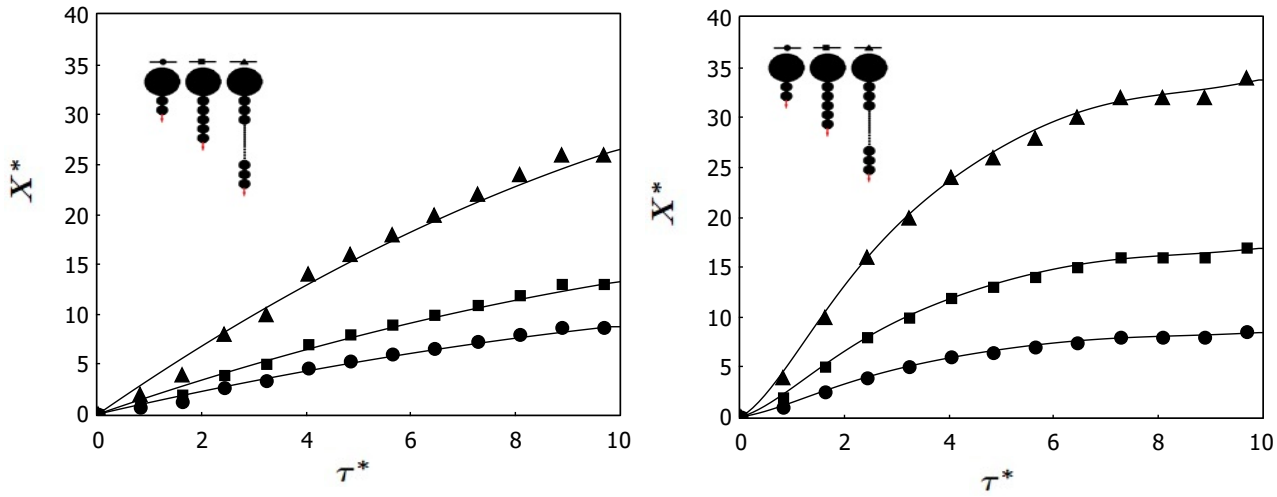

Figure 4.4: Non-dimensional displacement for three magnetic chain. Black circles are for chain of 3 particles, black rectangles are for chain of six particles, black triangle are for chain of more than six particles (Long chain). Results were obtained for $St = 0.2$ a) $Pe = 0.5$ and b) $Pe = 10$

.

Figure (4.5), depicts the normalized velocity for the three chains, moving with two different Péclet numbers, for different numbers of particles in the chains, again, we use chains of 3 particles, 6 particles and long chains of more than 6 particles respectively. Similar is the velocity profiles for the three chains, however, it must be noted that the bigger the chain achieves higher velocities despite. We also observed that as the number of particles decreases, the approximation of the velocity and curves becomes more compressed.

In figure (4.6) we show the variance of the displacements of an isolated chain free of inertia in the directions parallel and perpendicular to gravity for the three configurations simulated in figures (4.4) and (4.5). The results were obtained for $Pe = 0.01$ and $Pe = 10$. According to the figure we obtain results that are compatible with those predicted by the Brownian motion theory in the case as Pe is close to zero. Another analysis, if we increase the number of Peclet (Pe), the particle involves more its sedimentation consequently in its mean quadratic displacement deterministic effect. However, we see an average quadratic displacement parallel to gravity tending to be a curve of the parabola when Pe increases, this is of a uniform rectilinear movement. Other results that have been computed are the average velocities of a particle as a function of time. According to the figure (4.7) the velocities in the parallel direction it tends to Stokes' velocity when time increases, for all Pe low numbers of Péclet. A greater dispersion of results is observed for low numbers of Péclet (Pe).

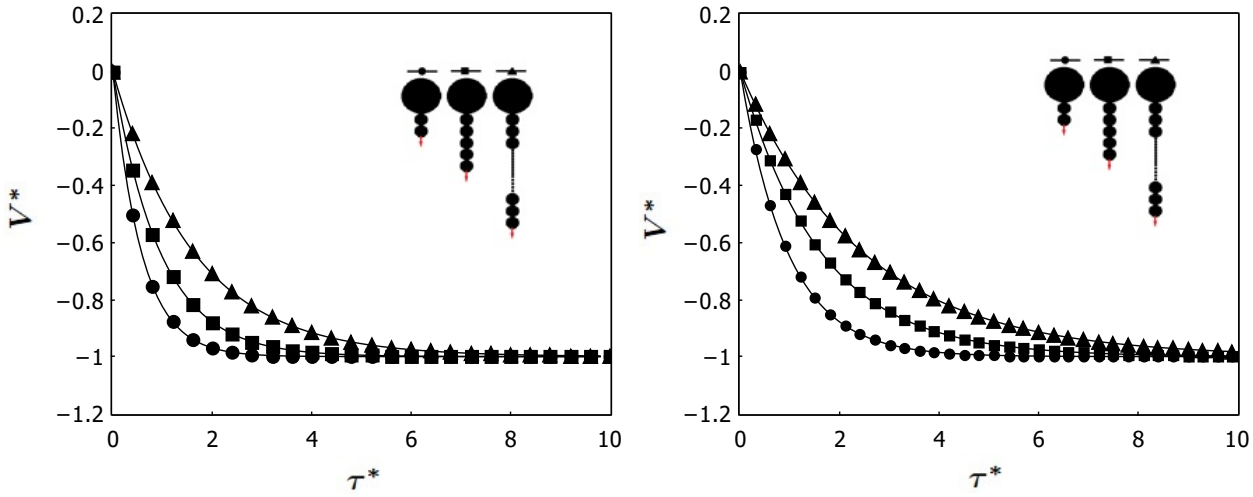

Figure 4.5: Non-dimensional velocity as a Non-dimensional time of the for chain for three magnetic chain. Black circles are for chain of 3 particles, black rectangles are for chain of six particles, black triangle are for chain of more than six particles (Long chain). . Results were obtained for $St = 0.2$ a) $Pe = 0.5$ and b) $Pe = 10$

4.5 Collective effect of Chains

Now we study the pairwise motion of magnetic spherical swimmer in a dilute sedimenting suspension. This analysis is fundamental and important to understand the physics of diluted magnetic colloidal suspensions, in which the magnetic interactions between pairs of particles dominate. The model problem, see figure (4.8), involves two identical magnetic chain of particles suspended in a Newtonian fluid with negligible wall boundary effects. The initial distance between the two particles is not fixed. The resulting particle-center trajectory is dependent on the initials positions. In all simulations and results we consider: $X_{\parallel}$ related to the motion in x direction, $X_{\perp}$ related to the motion in y direction. We define also, for the first particle , $X_1 = \sqrt{{X_1}_{\parallel}{}^2 + {X_1}_{\perp}{}^2}$ and for the second particle, $X_2 = \sqrt{{X_2}_{\parallel}{}^2 + {X_2}_{\perp}{}^2}$ and finally, $X^* = X_2 - X_1$. The same consideration is done for the velocity and we get: $V_{\parallel}$ related to the motion in x direction, $V_{\perp}$ related to the motion in y direction. We define also, for the first particle , $V_1 = \sqrt{{V_1}_{\parallel}{}^2 + {V_1}_{\perp}{}^2}$ and for the second particle, $V_2 = \sqrt{{V_2}_{\parallel}{}^2 + {V_2}_{\perp}{}^2}$ and finally, $V^* = V_2 - V_1$.

4.5.1 Non Magnetic Suspension

In this section we study the relative locomotion of two magnetic chain interacting in a dilute suspension. The simulations are based on the direct computations relative motion between each particles in the chain under the regime of non-zero Stokes number. First we consider non-magnetic

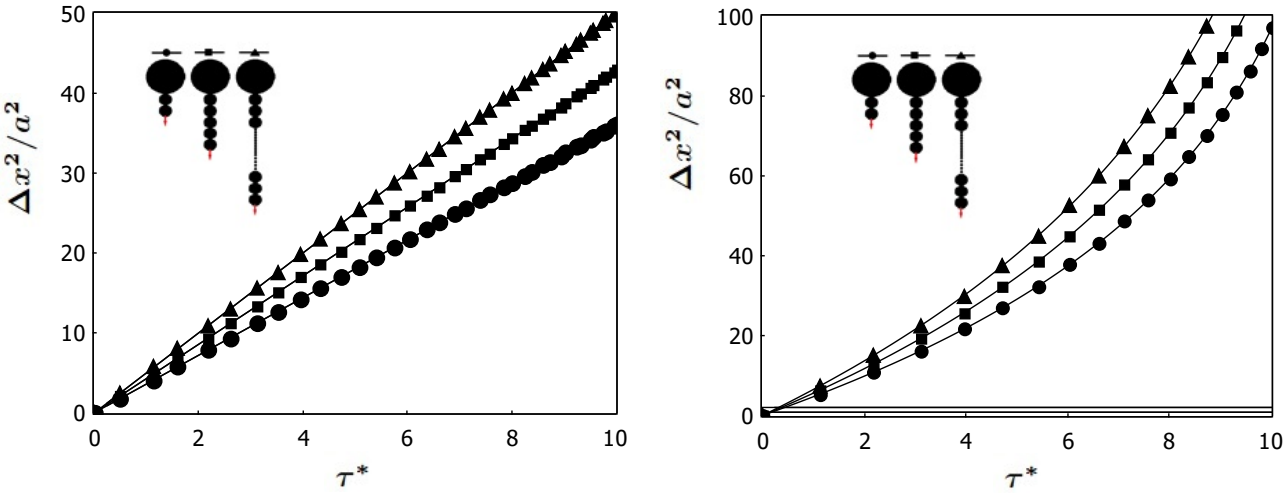

Figure 4.6: Quadratic displacement as a function of time. Results were obtained for $St = 0.2$, $Pe = 0.01$ and $Pe = 10$. Black circles are for chain of one particle, Black rectangles are for chain of three particles. Black triangle are for chain of six particles

suspensions and in this part of the work we perform a simulation of the kinematics of dilute suspensions composed of chains of spherical particles. The particles are immersed in a Newtonian fluid under gravity flowing in low Reynolds numbers, considering the particle scale.

In this part of the work, we will look at how the parameters Pe and the number of particles in the chain N influence the movement. We considered Brownian regime and we consider moderate Péclet number $Pe = 0.5$ and $Pe = 20$. The kinematics of the particles is investigated providing the relative trajectory and the variance of velocity. On the proposed particle chain model, one must take into account that the motion of a particle is dependent on the motion of other particles.

Typical relative trajectory are plotted in figure (4.9), numerical simulation was performed with $St = 0.5$, $Pe = 0.5$, and $Pe = 20$. At this point we also consider chain of 3 particles, chain of six particles, long chain where we have more than six particles. In this results, particle fluctuations are induced only by particle interactions at high Pe and by Brownian motion at low Pe. The near field forces can produce different transitions in the particle distribution, as shown by the relative trajectories, as well as they define the effect of Péclet number in the suspension. The sedimentation trajectory in this case show one peak of the relative trajectories is observed over time, outlining the time evolution of the most probable distances of particles and also the number of particles of the chain in the suspension.

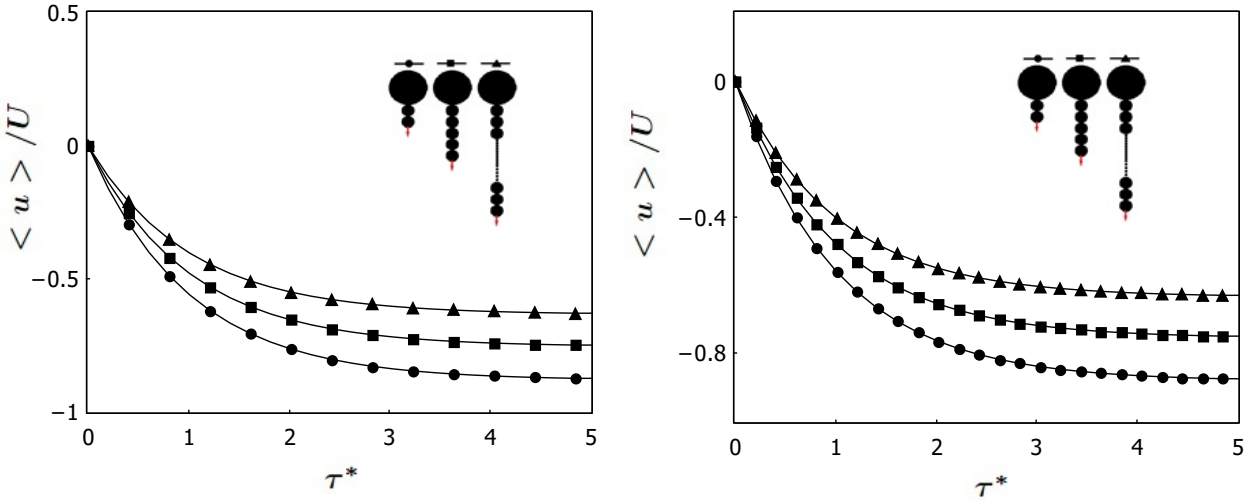

Figure 4.7: Average velocity as a function of time. Results were obtained for $St = 0.2$, $Pe = 0.01$ and $Pe = 10$. Black circles are for chain of one particle, Black rectangles are for chain of three particles. Black triangle are for chain of six particles

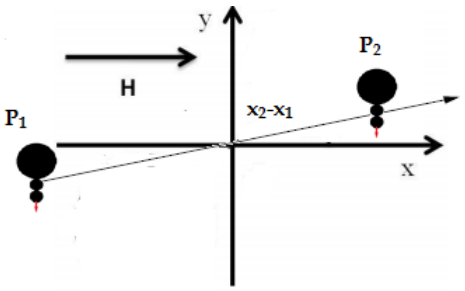

Figure 4.8: Configuration used for the particles, the model involves two identical magnetic chain.

Figure (4.10) denotes simulations of the normalized velocity fluctuation variances of three different chains of particles sedimenting under the effect of the gravitational field in the fluid domain. The figures are plotted for the following condition and dimensionless parameters: $St = 0.5$, $Pe = 0.5$, and $Pe = 20$. we also consider chain of 3 particles, chain of six particles, long chain where we have more than six particles. The variance of velocity fluctuations is observed growing with with time. As it is expected , in the initial moment the particles have few fluctuations of velocity and increase progressively over time. It is seen the velocity fluctuations are due to the Brownian motion at low Pe and by hydordynamic interaction and dipolar interaction at large Pe. Also, short range interaction and particle contact can produce some fluctuations in trajectory and consequently in velocity. Furthermore, if we increase the number of particles in the chain the fluctuations grow up too. On the other hand the velocity fluctuations has the influence of Brownian particles if we do not take into account the hydrodynamic interactions among the particles.

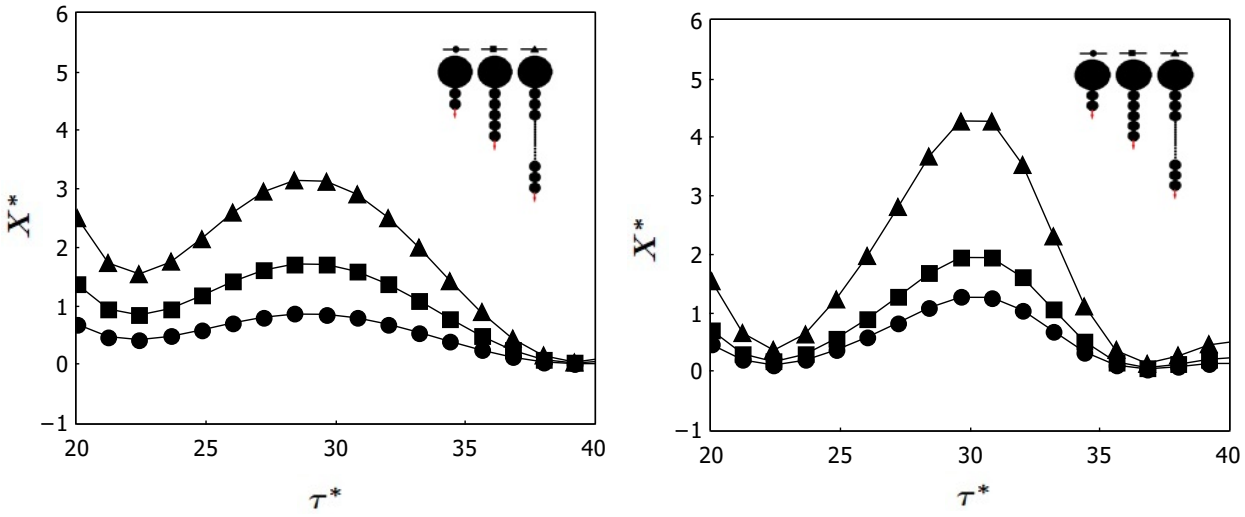

Figure 4.9: Relative trajectories of three chains of particles for non magnetic suspensions. Black circles are for chain of 3 particles, black rectangles are for chain of six particles, black triangles are for chain of more than six particles (Long chain). Results were obtained for $St = 0.5$ a) $Pe = 0.5$ and b) $Pe = 20$.

4.5.2 Influence of Magnetic Dipole

In this section, we present simulation results exploring the influence of the dipolar interactions between the chains. In this case we have $\lambda \neq 0$ and we consider here set up the magnetic to field $\alpha = 20$.

We propose using simulations to show how dipolar interactions influence the properties magnetic field influence the motion of the magnetic chain. We look at the time evolution of the suspension. We analyzed how the effect of dipolar interactions with a fixed magnetic field ($\alpha = 20$) influences the results. We also have performed simulations for larger interaction parameter with $\lambda = 30$ and $\lambda = 90$. The Stokes number in the all simulation is fixed as being 0.5.

We start describing results of the relative trajectories of three chains of particles in presence of the magnetic dipole, but with a fixed external magnetic field.

Figure (4.11) shows the relative trajectories in presence of the magnetic dipole but without external magnetic field. We remember that the particles are initially placed in a random way, during our simulation that evaluates the effect of the dipolar interactions to examine the trajectories. It is seen that the plots (a) and (b) shown in figure (4.11) are nearly the same of the results in figure (4.9) for $\lambda = 20$. However for large $\lambda = 90$) we can see larger fluctuation in the chains trajectories induced by the effect of the magnetic dipolar interactions.

The magnetic responses from moderate dipolar interactions similar and close to non-magnetic suspension. In the case with strong dipolar interactions, the results show greater amplitudes due to the stronger value of λ.

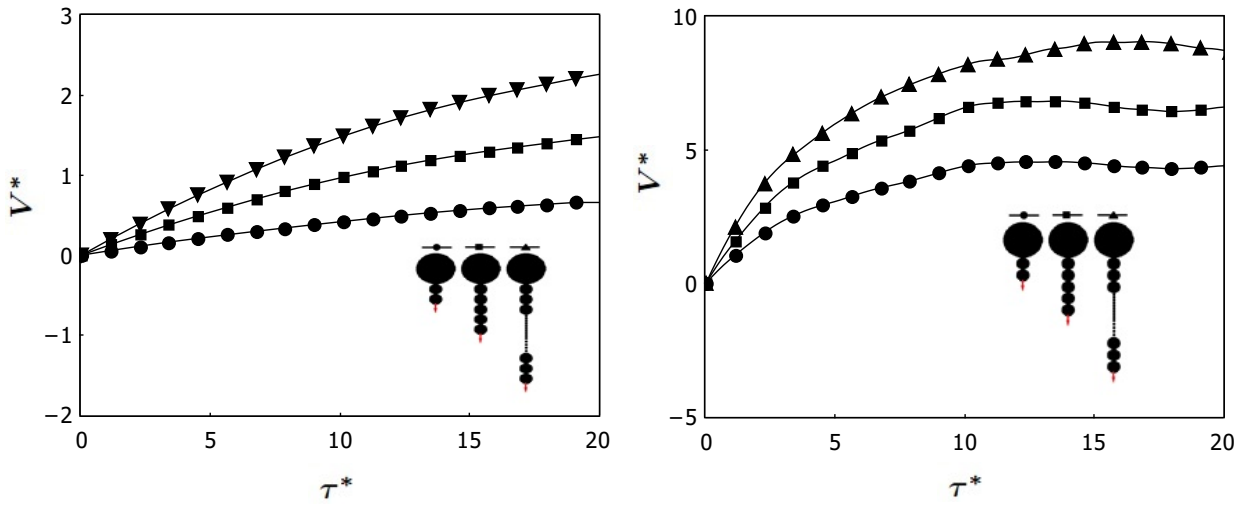

Figure 4.10: Non-dimensional velocity of three chains for non magnetic suspensions. Black circles are for chain of 3 particles, black rectangles are for chain of six particles, black triangles are for chain of more than six particles (Long chain). Results were obtained for $St = 0.5$ a) $Pe = 0.5$ and b) $Pe = 10$.

Addionally, we can observe that the trajectories have two peaks shifted to lower wavelengths, different to a greater separation of particles along during the motion. We argue that this type of orientation to the degree of dipolar interactions. We could attribute this type of orientation to the dipole interactions, since the particles with dipole moments aligned with the field present attractive interactions when their distance vectors are in the straight line to the field and repulsive interactions when these vectors are perpendicular to the field.

Now we analyze in detail the normalized velocity and we explain how the dipole interactions influence the relative velocity of the magnetic chain. We study the effect of dipolar interactions with a fixed magnetic field ($\alpha = 20$ influences the results. We consider moderate dipolar interactions $\lambda = 30$ and strong dipolar interactions $\lambda = 90$. We plot in figure (4.12) the non-dimensional velocity for the three different chains of particles. Here, black circles are for chain of 3 particles , black rectangles are for chain of six particles, black triangle are for chain of more than six particles (long chain). Results were shown for a) $\lambda = 20$ and b) $\lambda = 90$.

The value of the dipolar interaction leads to a difference in the velocity values for the depending on the strength λ of the dipolar interactions values, that can be seen in the figure (4.12). For $\lambda = 20$, the velocity increases and is almost always linear. For $\lambda = 90$, the velocity also increase but the curve is more parabolic and it is nearly monotonic and almost linear. However for $\lambda = 90$, the behavior of the chains velocities are not monotonic anymore and consequently perceptible velocity fluctuations can be observed as the chains evolve in time. Note that for a number of particles greater than six in the chain the velocity is significantly higher for the others for the two values of λ considered in low applied fields. we conclude that the velocity increases both with λ and with the number of particles in the chain for a fixed magnetic field. Basically, the velocity

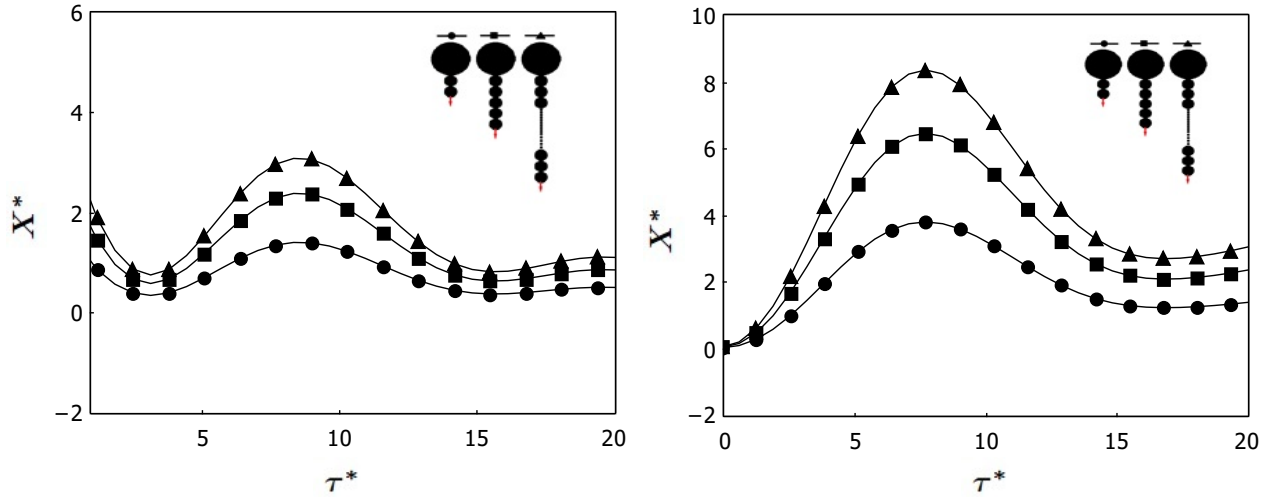

Figure 4.11: Relative trajectories of three chains of particles in presence of the magnetic dipole, but with a fixed external magnetic field. Black circles are for chain of 3 particles, black rectangles are for chain of six particles, black triangles are for chain of more than six particles (Long chain). Results were obtained for $St = 0.5$ a) $\lambda = 20$ and b) $\lambda = 90$.

of the chains increase both with the intensity of the dipolar interactions and with the number of particle in the aggregates. In addition, the intensity of the velocity fluctuation increase by about 14 percent compared with the results of $\lambda = 20$.

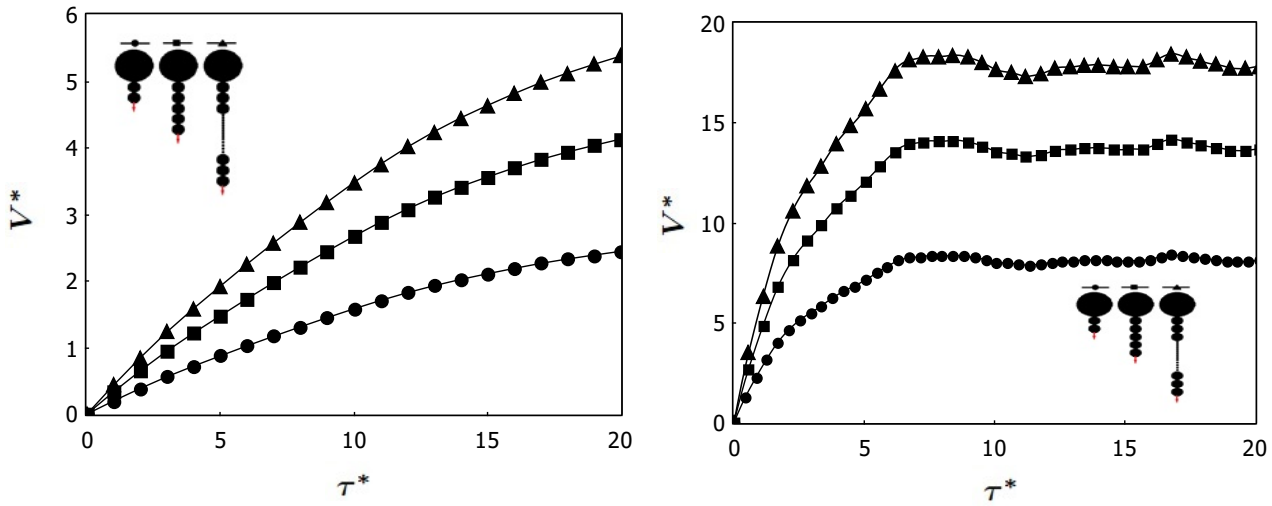

Figure 4.12: Non-dimensional velocity of three chains in presence of the magnetic dipole, but with fixed external magnetic field. Black circles are for chain of 3 particles, black rectangles are for chain of six particles, black triangles are for chain of more than six particles (Long chain). Results were obtained for $St = 0.5$ a) $\lambda = 20$ and b) $\lambda = 90$.

4.5.3 Influence of the External Field

In the present study, one of the main issues is to examine the influence of an external applied magnetic field in order to determine how it will affects the kinematic of the chains of particle simulated here. To investigate only the effect of the field on the motion of the chains, we keep fixed the parameter magnetic dipolar, on the other hand , the intensity of the applied external magnetic field is variable. In the simulations here λ is fixed and equal to 90. We simulate the suspension for two values of the non-dimensional field, $\alpha = 20$ and $\alpha = 80$.

The relative trajectories is shown in figure (4.13) considering the conditions of the simulations mentioned above. The results shows a comparison between $\alpha = 20$ and $\alpha = 80$ of the relative trajectory of the chain. Note the increase in the values of X^* with the growth of particles in the chain, resulting fixed dipole interactions combined with the magnetic field applied particles, the relative trajectories of chain increased. For the high magnetic field interaction regime, which X^* continues higher than the moderate magnetic field. Then, the trajectory is not monotonic and this effect is amplified as the intensity of the magnetic field is increased and the number of the particle in the chain increase. We note that the particles orient on average in the direction opposite to the field. In this case, it shows that the orientation action of magnetic forces dominates of the magnetic dipole in this particular instance, contributing to the orientation of the chain.

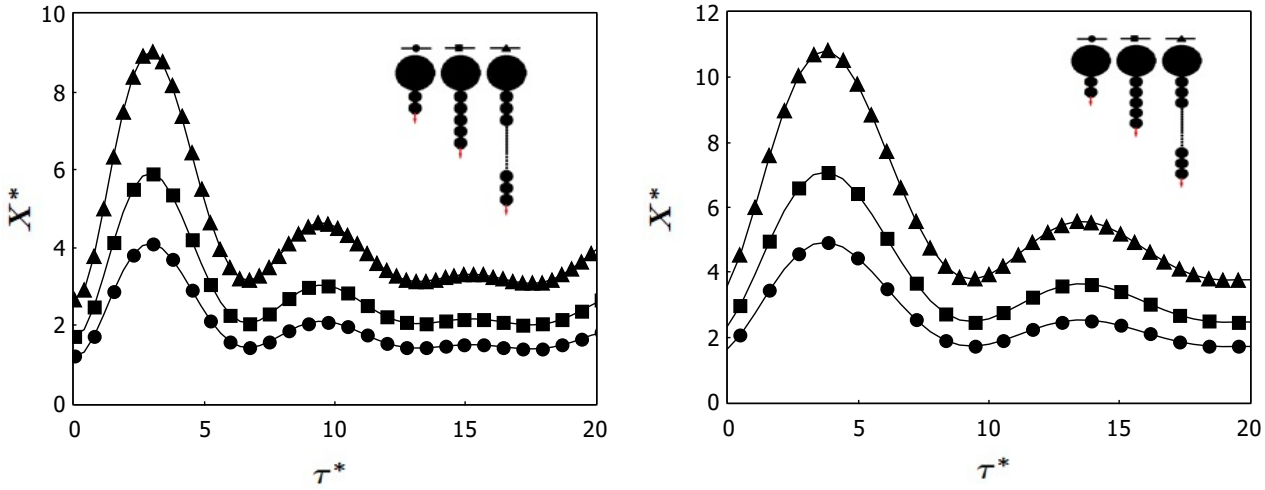

Figure 4.13: Relative trajectories of three chains of particles in presence of the magnetic field , but with a fixed magnetic dipole. Black circles are for chain of 3 particles, black rectangles are for chain of six particles, black triangles are for chain of more than six particles (long chain). Results were obtained for $St = 0.5$ a) $\alpha = 20$ and b) $\alpha = 80$

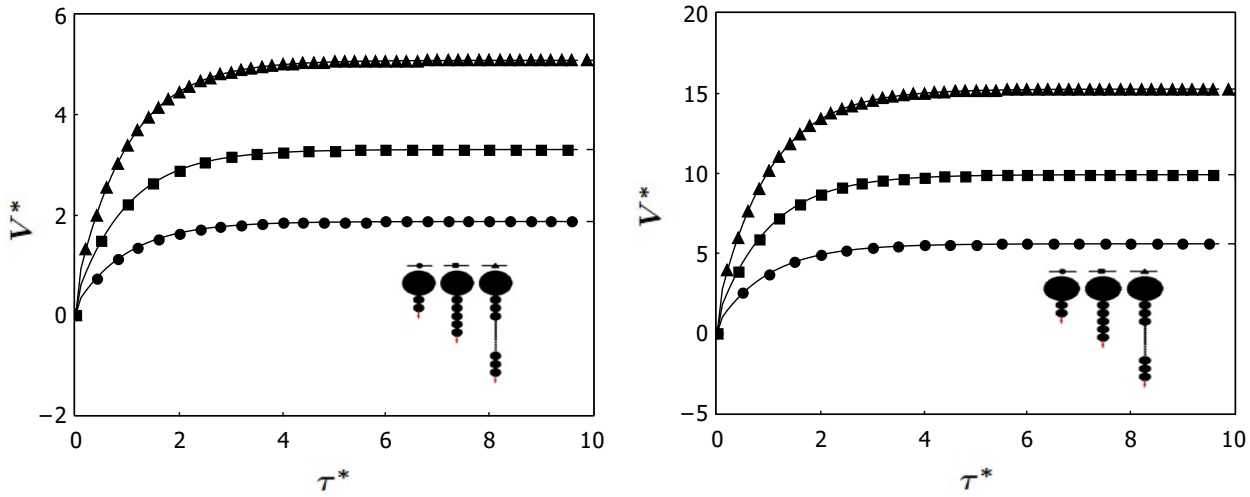

Figure 4.14: Non-dimensional velocity of three chains in presence of the magnetic field , but with fixed magnetic dipole. Black circles are for chain of 3 particles, black rectangles are for chain of six particles, black triangles are for chain of more than six particles (long chain). Results were obtained for $St = 0.5$ a) $\alpha = 20$ and b) $\alpha = 80$.

In figure (4.14), we have the normalized velocity of three chains in presence of the magnetic field, but for a fixed external magnetic dipole. We repeat again the same conditions, we put a fixed parameter magnetic dipolar and, the intensity of the applied external magnetic field change. Here, and a moderate magnetic field $\alpha = 20$ and strong dipolar interactions $\alpha = 80$. Conditions

over the particles chain are the same where we consider chain of 3 particles, chain of six particles, long chain where we have more than six particles. In this case its observed that the velocity grows along time at with the applied magnetic fields. The effect of the magnetic field on the velocity is pointed in figure (4.14), the normalized velocity of the particles at the two magnetic field parameters numbers, $\alpha = 20$ and $\alpha = 80$ at a fixed λ indicates the higher the magnetic field, the larger V^* implying that in addition to the parameters N number of particles in the chain defined, the parameter α is also a parameter governing chain kinematics. Therefore, the difference in magnetic property of the suspension (in this case characterized by the magnetic field α) also has substantial influence on the kinematics of the chain of magnetic particles.

Chapter 5

CONCLUSIONS AND FUTURE WORKS

5.1 Conclusions

This thesis has described analytic, experimental and numerical analyses for predicting the motion of particles in viscous fluids. In this context, initially a bibliographical review of the general theory of fluids was presented, showing the theoretical part and the mathematical development of the development of models that describe the movement of particles in fluids with a low Reynolds number. Here we present the main conclusions of the work.

5.1.1 On the Flagellum Motion in Creeping Flow

The creeping flow associated with the motion of particles and micro-swimmers is mainly due to their small size or the high viscosity of the liquid where they swim. In practical application we can use micro swimmers to realize minimally invasive medical procedures to detect and treat diseases. In the near future they are great aspirant for achieving targeted drug delivery, which can reduce the side effects of potent drugs and minimize the secondary complications of dangerous treatments. However, The locomotion microorganism at low Reynolds number environments such as bodily fluids needs breaking the time reversal symmetry to achieve propulsion, therefore swimming of micro structures in viscous environments presents a challenge. In this present work firstly, we have successfully investigated theoretically and experimentally the motion of helical swimmers at low Reynolds for both ambient fluids Newtonian and non-Newtonian. We designed a workbench to carried out some experiments with macroscopic model of swimmers. Three different helices were used in our experiments and the propulsive velocity of the particle, as well as propulsive force and torque exerted by the rotating helix in a very viscous fluid were measured. Additionally, experiments with the helical swimmers in a elastic fluid were also carried out. We have used Slender Body Theory (SBT) and also the method of regularized Stokeslest (RSM) in order to calculate theoretically the force and torque as function of the Strouhal number (Sh) produced by

the helical swimmers moving in a Newtonian fluid. The theoretical results were compared with experimental data and a very good agreement is observed specially for higher values of Sh within the error bars of the experimental data. Increasing the Deborah number the propulsive force and torque have increased for the three types of helices examined. The helical swimmer propulsive velocity was also examined in terms of the elastic parameter Deborah number and also compared with the experimental measurements for the case in which the base fluid was non-Newtonian. We have found that the swimming speed increases as the elastic effect in the ambient fluid increases until a critical Deborah number number O(1), when it saturates for a constant value within the experimental error bars. The velocity anisotropy measured experimentally as the ratio of the swimmer speed in two different directions was insensitive to the elastic effect of the surrounding fluid.

We also have presented a comparison between predictions of the speed velocity given by CFD simulation using a Finite Element Method, using an Oldroyd-B constitutive model for the base elastic fluid, and experimental data. The agreement between the two sets of results was very good within the experimental error bars for the Deborah varying from 0 to 2. However, we have noted that while the experimental data saturated at larger De the simulation results for the swimmer speed appeared to increase continuously according to the constitutive model used to describe the elastic liquid. Indeed, the Oldroyd B model used in this work assumed infinite extensibility of the polymer chain which plays a role when the fluid has an extensional component like in the flow problem explored. The Oldroyd Fluid - B is not only unrealistic but it leads to numerical difficulties as unlimited values of the stress tensor at higher De. Currently, we are changing the linear spring law to one with a finite spring extension that yields such as a dumbbell-FENE (finitely extensible nonlinear elasticity) model. We expect that using this new model in the CFD code, the simulation results will also present a saturation of v_{nn}/v_n for De above 1, as we have seen in our experiments with PAMA with a macromolecule volume fraction $\phi = 0.05$.

Additionally, the self-propulsion of the swimmer generated by elastic effects in the surrounding fluid was directly related to the stress anisotropy produced by the macromolecule stretching and orientation by the flow. This stress anisotropy possibly produced a resultant elastic force on the direction of the particle motion leading to a self-propulsion. Actually, streamlines surrounding the helical swimmer may produce this net force on the particle that pushes it enchaining its propulsion speed until a determined value, depending on the De and the concentration of macromolecules in the base fluid. In conclusion, this work has demonstrated that the presence of elastic effect in the surrounding fluid can produce propulsion of an artificial helical micro-swimmers. Inspired by the motion of active microorganisms, we have developed artificial particles that feature similar swimming behaviors based on helical mechanisms. These man-made micromachines hold a great potential as autonomous agents for health care, sustainability, and security applications as: biomedical microswimmers, future bacteria-interface systems, micro-biorobots and robotic manipulation at the micro- and macroscales. Artificial swimmers manipulation at low Reynolds number is a very interesting and a relatively young field to continue being explored.

5.1.2 On the Motion of Magnetic Chains

Understanding the behavior of a chain of magnetic particles is still an open question with little knowledge on the subject. There are several variables influencing the final behavior. Some, in certain situations, are controllable, such as the magnetic field and dipole interaction force. Others, in turn, are specific to a given fluid, such as particle size, number of particles in the chain, among others. It is essential to understand the action of these factors, separately and/or together, if the objective is to develop new applications, especially in medicine, or to optimize existing ones, which are not few. In the second part of this work, we attract attention to the studies on magnetotactic bacteria that have become the spotlight in research on fluid mechanics at low Reynolds number. This microorganisms can swim in blood and they have magnets within them. Therefore the investigation of the motion in viscous liquids of this kind of active particles for carrying drugs in the blood circulation under application of a magnetic field is still not known sufficiently. We numerically investigated the kinematics of magnetic chains and fluid flow in the presence of an external uniform magnetic field and magnetic dipole, with an emphasis on the effect of the Peclét number (Pe), the parameter of dipolar interactions (λ), the parameter of the intensity of magnetic field (α), the number of particles in the chain (N). The numerical simulations conducted are based on the Langevin dynamics and the problem was solved firstly for a single particle and subsequently for several particles in order to explore a collective effect. In the first case, the motion of the particle was analyzed directly through the trajectories and velocity. We emphasize that in these conditions the effect of the gravitational field is important, the movement in the direction of gravity loses its diffusive character, assuming a deterministic nature. The chain-kinematic was affected depending on the number of particle in the chain, the parameter of dipolar interactions and the parameter of the intensity of magnetic field. For each chain, the particles attract each order, but will nonetheless separate due to the increased of the magnetic field and consequently, the particle orientation increase thus the trajectories and the velocities of the chain are different under moderate and strong magnetic field.

5.2 Suggestions for Future Work

Our experiment was limited by starting with Newtonian fluids and in a second part we explored the influence of viscoelastic effects of a non-Newtonian medium on the kinematics and dynamics (force/torque) on the flagella body. It would be very important to study in another work the influence of one organism on the other's movement through the interaction of at least two of them. The movement of one produces hydrodynamic disturbances that change the behavior of the other. The aim would be to explore at least the problem of up to three bodies to characterize a more pronounced collective effect. It would be great because the collective effect can significantly change the force and torque on an individual organism as the other bodies create flow to the reference body. In this context, both modifications of the base fluid (Newtonian and non-Newtonian) with collective effect would be explored. Generally, the boundaries cause major challenges in swimming modeling. The velocity of the fluid right on a rigid boundary equals the velocity of the

boundary itself. Thus, the velocity gradient close to boundaries is large and the viscous effects play a dominant role. In several studies on the locomotion of helical bodies, the wall effect is not considered. In future work, imply the wall effect in order to capture the (averaged) flow phenomena close to boundaries.

In a next study, the average force and average torque on the structure could be calculated since we have the forces and torques that act on each particle in the simulations. It could verify if with the kinematic data the Force and Torque relationships based on slender body theory (SBT) could be used, feeding them, with determined kinematic quantities from the kinematic analysis simulations. In this sense, it would be interesting to try to compare the average forces and average torques obtained directly from particle simulation with the results based on SBT or other formulation used previously with that of [16], [98] among others. In a future work, can be investigated by particle direct numerical simulations the trajectories of the magnetic chains (magnetic bacterium) and the fluctuation in this trajectories produced by effect of the particle-particle dipolar interactions for different values of the parameter λ and the particle volume fraction ϕ. It can be try to explore the following configurations (i) chain with magnetic head and non-magnetic body (line of smaller particles) (ii) non-magnetic head and magnetic line.

In order to improve and expand the results obtained on magnetic chains, we can add also these other suggestions for future work.

- In the implementation part, it would be interesting to optimize the computational code using, for example, simulating interactions with three or more chains of particles. Also, looking to try to increase the number of particles in the simulations, it could be interesting to parallelize the code.
- In all simulations, the hydrodynamic interactions were turned off, so in the improvement part of the model, the effect of the hydrodynamic interactions between particles could be analyzed. This effect can be significant. In addition, the correlation between pairs of chains of particles in the intensity of Brownian motion could be included.
- Finally, for a practical applications, an oscillatory field could be imposed in the simulation domain to study, for example, a magnetohyperthermia model or others . The effect of dipole interactions and the formation of aggregates on the increase in fluid temperature is still an open question, showing different behaviors for different intensities and frequencies of the imposed oscillatory magnetic field.

REFERENCES

[1] ENGINEERING, B. U. M. *Mechanics of Materials, Slender Structures: Stress Transformation*. 2019. Disponível em: <https://www.bu.edu/moss/mechanics-of-materials-stress-transformation/>. Acesso em: 06 abr 2022. Cited on pages viii and 29.

[2] PEREIRA, I. D. O. Rheology of ferrofluids in shear flows. 2019. Cited on pages ix and 79.

[3] BARNES, H. A.; HUTTON, J. F.; WALTERS, K. *An introduction to rheology*. [S.l.]: Elsevier, 1989. Cited on pages ix and 79.

[4] GONTIJO, R. G. Micromecânica e microhidrodinâmica de suspensões magnéticas. 2013. Cited on pages x, 103, 104, and 106.

[5] KOCH, D. L.; SUBRAMANIAN, G. Collective hydrodynamics of swimming microorganisms: Living fluids. *Annual Review of Fluid Mechanics*, v. 43, p. 637–659, 2011. Cited on page 17.

[6] KELLER, E. F.; SEGEL, L. A. Model for chemotaxis. *Journal of theoretical biology*, v. 30 2, p. 225–34, 1971. Cited on pages 17 and 70.

[7] MCDONNELL, A. et al. Microfluidic extensional rheology of suspensions of motile microbes. *Chemeca 2011: Engineering a Better World: Sydney Hilton Hotel, NSW, Australia, 18-21 September 2011*, p. 106, 09 2011. Cited on page 17.

[8] YAMAGUCHI, T.; ISHIKAWA, T.; IMAI, Y. (Ed.). *6 - Swimming Microorganisms*. Boston: Elsevier, 2018. 175-216 p. (Micro and Nano Technologies). ISBN 978-0-323-38944-0. Cited on page 17.

[9] DEMIR, E. et al. Dynamics of pattern formation and emergence of swarming in c. elegans. *eLife*, v. 9, 04 2020. Cited on page 17.

[10] CHEN, Y.; FERRELL, J. C. elegans colony formation as a condensation phenomenon. *Nature Communications*, v. 12, p. 4947, 08 2021. Cited on page 17.

[11] LAVICKOVA, B.; LAOHAKUNAKORN, N.; MAERKL, S. A partially self-regenerating synthetic cell. *Nature Communications*, v. 11, 12 2020. Cited on page 17.

[12] MARIANO, G. et al. Oligomerization of the flif domains suggests a coordinated assembly of the bacterial flagellum ms ring. *Frontiers in Microbiology*, v. 12, 01 2022. Cited on page 17.

[13] PURCELL, E. M. Life at low reynolds number. *American Journal of Physics*, v. 45, n. 1, p. 3–11, 1977. Disponível em: <https://doi.org/10.1119/1.10903>. Cited on pages 17 and 59.

[14] DREYFUS, R. et al. Microscopic artificial swimmers. *Nature*, v. 437, p. 862–5, 11 2005. Cited on page 18.

[15] GRAY, J.; HANCOCK, G. J. The Propulsion of Sea-Urchin Spermatozoa. *Journal of Experimental Biology*, v. 32, n. 4, p. 802–814, 12 1955. Cited on pages 18, 59, 63, 65, 66, 67, 80, 81, 82, and 83.

[16] LIGHTHILL, J. Flagellar hydrodynamics: The john von neumann lecture, 1975. *SIAM Review*, Society for Industrial and Applied Mathematics, v. 18, n. 2, p. 161–230, 1976. ISSN 00361445. Cited on pages 18, 59, 61, 64, 65, 66, 67, 70, 71, 80, 81, 82, 83, 125, and 144.

[17] LUDWIG, W. Zur theorie der flimmerbewegung (dynamik, nutzeffekt, energiebilanz). *Zeitschrift fÃ1⁄4r vergleichende Physiologie*, v. 13, n. 2, p. 397–504, 1930. Cited on pages 18 and 19.

[18] TAYLOR, G. I. The action of waving cylindrical tails in propelling microscopic organisms. *Proc. R. Soc. Lond. A*, v. 211, n. 2, p. 225–239, 1952. Cited on page 18.

[19] MALVAR, S. et al. On the kinematics-wave motion of living particles in suspension. *Biomicrofluidics*, v. 11, n. 4, p. 044112, 2017. Cited on pages 18 and 91.

[20] ARMITAGE, J.; BERRY, R. Assembly and dynamics of the bacterial flagellum. *Annual Review of Microbiology*, v. 74, 09 2020. Cited on page 18.

[21] RAZAVI, S.; FARHANGMEHR, V.; MARANDI, E. Modeling of flagellum behavior and two-dimensional sperm cell motility within the context of fluid–solid interactions. *Journal of Mechanics in Medicine and Biology*, v. 21, p. 2150052, 08 2021. Cited on page 18.

[22] ZAITSEV, M.; KARABASOV, S. Mathematical modelling of flagellated microswimmers. *Computational Mathematics and Mathematical Physics*, v. 58, p. 1804–1816, 11 2018. Cited on page 18.

[23] XU, J. Motion simulation of an artificial flagellum nanorobot. In: *2013 13th IEEE International Conference on Nanotechnology (IEEE-NANO 2013)*. [S.l.: s.n.], 2013. p. 1208–1211. Cited on page 18.

[24] PARK, Y.; KIM, Y.; LIM, S. Flagellated bacteria swim in circles near a rigid wall. *Phys. Rev. E*, American Physical Society, v. 100, p. 063112, Dec 2019. Disponível em: <https://link.aps.org/doi/10.1103/PhysRevE.100.063112>. Cited on page 18.

[25] ROSENSWEIG, R. E. *Ferrohydrodynamics*. [S.l.]: Courier Corporation, 2013. Cited on pages 18, 103, and 107.

[26] HE-PENG, Z. et al. Propulsive matrix of a helical flagellum. *Chinese Physics B*, v. 23, p. 114703, 10 2014. Cited on pages 19 and 67.

[27] SHINDELL, O. et al. Using experimentally calibrated regularized stokeslets to assess bacterial flagellar motility near a surface. *Fluids*, v. 6, p. 387, 10 2021. Cited on page 19.

[28] TAJIMA, K.; MIKAMI, F. Propulsive forces of a model helical flagellum in various fluids with viscoelasticity. *Transactions of the JSME (in Japanese)*, v. 84, 10 2018. Cited on page 19.

[29] RODENBORN, B. et al. Propulsion of microorganisms by a helical flagellum. *Proceedings of the National Academy of Sciences*, v. 110, n. 5, p. E338–E347, 2013. Cited on pages 19, 62, 64, 65, 70, 80, 83, 84, and 144.

[30] Johnson, R. E. An improved slender-body theory for Stokes flow. *Journal of Fluid Mechanics*, v. 99, p. 411–431, jul. 1980. Cited on page 19.

[31] CORTEZ, R.; FAUCI, L.; MEDOVIKOV, A. The method of regularized stokeslets in three dimensions: Analysis, validation, and application to helical swimming. *Physics of Fluids*, v. 17, 02 2005. Cited on pages 19, 68, 80, and 84.

[32] GAGNON, D. A. et al. Fluid-induced propulsion of rigid particles in wormlike micellar solutions. *Physics of Fluids*, v. 26, p. 103101, 2014. Cited on page 19.

[33] THAWANI, A.; TIRUMKUDULU, M. S. Trajectory of a model bacterium. *Journal of Fluid Mechanics*, Cambridge University Press, v. 835, p. 252–270, 2018. Cited on page 19.

[34] MONTENEGRO-JOHNSON, T. D. et al. Flow analysis of the low-reynolds number swimmer c. elegans. *arXiv: Fluid Dynamics*, 2016. Cited on page 19.

[35] IRILAN, Y. G.; CUNHA, F. R. A study on the kinematics and dynamics of flagellum motion in creeping flows. In: . [S.l.]: 25th International Congress of Mechanical Engineering/10.26678/ABCM.COBEM2019.COB2019-1906, 2019. p. 1–9. Cited on pages 19 and 144.

[36] SHUM, H. Microswimmer propulsion by two steadily rotating helical flagella. *Micromachines*, v. 10, n. 1, 2019. ISSN 2072-666X. Disponível em: <https://www.mdpi.com/2072-666X/10/1/65>. Cited on page 19.

[37] JUNOT, G. et al. Swimming bacteria in poiseuille flow: The quest for active bretherton-jeffery trajectories. *EPL (Europhysics Letters)*, v. 126, p. 44003, 06 2019. Cited on page 20.

[38] QIN, B. et al. Flow resistance and structures in viscoelastic channel flows at low re. *Physical review letters*, v. 123 19, p. 194501, 2019. Cited on page 20.

[39] QIN, B. et al. Three-dimensional structures and symmetry breaking in viscoelastic cross-channel flow. *Soft matter*, 2020. Cited on page 20.

[40] DHAR, A.; BURADA, P.; SEKHAR, G. R. Hydrodynamics of active particles confined in a periodically tapered channel. *Physics of Fluids*, AIP Publishing LLC, v. 32, n. 10, p. 102005, 2020. Cited on page 20.

[41] Deußen, B.; Oberlack, M.; Wang, Y. Probability theory of active suspensions. *Physics of Fluids*, v. 33, n. 6, p. 061902, jun. 2021. Cited on page 20.

[42] Deußen, B.; Wang, Y.; Oberlack, M. A deterministic two-phase model for an active suspension with non-spherical active particles using the Eulerian spatial averaging theory. *Physics of Fluids*, v. 34, n. 2, p. 023302, fev. 2022. Cited on page 20.

[43] Vinze, P.; Choudhary, A.; Subramaniam, P. Motion of an active particle in linear concentration gradients. p. U03.007, jan. 2020. Cited on page 20.

[44] Roure, G. A.; Cunha, F. R. Hydrodynamic dispersion and aggregation induced by shear in non-Brownian magnetic suspensions. *Physics of Fluids*, v. 30, n. 12, p. 122002, dez. 2018. Cited on page 20.

[45] SINZATO, Y.; CUNHA, F. Capillary flow of magnetic fluids with effect of hydrodynamic dispersion. *Physics of Fluids*, AIP Publishing LLC, v. 33, n. 10, p. 102006, 2021. Cited on page 20.

[46] CUNHA, F. R.; ROSA, A. P. Effect of particle dipolar interactions on the viscoelastic response of dilute ferrofluids undergoing oscillatory shear. *Physics of Fluids*, AIP Publishing LLC, v. 33, n. 9, p. 092004, 2021. Cited on page 20.

[47] MALVAR, S.; CUNHA, F. R. A theoretical model for studying the nonlinear viscoelastic response of an active fluid undergoing oscillatory shear. *Physics of Fluids*, AIP Publishing LLC, v. 33, n. 9, p. 091903, 2021. Cited on page 20.

[48] YIGIT, B.; ALAPAN, Y.; SITTI, M. Cohesive self-organization of mobile microrobotic swarms. *Soft Matter*, Royal Society of Chemistry, v. 16, n. 8, p. 1996–2004, 2020. Cited on page 20.

[49] ZHANG, Z. et al. Robotic micromanipulation: Fundamentals and applications. *Annual Review of Control, Robotics, and Autonomous Systems*, Annual Reviews, v. 2, p. 181–203, 2019. Cited on page 20.

[50] LI, G.; LAUGA, E.; ARDEKANI, A. Microswimming in viscoelastic fluids. *Journal of Non-Newtonian Fluid Mechanics*, v. 297, p. 104655, 09 2021. Cited on page 21.

[51] LAUGA, E. Propulsion in a viscoelastic fluid. *Physics of Fluids*, AIP Publishing, v. 19, n. 8, p. 083104, Aug 2007. ISSN 1089-7666. Disponível em: <http://dx.doi.org/10.1063/1.2751388>. Cited on pages 21 and 94.

[52] BINAGIA, J.; SHAQFEH , E. Self-propulsion of a freely suspended swimmer by a swirling tail in a viscoelastic fluid. *Physical Review Fluids*, v. 6, 05 2021. Cited on page 21.

[53] SPAGNOLIE, S. E.; LIU, B.; POWERS, T. R. Locomotion of helical bodies in viscoelastic fluids: Enhanced swimming at large helical amplitudes. *Phys. Rev. Lett.*, American Physical Society, v. 111, p. 068101, Aug 2013. Disponível em: <https://link.aps.org/doi/10.1103/PhysRevLett.111.068101>. Cited on pages 21 and 94.

[54] LI, C. et al. Flagellar swimming in viscoelastic fluids: Role of fluid elastic stress revealed by simulations based on experimental data. *Journal of The Royal Society Interface*, v. 14, p. 20170289, 10 2017. Cited on page 21.

[55] IRILAN, Y.-G.; CUNHA, F. R. Experimental and theoretical studies of the fluid elasticity on the motion of macroscopic models of active helical swimmers. *Physics of Fluids*, AIP Publishing LLC, v. 33, n. 9, p. 092004, 2021. Cited on page 21.

[56] XU, Z. et al. Simulation study on the motion of magnetic particles in silicone rubber-based magnetorheological elastomers. *Mathematical Problems in Engineering*, v. 2019, p. 1–11, 07 2019. Cited on page 21.

[57] KONG, D. et al. Swimming motion of rod-shaped magnetotactic bacteria: the effects of shape and growing magnetic moment. *Frontiers in Microbiology*, v. 5, 2014. Cited on page 22.

[58] NADKARNI, R.; BARKLEY, S.; FRADIN, C. A comparison of methods to measure the magnetic moment of magnetotactic bacteria through analysis of their trajectories in external magnetic fields. *PloS one*, v. 8, p. e82064, 12 2013. Cited on page 22.

[59] CUI, Z. et al. On the swimming motion of spheroidal magnetotactic bacteria. *Fluid Dynamics Research - FLUID DYN RES*, v. 44, 10 2012. Cited on page 22.

[60] RINALDI, C. et al. Magnetic fluid rheology and flows. *Current Opinion in Colloid & Interface Science*, Elsevier, v. 10, n. 3-4, p. 141–157, 2005. Cited on pages 23 and 24.

[61] IVANOV, A. O.; KUZNETSOVA, O. B. Magnetic properties of dense ferrofluids: An influence of interparticle correlations. *Physical Review E*, APS, v. 64, n. 4, p. 041405, 2001. Cited on page 23.

[62] HIRABAYASHI, M.; CHEN, Y.; OHASHI, H. A lattice boltzmann analysis of the effects of the internal angular momentum on rheology of magnetic fluids. *Computer physics communications*, Elsevier, v. 142, n. 1-3, p. 148–150, 2001. Cited on page 23.

[63] LI, D. D. et al. Numerical modeling of magnetic nanoparticle and carrier fluid interactions under static and double-shear flows. *IEEE Transactions on Nanotechnology*, v. 16, n. 5, p. 798–805, 2017. Cited on page 23.

[64] IVANOV, A. O. et al. Magnetic properties of polydisperse ferrofluids: A critical comparison between experiment, theory, and computer simulation. *Phys. Rev. E*, American Physical Society, v. 75, p. 061405, Jun 2007. Disponível em: <https://link.aps.org/doi/10.1103/PhysRevE.75.061405>. Cited on page 23.

[65] BERKOV N.L. GORN, D. S. D. Simulations of ferrofluid dynamics: Rigid dipoles model versus particles with internal degrees of freedom. *Journal of Magnetism and Magnetic Materials*, Elsevier, v. 310, n. 1-3, p. 1015–11016, 2007. Cited on page 24.

[66] ZUBIETA, M. et al. Magnetorheological fluids: characterization and modeling of magnetization. *Smart Materials and Structures*, IOP Publishing, v. 18, n. 9, p. 095019, 2009. Cited on page 24.

[67] SHLIOMIS, M. Effective viscosity of magnetic suspensions. *Sov. Phys. JETP*, v. 34, p. 1291–1294, 01 1972. Cited on page 24.

[68] Zubarev, A. Y.; Odenbach, S.; Fleischer, J. Rheological properties of dense ferrofluids. Effect of chain-like aggregates. *Journal of Magnetism and Magnetic Materials*, v. 252, p. 241–243, nov. 2002. Cited on page 24.

[69] ODENBACH, S. Magnetic fluids-suspensions of magnetic dipoles and their magnetic control. *Journal of physics: condensed matter*, IOP Publishing, v. 15, n. 15, p. S1497, 2003. Cited on page 24.

[70] ILG, P. Importance of depletion interactions for structure and dynamics of ferrofluids. *The European Physical Journal E*, Springer, v. 26, n. 1, p. 169–176, 2008. Cited on page 24.

[71] HOLM, C.; WEIS, J.-J. The structure of ferrofluids: A status report. *Current opinion in colloid & interface science*, Elsevier, v. 10, n. 3-4, p. 133–140, 2005. Cited on page 24.

[72] LIU, T. et al. Structural and rheological study of magnetic fluids using molecular dynamics. *Magnetohydrodynamics*, Citeseer, v. 46, n. 3, p. 257–269, 2010. Cited on page 24.

[73] KRISTÓF, T.; SZALAI, I. Magnetic properties and structure of polydisperse ferrofluid models. *Physical Review E*, APS, v. 68, n. 4, p. 041109, 2003. Cited on page 24.

[74] Sobral, Y. D.; Cunha, F. R. A stability analysis of a magnetic fluidized bed. *Journal of Magnetism and Magnetic Materials*, v. 258, p. 464–467, mar. 2003. Cited on page 25.

[75] CUNHA, F.; SOBRAL, Y. Characterization of the physical parameters in a process of magnetic separation and pressure-driven flow of a magnetic fluid. *Physica A: Statistical Mechanics and its Applications*, v. 343, p. 36–64, 2004. ISSN 0378-4371. Disponível em: <https://www.sciencedirect.com/science/article/pii/S0378437104005394>. Cited on page 25.

[76] CUNHA, F. R.; COUTO, H. L. G. Transverse gradient diffusion in a polydisperse dilute suspension of magnetic spheres during sedimentation. *Journal of Physics: Condensed Matter*, IOP Publishing, v. 20, n. 20, p. 204129, may 2008. Disponível em: <https://doi.org/10.1088/0953-8984/20/20/204129>. Cited on page 25.

[77] CUNHA, F.; SOBRAL, Y.; GONTIJO, R. Stabilization of concentration waves in fluidized beds of magnetic particles. *Powder technology*, Elsevier, v. 241, p. 219–229, 2013. Cited on page 25.

[78] WANG, Z.; HOLM, C.; MÜLLER, H. W. Molecular dynamics study on the equilibrium magnetization properties and structure of ferrofluids. *Physical Review E*, APS, v. 66, n. 2, p. 021405, 2002. Cited on page 25.

[79] ABADE, G. C.; CUNHA, F. R. Computer simulation of particle aggregates during sedimentation. *Computer methods in applied mechanics and engineering*, Elsevier, v. 196, n. 45-48, p. 4597–4612, 2007. Cited on page 25.

[80] LINDNER, J.; MENZEL, K.; NIRSCHL, H. Simulation of magnetic suspensions for hgms using cfd, fem and dem modeling. *Computers & chemical engineering*, Elsevier, v. 54, p. 111–121, 2013. Cited on page 25.

[81] OSAKA, T. et al. Synthesis of magnetic nanoparticles and their application to bioassays. *Analytical and Bioanalytical Chemistry*, Springer, v. 384, n. 3, p. 593–600, 2006. Cited on page 26.

[82] Timko, M. et al. Dielectric properties of transformer paper impregnated by mineral oil based magnetic fluid. In: *Journal of Physics Conference Series*. [S.l.: s.n.], 2010. (Journal of Physics Conference Series, v. 200), p. 072099. Cited on page 26.

[83] MOREIRA, N. A. *Nonlinear behavior of elastic suspensions subject to different flow fields: mathematical modeling and simulation*. Tese (Thesis) — University of Brasilia, 2018. Cited on pages 28 and 48.

[84] EVANGELISTA, F. H. d. S. *Microstructure and velocity fluctuations in a sedimenting megnetic suspension*. Dissertação (Dissertation) — University of Brasilia, 2019. Cited on pages 28 and 110.

[85] PEREIRA, I. D. O. Rheology of viscoelastic and thermosensitive liquids in shear. Projeto de TCC, University of Brasilia, 2017. Cited on page 28.

[86] CUNHA, F. R. Fundamental concepts of micro-hydrodynamic. Lectures notes , University of Brasilia, 2018. Cited on pages 28, 37, and 38.

[87] GUAZZELLI, E.; MORRIS, J. F. *A physical introduction to suspension dynamics*. [S.l.]: Cambridge University Press, 2011. Cited on pages 35 and 36.

[88] TAYLOR, G. I. Low reynolds number flows. Chicago, Ill. : Released by Encyclopaedia Britannica Educational Corp, 1966. Cited on page 36.

[89] ABELSON, H. et al. Amorphous computing. *Communications of the ACM*, ACM New York, NY, USA, v. 43, n. 5, p. 74–82, 2000. Cited on page 36.

[90] CUNHA, F. D.; HINCH, E. Shear-induced dispersion in a dilute suspension of rough spheres. *Journal of fluid mechanics*, Cambridge University Press, v. 309, p. 211–223, 1996. Cited on page 36.

[91] OLIVEIRA, T. F. D. *MICROHIDRODINÂMICA E REOLOGIA DE EMULSÕES*. Tese (Thesis) — PONTIFÍCIA UNIVERSIDADE CATOLICA DO RIO DE JANEIRO, 2007. Cited on page 36.

[92] KIM, S.; KARRILA, S. *Microhydrodynamics: Principles and Selected Applications*. Butterworth-Heinemann, 1991. (Butterworth-Heinemann series in chemical engineering). ISBN 9780750691734. Disponível em: <https://books.google.st/books?id=P_VQAAAAMAAJ>. Cited on pages 38, 39, 45, and 102.

[93] OLDROYD, J. G. On the formulation of rheological equations of state. *Proceedings of the Royal Society of London. Series A. Mathematical and Physical Sciences*, The Royal Society London, v. 200, n. 1063, p. 523–541, 1950. Cited on page 49.

[94] STEWARTSON, K. Vectors, tensors, and the basic equations of fluid mechanics. rutherford aris. prentice-hall, london. 1962. 286 pp. illustrated. 42s. *The Aeronautical Journal*, Cambrige University Press, v. 67, n. 632, p. 532–532, 1963. Cited on page 55.

[95] BATCHELOR, G. K. The stress system in a suspension of force-free particles. *Journal of Fluid Mechanics*, v. 41, n. 3, p. 545–570, 1970. Cited on pages 59 and 105.

[96] TAYLOR, G. I. The action of waving cylindrical tails in propelling microscopic organisms. *Proceedings of the Royal Society of London. Series A. Mathematical and Physical Sciences*, The Royal Society London, v. 211, n. 1105, p. 225–239, 1952. Cited on page 66.

[97] LIGHTHILL, J. Reinterpreting the basic theorem of flagellar hydrodynamics. Springer Netherlands, Dordrecht, p. 25–34, 1996. Cited on page 67.

[98] JOHNSON, R. E. An improved slender-body theory for stokes flow. *Journal of Fluid Mechanics*, Cambridge University Press, v. 99, n. 2, p. 411–431, 1980. Cited on pages 67, 125, and 144.

[99] COX, R. G. The motion of long slender bodies in a viscous fluid. part 2. shear flow. *Journal of Fluid Mechanics*, v. 45, p. 625–657, 1971. Cited on page 67.

[100] BOUZARTH, E. L.; MINION, M. L. Modeling slender bodies with the method of regularized stokeslets. *Journal of Computational Physics*, Elsevier, v. 230, n. 10, p. 3929–3947, 2011. Cited on pages 68 and 69.

[101] CORTEZ, R.; FAUCI, L.; MEDOVIKOV, A. The method of regularized stokeslets in three dimensions: analysis, validation, and application to helical swimming. *Physics of Fluids*, American Institute of Physics, v. 17, n. 3, p. 031504, 2005. Cited on pages 68, 69, and 144.

[102] PEÑA, N. et al. Instrumento livre para medidas de movimento. *Revista Brasileira de Ensino de Física*, v. 35(3), p. 1–5, 9 2013. Cited on page 73.

[103] KLINE, S. J. Describing uncertainties in single-sample experiments. *Mechanical Engineering*, v. 75, p. 3–8, 1953. Cited on page 77.

[104] SINGH, M. et al. Effect of addition of silicone oil on the rheology of fumed silica and polyethylene glycol shear thickening suspension. *Journal of Polymer Engineering*, v. 39, p. 48 – 57, 2018. Cited on page 77.

[105] PEARSON, J. Dynamics of polymeric liquids. volume 1. fluid mechanics. by rb bird, rc armstrong and 0. hassager. 470 pp. 222.00. volume 2. kinetic theory. by rb bird, 0. hassager, rc armstrong and cf curtiss. 257 pp.£ 20.00. wiley, 1977. *Journal of Fluid Mechanics*, Cambridge University Press, v. 86, n. 1, p. 204–207, 1978. Cited on pages 77 and 86.

[106] BATCHELOR, G. K. *An Introduction to Fluid Dynamics*. [S.l.]: Cambridge University Press, 2000. (Cambridge Mathematical Library). Cited on page 80.

[107] KIM, S.; KARRILA, S. *Microhydrodynamics: Principles and Selected Applications*. Butterworth-Heinemann, 1991. (Butterworth-Heinemann series in chemical engineering). ISBN 9780750691734. Disponível em: <https://books.google.st/books?id=P_VQAAAAMAAJ>. Cited on page 81.

[108] JOHNSON, R. E. An improved slender-body theory for stokes flow. *Journal of Fluid Mechanics*, Cambridge University Press, v. 99, n. 2, p. 411–431, 1980. Cited on page 83.

[109] Batchelor, G. K. Slender-body theory for particles of arbitrary cross-section in Stokes flow. *Journal of Fluid Mechanics*, v. 44, p. 419–440, jan. 1970. Cited on page 83.

[110] HINCH, E. Mechanical models of dilute polymer solutions in strong flows. *The Physics of Fluids*, American Institute of Physics, v. 20, n. 10, p. S22–S30, 1977. Cited on page 86.

[111] RALLISON, J. M.; HINCH, E. J. Do we understand the physics in the constitutive equation? *Journal of Non-Newtonian Fluid Mechanics*, v. 29, n. none, p. 37–55, 1988. Cited on page 86.

[112] ABSI, F.; OLIVEIRA, T.; CUNHA, F. A note on the extensional viscosity of elastic liquids under strong flows. *Mechanics Research Communications*, v. 33, p. 401–414, 05 2006. Cited on page 86.

[113] BEHR, M.; ARORA, D.; PASQUALI, M. Stabilized finite element methods of gls type for oldroyd-b viscoelastic fluid. *European Congress on Computational Methods in Applied Sciences and Engineering ECCOMAS*, p. 24–28, 08 2004. Cited on page 87.

[114] CRAVEN, T. J.; REES, J. M.; ZIMMERMAN, W. B. Stabilised finite element modelling of oldroyd-b viscoelastic flows. In: *COMSOL Conference*. [S.l.: s.n.], 2006. Cited on page 87.

[115] MALVAR, S.; CARMO, B.; CUNHA, F. Rheology of a nematic active suspension undergoing oscillatory shear and step strain flows. *Rheologica Acta*, v. 58, 12 2019. Cited on page 91.

[116] RUSSEL, W. B. et al. *Colloidal dispersions*. [S.l.]: Cambridge university press, 1991. Cited on pages 102 and 106.

[117] ODENBACH, S. *Colloidal magnetic fluids: basics, development and application of ferrofluids*. [S.l.]: Springer, 2009. Cited on page 103.

ANEXOS

I. APENDIX

I. STOKES SOLUTION PAST A SPHERE

We consider the classic solution of the Stokes equations representing the uniform motion of a sphere of radius a in an infinite expanse of fluid. We shall first consider this problem using the natural coordinates for the available symmetry, namely spherical polar coordinates.

We consider a fixed sphere in the x-direction the fluid approaches with velocity. On the surface of the sphere ($r = a$). All points have zero velocity (non-slip) therefore a ($r = a$) is a current line and v_θ is zero. The Navier-Stokes equation for an incompressible fluid is:

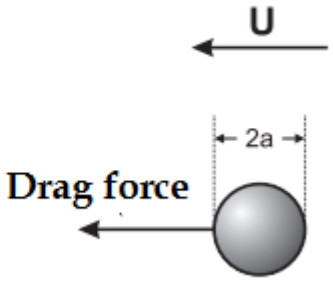

Figure I.1: Stationary sphere immersed in a fluid with uniform velocity U.

$$\rho(\frac{\partial \boldsymbol{u}}{\partial t} + (\boldsymbol{u} \cdot \nabla)\boldsymbol{u}) = -\nabla \boldsymbol{p} + \mu \nabla^2 \boldsymbol{u} + \boldsymbol{f}. \tag{I.1}$$

where ρ is the specific mass of the fluid, $\mathbf{u}$ is the velocity field, $\boldsymbol{p}$ is the pressure, μ is the viscosity and $\boldsymbol{f}$ indicates any external force of the body. We assume a very low Reynolds number. This means that the viscous forces are dominant, so that we can disregard inertial term $(\boldsymbol{u} \cdot \nabla)\boldsymbol{u})$, in addition, we look for a stationary solution so that the Navier-Stokes equation reduces to:

$$\nabla \boldsymbol{p} = \mu \nabla^2 \boldsymbol{u}. \tag{I.2}$$

Keeping in mind identitiy of derivatives $\nabla \times (\nabla \times \boldsymbol{u}) = \nabla(\nabla.\boldsymbol{u}) - \nabla^2 \boldsymbol{u}$ and the fact that $\nabla.\boldsymbol{u}$ is zero for an incompressible fluid due to the continuity equation, we can rewrite the Navier-Stokes equation as:

$$\nabla p = -\mu \nabla \times (\nabla \times \boldsymbol{u}) = -\mu \nabla \times \Omega, \tag{I.3}$$

where we introduce the vorticity field, $\Omega = \nabla \times \boldsymbol{u}$ the spherical symmetry of the problem leads us to seek an axissimetric velocity. Let:

$$\boldsymbol{u} = u_{r,\theta}\, \mathbf{e_r} + u_\theta(r, \theta)\mathbf{e}_\theta.$$

Next we will use the current function of Stokes. In spherical coordinates the divergence $\nabla.\boldsymbol{u}$ of an axissimetric velocity field, is given as:

$$\nabla.\boldsymbol{u} = \frac{1}{r^2}\frac{\partial(r^2 u_r)}{\partial r} + \frac{1}{r \sin\theta}\frac{\partial(u_\theta \sin\theta)}{\partial \theta}$$

.

To automatically satisfy the condition of incompressibility of the fluid, $\boldsymbol{\nabla . u} = 0$, we introduce the Stokes current function $\psi(r, \theta)$ as:

$$u_r = \frac{1}{r^2 \sin\theta}\frac{\partial\psi}{\partial\theta}, u_\theta = \frac{1}{r\sin\theta}\frac{\partial\psi}{\partial r}. \tag{I.4}$$

Thus, the velocity field is defined exclusively by the stream function: $\psi(r, \theta)$ we determine the current function from the reduced Navier-Stokes equation I.4 we continue to calculate the vorticity:

$$\Omega = \nabla \times \boldsymbol{u} = \Omega\mathbf{e_r} + \Omega\mathbf{e}_\theta + \Omega\mathbf{e_\Phi}.$$

Now, since $\boldsymbol{u}$ is axissimetric, the vorticity must be axial, having only a Φ component. Using Equation I.4, we find:

$$\Omega_\theta = \frac{1}{r}(\frac{\partial(ru_\theta)}{\partial r} - \frac{\partial u_r}{\partial\theta})$$
$$\Omega = \frac{1}{r}[\frac{\partial}{\partial r}(\frac{-1}{\sin\theta}\frac{\partial\psi}{\partial r}) - \frac{\partial}{\partial\theta}(\frac{1}{r^2}\frac{\partial\psi}{\partial\theta})]$$
$$\Omega = \frac{1}{r\sin\theta}[\frac{\partial^2\psi}{\partial^2 r^2} + \frac{\sin\theta}{r^2}\frac{\partial}{\partial\theta}(\frac{1}{r\sin\theta}\frac{\partial\psi}{\partial\theta})]$$
$$\Omega = \frac{-1}{r\sin\theta}E^2\psi,$$

where we introduce the differential operator:

$$E^2 = [\frac{\partial^2\psi}{\partial^2 r^2} + \frac{\sin\theta}{r^2}\frac{\partial}{\partial\theta}(\frac{1}{r\sin\theta}\frac{\partial\psi}{\partial\theta})]. \tag{I.5}$$

We insert this result into the equation of momentum and we find:

$$\nabla\boldsymbol{p} = -\mu \times \nabla\Omega$$
$$= \frac{-\mu}{r\sin\theta}\frac{\partial\frac{-E^2\psi}{r}}{\partial\theta}\mathbf{e_r} + \frac{\mu}{r}\frac{\partial\frac{-E^2\psi}{r}}{\partial r}\mathbf{e}_\theta$$
$$= \frac{\mu}{r^2\sin\theta}\frac{\partial E^2\psi}{\partial\theta}\mathbf{e_r} - \frac{\mu}{r\sin\theta}\frac{\partial E^2\psi}{\partial r}\mathbf{e}_\theta$$

.

The left side of this equation is given in spherical coordinates as:

$$\nabla p = \frac{\partial p}{\partial r}\mathbf{e_r} + \frac{1}{r}\frac{\partial p}{\partial\theta}\mathbf{e}_\theta + \frac{1}{r\sin\theta}\frac{\partial r}{\partial\Phi}\mathbf{e_\Phi}$$

.

By identification, equating each terms e_r e e_θ we obtain to two equations for the pressure:

$$\frac{\partial p}{\partial r} = \frac{\mu}{r^2\sin\theta}\frac{\partial E^2\psi}{\partial\theta}; \frac{\partial p}{\partial\theta} = \frac{-\mu}{\sin\theta}\frac{\partial E^2\psi}{\partial r}. \tag{I.6}$$

Since these cross-differentiations must be equal, we find:

$$\frac{\partial^2 E^2\psi}{\partial r^2} + \frac{\sin\theta}{r^2}\frac{\partial\frac{1}{\sin\theta}\frac{\partial E^2\psi}{\partial\theta}}{\partial\theta} = 0$$

.

$$E^2E^2\psi = 0. \tag{I.7}$$

Finally, by inserting the original definition of the differential operator we arrive at a differential equation for the current Stokes function:

$$[\frac{\partial^2}{\partial^2 r^2} + \frac{\sin\theta}{r^2}\frac{\partial}{\partial\theta}\frac{1}{\sin\theta}\frac{\partial}{\partial\theta}]^2\psi = 0. \tag{I.8}$$

We impose the following boundary conditions on the solution:
i) Non-slip condition on the surface of the sphere, $u(a,\theta) = 0$, ii) uniform velocity flow U away from the sphere.

Using the non-slip condition, equation I.4 provides:

$$\frac{\partial\psi}{\partial r}|_{r=a} = 0; \frac{\partial\psi}{\partial\theta}|_{r=a} = 0. \tag{I.9}$$

The uniform flow condition away from the sphere can be formulated as:

$$\lim_{x\to\infty} U_r = U\cos\theta; \lim_{x\to\infty} U_\theta = -U\sin\theta$$

.

This threshold condition will have to be reformulated as using ψ instead of U. Using equation (I.4) to insert expressions in ψ instead of u_r u_θ, this can be achieved through two integrations, producing:

$$\frac{1}{r^2\sin\theta}\frac{\partial\psi}{\partial\theta} = U\cos\theta \Rightarrow \psi = \frac{1}{2}U^2\sin\theta + f(r)$$
$$\frac{-1}{r\sin\theta}\frac{\partial\psi}{\partial r} = -U\sin\theta \Rightarrow \psi = \frac{1}{2}Ur^2\sin\theta^2 + f(\theta)$$

Thus $f(r) = f(\theta) = 0$ and the boundary condition can be reformulated as:

$$\lim_{x\to\infty} \psi = \frac{1}{2}Ur^2\sin\theta^2. \tag{I.10}$$

This leads us to look for a form solution:

$$\psi = f(r)\sin\theta^2. \tag{I.11}$$

Let us examine the effect of the differential operator E^2on a solution of this format

$$E^2 f(r)\sin\theta^2 = \frac{\partial^2}{\partial^2 r^2}(f(r)\sin\theta^2) + \frac{\sin\theta}{r^2}\frac{\partial}{\partial\theta}\frac{1}{\sin\theta}\frac{\partial}{\partial\theta}(f(r)\sin\theta^2)$$

.

We find:

$$E^2 f(r)\sin\theta^2 = \frac{d^2}{d^2r^2} - \frac{2}{r^2}f(r)\sin\theta^2$$

.

We can write a new function

$$g(r) = (\frac{d^2}{d^2r^2} - \frac{2}{r^2})f(r)$$

.

We obtain :

$$E^2(E^2(f(r)\sin\theta^2)) = E^2(g(r)\sin\theta^2))$$
$$= (\frac{d^2}{d^2r^2} - \frac{2}{r^2})f(r)\sin\theta^2)$$

.

If the test function $f(r)\sin\theta^2$ 2 satisfies the differential equation for ψ the equation (I.6), this expression must be zero. Thus, we arrive at a requirement for the function $f(r)$ in the form of an ordinary differential equation in the form:

$$(\frac{d^2}{d^2r^2} - \frac{2}{r^2})_2 f = 0$$

The form of this differential equation suggests solutions of type $f(r) = r^\alpha$ inserting in the last equation we arrive at a fourth order equation in α

$$\alpha((\alpha - 1) - 2((\alpha - 2)(\alpha - 3) - 2 = 0$$

The solutions of this equation are $\alpha = -1, 1, 2, 4$. Thus, we arrive at a solution for the differential equation for ψ of the form:

$$\psi = (Ar^{-1} + Br + Cr^2 + Dr^4)\sin\theta^2$$

The four arbitrary constants are determined by the application of boundary conditions. The uniform coring condition far from the sphere requires that Cr^2 be the dominant term as $r \to \infty$, which in turn implies $D = 0$. The precise formulation of the boundary condition, 10 equation gives $C = \frac{1}{2}U$ The non-slip condition leads to two requirements of the derivatives of ψ. These are used to determine the remaining two constants, A and B. Using equation (I.8) we find: The non-slip condition leads to two requirements of the derivatives of psi. These are used to determine the remaining two constants, A and B. Using equation (I.9) we find:

$$A = \frac{1}{4}Ua^3$$

,

$$B = \frac{-3}{4}Ua$$

.

Having now determined all the arbitrary constants, we obtain the current function:

$$\psi = \frac{1}{4}U(2r^2 - 3ar + a^3r^{-1})\sin\theta^2. \tag{I.12}$$

Inserting in the equation I.3 we obtain the velocity:

$$U_r = U\cos\theta(1 - \frac{3a}{2r} + \frac{a^3}{2r^3}), \tag{I.13}$$

$$U_\theta = -U\sin\theta(1 - \frac{3a}{4r} - \frac{a^3}{4r^3}). \tag{I.14}$$

After determining the velocity expression, we can find an expression for the pressure and then determine an expression for the total drag force on the sphere. An expression for the pressure is more easily obtained by integrating equation (I.4). The first step is to determine the effect of the E^2 operator on the current function;

$$\begin{aligned} E^2\psi &= (\frac{\partial^2}{\partial^2 r^2} + \frac{\sin\theta}{r^2}\frac{\partial}{\partial\theta}(\frac{1}{\sin\theta}\frac{\partial}{\partial\theta}))(\frac{U}{4}(2r^2 - 3ar + ar^{-1}\sin\theta^2)) \\ &= \frac{U}{4}\sin\theta^2(4 + \frac{2a}{r^3} - \frac{U}{2}(\sin\theta^2(2 + \frac{a^3}{r^3} - \frac{3a}{r}) \\ &= \frac{3Ua\sin\theta^2}{2r} \end{aligned}$$

.

Having found this, we can proceed by integrating equation (I.8) to find:

$$p_\infty - p_r = \int_r^\infty \frac{\mu}{r^2\sin\theta}\frac{\partial}{\partial\theta}(\frac{3Ua\sin\theta^2}{2r})dr$$

,

$$p_\infty - p_r = \frac{3\mu Ua\cos\theta}{r^2}. \tag{I.15}$$

To find the force we need the tension first, we can find the tensions in the expressions for the tensors in spherical coordinates

$$\begin{aligned} \sigma_r = T_{rr} &= -p + 2\mu\frac{\partial u}{\partial r} \\ &= -p_\infty + \frac{3\mu U\cos\theta}{2a} \end{aligned}$$

.

We obtain:

$$\sigma_\theta = \frac{3\mu U\cos\theta}{2a}$$

.

Because of the symmetry of the problem, the drag force is the direction of the uniform current away from the sphere. The component of the tensor in this direction is given by:

$$\begin{aligned} \sigma &= \sigma_r\cos\theta - \sigma_\theta\sin\theta \\ &= -p_\infty\cos\theta + \frac{3\mu U}{2a} \end{aligned}$$

.

Thus, we can calculate the total drag force experienced by the sphere, integrating this expression on the surface of the sphere, resulting in the well-known expression for the Stokes drag:

$$F = -6\pi\mu Ua. \tag{I.16}$$

I. HX711 CALIBRATION

Calibration Steps:

Here we described the steps to calibrate the HX711

- Remove any weight on the load cells
- After the balance has been reset by the program, place a known weight on the load cell
- Press the a, s, d, f keys to increase the Calibration Factor by 10,100,1000,10000 respectively or
- Press the z, x, c, v keys to decrease Calibration Factor by 10,100,1000,10000 respectively
- Press ENTER after typing the letter
- Repeat steps 3 through 5 until the measured weight corresponds to the known weight
- Remove the weight again, and reset the Scale (type t + ENTER to zero)
- Put the weight back on and repeat steps 3 through 6 to redo the calibration.

Each load cell may have a different value for the calibration factor. If any measured weight is giving negative value, reverse the A + and A- pin wires. If your balance allows two cells to be used at the same time, perform the calibration procedure with the two cells mounted below the base of the balance. When the balance is of adequate accuracy, stop the procedure and note the value of the Calibration Factor. Redo the calibration process with other known weights if necessary.

I. NUMERIC CODE IN MATLAB

For the computation of the numerical results of force and torque for a helical flagellum, the numerical code in MATLAB language, developed by [29] was used. The code simulates a rotating helix at low Reynolds number using the regularized Stokeslet method of [101], the slender body theory of [16], the slender body theory of [98] and resistive force theory. The method of regularized Stokeslets, originally introduced by [35], is based on the computation of the velocity field due to a distribution of modified expressions for the Stokeslet in which the singularity has been removed. The regularized expression is derived as the exact solution to the Stokes equations consistent with forces given by regularized delta functions. In this Lagrangian method, trajectories of fluid particles are tracked throughout the simulation. The method is particularly useful when the particles are placed along a surface that deforms due to time-dependent, force-driven fluid motion. Since the Stokes equations are linear, direct summation may be used to compute the velocity at each of the immersed boundary points in order to advance a time step. This method is related to boundary integral methods when the forces lie on the surface of a smooth connected set. However, the method of regularized Stokeslets can also be used in cases where the forces are applied at a discrete collection of points that do not necessarily approximate a smooth interface, [101].

The program calculates the propulsive matrix elements, which can be used to estimate the forces and torques on a helical flagellum from measurements of velocity and rotation for a helical geometry. The GUI allows the user to specify a single helical geometry or a range. The results are given in a non-dimensional form. The program is useful for both biological measurements and construction of a bio-mimetic swimmer that uses a helical flagellum for propulsion. The following codes are used in the simulations.

```
function varargout = Simulation_GUI(varargin)
% SIMULATION_GUI M-file for Simulation_GUI.fig
%      SIMULATION_GUI, by itself, creates a new SIMULATION_GUI or raises the
existing
%      singleton*.
%
%      H = SIMULATION_GUI returns the handle to a new SIMULATION_GUI or the
handle to
%      the existing singleton*.
%
%      SIMULATION_GUI('CALLBACK',hObject,eventData,handles,...) calls the local
%      function named CALLBACK in SIMULATION_GUI.M with the given input
arguments.
%
%      SIMULATION_GUI('Property','Value',...) creates a new SIMULATION_GUI or
raises the
%      existing singleton*.  Starting from the left, property value pairs are
%      applied to the GUI before Cross_Section_Gui_OpeningFunction gets called.
An
%      unrecognized property name or invalid value makes property application
%      stop.  All inputs are passed to Simulation_GUI_OpeningFcn via
%      varargin.
%
%      *See GUI Options on GUIDE's Tools menu.  Choose "GUI allows only one
%      instance to run (singleton)".
%
% See also: GUIDE, GUIDATA, GUIHANDLES
% Edit the above text to modify the response to help Simulation_GUI
% Last Modified by GUIDE v2.5 14-Mar-2011 15:39:34
% Begin initialization code - DO NOT EDIT
gui_Singleton = 1;
gui_State = struct('gui_Name',       mfilename, ...
                   'gui_Singleton',  gui_Singleton, ...
                   'gui_OpeningFcn', @Simulation_GUI_OpeningFcn, ...
                   'gui_OutputFcn',  @Simulation_GUI_OutputFcn, ...
                   'gui_LayoutFcn',  [] , ...
                   'gui_Callback',   []);
if nargin && ischar(varargin{1})
    gui_State.gui_Callback = str2func(varargin{1});
end
if nargout
    [varargout{1:nargout}] = gui_mainfcn(gui_State, varargin{:});
else
    gui_mainfcn(gui_State, varargin{:});
end
% End initialization code - DO NOT EDIT
% --- Executes just before Simulation_GUI is made visible.
function Simulation_GUI_OpeningFcn(hObject, eventdata, handles, varargin)
% This function has no output args, see OutputFcn.
% hObject    handle to figure
% eventdata  reserved - to be defined in a future version of MATLAB
% handles    structure with handles and user data (see GUIDATA)
% varargin   command line arguments to Simulation_GUI (see VARARGIN)
% Choose default command line output for Simulation_GUI
handles.output = hObject;
% Update handles structure
guidata(hObject, handles);
% UIWAIT makes Simulation_GUI wait for user response (see UIRESUME)
% uiwait(handles.figure1);
% --- Outputs from this function are returned to the command line.
function varargout = Simulation_GUI_OutputFcn(hObject, eventdata, handles)
% varargout  cell array for returning output args (see VARARGOUT);
```

```
% hObject    handle to figure
% eventdata  reserved - to be defined in a future version of MATLAB
% handles    structure with handles and user data (see GUIDATA)
% Get default command line output from handles structure
varargout{1} = handles.output;
% --- Executes on button press in simulate_forces.
function simulate_forces_Callback(hObject, eventdata, handles)
% hObject    handle to simulate_forces (see GCBO)
% eventdata  reserved - to be defined in a future version of MATLAB
% handles    structure with handles and user data (see GUIDATA)
%% Input arguments from the GUI
%   -R the helical radius (single valued)
%   -a the filament radius (vector)
%   -lambda helical pitch or wavelength (vector)
%   -L axial length of the helix (vector)
%% Read variables %%
R = str2double(get(handles.helical_radius,'String'));
a = str2double(get(handles.filament_radius_min,'String')): ...  % Read a as a
vector as
    str2double(get(handles.filament_radius_step,'String')): ... % [min:step:max]
    str2double(get(handles.filament_radius_max,'String'));
lambda = str2double(get(handles.lambda_min,'String')): ...      % Read lambda
    str2double(get(handles.lambda_step,'String')): ...          % [min:step:max]
    str2double(get(handles.lambda_max,'String'));
L = str2double(get(handles.length_min,'String')): ...           % Read L
    str2double(get(handles.length_step,'String')): ...          % [min:step:max]
    str2double(get(handles.length_max,'String'));
%% Read simulation type(s) and call simulation functions %%
RSM_flag    = get(handles.sim_type_RegSM,'Value');
LH_SBT_flag = get(handles.sim_type_LH_SBT,'Value');
J_SBT_flag  = get(handles.sim_type_J_SBT,'Value');
addpath SBT_Scripts
addpath RSM_Scripts
global force_RSM torque_RSM drag_RSM
global force_LH torque_LH drag_LH
global force_J torque_J drag_J
% global force_GH_RFT torque_GH_RFT drag_GH_RFT
% global force_LH_RFT torque_LH_RFT drag_LH_RFT
global A
if (RSM_flag == 1)
    userchoice=input('Regularized Stokeslet simulations require large amounts of
memory, sometimes in excess of 32 GB.  Do you want to proceed [y/n]: ', 's');
    if userchoice=='y'
        F_T_D_RSM(R, a, lambda, L)
    else
        return
    end
end

if (LH_SBT_flag == 1)
    F_T_D_SBT_LH(R, a, lambda, L)
end
if (J_SBT_flag == 1)
    F_T_D_SBT_Johnson(R, a, lambda, L)
end
%% Save data if selected in GUI %%
if (get(handles.save_data,'Value')==1);
    filename = strcat(get(handles.data_filename,'String'), '.mat');
%     filename = filename{1};   %Matlab decided to add quotes so this removes
them
   save(filename, 'R', 'a', 'lambda', 'L', ...
     'RSM_flag', 'LH_SBT_flag', 'J_SBT_flag', ...
```

```
     'force_RSM', 'torque_RSM', 'drag_RSM', ...
     'force_LH', 'torque_LH', 'drag_LH',  ...
     'force_J', 'torque_J', 'drag_J')
 end
%% Print data into GUI axes
print_data(handles, R,a, lambda, L, ...
    RSM_flag,LH_SBT_flag, J_SBT_flag, ...
    force_RSM, torque_RSM, drag_RSM,...
    force_LH, torque_LH, drag_LH,  ...
    force_J, torque_J, drag_J)
% --- Executes on button press in plot_data.
function plot_data_Callback(hObject, eventdata, handles)
% hObject    handle to plot_data (see GCBO)
% eventdata  reserved - to be defined in a future version of MATLAB
% handles    structure with handles and user data (see GUIDATA)
%% Plot saved data
filename = strcat(get(handles.data_filename,'String'), '.mat');
load(filename)
print_data(handles, R,a, lambda, L, ...
    RSM_flag, LH_SBT_flag, J_SBT_flag, ...
    force_RSM, torque_RSM, drag_RSM,...
    force_LH, torque_LH, drag_LH,  ...
    force_J, torque_J, drag_J)



%% --- Print data from new simulations or loaded data
function print_data(handles, R, a, lambda, L, ...
    RSM_flag, LH_SBT_flag, J_SBT_flag, ...
    force_RSM, torque_RSM, drag_RSM,...
    force_LH, torque_LH, drag_LH,  ...
    force_J, torque_J, drag_J)
%% Calculate RFT values if selected
RFT_flag = get(handles.add_RFT,'Value');
if RFT_flag == 1;
    addpath RFT_Scripts
    [force_GH_RFT, torque_GH_RFT, drag_GH_RFT,force_LH_RFT, torque_LH_RFT,
drag_LH_RFT] = RFT_Calculations(R, a, lambda, L);
end
%% Allow selection of other parameters
    a_to_plot = find(a == str2double(get(handles.a_to_plot,'String')));
        if(a_to_plot > 0); else disp('Selected filament radius value not found,
using first in filament radius (a) vector.');end
    lambda_to_plot = find(lambda ==
str2double(get(handles.lambda_to_plot,'String')));
        if(lambda_to_plot>0); else disp('Selected lambda value not found, using
first in lambda vector.');end
    L_to_plot = find(L == str2double(get(handles.length_to_plot,'String')));
        if(L_to_plot>0); else disp('Selected length value not found, using first
in length (L) vector.');end

%%  Determine plot type, set x variable and dimensions of forces to plot %%
if (get(handles.plot_type_a_dep,'Value') == 1)
    x_var=a;
    x_label = '$a/R$';
    dim1 = [1:length(a)];
    if(lambda_to_plot > 0); dim2=lambda_to_plot; else dim2=1; end
    if(L_to_plot > 0); dim3=L_to_plot; else dim3=1; end
    legend_location = 'NorthWest';
elseif (get(handles.plot_type_lambda_dep,'Value') == 1)
    x_var=lambda;
```

```
    x_label = '$\lambda/R$';
    if(a_to_plot > 0); dim1=a_to_plot; else dim1=1; end
    dim2 = [1:length(lambda)];
    if(L_to_plot > 0); dim3=L_to_plot; else dim3=1; end
    legend_location = 'NorthEast';
elseif (get(handles.plot_type_L_dep,'Value') == 1 )
    x_var=L;
    x_label = '$L/R$';
    if(a_to_plot > 0); dim1=a_to_plot; else dim1=1; end
    if(lambda_to_plot > 0); dim2=lambda_to_plot; else dim2=1; end
    dim3 = [1:length(L)];
    legend_location = 'NorthWest';
end
legend_text = {};  % Initialize legend labels variable
%%  plot thrust %%
 if (get(handles.plot_in_figure,'Value')==1);
     figure; subplot(3,1,1); hold on
 else
    axes(handles.F_plot); cla reset; hold on
 end
    if (RSM_flag == 1);
        plot(x_var, squeeze(force_RSM(dim1, dim2, dim3)), 'k-', 'Linewidth', 2);
        ylim([0,max(1.1*force_RSM(dim1, dim2, dim3))])
        legend_text = [legend_text, 'RSM'];
    end
    if (LH_SBT_flag == 1);
        plot(x_var,squeeze(force_LH(dim1,dim2,dim3)), 'b-', 'Linewidth', 2);
        ylim([0,max(1.1*force_LH(dim1, dim2, dim3))])
        legend_text = [legend_text, 'LH SBT'];
    end
    if (J_SBT_flag == 1);
        plot(x_var, squeeze(force_J(dim1, dim2, dim3)), 'r-', 'Linewidth', 2);
        ylim([0,1.1*max(force_J(dim1, dim2, dim3))])
        legend_text = [legend_text, 'J SBT'];
    end

    if (RFT_flag == 1);
        plot(x_var, squeeze(force_GH_RFT(dim1, dim2, dim3)), 'g-', 'Linewidth',
2);
        ylim([0,1.1*max(force_GH_RFT(dim1, dim2, dim3))])
        plot(x_var, squeeze(force_LH_RFT(dim1, dim2, dim3)), 'b--', 'Linewidth',
2);
        ylim([0,1.1*max(force_LH_RFT(dim1, dim2, dim3))])
        legend_text = [legend_text, 'LH SBT', 'GH SBT'];
    end

    if (get(handles.add_legend,'Value')==1)
        legend(legend_text)
        legend('Location', legend_location)
        legend('boxoff')
    end

xlim([0 1.1*max(x_var)]); set(gca,'XTickLabel',[]);
ylabel('$F/(\mu \Omega R^2)$', 'Interpreter', 'Latex','Fontsize', 14)
%%  plot torque %%
    if (get(handles.plot_in_figure,'Value')==1);
         subplot(3,1,2); hold on
     else
        axes(handles.T_plot); cla reset; hold on;
     end
    if (RSM_flag == 1);
        plot(x_var, squeeze(torque_RSM(dim1, dim2, dim3)), 'k-', 'Linewidth', 2);
```

```
        ylim([0,max(1.1*torque_RSM(dim1, dim2, dim3))])
    end
    if (LH_SBT_flag == 1);
        plot(x_var, squeeze(torque_LH(dim1, dim2, dim3)), 'b-', 'Linewidth', 2);
        ylim([0,max(1.1*torque_LH(dim1, dim2, dim3))])
    end
    if (J_SBT_flag == 1);
        plot(x_var, squeeze(torque_J(dim1, dim2, dim3)), 'r-', 'Linewidth', 2);
        ylim([0,1.1*max(torque_J(dim1, dim2, dim3))])
    end

    if (RFT_flag == 1);
        plot(x_var, squeeze(torque_GH_RFT(dim1, dim2, dim3)), 'g-', 'Linewidth',
2);
        ylim([0,1.1*max(torque_GH_RFT(dim1, dim2, dim3))])
        plot(x_var, squeeze(torque_LH_RFT(dim1, dim2, dim3)), 'b--', 'Linewidth',
2);
        ylim([0,1.1*max(torque_LH_RFT(dim1, dim2, dim3))])
    end

    if (get(handles.add_legend,'Value')==1)
        legend(legend_text)
        legend('Location', legend_location)
        legend('boxoff')
    end

xlim([0 1.1*max(x_var)]); set(gca, 'XTickLabel',[]);
ylabel('$T/(\mu \Omega R^3)$', 'Interpreter', 'Latex','Fontsize', 14)
%%  plot drag %%
if (get(handles.plot_in_figure,'Value')==1);
    subplot(3,1,3); hold on
 else
    axes(handles.D_plot); cla reset; hold on;
end

    if (RSM_flag == 1);
        plot(x_var, squeeze(drag_RSM(dim1, dim2, dim3)), 'k-', 'Linewidth', 2);
        ylim([0,1.1*max(drag_RSM(dim1, dim2, dim3))])
    end
    if (LH_SBT_flag == 1);
        plot(x_var, squeeze(drag_LH(dim1, dim2, dim3)), 'b-', 'Linewidth', 2);
        ylim([0,1.1*max(drag_LH(dim1, dim2, dim3))])
    end
    if (J_SBT_flag == 1);
        plot(x_var, squeeze(drag_J(dim1, dim2, dim3)), 'r-', 'Linewidth', 2);
        ylim([0,1.1*max(drag_J(dim1, dim2, dim3))])
    end

    if (RFT_flag == 1);
        plot(x_var, squeeze(drag_GH_RFT(dim1, dim2, dim3)), 'g-', 'Linewidth',
2);
        ylim([0,1.1*max(drag_GH_RFT(dim1, dim2, dim3))])
        plot(x_var, squeeze(drag_LH_RFT(dim1, dim2, dim3)), 'b--', 'Linewidth',
2);
        ylim([0,1.1*max(drag_LH_RFT(dim1, dim2, dim3))])
    end

    if (get(handles.add_legend,'Value')==1)
        legend(legend_text)
        legend('Location', legend_location)
        legend('boxoff')
    end
```

```
xlim([0 1.1*max(x_var)]); xlabel(x_label, 'Interpreter', 'Latex','Fontsize', 14);
ylabel('$D/(\mu UR)$', 'Interpreter', 'Latex', 'Fontsize', 14)

function length_min_Callback(hObject, eventdata, handles)
% hObject    handle to length_min (see GCBO)
% eventdata  reserved - to be defined in a future version of MATLAB
% handles    structure with handles and user data (see GUIDATA)
% Hints: get(hObject,'String') returns contents of length_min as text
%        str2double(get(hObject,'String')) returns contents of length_min as a
double
% --- Executes during object creation, after setting all properties.
function length_min_CreateFcn(hObject, eventdata, handles)
% hObject    handle to length_min (see GCBO)
% eventdata  reserved - to be defined in a future version of MATLAB
% handles    empty - handles not created until after all CreateFcns called
% Hint: edit controls usually have a white background on Windows.
%       See ISPC and COMPUTER.
if ispc && isequal(get(hObject,'BackgroundColor'),
get(0,'defaultUicontrolBackgroundColor'))
    set(hObject,'BackgroundColor','white');
end
function length_max_Callback(hObject, eventdata, handles)
% hObject    handle to length_max (see GCBO)
% eventdata  reserved - to be defined in a future version of MATLAB
% handles    structure with handles and user data (see GUIDATA)
% Hints: get(hObject,'String') returns contents of length_max as text
%        str2double(get(hObject,'String')) returns contents of length_max as a
double
% --- Executes during object creation, after setting all properties.
function length_max_CreateFcn(hObject, eventdata, handles)
% hObject    handle to length_max (see GCBO)
% eventdata  reserved - to be defined in a future version of MATLAB
% handles    empty - handles not created until after all CreateFcns called
% Hint: edit controls usually have a white background on Windows.
%       See ISPC and COMPUTER.
if ispc && isequal(get(hObject,'BackgroundColor'),
get(0,'defaultUicontrolBackgroundColor'))
    set(hObject,'BackgroundColor','white');
end
function lambda_min_Callback(hObject, eventdata, handles)
% hObject    handle to lambda_min (see GCBO)
% eventdata  reserved - to be defined in a future version of MATLAB
% handles    structure with handles and user data (see GUIDATA)
% Hints: get(hObject,'String') returns contents of lambda_min as text
%        str2double(get(hObject,'String')) returns contents of lambda_min as a
double
% --- Executes during object creation, after setting all properties.
function lambda_min_CreateFcn(hObject, eventdata, handles)
% hObject    handle to lambda_min (see GCBO)
% eventdata  reserved - to be defined in a future version of MATLAB
% handles    empty - handles not created until after all CreateFcns called
% Hint: edit controls usually have a white background on Windows.
%       See ISPC and COMPUTER.
if ispc && isequal(get(hObject,'BackgroundColor'),
get(0,'defaultUicontrolBackgroundColor'))
    set(hObject,'BackgroundColor','white');
end
function lambda_max_Callback(hObject, eventdata, handles)
% hObject    handle to lambda_max (see GCBO)
% eventdata  reserved - to be defined in a future version of MATLAB
% handles    structure with handles and user data (see GUIDATA)
% Hints: get(hObject,'String') returns contents of lambda_max as text
```

```
%        str2double(get(hObject,'String')) returns contents of lambda_max as a
double
% --- Executes during object creation, after setting all properties.
function lambda_max_CreateFcn(hObject, eventdata, handles)
% hObject    handle to lambda_max (see GCBO)
% eventdata  reserved - to be defined in a future version of MATLAB
% handles    empty - handles not created until after all CreateFcns called
% Hint: edit controls usually have a white background on Windows.
%       See ISPC and COMPUTER.
if ispc && isequal(get(hObject,'BackgroundColor'),
get(0,'defaultUicontrolBackgroundColor'))
    set(hObject,'BackgroundColor','white');
end
function helical_radius_Callback(hObject, eventdata, handles)
% hObject    handle to helical_radius (see GCBO)
% eventdata  reserved - to be defined in a future version of MATLAB
% handles    structure with handles and user data (see GUIDATA)
% Hints: get(hObject,'String') returns contents of helical_radius as text
%        str2double(get(hObject,'String')) returns contents of helical_radius as
a double
% --- Executes during object creation, after setting all properties.
function helical_radius_CreateFcn(hObject, eventdata, handles)
% hObject    handle to helical_radius (see GCBO)
% eventdata  reserved - to be defined in a future version of MATLAB
% handles    empty - handles not created until after all CreateFcns called
% Hint: edit controls usually have a white background on Windows.
%       See ISPC and COMPUTER.
if ispc && isequal(get(hObject,'BackgroundColor'),
get(0,'defaultUicontrolBackgroundColor'))
    set(hObject,'BackgroundColor','white');
end
function filament_radius_min_Callback(hObject, eventdata, handles)
% hObject    handle to filament_radius_min (see GCBO)
% eventdata  reserved - to be defined in a future version of MATLAB
% handles    structure with handles and user data (see GUIDATA)
% Hints: get(hObject,'String') returns contents of filament_radius_min as text
%        str2double(get(hObject,'String')) returns contents of
filament_radius_min as a double
% --- Executes during object creation, after setting all properties.
function filament_radius_min_CreateFcn(hObject, eventdata, handles)
% hObject    handle to filament_radius_min (see GCBO)
% eventdata  reserved - to be defined in a future version of MATLAB
% handles    empty - handles not created until after all CreateFcns called
% Hint: edit controls usually have a white background on Windows.
%       See ISPC and COMPUTER.
if ispc && isequal(get(hObject,'BackgroundColor'),
get(0,'defaultUicontrolBackgroundColor'))
    set(hObject,'BackgroundColor','white');
end
function filament_radius_max_Callback(hObject, eventdata, handles)
% hObject    handle to filament_radius_max (see GCBO)
% eventdata  reserved - to be defined in a future version of MATLAB
% handles    structure with handles and user data (see GUIDATA)
% Hints: get(hObject,'String') returns contents of filament_radius_max as text
%        str2double(get(hObject,'String')) returns contents of
filament_radius_max as a double
% --- Executes during object creation, after setting all properties.
function filament_radius_max_CreateFcn(hObject, eventdata, handles)
% hObject    handle to filament_radius_max (see GCBO)
% eventdata  reserved - to be defined in a future version of MATLAB
% handles    empty - handles not created until after all CreateFcns called
% Hint: edit controls usually have a white background on Windows.
```

```
%       See ISPC and COMPUTER.
if ispc && isequal(get(hObject,'BackgroundColor'),
get(0,'defaultUicontrolBackgroundColor'))
    set(hObject,'BackgroundColor','white');
end
% --- Executes on button press in save_data.
function save_data_Callback(hObject, eventdata, handles)
% hObject    handle to save_data (see GCBO)
% eventdata  reserved - to be defined in a future version of MATLAB
% handles    structure with handles and user data (see GUIDATA)
% Hint: get(hObject,'Value') returns toggle state of save_data
% --- Executes on button press in plot_in_figure.
function plot_in_figure_Callback(hObject, eventdata, handles)
% hObject    handle to plot_in_figure (see GCBO)
% eventdata  reserved - to be defined in a future version of MATLAB
% handles    structure with handles and user data (see GUIDATA)
% Hint: get(hObject,'Value') returns toggle state of plot_in_figure
% --- Executes on selection change in plot_type.
function plot_type_Callback(hObject, eventdata, handles)
% hObject    handle to plot_type (see GCBO)
% eventdata  reserved - to be defined in a future version of MATLAB
% handles    structure with handles and user data (see GUIDATA)
% Hints: contents = cellstr(get(hObject,'String')) returns plot_type contents as
cell array
%        contents{get(hObject,'Value')} returns selected item from plot_type
% --- Executes during object creation, after setting all properties.
function plot_type_CreateFcn(hObject, eventdata, handles)
% hObject    handle to plot_type (see GCBO)
% eventdata  reserved - to be defined in a future version of MATLAB
% handles    empty - handles not created until after all CreateFcns called
% Hint: popupmenu controls usually have a white background on Windows.
%       See ISPC and COMPUTER.
if ispc && isequal(get(hObject,'BackgroundColor'),
get(0,'defaultUicontrolBackgroundColor'))
    set(hObject,'BackgroundColor','white');
end;
% --- Executes on button press in sim_type_RegSM.
function checkbox3_Callback(hObject, eventdata, handles)
% hObject    handle to sim_type_RegSM (see GCBO)
% eventdata  reserved - to be defined in a future version of MATLAB
% handles    structure with handles and user data (see GUIDATA)
% Hint: get(hObject,'Value') returns toggle state of sim_type_RegSM
% --- Executes on button press in sim_type_LH_SBT.
function sim_type_LH_SBT_Callback(hObject, eventdata, handles)
% hObject    handle to sim_type_LH_SBT (see GCBO)
% eventdata  reserved - to be defined in a future version of MATLAB
% handles    structure with handles and user data (see GUIDATA)
% Hint: get(hObject,'Value') returns toggle state of sim_type_LH_SBT
% --- Executes on button press in sim_type_J_SBT.
function sim_type_J_SBT_Callback(hObject, eventdata, handles)
% hObject    handle to sim_type_J_SBT (see GCBO)
% eventdata  reserved - to be defined in a future version of MATLAB
% handles    structure with handles and user data (see GUIDATA)
% Hint: get(hObject,'Value') returns toggle state of sim_type_J_SBT
% --- Executes on button press in sim_type_RegSM.
function sim_type_RegSM_Callback(hObject, eventdata, handles)
% hObject    handle to sim_type_RegSM (see GCBO)
% eventdata  reserved - to be defined in a future version of MATLAB
% handles    structure with handles and user data (see GUIDATA)
% Hint: get(hObject,'Value') returns toggle state of sim_type_RegSM
function lambda_step_Callback(hObject, eventdata, handles)
% hObject    handle to lambda_step (see GCBO)
```

```
% eventdata  reserved - to be defined in a future version of MATLAB
% handles    structure with handles and user data (see GUIDATA)
% Hints: get(hObject,'String') returns contents of lambda_step as text
%        str2double(get(hObject,'String')) returns contents of lambda_step as a
double
% --- Executes during object creation, after setting all properties.
function lambda_step_CreateFcn(hObject, eventdata, handles)
% hObject    handle to lambda_step (see GCBO)
% eventdata  reserved - to be defined in a future version of MATLAB
% handles    empty - handles not created until after all CreateFcns called
% Hint: edit controls usually have a white background on Windows.
%       See ISPC and COMPUTER.
if ispc && isequal(get(hObject,'BackgroundColor'),
get(0,'defaultUicontrolBackgroundColor'))
    set(hObject,'BackgroundColor','white');
end
function length_step_Callback(hObject, eventdata, handles)
% hObject    handle to length_step (see GCBO)
% eventdata  reserved - to be defined in a future version of MATLAB
% handles    structure with handles and user data (see GUIDATA)
% Hints: get(hObject,'String') returns contents of length_step as text
%        str2double(get(hObject,'String')) returns contents of length_step as a
double
% --- Executes during object creation, after setting all properties.
function length_step_CreateFcn(hObject, eventdata, handles)
% hObject    handle to length_step (see GCBO)
% eventdata  reserved - to be defined in a future version of MATLAB
% handles    empty - handles not created until after all CreateFcns called
% Hint: edit controls usually have a white background on Windows.
%       See ISPC and COMPUTER.
if ispc && isequal(get(hObject,'BackgroundColor'),
get(0,'defaultUicontrolBackgroundColor'))
    set(hObject,'BackgroundColor','white');
end
function filament_radius_step_Callback(hObject, eventdata, handles)
% hObject    handle to filament_radius_step (see GCBO)
% eventdata  reserved - to be defined in a future version of MATLAB
% handles    structure with handles and user data (see GUIDATA)
% Hints: get(hObject,'String') returns contents of filament_radius_step as text
%        str2double(get(hObject,'String')) returns contents of
filament_radius_step as a double
% --- Executes during object creation, after setting all properties.
function filament_radius_step_CreateFcn(hObject, eventdata, handles)
% hObject    handle to filament_radius_step (see GCBO)
% eventdata  reserved - to be defined in a future version of MATLAB
% handles    empty - handles not created until after all CreateFcns called
% Hint: edit controls usually have a white background on Windows.
%       See ISPC and COMPUTER.
if ispc && isequal(get(hObject,'BackgroundColor'),
get(0,'defaultUicontrolBackgroundColor'))
    set(hObject,'BackgroundColor','white');
end
function data_filename_Callback(hObject, eventdata, handles)
% hObject    handle to data_filename (see GCBO)
% eventdata  reserved - to be defined in a future version of MATLAB
% handles    structure with handles and user data (see GUIDATA)
% Hints: get(hObject,'String') returns contents of data_filename as text
%        str2double(get(hObject,'String')) returns contents of data_filename as a
double
% --- Executes during object creation, after setting all properties.
function data_filename_CreateFcn(hObject, eventdata, handles)
% hObject    handle to data_filename (see GCBO)
```

```
% eventdata  reserved - to be defined in a future version of MATLAB
% handles    empty - handles not created until after all CreateFcns called
% Hint: edit controls usually have a white background on Windows.
%       See ISPC and COMPUTER.
if ispc && isequal(get(hObject,'BackgroundColor'),
get(0,'defaultUicontrolBackgroundColor'))
    set(hObject,'BackgroundColor','white');
end

function lambda_to_plot_Callback(hObject, eventdata, handles)
% hObject    handle to lambda_to_plot (see GCBO)
% eventdata  reserved - to be defined in a future version of MATLAB
% handles    structure with handles and user data (see GUIDATA)
% Hints: get(hObject,'String') returns contents of lambda_to_plot as text
%        str2double(get(hObject,'String')) returns contents of lambda_to_plot as
a double
% --- Executes during object creation, after setting all properties.
function lambda_to_plot_CreateFcn(hObject, eventdata, handles)
% hObject    handle to lambda_to_plot (see GCBO)
% eventdata  reserved - to be defined in a future version of MATLAB
% handles    empty - handles not created until after all CreateFcns called
% Hint: edit controls usually have a white background on Windows.
%       See ISPC and COMPUTER.
if ispc && isequal(get(hObject,'BackgroundColor'),
get(0,'defaultUicontrolBackgroundColor'))
    set(hObject,'BackgroundColor','white');
end
function edit54_Callback(hObject, eventdata, handles)
% hObject    handle to edit54 (see GCBO)
% eventdata  reserved - to be defined in a future version of MATLAB
% handles    structure with handles and user data (see GUIDATA)
% Hints: get(hObject,'String') returns contents of edit54 as text
%        str2double(get(hObject,'String')) returns contents of edit54 as a double
% --- Executes during object creation, after setting all properties.
function edit54_CreateFcn(hObject, eventdata, handles)
% hObject    handle to edit54 (see GCBO)
% eventdata  reserved - to be defined in a future version of MATLAB
% handles    empty - handles not created until after all CreateFcns called
% Hint: edit controls usually have a white background on Windows.
%       See ISPC and COMPUTER.
if ispc && isequal(get(hObject,'BackgroundColor'),
get(0,'defaultUicontrolBackgroundColor'))
    set(hObject,'BackgroundColor','white');
end
function length_to_plot_Callback(hObject, eventdata, handles)
% hObject    handle to length_to_plot (see GCBO)
% eventdata  reserved - to be defined in a future version of MATLAB
% handles    structure with handles and user data (see GUIDATA)
% Hints: get(hObject,'String') returns contents of length_to_plot as text
%        str2double(get(hObject,'String')) returns contents of length_to_plot as
a double
% --- Executes during object creation, after setting all properties.
function length_to_plot_CreateFcn(hObject, eventdata, handles)
% hObject    handle to length_to_plot (see GCBO)
% eventdata  reserved - to be defined in a future version of MATLAB
% handles    empty - handles not created until after all CreateFcns called
% Hint: edit controls usually have a white background on Windows.
%       See ISPC and COMPUTER.
if ispc && isequal(get(hObject,'BackgroundColor'),
get(0,'defaultUicontrolBackgroundColor'))
    set(hObject,'BackgroundColor','white');
end
```

```
function edit57_Callback(hObject, eventdata, handles)
% hObject    handle to edit57 (see GCBO)
% eventdata  reserved - to be defined in a future version of MATLAB
% handles    structure with handles and user data (see GUIDATA)
% Hints: get(hObject,'String') returns contents of edit57 as text
%        str2double(get(hObject,'String')) returns contents of edit57 as a double
% --- Executes during object creation, after setting all properties.
function edit57_CreateFcn(hObject, eventdata, handles)
% hObject    handle to edit57 (see GCBO)
% eventdata  reserved - to be defined in a future version of MATLAB
% handles    empty - handles not created until after all CreateFcns called
% Hint: edit controls usually have a white background on Windows.
%       See ISPC and COMPUTER.
if ispc && isequal(get(hObject,'BackgroundColor'),
get(0,'defaultUicontrolBackgroundColor'))
    set(hObject,'BackgroundColor','white');
end
function a_to_plot_Callback(hObject, eventdata, handles)
% hObject    handle to a_to_plot (see GCBO)
% eventdata  reserved - to be defined in a future version of MATLAB
% handles    structure with handles and user data (see GUIDATA)
% Hints: get(hObject,'String') returns contents of a_to_plot as text
%        str2double(get(hObject,'String')) returns contents of a_to_plot as a
double
% --- Executes during object creation, after setting all properties.
function a_to_plot_CreateFcn(hObject, eventdata, handles)
% hObject    handle to a_to_plot (see GCBO)
% eventdata  reserved - to be defined in a future version of MATLAB
% handles    empty - handles not created until after all CreateFcns called
% Hint: edit controls usually have a white background on Windows.
%       See ISPC and COMPUTER.
if ispc && isequal(get(hObject,'BackgroundColor'),
get(0,'defaultUicontrolBackgroundColor'))
    set(hObject,'BackgroundColor','white');
end
function edit59_Callback(hObject, eventdata, handles)
% hObject    handle to edit59 (see GCBO)
% eventdata  reserved - to be defined in a future version of MATLAB
% handles    structure with handles and user data (see GUIDATA)
% Hints: get(hObject,'String') returns contents of edit59 as text
%        str2double(get(hObject,'String')) returns contents of edit59 as a double
% --- Executes during object creation, after setting all properties.
function edit59_CreateFcn(hObject, eventdata, handles)
% hObject    handle to edit59 (see GCBO)
% eventdata  reserved - to be defined in a future version of MATLAB
% handles    empty - handles not created until after all CreateFcns called
% Hint: edit controls usually have a white background on Windows.
%       See ISPC and COMPUTER.
if ispc && isequal(get(hObject,'BackgroundColor'),
get(0,'defaultUicontrolBackgroundColor'))
    set(hObject,'BackgroundColor','white');
end
function edit60_Callback(hObject, eventdata, handles)
% hObject    handle to edit60 (see GCBO)
% eventdata  reserved - to be defined in a future version of MATLAB
% handles    structure with handles and user data (see GUIDATA)
% Hints: get(hObject,'String') returns contents of edit60 as text
%        str2double(get(hObject,'String')) returns contents of edit60 as a double
% --- Executes during object creation, after setting all properties.
function edit60_CreateFcn(hObject, eventdata, handles)
% hObject    handle to edit60 (see GCBO)
% eventdata  reserved - to be defined in a future version of MATLAB
```

```
% handles    empty - handles not created until after all CreateFcns called
% Hint: edit controls usually have a white background on Windows.
%       See ISPC and COMPUTER.
if ispc && isequal(get(hObject,'BackgroundColor'),
get(0,'defaultUicontrolBackgroundColor'))
    set(hObject,'BackgroundColor','white');
end
% --- Executes on button press in add_RFT.
function add_RFT_Callback(hObject, eventdata, handles)
% hObject    handle to add_RFT (see GCBO)
% eventdata  reserved - to be defined in a future version of MATLAB
% handles    structure with handles and user data (see GUIDATA)
% Hint: get(hObject,'Value') returns toggle state of add_RFT
% --- Executes on button press in add_legend.
function add_legend_Callback(hObject, eventdata, handles)
% hObject    handle to add_legend (see GCBO)
% eventdata  reserved - to be defined in a future version of MATLAB
% handles    structure with handles and user data (see GUIDATA)
% Hint: get(hObject,'Value') returns toggle state of add_legend


%%%%%%%%%%%%%%%%%%%%%%%%%%%%%%%%%%%%%%%%%%%%%%%%%%%%%%%%%%%%%%%%%%%%%%%

function[force_GH_RFT, torque_GH_RFT, drag_GH_RFT,force_LH_RFT torque_LH_RFT
drag_LH_RFT] = RFT_Calculations(R, a, lambda, L)
%Gray and Hancock resistive force theory
%
% Input arguments:
%   -R helical radius
%   -a filament radius
%   -lambda is the helical pitch
%   -L is axial length
%
% Output arguments:
%   -force_GH_RFT torque_GH_RFT drag_GH_RFT are the Gray and Hancock RFT axial
force, torque and drag, respectively
%   -force_LH_RFT torque_LH_RFT drag_LH_RFT are the Lighthill RFT axial force,
torque and drag, respectively
%       *Note that these output forces are normalized by 4 pi mu R
%
% global force_GH_RFT torque_GH_RFT drag_GH_RFT
% global force_LH_RFT torque_LH_RFT drag_LH_RFT
theta=atan(2*pi./lambda);  % Determine pitch angle
for i = 1:length(a)
    for j=1:length(lambda)
        for k= 1:length(L)

            %%  Gray and Hancock RFT
            Ct=2*pi/[log(2*lambda(j)/a(i))-.5];  %No mu because will be
nondimensionalized
            Cn=4*pi/[log(2*lambda(j)/a(i))+.5];
            force_GH_RFT(i,j,k)=(Cn-Ct)*sin(theta(j))*L(k); %No omega*R

torque_GH_RFT(i,j,k)=[Cn*cos(theta(j))^2+Ct*sin(theta(j))^2]*L(k)/cos(theta(j));
%No omega*R^2

drag_GH_RFT(i,j,k)=[Cn*sin(theta(j))^2+Ct*cos(theta(j))^2]*L(k)/cos(theta(j));
%No omega*R^2
            %%  Lighthill RFT
            Ct=2*pi/[log(0.18*lambda(j)/a(i)/cos(theta(j)))];  %No mu because
nondimensionalized
            Cn=4*pi/[log(0.18*lambda(j)/a(i)/cos(theta(j)))+.5];
```

```
            force_LH_RFT(i,j,k)=(Cn-Ct)*sin(theta(j))*L(k); %No omega*R

torque_LH_RFT(i,j,k)=[Cn*cos(theta(j))^2+Ct*sin(theta(j))^2]*L(k)/cos(theta(j));
%No omega*R^2

drag_LH_RFT(i,j,k)=[Cn*sin(theta(j))^2+Ct*cos(theta(j))^2]*L(k)/cos(theta(j));
%No U*R
        end
    end
end


%%%%%%%%%%%%%%%%%%%%%%%%%%%%%%%%%%%%%%%%%%%%%%%%%%%%%%%%%%%%%%%%%%%%%%%%%%%

function BuildMatrixRegStokes3D(x,X0,N,N0,d)
%%
%% BUILD THE MATRIX A FOR STOKES FLOW
%%
% d is the regularization parameter
% miu is the viscosity
%  the Kernal Matrix as the global variable
global A
mu = 1;
fac0 = 1/(8*pi*mu);
%fac0 = 1;
AXX = zeros(N,1);
AYY = zeros(N,1);
AZZ = zeros(N,1);
AXY = zeros(N,1);
AXZ = zeros(N,1);
AYZ = zeros(N,1);
N3 = 3*N;
d2 = d^2;
for i=1:N0
  dx = X0(i,1)-x(:,1); dy = X0(i,2)-x(:,2);
  dz = X0(i,3)-x(:,3);
  %dz = dx - dx;
  r2 = dx.^2 + dy.^2 + dz.^2;
%% FOR STOKES FLOWS
 tmp = (r2+d2).^(3/2);
 H2 = 1./tmp;
 H1 = (r2+2*d2).*H2;

%--------------------------
  AXX = H1 + H2.*dx.*dx ;
  AYY = H1 + H2.*dy.*dy ;
  AZZ = H1 + H2.*dz.*dz;
  AXY = H2.*dx.*dy;
  AXZ = H2.*dx.*dz;
  AYZ = H2.*dy.*dz;
  A(3*i-2,1:3:N3) = AXX;
  A(3*i-2,2:3:N3) = AXY;
  A(3*i-2,3:3:N3) = AXZ;

  A(3*i-1,1:3:N3) = AXY;
  A(3*i-1,2:3:N3) = AYY;
  A(3*i-1,3:3:N3) = AYZ;

  A(3*i,1:3:N3) = AXZ;
  A(3*i,2:3:N3) = AYZ;
  A(3*i,3:3:N3) = AZZ;
```

```
end
A = A*fac0;
end


%%%%%%%%%%%%%%%%%%%%%%%%%%%%%%%%%%%%%%%%%%%%%%%%%%%%%%%%%%%%%%%%%%%%%%%%

function [F1,F2,F3,T1,T2,T3,A1,A2,A3] =
ExpFlagellumFullTubeMatrix(Sep,Fila_Radius,Radius,Length,Lambda_in)
% compute the force on a rotating helix by regularized Stokeslets.
% clean code / nov. 7
% compute torque and drag coefficient
%%%%%%%%%%%%%%%%%%%%%%%%% parameters %%%%%%%%%%%%%%%%%%%%%%%%%55
% Sep: distance from boundary;
% Fila_Radius: radius of the filament;
% Radius: radius of the helix;
% Length: total length of the helix;
% Lambda_in: wavelength of the helix;
%%%%%%%%%%%%%%%%%%%%%%%%%%%%%%%%%%%%%%%%%%%%%%%%%%%%%%%%%%%%%%%%%%%%%%%%
%  the Kernal Matrix as the global variable
global A
% regularization parameter and grid spacing
Reg = Fila_Radius*0.25;
PointsPerCross = 12;
% filament radius
F_r = Fila_Radius;
% construct a flagellum
Omega = -1;
h = Radius;
Lambda = Lambda_in;
K = 2*pi/Lambda;
KE = 1;
Phi = atan(2*pi*h/Lambda);
% s is the paramter along axis
s = 0:Fila_Radius*cos(Phi)*0.5:Length;
TotalPoints = length(s);
% Ensure enough memory is available by checking architecture
mem_required = 8*(3*TotalPoints)^2;
hard_type=ispc;
mat_version = version;
    mat_version=mat_version(length(mat_version)-5:length(mat_version)-2);
    mat_version=str2num(mat_version);
if hard_type==0
    if mat_version>2012
        max_array=memory;
        if max_array.MaxPossibleArrayBytes<mem_required
            userchoice=input('You do not have enough memory for this simulation.
The program will now end with errors.');
        end
    end
else
    max_array=memory;
    if max_array.MaxPossibleArrayBytes<mem_required
        userchoice=input('You do not have enough memory for this simulation.  The
program will now end with errors.');
    end

end
E_x = s-s + 1;
% displacement from the boundary
Dz = Sep;
% up-right flagellum along z axis
```

```
Grid_z = s;
Grid_x = E_x.*cos(-K*Grid_z)*h;
Grid_y = E_x.*sin(-K*Grid_z)*h;
%%% construct mesh
[x_o,y_o,z_o]=tubeplot(Grid_x,Grid_y,Grid_z,F_r,Grid_z,PointsPerCross);
x_o = x_o';
y_o = y_o';
z_o = z_o';
% cap points
cap1_x = mean(x_o(:,1));
cap1_y = mean(y_o(:,1));
cap1_z = mean(z_o(:,1));
cap2_x = mean(x_o(:,end));
cap2_y = mean(y_o(:,end));
cap2_z = mean(z_o(:,end));
x_o1 = x_o(1:PointsPerCross,:);
x_o1 = x_o1(:)';
y_o1 = y_o(1:PointsPerCross,:);
y_o1 = y_o1(:)';
z_o1 = z_o(1:PointsPerCross,:);
z_o1 = z_o1(:)';
ttt = length(y_o1);
x_o = [];y_o = [];z_o = [];
% add cap points
y_o(1) = cap1_y;
y_o(2:1+ttt) = y_o1;
y_o(ttt+2) = cap2_y;
x_o(1) = cap1_x;
x_o(2:1+ttt) = x_o1;
x_o(ttt+2) = cap2_x;
z_o(1) = cap1_z;
z_o(2:1+ttt) = z_o1;
z_o(ttt+2) = cap2_z;
PointsOnAFlagellum = length(x_o);
% loop over time axis
Time_Steps = 3;
Time_i = linspace(0,2*pi/abs(Omega),Time_Steps);
for ijk = 1:length(Time_i)-1

    % rotate along z axis by a phase determined by time
    Angle = - Time_i(ijk)*Omega;
    Grid_z = z_o;
    Grid_x =  x_o*cos(Angle) + y_o*sin(-Angle);
    Grid_y =  x_o*sin(Angle) + y_o*cos(Angle);

    V_x = Grid_y*Omega;
    V_y = -1*Grid_x*Omega;
    V_z = V_y - V_y;
    % rotate the flagellum along y axis
    Angle = -pi/2;
    Grid_x_r =  Grid_x*cos(Angle) + Grid_z*sin(-Angle);
    Grid_z_r =  Grid_x*sin(Angle) + Grid_z*cos(Angle);
    Grid_y_r = Grid_y;
    V_x_r = V_x*cos(Angle) + V_z*sin(-Angle);
    V_z_r = V_x*sin(Angle) + V_z*cos(Angle);
    V_y_r = V_y;

    % move to upspace
    % displace flagella and make an array

    Dx = 4.5;
    Dy = 2;
```

```
% set PairsX, PairsY to be 1
PairsX = 1;
PairsY = 1;
% displace Grid_z
Grid_z_r = Grid_z_r + Dz;
Grid_x = [];
Grid_y = [];
Grid_z = [];
V_x = [];
V_y = [];
V_z = [];
for ij = 1:PairsX
    for kk = 1:PairsY
        Grid_x = [Grid_x,Grid_x_r];
        Grid_y = [Grid_y,Grid_y_r];
        Grid_z = [Grid_z,Grid_z_r];
        V_x = [V_x,V_x_r];
        V_y = [V_y,V_y_r];
        V_z = [V_z,V_z_r];
        Grid_y_r = Grid_y_r + Dy;
    end
    Grid_y_r = Grid_y_r - PairsY*Dy;
    Grid_x_r = Grid_x_r + Dx;
end
Grid = [Grid_x; Grid_y; Grid_z]';
TotalPoints = length(Grid_x);

V_All = zeros(TotalPoints*3,1);
V_All(1:3:end) = V_x;
V_All(2:3:end) = V_y;
V_All(3:3:end) = V_z;

% construct the Kernal Matrix
if (ijk==1)
    A = zeros(3*TotalPoints,3*TotalPoints);
end

BuildMatrixRegStokes3D(Grid,Grid,TotalPoints,TotalPoints,Reg);

tmp1 = gmres(A,V_All,10,1e-10,100);
tmp1 = tmp1';

FX(ijk)= sum(tmp1(1:3:end));
FY(ijk)= sum(tmp1(2:3:end));
FZ(ijk)= sum(tmp1(3:3:end));

Grid_z = Grid_z - Dz;
% compute torque r x F
TX(ijk) = sum(Grid_y.*tmp1(3:3:end) - Grid_z.*tmp1(2:3:end));
TY(ijk) = sum(Grid_z.*tmp1(1:3:end) - Grid_x.*tmp1(3:3:end));
TZ(ijk) = sum(Grid_x.*tmp1(2:3:end) - Grid_y.*tmp1(1:3:end));

% compute translation
V_All(1:3:end) = 1;
V_All(2:3:end) = 0;
V_All(3:3:end) = 0;

%tmp1 = qmr(A,V_All,1e-10,500);%L1,U1);
tmp1 = gmres(A,V_All,10,1e-10,100);
AX(ijk)= sum(tmp1(1:3:end));
AY(ijk)= sum(tmp1(2:3:end));
AZ(ijk)= sum(tmp1(3:3:end));
```

```
    ijk  % Put loop count out to terminal

end
F1 = mean(FX);
F2 = mean(FY);
F3 = mean(FZ);
T1 = mean(TX);
T2 = mean(TY);
T3 = mean(TZ);
A1 = mean(AX);
A2 = mean(AY);
A3 = mean(AZ);
clear global A


%%%%%%%%%%%%%%%%%%%%%%%%%%%%%%%%%%%%%%%%%%%%%%%%%%%%%%%%%%%%%%%%%%%%%%%

function F_T_D_RSM(R, a, lambda, L)
% Input Arguments
%   -R the helical radius (single valued)
%   -a the filament radius (vector)
%   -lambda helical pitch or wavelength (vector)
%   -L axial length of the helix (vector)
global force_RSM torque_RSM drag_RSM
zz = 250;
for i = 1:length(a)
    for j=1:length(lambda)
        for k= 1:length(L)

           [F1,F2,F3,T1,T2,T3,A1,A2,A3] =
ExpFlagellumFullTubeMatrix(zz,a(i),R,L(k),lambda(j));
            force_RSM(i,j,k) = F1;
            force_RSM_Y(i,j,k) = F2;  %% Y and Z values are not used
            force_RSM_Z(i,j,k) = F3;
            torque_RSM(i,j,k) = T1;
            torque_RSM_Y(i,j,k) = T2;
            torque_RSM_Z(i,j,k) = T3;
            drag_RSM(i,j,k) = A1;
            drag_RSM_Y(i,j,k) = A2;
            drag_RSM_Z(i,j,k) = A3;

        end
    end
end


%%%%%%%%%%%%%%%%%%%%%%%%%%%%%%%%%%%%%%%%%%%%%%%%%%%%%%%%%%%%%%%%%%%%%%%

function [T,N,B,k,t] = frenet(x,y,z),
% FRENET - Frenet-Serret Space Curve Invarients
%
%   [T,N,B,k,t] = frenet(x,y);
%   [T,N,B,k,t] = frenet(x,y,z);
%
%   Returns the 3 vector and 2 scaler invarients of a space curve defined
%   by vectors x,y and z.  If z is omitted then the curve is only a 2D,
%   but the equations are still valid.
%
%        r'
%    T = ----  (Tangent)
```

```
%        |r'|
%
%     _     T'
%     N = ----  (Normal)
%         |T'|
%
%     _   _   _
%     B = T x N (Binormal)
%
%     k = |T'|  (Curvature)
%
%     t = dot(-B',N) (Torsion)
%
%
%     Example:
%     theta = 2*pi*linspace(0,2,100);
%     x = cos(theta);
%     y = sin(theta);
%     z = theta/(2*pi);
%     [T,N,B,k,t] = frenet(x,y,z);
%     line(x,y,z), hold on
%     quiver3(x,y,z,T(:,1),T(:,2),T(:,3),'color','r')
%     quiver3(x,y,z,N(:,1),N(:,2),N(:,3),'color','g')
%     quiver3(x,y,z,B(:,1),B(:,2),B(:,3),'color','b')
%     legend('Curve','Tangent','Normal','Binormal')
%
%
% See also: GRADIENT
if nargin == 2,
    z = zeros(size(x));
end
% CONVERT TO COLUMN VECTOR
x = x(:);
y = y(:);
z = z(:);
% SPEED OF CURVE
dx = gradient(x);
dy = gradient(y);
dz = gradient(z);
dr = [dx dy dz];
ddx = gradient(dx);
ddy = gradient(dy);
ddz = gradient(dz);
ddr = [ddx ddy ddz];
% TANGENT
T = dr./mag(dr,3);
% DERIVIATIVE OF TANGENT
dTx =  gradient(T(:,1));
dTy =  gradient(T(:,2));
dTz =  gradient(T(:,3));
dT = [dTx dTy dTz];
% NORMAL
N = dT./mag(dT,3);
% BINORMAL
B = cross(T,N);
% CURVATURE
% k = mag(dT,1);
k = mag(cross(dr,ddr),1)./((mag(dr,1)).^3);
% TORSION
t = dot(-B,N,2);
function N = mag(T,n),
% MAGNATUDE OF A VECTOR (Nx3)
%  M = mag(U)
```

```
N = sum(abs(T).^2,2).^(1/2);
d = find(N==0);
N(d) = eps*ones(size(d));
N = N(:,ones(n,1));


%%%%%%%%%%%%%%%%%%%%%%%%%%%%%%%%%%%%%%%%%%%%%%%%%%%%%%%%%%%%%%%%%%%%%%%

function [varargout]=tubeplot(x,y,z,varargin)
% TUBEPLOT - plots a tube r along the space curve x,y,z.
%
% tubeplot(x,y,z) plots the basic tube with radius 1
% tubeplot(x,y,z,r) plots the basic tube with variable radius r (either a vector
or a value)
% tubeplot(x,y,z,r,v) plots the basic tube with coloring dependent on the values
in the vector v
% tubeplot(x,y,z,r,v,s) plots the tube with s tangential subdivisions (default is
6)
%
% [X,Y,Z]=tubeplot(x,y,z) returns [Nx3] matrices suitable for mesh or surf
%
% Note that the tube may pinch at points where the normal and binormal
% misbehaves. It is suitable for general space curves, not ones that
% contain straight sections. Normally the tube is calculated using the
% Frenet frame, making the tube minimally twisted except at inflexion points.
%
% To deal with this problem there is an alternative frame:
% tubeplot(x,y,z,r,v,s,vec) calculates the tube by setting the normal to
% the cross product of the tangent and the vector vec. If it is chosen so
% that it is always far from the tangent vector the frame will not twist unduly
%
% Example:
%
%  t=0:(2*pi/100):(2*pi);
%  x=cos(t*2).*(2+sin(t*3)*.3);
%  y=sin(t*2).*(2+sin(t*3)*.3);
%  z=cos(t*3)*.3;
%  tubeplot(x,y,z,0.14*sin(t*5)+.29,t,10)
%
% Written by Anders Sandberg, asa@nada.kth.se, 2005
  subdivs = 6;
  N=size(x,1);
  if (N==1)
    x=x';
    y=y';
    z=z';
    N=size(x,1);
  end
  if (nargin == 3)
    r=x*0+1;
  else
    r=varargin{1};
    if (size(r,1)==1 & size(r,2)==1)
      r=r*ones(N,1);
    end
  end
  if (nargin > 5)
    subdivs=varargin{3}+1;
  end
  if (nargin > 6)
    vec=varargin{4};
    [t,n,b]=frame(x,y,z,vec);
```

```
  else
    [t,n,b]=frenet(x,y,z);
  end



  X=zeros(N,subdivs);
  Y=zeros(N,subdivs);
  Z=zeros(N,subdivs);
  theta=0:(2*pi/(subdivs-1)):(2*pi);
  for i=1:N
    X(i,:)=x(i) + r(i)*(n(i,1)*cos(theta) + b(i,1)*sin(theta));
    Y(i,:)=y(i) + r(i)*(n(i,2)*cos(theta) + b(i,2)*sin(theta));
    Z(i,:)=z(i) + r(i)*(n(i,3)*cos(theta) + b(i,3)*sin(theta));
  end
  if (nargout==0)
    if (nargin > 4)
      V=varargin{2};
      if (size(V,1)==1)
       V=V';
      end
      V=V*ones(1,subdivs);
      surf(X,Y,Z,V);
    else
      surf(X,Y,Z);
    end
  else
    varargout(1) = {X};
    varargout(2) = {Y};
    varargout(3) = {Z};
  end

%%%%%%%%%%%%%%%%%%%%%%%%%%%%%%%%%%%%%%%%%%%%%%%%%%%%%%%%%%%%%%%%%%%%%%%%%%%

function F_T_D_SBT_Johnson(R, a, lambda, L)
%
% Input arguments:
%   -a_lambda is the ratio of filament radius "a" to the wavelength
%       "lambda", i.e., a_lambda=a/lambda
%   -theta is the pitch angle
%   -nlength is the axial length of helix in the unit of its wavelength
%       for one period of helix, nlength = 1.
%       when nlength is a vector, it stores the length of a set of helixes
%       to compute for the force.
%   -res is the number of meshes per wave length, typally I set res=20.
%
%   -omega is the linear rotation speed
%   -V is the translation speed
%
% Output arguments:
%   -F, T are the mean forces per arclength along the translation and rotation
%       directions, respectively. which are stored as vectors of the same size as
%       as nlength.
%       *Note that these output forces are normalized by 4 pi mu R
%
%   vphi is the mesh of helical phase, which is stored as a vector
%
global force_J torque_J drag_J
theta = atan(2*pi*R./lambda);    %Pitch angle

for j = 1:length(lambda)
```

```
        a_lambda(:,j) = a(:)./lambda(j)*4/pi;  %Adjust filament radius to be
equivalent to RSM and Lighthill SBT sims
end

for j = 1:length(lambda)
        nlength(j,:) = L./lambda(j);
        contour_length(j,:) = lambda(j)./cos(theta(j)) .* nlength(j,:);
end
phirange = nlength*2*pi;
res = 20;
nres=floor(nlength*res+.5);
% contour_length = lambda./cos(theta) .* nlength;
arc_length = contour_length./nres;
%Get F and T for nontranslating flagellum
omega = 1.0;    %Set rotation rate to unity
V = 0.0;        %Set velocity to zero
for i = 1:length(a)
    for j=1:length(lambda)
        for k= 1:length(L)
            [F_J, T_J] = SBT_helical_Johnson(a_lambda(i,j), theta(j),
nlength(j,k), res, omega, V);
            force_J(i,j,k)=-sum(F_J)*4*pi*arc_length(j,k);
            torque_J(i,j,k)=sum(T_J)*4*pi*arc_length(j,k);
        end
    end
end
%Get F and T for nonrotating flagellum
omega = 0.0;    %Set rotation rate to zero
V = 1.0;        %Set velocity to unity
for i = 1:length(a)
    for j=1:length(lambda)
        for k= 1:length(L)
            [F_J, T_J] = SBT_helical_Johnson(a_lambda(i,j), theta(j),
nlength(j,k), res, omega, V);
            drag_J(i,j,k)=sum(F_J)*4*pi*arc_length(j,k);
        end
    end
end


%%%%%%%%%%%%%%%%%%%%%%%%%%%%%%%%%%%%%%%%%%%%%%%%%%%%%%%%%%%%%%%%%%%%%%%%

function F_T_D_SBT_LH(R, a, lambda, L)
%
% Input arguments:
%   -a_lambda is the ratio of filament radius "a" to the wavelength
%       "lambda", i.e., a_lambda=a/lambda
%   -theta is the pitch angle
%   -nlength is the axial length of helix in the unit of its wavelength
%       for one period of helix, nlength = 1.
%       when nlength is a vector, it stores the length of a set of helixes
%       to compute for the force.
%   -res is the number of meshes per wave length, typally I set res=20.
%
%   -omega is the linear rotation speed
%   -V is the translation speed
%
% Output arguments:
%   -F, T are the mean forces per arclength along the translation and rotation
%       directions, respectively. which are stored as vectors of the same size as
%       as nlength.
%       *Note that these output forces are normalized by 4 pi mu R
```

```
%
%   vphi is the mesh of helical phase, which is stored as a vector
%
global force_LH torque_LH drag_LH
theta = atan(2*pi*R./lambda);    %Pitch angle

for j = 1:length(lambda)
        a_lambda(:,j) = a(:)./lambda(j);
end

for j = 1:length(lambda)
        nlength(j,:) = L./lambda(j);
        contour_length(j,:) = lambda(j)./cos(theta(j)) .* nlength(j,:);
end
phirange = nlength*2*pi;
res = 20;
nres=floor(nlength*res+.5);
% contour_length = lambda./cos(theta) .* nlength;
arc_length = contour_length./nres;
%Get F and T for nontranslating flagellum
omega = 1.0;    %Set rotation rate to unity
V = 0.0;        %Set velocity to zero
for i = 1:length(a)
    for j=1:length(lambda)
        for k= 1:length(L)
            [F_LH, T_LH] = SBT_helical_Lighthill(a_lambda(i,j), theta(j),
nlength(j,k), res, omega, V);
            force_LH(i,j,k)=-sum(F_LH)*4*pi*arc_length(j,k);
            torque_LH(i,j,k)=sum(T_LH)*4*pi*arc_length(j,k);
        end
    end
end
%Get F and T for nonrotating flagellum
omega = 0.0;    %Set rotation rate to zero
V = 1.0;        %Set velocity to unity
for i = 1:length(a)
    for j=1:length(lambda)
        for k= 1:length(L)
            [F_LH, T_LH] = SBT_helical_Lighthill(a_lambda(i,j), theta(j),
nlength(j,k), res, omega, V);
            drag_LH(i,j,k)=sum(F_LH)*4*pi*arc_length(j,k);
        end
    end
end
% save Length_Dep_SBT_Data.mat force_LH torque_LH drag_LH force_J torque_J drag_J
lambda L a R


%%%%%%%%%%%%%%%%%%%%%%%%%%%%%%%%%%%%%%%%%%%%%%%%%%%%%%%%%%%%%%%%

function [F, T] = SBT_helical_Johnson(a_lambda, theta, nlength, res, omega, V)
%
% Input arguments:
%   -a_lambda is the ratio of filament radius "a" to the wavelength
%       "lambda", i.e., a_lambda=a/lambda
%   -theta is the pitch angle
%   -nlength is the axial length of helix in the unit of its wavelength
%       for one period of helix, nlength = 1.
%       when nlength is a vector, it stores the length of a set of helixes
%       to compute for the force.
%   -res is the number of meshes per wave length, typally I set res=20.
%
```

```
%   -omega is the linear rotation speed
%   -V is the translation speed
%
% Output arguments:
%   -F, T are the mean forces per arclength along the translation and rotation
%       directions, respectively. which are stored as vectors of the same size as
%       as nlength.
%       *Note that these output forces are normalized by 4 pi mu R
%
%   vphi is the mesh of helical phase, which is stored as a vector
%
    function m = rotmatrix(angle)
        m=[cos(angle), sin(angle), 0; -sin(angle), cos(angle), 0; 0, 0, 1];
    end
F=zeros(size(nlength));
T=zeros(size(nlength));
for k=1:numel(nlength)

phimin=0; phimax=nlength(k)*(2*pi);
xi=@(phi) sqrt(2 - 2*cos(phi(2)-phi(1))+(phi(2)-phi(1))^2/(tan(theta)^2));
fx12=@(phi) [cos(phi(1))-cos(phi(2)), sin(phi(1))-sin(phi(2)), (phi(1)-
phi(2))/tan(theta)];
px12=@(phi) (rotmatrix(phi(1))*(fx12(phi)'*fx12(phi))*rotmatrix(-
phi(2))/xi(phi)^3+rotmatrix(phi(1)-phi(2))/xi(phi));
nres=floor(nlength(k)*res+.5);
dphi=(phimax-phimin)/nres;
vphi=phimin+.5*dphi:dphi:phimax-.5*dphi;
mattr=zeros(3*nres, 3*nres);
epsilon=a_lambda*cos(theta)/nlength(k);
cl0=-log(epsilon)-.5;
for i=1:nres
cnt=abs([1:nres]-i);
cnt=cnt(find(cnt>0));
cl=cl0-.5*sum(ones(1, nres-1)./cnt);
mattr(i,i)=1+cl;
mattr([nres+i, 2*nres+i], [nres+i, 2*nres+i])=[cos(theta)^2+(1+sin(theta)^2)*cl,
(cl-1)*sin(theta)*cos(theta); (cl-1)*cos(theta)*sin(theta),
sin(theta)^2+(1+cos(theta)^2)*cl];
end
for i=1:nres
for j=1:nres
if i==j
continue;
end
mattr([i, nres+i, 2*nres+i], [j, nres+j, 2*nres+j])=px12([vphi(i),
vphi(j)])*dphi*.5/sin(theta);
end
end
v=zeros(1, 3*nres);
v(nres+1:2*nres)=omega;
v(2*nres+1:3*nres)=V;
f=mattr\v';
F(k)=sum(f(2*nres+1:3*nres));%/nres;
T(k)=sum(f(nres+1: 2*nres));%/nres;
end
end
%%%%%%%%%%%%%%%%%%%%%%%%%%%%%%%%%%%%%%%%%%%%%%%%%%%%%%%%%%%%%%%%%%%%%%%%%%%%

function [F, T] = SBT_helical_Lighthill(a_lambda, theta, nlength, res, omega, V)
%
% Input arguments:
%   -a_lambda is the ratio of filament radius "a" to the wavelength
```

```
%       "lambda", i.e., a_lambda=a/lambda
%   -theta is the pitch angle
%   -nlength is the axial length of helix in the units of wavelength
%       for one period of the helix, nlength = 1.
%       when nlength is a vector, it stores the length of a set of helixes
%       to compute for the force.
%   -res is the number of meshes per wave length, typally I set res=20.
%
%   -omega is the linear rotation speed
%   -V is the translation speed
%
% Output arguments:
%   -F, T are the mean forces per arclength along the translation and rotation
%       directions, respectively. which are stored as vectors of the same size as
%       as nlength.
%       *Note that these output forces are normalized by 4 pi mu R
%

    function m = rotmatrix(angle)
        m=[cos(angle), sin(angle), 0; -sin(angle), cos(angle), 0; 0, 0, 1];
    end
F=zeros(size(nlength));
T=zeros(size(nlength));
for k=1:numel(nlength)

phimin=0; phimax=nlength(k)*(2*pi);
xi=@(phi) sqrt(2 - 2*cos(phi(2)-phi(1))+(phi(2)-phi(1))^2/(tan(theta)^2));
fx12=@(phi) [cos(phi(1))-cos(phi(2)), sin(phi(1))-sin(phi(2)), (phi(1)-
phi(2))/tan(theta)];
px12=@(phi) (rotmatrix(phi(1))*(fx12(phi)'*fx12(phi))*rotmatrix(-
phi(2))/xi(phi)^3+rotmatrix(phi(1)-phi(2))/xi(phi));
nres=floor(nlength(k)*res+.5);
dphi=(phimax-phimin)/nres;
vphi=phimin+.5*dphi:dphi:phimax-.5*dphi;
mattr=zeros(3*nres, 3*nres);
cutofflen=a_lambda*pi*exp(0.5)*cos(theta);
cl=log(.5*dphi/cutofflen);
for i=1:nres

mattr(i,i)=1+cl;
mattr([nres+i, 2*nres+i], [nres+i, 2*nres+i])=[cos(theta)^2+(1+sin(theta)^2)*cl,
(cl-1)*sin(theta)*cos(theta); (cl-1)*cos(theta)*sin(theta),
sin(theta)^2+(1+cos(theta)^2)*cl];
end
for i=1:nres
for j=1:nres
if (abs(vphi(i)-vphi(j))<cutofflen+.5*dphi)
continue;
end
mattr([i, nres+i, 2*nres+i], [j, nres+j, 2*nres+j])=px12([vphi(i),
vphi(j)])*dphi*.5/sin(theta);
end
end
v=zeros(1, 3*nres);
v(nres+1:2*nres)=omega;
v(2*nres+1:3*nres)=V;
f=mattr\v';
F(k)=sum(f(2*nres+1:3*nres));%/nres;
T(k)=sum(f(nres+1: 2*nres));%/nres;
end
end
```

I. HX711 PROGRAM

```
#include "HX711.h"                  // Biblioteca HX711

#define DOUT  A0                    // HX711 DATA OUT = pino A0 do Arduino
#define CLK  A1                     // HX711 SCK IN = pino A1 do Arduino

HX711 balanca;          // define instancia balança HX711

float calibration_factor = 42130;     // fator de calibração para teste inicial

void setup()
{
  Serial.begin(9600);           // monitor serial 9600 Bps
  balanca.begin(DOUT, CLK);      // inicializa a balança
  Serial.println();             // salta uma linha
  Serial.println("HX711 - Calibracao da Balança");                // imprime no monitor
serial
  Serial.println("Remova o peso da balanca");
  Serial.println("Depois que as leituras começarem, coloque um peso conhecido sobre a
Balança");
  Serial.println("Pressione a,s,d,f para aumentar Fator de Calibração por
10,100,1000,10000 respectivamente");
  Serial.println("Pressione z,x,c,v para diminuir Fator de Calibração por
10,100,1000,10000 respectivamente");
  Serial.println("Após leitura correta do peso, pressione t para TARA(zerar) ");

  balanca.set_scale();                                  // configura a escala da Balança
  zeraBalanca ();                                      // zera a Balança
}

void zeraBalanca ()
{
  Serial.println();                                    // salta uma linha
  balanca.tare();                                      // zera a Balança
  Serial.println("Balança Zerada ");
}

void loop()
{
  balanca.set_scale(calibration_factor);                  // ajusta fator de calibração
  Serial.print("Peso: ");                               // imprime no monitor serial
  Serial.print(balanca.get_units(), 3);                   // imprime peso da balança com 3
casas decimais
  Serial.print(" kg");
  Serial.print("      Fator de Calibração: ");             // imprime no monitor serial
  Serial.println(calibration_factor);                    // imprime fator de calibração
  delay(500) ;                                         // atraso de 0,5 segundo

  if (Serial.available())                              // reconhece letra para ajuste do fator de
calibração
```

```
#include "HX711.h"                  // Biblioteca HX711

#define DOUT  A0                    // HX711 DATA OUT = pino A0 do Arduino
#define CLK  A1                     // HX711 SCK IN = pino A1 do Arduino

HX711 balanca;          // define instancia balança HX711

float calibration_factor = 42130;     // fator de calibração para teste inicial

void setup()
{
  Serial.begin(9600);           // monitor serial 9600 Bps
  balanca.begin(DOUT, CLK);      // inicializa a balança
  Serial.println();             // salta uma linha
  Serial.println("HX711 - Calibracao da Balança");                // imprime no monitor
serial
  Serial.println("Remova o peso da balanca");
  Serial.println("Depois que as leituras começarem, coloque um peso conhecido sobre a
Balança");
  Serial.println("Pressione a,s,d,f para aumentar Fator de Calibração por
10,100,1000,10000 respectivamente");
  Serial.println("Pressione z,x,c,v para diminuir Fator de Calibração por
10,100,1000,10000 respectivamente");
  Serial.println("Após leitura correta do peso, pressione t para TARA(zerar) ");

  balanca.set_scale();                                  // configura a escala da Balança
  zeraBalanca ();                                      // zera a Balança
}

void zeraBalanca ()
{
  Serial.println();                                   // salta uma linha
  balanca.tare();                                     // zera a Balança
  Serial.println("Balança Zerada ");
}

void loop()
{
  balanca.set_scale(calibration_factor);                  // ajusta fator de calibração
  Serial.print("Peso: ");                               // imprime no monitor serial
  Serial.print(balanca.get_units(), 3);                   // imprime peso da balança com 3
casas decimais
  Serial.print(" kg");
  Serial.print("      Fator de Calibração: ");             // imprime no monitor serial
  Serial.println(calibration_factor);                    // imprime fator de calibração
  delay(500) ;                                        // atraso de 0,5 segundo

  if (Serial.available())                               // reconhece letra para ajuste do fator de
calibração
```

```
  {
    char temp = Serial.read();
    if (temp == '+' || temp == 'a')               // a = aumenta 10
      calibration_factor += 10;
    else if (temp == '-' || temp == 'z')          // z = diminui 10
      calibration_factor -= 10;
    else if (temp == 's')                         // s = aumenta 100
      calibration_factor += 100;
    else if (temp == 'x')                         // x = diminui 100
      calibration_factor -= 100;
    else if (temp == 'd')                         // d = aumenta 1000
      calibration_factor += 1000;
    else if (temp == 'c')                         // c = diminui 1000
      calibration_factor -= 1000;
    else if (temp == 'f')                         // f = aumenta 10000
      calibration_factor += 10000;
    else if (temp == 'v')                         // v = dimuni 10000
      calibration_factor -= 10000;
    else if (temp == 't') zeraBalanca ();         // t = zera a Balança
  }
}
```